INTEGRATED ANALYSIS OF STEEL BUILDINGS UNDER FIRE AND EXPLOSION

A thesis submitted for the degree of

Doctor of Philosophy

in the Faculty of Engineering
of the University of London

by

Limin Song BSc, MSc

Civil Engineering Department

Imperial College of Science Technology and Medicine

May 1998

DEDICATION

To my parents
for their love, affection and support
To my husband
for his love, care and patience

ABSTRACT

This thesis describes the development of an integrated environment for the nonlinear analysis of steel building structures subjected to explosion and fire. The proposed environment is implemented within the nonlinear analysis program ADAPTIC, where adaptive techniques are utilised to achieve accurate and simultaneously efficient analysis.

The deterioration in material properties of steel at elevated temperatures is considered first. Three material models are developed, providing various degrees of efficiency and accuracy, with consideration also given to the effect of creep at elevated temperatures. Verification is carried out against available experimental results on the member and the structural levels. In all cases, computational predictions show good agreement with the experimental results.

The material model for steel at elevated temperature is then extended to account for the strain-rate effect by utilising an existing rate-sensitive model. An integrated analysis environment is developed for steel frames under the successive actions of explosion and fire loading, utilising adaptive analysis techniques.

The integrated environment for steel frames is enhanced by considering the effect of the composite floor slab on the structural response. A novel slab formulation is developed which employs the concepts of two-level interpolation, on the level of one element and one block, and of additional rib freedoms. These two concepts lead to a realistic elastic composite slab element. Examples are presented to illustrate the significance of these new concepts in representing the 'geometric orthotropy' of composite slabs. Furthermore, very good agreement is established against available experimental results in the linear elastic range.

The full-scale fire test carried out by BRE with a natural fire is used to calibrate the developed nonlinear fire analysis tools implemented within ADAPTIC. Good agreement is shown between the analytical predictions and the experimental results. A parametric study is also performed to investigate the effect of blast on the fire resistance of steel columns and frames. This study shows that blast can significantly reduce the resistance of steel frames to fire, although in some cases it can have a favourable influence on fire resistance of columns.

IMPERIAL COLLEGE LONDON UNIV

ACKNOWLEDGEMENTS

No in-depth work of research is possible without accumulating a debt of gratitude to many people; while such debts vary in size, they are enduring and will be honoured always.

Acknowledgement is due to my supervisors Dr. Bassam A Izzuddin and Prof. Amr Elnashai. Dr. Izzuddin has given constantly guidance, without which many of the ideas in this work would not have fallen into shape. I am deeply grateful for his supervision. I am truly grateful to Prof. Elnashai, who has always been supportive and taken a keen interest in the success of my work.

Prof. Dowling and EPSRC are gratefully acknowledged for the grant (GR/J14134) under which this research work was undertaken.

During my years in Imperial College, I have made friends, many of whom deserve my warmest thank for the support they have offered. I particularly would like to thank Mr. Manfred Schüetze and Miss Amel Siyam for their care and friendship and Ms Sue Peneycad for always being there to help. Also my thanks go to my colleagues Mrs Marilyn Treadaway, Ms Alison Ahearn, Andy Dixion, Jon Parkinson, Dr. Mohammed Sidam (then a PhD candidate), Maria and others in Room 317A for providing cheerful smiles, help and advice whenever consulted.

This thesis would never have come into being without the entire and endless support of my parents. My love, respect and gratitude to them is beyond words.

The most special acknowledgement is due to my husband, Fancheng, for his unwavering support, help, care and patience. These acknowledgements would not be complete if I did not mention my dear son Jiakai, who not only brings enormous happiness into my life, but also gave me impetus to complete this PhD.

TABLE OF CONTENTS

Abstract 3

Acknowledgements 4

Table of Contents 5

Chapter 1 Introduction 12

1.1 Background 12

1.2 Blast And Fire Resistance Design 13
1.2.1 Blast Resistance Design 13
1.2.2 Fire Resistance Design 14

1.3 Behaviour of Steel Structures under Blast and Fire 16
1.3.1 Structural Response under Blast 16
1.3.1.1 Explosion loading 16
1.3.1.2 Structural response 17
1.3.2 Structural Response under Fire 18
1.3.2.1 Fire Loading 18
1.3.2.3 Structural Response 18

1.4 Study on Structural Response under Fire 19
1.4.1 Experimental Approaches 19
1.4.1.1 Standard Fire Tests on Structural Members 19
1.4.1.2 Small Scale and Full Scale Fire Tests 20
1.4.2 Analytical Approaches 21
1.4.2.1 Deformational Approach 22
1.4.2.2 Numerical Approach 25

1.5 Nonlinear Analysis 27
1.5.1 Conventional Nonlinear Analysis 28
1.5.2 Adaptive Analysis Approach 28
1.5.3 Adaptive Nonlinear Analysis Program ADAPTIC 28

1.6 Objectives and Originality of the Present Work 30

1.7 Organisation of the Thesis 31

Chapter 2 Modelling Steel Behaviour at Elevated Temperatures 33

2.1 Thermal Strain 33

2.2 Poisson's Ratio 35

2.3 Steel Behaviour 35

2.4 Material Modelling 37
2.4.1 Stress-strain-temperature Relationship 37
2.4.1.1 Stress-strain at room temperature 37
2.4.1.2 Stress-strain at elevated temperatures 39
2.4.2 Young's Modulus E 40
2.4.3 Effective Yield Stress 40
2.4.4 Strain-hardening 41

2.5 Bilinear Material Model 42
2.5.1 Basic Assumptions 42
2.5.2 Details of Bilinear Material Model 43
2.5.2.1 Strain component 44
2.5.2.2 Determination of stress 44
2.5.2.3 Yield Strength 45
2.5.2.4 Evaluation of plastic strain 45
2.5.2.5 Tangent modulus 46
2.5.3 Implementation into ADAPTIC 46
2.5.4 Examples 47
2.5.4.1 Stress-strain relationship at elevated temperatures 49
2.5.4.2 Loading and unloading 50

2.6 Elliptical Material Model 52
2.6.1 Basic Assumptions 52
2.6.2 Details of Model 54
2.6.2.1 Strain component 54
2.6.2.2 Determination of stress 54
2.6.2.3 Plastic strain 55
2.6.2.4 Proportional limit 55
2.6.2.5 Tangent modulus 56
2.6.3 Implementation into ADAPTIC 56
2.6.4 Examples 57
2.6.4.1 Stress-strain relationship at elevated temperatures 57
2.6.4.2 Loading and unloading 58

Chapter 3 Modelling Creep Effects 61

3.1 Creep Models of Steel 61
3.1.1 Steady State Creep Response 62
3.1.2 Transient Creep Response 65
3.1.2.1 Time-hardening 67
3.1.2.2 Strain-hardening 67
3.1.2.3 Work-hardening 68
3.1.2.4 Life-fraction rule 68
3.1.2.5 State variable 69

3.2 Adopted Creep Model 70

3.3 Implementation into ADAPTIC 72

3.4 Verification Examples 72
3.4.1 Verification on Material Level 74
3.4.1.1 Linearly varying stress 74
3.4.1.2 Stepped stress 74
3.4.2 Effect of Heating Rate 76

Chapter 4 Analysis of Steel Frames under Fire Conditions 78

4.1 Verification Against Experimental Results 78
4.1.1 Verification against Experiments on Individual Members 78
4.1.1.1 Members with uniform temperature 78
4.1.1.2 Member with temperature gradient 82
4.1.2 Verification against Experiments on Frames 85

4.2 Illustrative Examples 91
4.2.1 One Bay Frame 91
4.2.2 Three Storey Frame 92

4.3 Conclusions 94

Chapter 5 Integrated Nonlinear Analysis Environment for Combined Explosion and Fire Loading 95

5.1 Modelling Steel Behaviour under Explosion and Fire 95
5.1.1 Rate-sensitive Response of Steel 96
5.1.1.1 Elastic behaviour 96
5.1.1.2 Plastic behaviour 97
5.1.1.3 Effect of temperatures 98
5.1.2 Rate-sensitive Models 98
5.1.2 Adopted Rate-sensitive Model 99
5.1.3 Thermal Model 101

5.2 Integrated Analysis Environment 101

5.3 Adaptive Explosion and Fire Analysis 101
5.3.1 Elastic Formulation 102
5.3.2 Elasto-plastic Formulation 103
5.3.3 Adaptive Procedure 104
5.3.3.1 Accuracy checking 105
5.3.3.2 Automatic subdivision 106

5.4 Illustrative Examples 106
5.4.1 Three-storey Frame under Explosion and Fire 106

5.4.2 Four Storey Frame under Fire Condition 109

5.6 Discussion 115

Chapter 6 Analysis of Composite Steel Decked Slab 116

6.1 Introduction 116
6.1.1 Background 116
6.1.2 Review of Previous Research Work 119
6.1.3 Overview of the Proposed Work 121

6.2 Element Formulation 121
6.2.1 Basic Assumptions 121
6.2.2 Element Geometry 123
6.2.3.1 Two level displacement interpolation 124
6.2.3.2 Displacement interpolation over block domain 125
6.2.3 Rib Freedoms 128
6.2.4 Kinematics for Trapezoidal Ribs 129
6.2.5 Strains 131
6.2.5.1 Concrete slab cover 132
6.2.5.2 Concrete ribs 134
6.2.5.3 Steel decking 135
6.2.6 Element Stiffness 135

6.3 Thermal Effect 138
6.3.1 Temperature Field 139
6.3.2 Thermal Stresses 139

6.4 Uniformly Distributed Loading 140

6.5 Applicability of Proposed Element 141

Chapter 7 Verification of the Slab Element 142

7.1 Uniform Slab 142
7.1.1 Axial Force 143
7.1.2 Vertical Load 143
7.1.3 Moment 144

7.2 Significance of Two Level Displacement Interpolation 146

7.3 Ribbed Concrete Slab — Longitudinal Direction 148
7.3.1 Prescribed Displacement Field 148
7.3.2 Vertical Edge Load 150

7.4 Ribbed Concrete Slab — Transverse Direction 151
7.4.1 Case A: ($w_r \rightarrow 0$) 151

7.4.2 Case B: ($s \rightarrow 0$) 156

7.5 Effect of Rib Depth on Longitudinal and Transverse Response 162

7.6 Thermal Effects 165
7.6.1 Uniform Expansion 165
7.6.2 Thermal Gradient 166

7.7 Effect of Number of Elements on Accuracy 168
7.7.1 Cantilever 168
7.7.2 Slab Supported on Steel Beams 169

7.8 Effect of Rib Depth on Load Distribution 170

7.9 Continuously Spanned Slab 172

7.10 Verification Against Experimental Results 175
7.10.1 Description of Test 175
7.10.2 Analysis of the Tested Slabs 177

7.11 Summary 179

Chapter 8 Calibration against Cardington Full-scale Fire Test 180

8.1 The Full-scale Test 180
8.1.1 Compartment Configuration 180
8.1.1.1 Beams and Columns 182
8.1.1.2 Slab 183
8.1.2 Compartment Temperatures 184
8.1.2.1 Columns 184
8.1.2.2 Beams 184
8.1.2.3 Slab 184
8.1.3 Displacement Response 189

8.2 Modelling the Compartment Test 189
8.2.1 Material Properties 190
8.2.1.1 Steel 190
8.2.1.2 Concrete 192
8.2.2 Structural Model 192
8.2.2.1 Bare steel frame model 192
8.2.2.2 Steel frame with slab 193
8.2.2.3 Compartment slab represented by beams 193
8.2.3 Temperature Profile Used in Analysis 195
8.2.3.1 Temperature along member length 195
8.2.3.2 Temperature over cross section 196
8.2.3.3 Temperature-time history 197
8.2.3.4 Temperature in slab 197
8.2.3.5 Comparison between applied and measured temperature 197

8.2.4 Loading 201
8.2.4.1 Distributed load on beam/slab 201
8.2.4.2 Loads on columns 202

8.3 Conducted Analyses 203
8.3.1 Skeletal Steel Frame 203
8.3.2 Compartment Slab Represented by Beams 203

8.4 Results 204

8.5 Conclusions 206

Chapter 9 Parametric Study on Structures under Fire and Explosion 208

9.1 Column Under Blast and Fire 208
9.1.1 Material Properties 209
9.1.2 Loading 210
9.1.3 Parameteric Study 210
9.1.4 Results 211

9.2 Steel Frame under Explosion and Fire 214
9.2.1 Material Properties 215
9.2.2 Loading 215
9.2.3 Parametric Study 215
9.2.4 Results 216

Chapter 10 Summary and Conclusions 219

10.1 Nonlinear Material Models for Elevated Temperature 219
10.1.1 Bilinear Model 220
10.1.2 Elliptical model 220
10.1.3 Creep Model 221
10.1.4 Combined Material Model for Rate-sensitivity and Elevated Temperatures 221

10.2 Formulation For Steel Decked Composite Slab 221

10.3 Integrated Adaptive Analysis of Steel Frames Subject to Fire and Explosion 222

10.4 Verification and Calibration 222
10.4.1 Verification on Beams 223
10.4.2 Verification on Scaled Frame Tests 223
10.4.3 Calibration against the Cardington Full-scale Fire Test 223

10.5 Parametric Study 224

10.6 Future Work 224

Reference 226

Appendix A Parameters in Material Models 239

A.1 Bilinear Model 239

A.2 Elliptical Model 241

A.3 Creep Model 242

Appendix B Parameters for the Slab Element 243

B.1 Geometry 243

B.2 Slab Element 243

Appendix C Block Internal Displacements 245

CHAPTER 1
INTRODUCTION

Building structures are frequently subjected to unexpected events of fire and blast. To safeguard human life and minimise substantial loss of possessions in such events, it is important that buildings are designed with adequate fire and blast resistance; this is normally achieved through applying various codes of practice enforced by building regulations. The statutory provisions are continually optimised along with improvements in the understanding of the structural behaviour under fire and blast conditions. Both of these rely heavily on the development and application of new nonlinear analysis methods.

This chapter begins by providing an overview of the requirements of blast and fire resistance design, covering a brief description of the design philosophy and summarising the design criteria in various design codes. Discussion then moves onto the structural behaviour under explosion and fire, with particular attention given to the structural response under fire loading. The concept of fire resistance is then introduced, and experimental and analytical approaches for determining the fire resistance of steel members are summarised. This is followed by a review of previous research work in the field of fire engineering.

Nonlinear analysis methods are subsequently discussed, emphasising the advantages of adaptive analysis methods over the conventional nonlinear analysis approach in terms of modelling and computational efficiency. The capabilities of the nonlinear analysis program ADAPTIC (Izzuddin, 1991), developed at Imperial College, are then briefly discussed, as it provides the main implementation platform for the present work.

This chapter concludes with a description of the objectives, originality and arrangement of the work in this thesis.

1.1 BACKGROUND

Developed societies have become highly dependent on complex and vulnerable systems, for example gas pipelines and large shopping and business centres. The structures used for these systems inevitably face the risk of potential damage from incidents such as fire and explosion. An accident survey on explosions reported by

Bangash (1993) showed that, between 1966 and 1989, there were over 120 explosions in the UK alone. Damage in such incidents can be substantial, as evidenced by the explosions at the Ronan Point multi-storey building in London, which claimed several lives in 1968, and at the Piper Alpha oil platform in the North Sea, which occurred in July 1988.

These two events had one thing in common: the explosion was accompanied by fire. Although it is very well known that a fire often accompanies an explosion, the current building regulations treat them as separate events; in other words, structures are designed to resist explosion in the absence of fire, and fire in the absence of explosion. A general question that should be asked, however, is whether the fire resistance of a structure is affected if the fire commences after an explosion. If so, does the structure designed with the required fire resistance still possess at least the same fire resistance capacity when subjected to a combined explosion and fire? To answer these questions, not only do we require an understanding of the structural response under fire, but also an integrated environment which can predict the structural behaviour under combined fire and explosion loading. The development of such an environment has been one of the main motivations for this work.

1.2 BLAST AND FIRE RESISTANCE DESIGN

In structural design, both explosion and fire incidents are treated as unusual events. However, due to their different natures, the discussion pertinent to blast and fire will be presented separately in the following sections.

1.2.1 Blast Resistance Design

The prime objective in designing blast resistant structural elements is to provide sufficient ductility to enable the element to deflect by an amount consistent with the degree of damage permitted. This entails an initial design based upon extensive flexural plastic deformation. In so deforming, the element should not fail prematurely due to other load effects, for example shear or local instability (Mays, 1995; Jackson, et al., 1995). Therefore, when designing structural elements against blast loading in accordance with limit state principles, some plastic deformation is normally permitted for economic reasons. The level of damage is normally specified in terms of member deflection at mid span, or rotation at the supports. A limit is usually placed on the damage of members to permit some functionality after the event (Mays, 1995). In this way, the degree of damage sustained by the element may be controlled. The damage

level that may be tolerated depends on what is to be protected, for example, the structure itself, the occupants of the building or the facilities within the building.

There are two methods by which limiting element deformations may be specified. The first employs the rotation θ at the support, while the second uses the ductility ratio μ, defined as follows:

$$\mu = \frac{\text{total deflection}}{\text{deflection at elastic limit}} \tag{1.1}$$

Typically, limiting deformations for reinforced concrete elements are expressed in terms of support rotations, whilst ductility ratios are used for structural steel elements (Mays, 1995).

In addition to the previous considerations for individual elements, there remains a requirement for the overall structure to retain its stability when subjected to blast loading. TM5-1300 (1990) recommends that the maximum member end rotation θ should be 2° and the maximum side sway deflection δ should be limited to 1/25 of the storey height H in framed steel structures. The Building Regulations (HMSO, 1985) specify that a local collapse should not prejudice the overall stability of a structure, since the ability of the building to survive without collapse, except in the immediate locality of the explosion, will save lives and assist the rescue of those trapped. This requirement was included as a result of the collapse of the Ronan Point block of flats in 1968, caused by a gas explosion.

1.2.2 Fire Resistance Design

It is necessary to introduce the concept of *fire resistance* before moving to fire resistance design. The fire resistance of a structure is given in terms of the length of time for which the structure can perform its function without either local or overall failure during a fire, or in terms of the maximum temperature that the structure can withstand. This covers the imposition of stability and integrity on the structure as a whole, or in part, during a fire.

BS 5950, Part 8 (1990), recommends that the fire resistance of members may be determined by either of the following methods:

1) fire test in accordance with BS 476, Parts 20 and 21(BSI, 1987) for all types of members;

2) calculation in the case of hot finished steel members only.

In the case of load bearing beams, British Standard BS476 Part 20 (1987) gives two displacement criteria which can be used to established the member fire resistance, whichever is exceeded first:

1) a deflection of $L/20$; or

2) a rate of deflection, calculated over 1 min intervals from the start of the heating period, given by:

$$\text{rate} = \frac{L^2}{9000d} \tag{1.2}$$

except that this rate of deflection limit shall not apply before a deflection of $L/30$ is achieved,

where L is the clear span of the member in mm, and d is the cross section depth.

The traditional approach is to design the structure for ambient temperature, ignoring fire in the structural calculations. As a result, in order to satisfy the fire resistance requirement, it is always necessary to protect steel structures to ensure that the material remains cool during fire, thus preventing the structure from losing its rigidity and load-bearing capacity (Robinson, 1995). The extent of fire protection depends largely on the level of loading considered with fire, and its cost may sometimes be even more expensive than the structure itself.

In view of the above, it was decided to design the structure itself to withstand fire. Instead of ignoring the effects of fire in design calculations and applying fire protection, it was considered rational to use the properties of steel at elevated temperatures in the calculations, accepting that the structure will become hot (Robinson, 1995). In doing so, it became possible to minimise, even eliminate, the need for fire protection and reallocate the resources spent on passive protection to other more effective life safety measures. This design philosophy of considering temperature attended by the structures was revolutionary in fire resistance design, and was incorporated in the design code BS5950: Part 8 (1990) and EC3, Part 1.2 (1993), enabling more economic design of structures against fire. A new concept for designing steel structures against fire is to compare the fire resistance of the structure against the fire resistance requirement imposed by the Authority (Cooke, 1987), which requires the ability to predict the structural response under fire.

Unfortunately, the current design approaches deal with structural members as individual elements. In reality, members exposed to fire are not the isolated beams or columns that are tested in standard fire tests, but are part of a larger structure, much of which may remain cold and may support the fire weakened members. Comprehending the interaction effects between members would undoubtedly lead to safer and more cost effective design of fire resistant structures.

In view of the above, it is important for designers to have access to accurate and efficient analytical tools which can predict the overall structural response to fire, not just that of individual elements. The development of such analytical tools is an essential step towards the development of an integrated fire safety design philosophy for steel framed buildings.

1.3 BEHAVIOUR OF STEEL STRUCTURES UNDER BLAST AND FIRE

Irrespective of the criteria used in design, it is important to be able to establish the structural response under blast and fire, from test or analysis. The main characteristics of the response of steel structures to blast and fire are discussed below.

1.3.1 Structural Response under Blast

Explosion affects structures at both material and structural levels. Overpressures generated in an explosion lead to dynamic effects in the structural response. On the other hand, the material experiences deformation over a very short duration, hence the high strain rate, which can modify the response of rate-sensitive materials such as steel.

1.3.1.1 Explosion loading

The explosion is mainly characterised by two parameters, namely the maximum pressure and the rate of pressure rise. Important references on explosion loading include the works of Mays and Smith (1995), Smith and Hetherington (1994), and Bangash (1993).

The pressure pulse generated by a condensed high explosive has almost zero rise time while that generated by the explosion of fine dust or gas is characterised by a finite rise time and a somewhat longer duration. This is illustrated in Figure 1.1 (Smith & Hetherington, 1994), in which pressure-time histories for a 1 kg charge of TNT and a

vented confined natural gas explosion in a cubical enclosure, containing energy equivalent to 1 kg TNT, are compared.

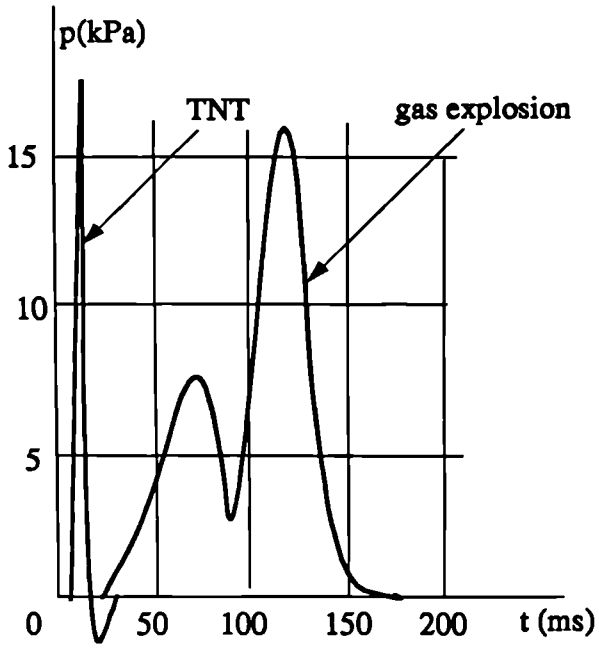


Figure 1.1 Comparison of pressure time histories for TNT and gas explosion of equivalent energy (from Smith and Hetherington, 1994)

As for the maximum pressure, most hydrocarbon gases, when mixed with air at atmospheric pressure, can produce a pressure of more than 800 kPa on ignition (Smith & Hetherington, 1994). The explosion reaction of a condensed high explosive, on the other hand, generates hot gas, producing a pressure between 10 and 30 GPa and at a temperature of about 3000 - 4000°C (Smith, 1995).

1.3.1.2 Structural response

The response of structures to blast loading (a form of dynamic loading) has been studied extensively. A large number of references (Paz, 1980; Irvine, 1986; Thomson, 1988; Berg, 1989) deal with the subject comprehensively.

Blast loading is transient, so both the ductility and natural period of vibration of a structure govern its response to a given explosion (Jackson, et al., 1995). In general, a taller building will have a lower natural frequency, and thus a longer response time in relation to the duration of the load. Individual elements, such as columns and beams, will have natural response times close to the loading duration.

Ductile elements made of steel and reinforced concrete can absorb considerable strain energy, that is they can undergo substantial deformation without breaking, while elements made of brittle materials such as glass, brick, timber and cast-iron fail abruptly with little prior deformation.

Flexible high-mass components such as long span beams and floors can absorb a great deal of the energy delivered by a blast load. On the other hand, rigid short span light weight elements, for example conventional glazing components, are poor energy absorbers and can fail catastrophically.

1.3.2 Structural Response under Fire

The behaviour of steel structures under fire conditions is extremely complicated and involves both material and geometric nonlinearities. Traditionally, the experimental approach played an important role in the study of structural behaviour under fire. The current trend is moving towards acceptance of the analytical approach following substantial advances over the last two decades.

1.3.2.1 Fire Loading

When a steel structure is exposed to fire, the temperature in component members may increase dramatically. In general, the temperatures in structural members under fire are functions of time and the spatial position of the member. For design purposes, the thermal gradient through members is often ignored for the sake of simplicity, which means the temperature rises are entirely a function of time. However, account is taken of the proportion of the element exposed to the effects of the fire, i.e. a column or stanchion may be exposed on four sides or a beam element on three sides (Purkiss, 1996).

1.3.2.3 Structural Response

Regarding the real behaviour of steel structures in fire, it has been shown that the fire resistance of whole structures is significantly better than that of single elements on which fire resistance is universally assessed (Martin, 1994). In fact, consideration of the fire behaviour of a single member cannot give appropriate assessment of the behaviour of the whole structure in fire, as evidenced by a major fire in a 14-storey building under construction at Broadgate, London, in 1990 (The Steel Construction Institute, 1990). In this incident, the steel framed building was incomplete and so

lacked the benefit of passive or active fire protection systems. Investigations after the fire revealed that although a number of structural members in the vicinity of the fire were considerably distorted and had to be replaced, the overall structure remained intact. This highlights a very important difference between the behaviour of individual structural elements and the overall behaviour of steel-framed structures.

It is also worth noting that significant changes have taken place over the last decade regarding construction methods for steel intensive structures. In the UK, in particular, the development of composite floor systems has gained popularity. There is, however, a concern that the structural contribution of the steel deck floor system is under-utilised in current procedures, particularly for the fire limit state (Martin, 1994). It appears that developing an appropriate representation for the action of steel decked slab on the overall and local structure is critical in assessing the fire resistance of the whole structure.

1.4 STUDY ON STRUCTURAL RESPONSE UNDER FIRE

Considering the importance of determining the structural response under fire, this section will review previous work in this area, covering both experimental and analytical approaches, with particular emphasis given to steel building structures.

1.4.1 Experimental Approaches

The behaviour of steel structures may be investigated by direct experimental study. This has been mostly undertaken by subjecting the steel member to a standard fire exposure. Tests on steel frames, sub-assemblies or elements exposed to natural fire are limited due to both high cost and difficulties in setting up the test.

1.4.1.1 Standard Fire Tests on Structural Members

Traditionally, the fire resistance of a steel member is determined from the results of standard fire tests. In such tests, the load-bearing element is exposed to a standard fire in a furnace, in which the temperature is controlled to vary with time according to a prescribed standard temperature-time relationship until failure. The standard temperature-time curve, shown in Figure 1.2, has the form:

$$\theta = 20 + 345\log(8t + 1) \tag{1.3}$$

where θ is the temperature in °C, and t is the time in minutes.

The standard fire test is the generally accepted method for quantifying the fire resistance of a structural member. It has not only provided a large amount of useful data, but also, for many types of structures, it represents the only way of obtaining the information required for a structural fire resistance design (ECCS, 1983). However, such experimental methods suffer the disadvantage of being expensive and time consuming. Also a considerable variation can arise in fire resistance for the same structural element when tested in different fire laboratories with varying furnace characteristics and varying support and restraint conditions (Purkiss, 1996). More importantly, most of the fire tests have been conducted on isolated structural components due to the limitation of the size of the furnace.

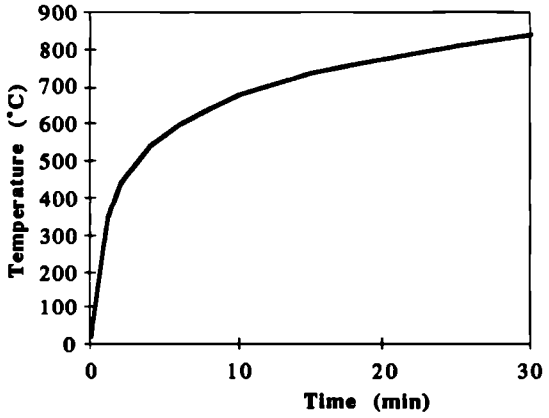


Figure 1.2 Standard furnace temperature-time response

British Steel Corporation (BSC) tested a large amount of steel members with different material properties, cross section types, loading arrangements (Wainman & Kirby, 1987). Cooke (1987) tested some small scale beams and columns to study the effect of nonlinear temperature distribution across the cross section.

1.4.1.2 Small Scale and Full Scale Fire Tests

Small scale braced and unbraced portal frames subjected to furnace fire tests were studied by Witteveen (1977). Rubert and Schumann (1986) reported a series of tests on 1/4 and 1/2 scale steel subassemblies heated along some elements. Kruppa (1981/1982) presented test results on external steel columns in a compartment fire.

Due to their high cost and complexity, full scale tests, particularly on multi-storey buildings, are rare. Cooke and Latham (1987) described a fire test on a full size, fully loaded, 2D steel frame. This test, conducted in the FRS Cardington Laboratory, was the first of its kind in Europe. In this test, a loaded portal frame, composed of 203×203UC52 columns and 406×178UB50 beam, was exposed to fire produced by burning wood cribs. The test showed that the performance of the frame was better than that of the individual elements in isolation.

In 1995, the Building Research Establishment (BRE) conducted a corner fire test on a full scale eight storey steel framed building at Cardington. The floor construction is a steel deck and in situ concrete composite floor. The fire took place on the second floor in a corner compartment, with a fire load consisting of twelve timber cribs placed within the compartment. The columns forming the boundaries of the compartment were protected so as to ensure overall structural integrity. Temperatures in steel members were recorded, and the deflection for the concrete slab was measured. This test is of great importance for studying the behaviour of a multi-storey steel framed building subjected to natural fires, and more importantly, for calibrating the analytical models whilst taking into account continuity and ductility of the overall steel frame.

Although in most circumstances, it is still very difficult to provide a complete assessment of the structural performance under fire by pure experimental means, experimental studies provide the only means to validate and calibrate various analytical models.

1.4.2 Analytical Approaches

Analytical methods provide an alternative means for predicting the structural behaviour under fire conditions. Generally, analytical methods, known as *fire engineering analysis,* have been used to establish:

1) the distribution of temperatures within the structural members and;
2) the response of the structure to prescribed temperature variation.

The first class of analysis method, known as *thermal analysis*, has been the subject of extensive research and development (Lie, 1972; Latham et al. 1987; Wickström, 1979, 1981/1982, 1985, 1986). The second class of analysis, and the subject of this thesis, may be further categorised by the approach employed in the analysis: the deformational approach or the numerical approach. A review of the two types of the

analytical approaches for predicting the structural behaviour under fire conditions is summarised below.

1.4.2.1 Deformational Approach

The deformational approach is a conventional method for analysing structural members. In this approach, the curvature of a structural member at any cross-section is first determined. The deflection of the member is then obtained by integrating the curvature along the length of the member, allowing for the different boundary conditions. Due to the complexity of the resulting equation, numerical integration techniques are used to obtain the overall member response. When used to consider structural members under fire, the same principle is used to determine the deflection at any particular time interval. At each interval, the material properties corresponding to the current elevated temperatures are adopted. By repeating these steps, the variation of the relevant deflections with time is established. The fire resistance time of the structure is determined by finding the time at which the limiting deflection or deflection rate is reached. The essence of this approach is to find the correct strain distribution, at each time interval, which satisfies both equilibrium and the compatibility requirements.

The inclusion of thermal strain, thermal stress, creep strain, residual stress and the nonlinear stress-strain relationship of steels at elevated temperatures results in a complex problem. Various simplifying assumptions have been introduced by researchers to solve the problem. The most relevant work on this is summarised below.

Harmathy (1967-a) considered a simply supported I-beam using the deformational approach. It was assumed that the deflection at mid-span was of primary interest and that the deflected shape may be approximated by a half sine wave. A linear material behaviour with reduced elastic modules varying with temperature was adopted and creep effect was considered as well.

Thor (1973) expressed the total strain at each point on the beam cross-section in terms of two unknowns: a uniform axial strain and a strain due to curvature. The creep strain was incorporated into the stress-strain relationship at elevated temperatures, which was modelled by a piece-wise linear curve. Equating internal stress resultants with externally applied loads results in a set of linear equations, from which the two strain unknowns, and thus the strain distributions across the section, are found. Iteration is

required due to the nonlinearity of the stress-strain relationship and due to the moment redistribution for indeterminate members.

Cooke (1987) approximated the displaced shape by superimposing the thermal and applied load displacement in order to consider the thermal bowing of structural members subjected to temperature gradient. The thermal displacement was considered as an initial deflection and was determined from the thermal gradient across the cross-section. A simplification made in calculating this displacement was to replace the curvilinear temperature distribution with an equivalent linear distribution. Linear elastic theory with an elevated temperature elastic modulus is used to calculated the applied load displacement.

Skowronski (1988) studied I-section beams with a linear temperature distribution across the cross-section. It was assumed that the static moment distribution along the member was known regardless of the supporting conditions, and the effect of thermal stress was ignored. The curvature of the beam was assumed to compose of 4 curvatures due to linear elastic strain, nonlinear elastic strain, creep strain and thermal strain, and the total curvature was expressed as a function of stress and temperature. The Ramberg-Osgood function was adopted to model the stress-strain-temperature relationship, and the effects of creep were considered.

The deformational approach has also been widely employed in analysing steel columns under fire conditions. The same differential equation used to determine the buckling load of columns at room temperature has commonly been adopted. It is therefore only applicable to straight columns with a uniform temperature distribution across the section and a longitudinal temperature gradient. Research has also been carried out to enable the above approach to account for the nonlinear temperature distribution across the section and along the length.

Ossenbruggen (et al, 1973) proposed a deformational method for steel columns with the temperature varying linearly over the cross sections and along the members, where the moment-thrust-curvature-temperature (M-P-ϕ-T) approach was employed.

The first step in this approach is to determine the M-P-ϕ-T relationship at a cross-section of a column. This is achieved by first assuming a curvature value at the cross-section. Using a trial and error technique, the stress distribution, which satisfies the applied axial load, is then found. The resultant moment is then obtained by integrating the stress function over the whole cross-section. A set of unique M-P-ϕ-T

relationships are thus obtained. The second step is then to find the displaced shape of the column. This is done by initially choosing the thermal bowing of the element under the temperature gradient. The moment at each cross-section is found by multiplying the applied axial force by the deflection. Using the M-P-ϕ-T curves derived above, the curvature is obtained. Integrating the curvature along the length, a new deflected shape is determined. Repeating the procedure will yield the correct deflected shape of the element once convergence is reached.

Curver et al. (1973) utilised the above described method to calculate the ultimate load of steel columns at elevated temperatures. An analytical formula was proposed for the critical stress at elevated temperature as a function of temperature and of the critical stress and the slenderness at 20°C.

Poh and Bennets (1995-a; 1995-b) also presented a method based on a moment-thrust-curvature relationship for structural members at elevated temperatures. Temperature variations over the cross section and along the member are taken into consideration through dividing the member cross section into a number of small subareas.

Skowronski (1993) formulated and solved the differential equation of buckling for steel columns during fire, particularly considering the creep effects of structural steel under a fire. It was pointed out that a temperature change in ASTM A36 steel from 450°C to 500°C results in a 300-fold increase of creep deflection rate, thus showing that creep strain can have considerable influence on the elevated temperature response.

Burgess & Najjar (1994) developed an analytical approach based on the 'Perry-Robertson' principle to investigate the behaviour of steel columns under fire conditions, including the effects of thermal gradient in the cross section.

Despite its accuracy, the complexity of the deformational approach has restricted its use mainly to single members. However, it has the conceptual advantage of providing a good qualitative description of the behaviour, allowing the parameters affecting columns in fire to be easily separated out and their influences studied. Moreover, it provides a physical basis for the simplified analysis method widely adopted in the fire engineering design codes, as represented by the BS 5950 part 8 (1991) and Eurocode 3 Part 1.2 (1993).

1.4.2.2 Numerical Approach

In contrast to the limited deformational approach, the availability of powerful computers has enabled numerical analysis based on the versatile finite element method to be used extensively. Through this technique, the inclusion of nonlinear temperature distribution across the section and along the member, the effects of material and geometric nonlinearity, thermal strain and creep strain at elevated temperatures, is made possible. The varying frame configuration with time can be obtained readily and, adopting various failure criteria, the fire resistance of the steel structure may be determined. This approach has been used by many researchers with very promising results. The versatility of the numerical method enables its application for undertaking detailed study on various aspects of the structural behaviour.

Setti (1983) developed a numerical method for steel beam-columns with uniform temperature. In this method, the column is made of rigid parts connected by elementary cells in which both axial and flexural flexibility are considered. The material was assumed to have elastic-perfectly plastic behaviour.

Burgess, Elrimawi & Plank (1988, 1990, 1991) developed a secant stiffness method to study steel beams under fire, with the Ramberg-Osgood adopted for the material properties at elevated temperatures. The effects of thermal gradient, structural continuity and boundary conditions on the fire resistance were studied. It was concluded that they had a significant effect on the fire resistance.

Olawale and Plank (1988) used the finite strip method to find the bifurcation load of steel columns in fire. In their study, consideration was given to both local and overall buckling modes, as well as the interaction between them.

Burgess *et al.* (1993) considered the buckling of perfect pin-ended struts in fire using the finite strip method. Although limited in scope by its initially perfect nature, this approach is capable of considering local buckling of the flange as well as overall bifurcation instability.

Chou and Lin (1992) developed a method for the quantitative evaluation of the response of unprotected flexibly jointed steel frames. The effects of thermal, plastic strains, creep, and rotational stiffness of the connections were considered. The inelastic beam-column theory was used to formulate the analytical model. The characteristics of

the flexible joints were determined using experimental data on steel beam-to-column connection (Chen & Kishi, 1986).

Using the finite element method, a number of formulations or computer packages were developed (Cheng & Mak, 1975; Cheng, 1983; Jain & Rao, 1983; Wang & Moore, 1995; Saab & Nathercot, 1991; Kouhia et al., 1988; Liu, 1996). The accuracy of the method mainly depends on the models adopted to simulate the nonlinear material properties and the creep law.

The numerical approach has been used extensively in simulating tested structures. Rubert et al. (1986) investigated the critical temperature of plane frames under fire action by using the finite element method. Cooke and Latham (1987) studied numerically the frame tested at FRS (Fire Research Station). Franssen et al. (1995) reported the results of a number of numerical simulations of the behaviour of a full-size, two dimensional steel frame in a real fire.

More importantly, the numerical approach can then be used to assess the structural damage to a steel structure caused by a fire and to determine the residual structural capacity of the fire damaged structure. The information obtained from such a detailed analysis is very useful in the future development of a simple and rational procedure for fire safety design.

Cheng (1983) investigated the thermo-creep buckling behaviour of steel structures at elevated temperature. It was observed that, when the maximum temperature attained in the beam is below 800°F (427°C), the effect of creep is not significant and the deflection is caused mainly by the thermal strain components; while when the temperature is beyond 800°F, creep effect becomes significant. Beyond 1000°F (538°C), the deflection increases rapidly and the increase in deflection is mainly caused by the creep deflection, even though the instantaneous plastic strain rate also decreases rapidly at 1150°F (621°C).

Corradi et al. (1990) performed a parametric study on the iteration curves for steel beam-columns under fire conditions. The study was based on a trilinear idealisation of the uniaxial stress-strain relation for steel at elevated temperature, and aimed at assessing the influence of the slope of the hardening branch, on which results were found to be strongly dependent.

Franseen et al. (1995; 1996) used extensively a nonlinear analysis program to determine the buckling load of axially loaded members. A simple proposal was made for a buckling curve valid at elevated temperatures, similar in its form to what exists for room temperature in the Eurocode 3 Part 1.1 (1992). The ultimate load or ultimate temperature can be determined by the proposed analytical formula or directly by interpolation in tables which give the ratio between the ultimate load and the plastic load at room temperature. A severity factor of 1.2 was established for the analytical formula deduced from the numerical simulations to ensure an appropriate safety level.

Wang et al. (1995) and Wang (1997) varied various parameters in studying steel frame behaviour under fire conditions. The effect of frame continuity on the behaviour of steel columns under fire conditions was quantified. A simple method was developed to calculate the column limiting temperature, and recommendations were suggested to simplify the design procedure.

Bailey et al. (1996) investigated the ultimate behaviour of uniformly heated unrestrained simply supported beams. A series of different sections and spans were studied for different loading patterns and load ratios. The results presented indicate that both BS 5950 Part 8 and EC3 part 1.2 overestimate the limiting temperatures for unrestrained simple beams in fire resistance calculations. The influence of connection stiffness on the behaviour of steel beams in fire was also studied using a numerical approach (El-Rimawi et al., 1997). It was concluded that the connection has an important effect with significant increases in failure temperature compared with the simply supported condition. A simple approach for estimating the elevated temperature connection characteristics was suggested.

Analytical methods provide several advantages over the experimental approach once their validation and calibration against experimental results have been performed. The most obvious advantages are that the analytical method are both less time consuming and less costly. However, more importantly, analytical methods can provide a complete profile of the structural behaviour. Moreover, analytical methods are ideal for undertaking parametric studies, where the effects of parameters, such as member dimensions, material, loading etc., can be readily investigated, particularly when such investigation can be carried out at low computational cost.

1.5 NONLINEAR ANALYSIS

The structural response under explosion and fire loading involves both material and

geometric nonlinearities due to material plasticity, strain-rate effect and the influence of elevated temperatures, as well as large displacements. The primary objective of nonlinear structural analysis methods is to provide computational formulations which model the response of component members using one or more discrete units, and which can be employed within a global assembly procedure to obtain the response of the overall structure. Although several methods can be used to achieve this goal, the finite element method is considered to be the most effective, convenient and practical approach.

1.5.1 Conventional Nonlinear Analysis

In the conventional nonlinear analysis approach, analysis is based on a user-specified model of elements applied over the whole of the time domain. Therefore, a large number of computationally expensive elements has to be employed to predict the nonlinear response with reasonable accuracy. Consequently, the analysis necessitates a complex model of elements requiring considerable modelling effort and posing prohibitively expensive computational demands. The analytical works reviewed in section 1.4.2 all employ various conventional nonlinear analysis techniques.

1.5.2 Adaptive Analysis Approach

A new approach to nonlinear structural analysis, the *adaptive analysis* approach, originally proposed by Izzuddin and Elnashai (1993) for steel frames, addresses the disadvantages of the conventional approach by means of an adaptive selection of elements for the various parts of the structure and for the different stages of analysis. The adaptive procedure is based on maximising the use of computationally efficient elements, and replacing them into more computationally expensive elements only *when* and *where* the previous elements become inaccurate.

The advantages of the adaptive approach in structural modelling are significant; in the first place, a simple model of elements, often equivalent to that used in linear analysis, can be initially employed. More significantly, the computational savings have been shown to be substantial, often exceeding 75% (Izzuddin et al., 1995).

1.5.3 Adaptive Nonlinear Analysis Program ADAPTIC

The computational models developed in the present work have been implemented within the nonlinear analysis program ADAPTIC. This section is, therefore, dedicated

to providing only an essential description of this program. A detailed account of the capabilities of ADAPTIC is given by Izzuddin (1991).

ADAPTIC is an adaptive static and dynamic structural analysis program. This computer program has been developed to provide an efficient tool for the analysis of concrete, steel and composite frames accounting for geometric and material nonlinearities. It provides a range of elements generally divided into two types: quartic and cubic elements, with quartic and cubic shape functions, respectively. The quartic element assumes elastic material responses, and the cubic element elasto-plastic material responses. A more detailed description of these formulations is given in Chapter 5. Since the material models discussed in Chapters 2 and 3 are implemented within the elasto-plastic cubic formulation, the key features of this formulation are summarised below.

The cubic formulation is a fibre-based element in which the stress-strain response is considered at the material level. The element response is assembled from contributions at two Gauss points where the cross-section is discretised into a number of monitoring areas (Izzuddin & Elnashai, 1993), as illustrated in Figure 1.3 for an I-section. This formulation utilises a relationship between the direct material stresses and strains, and allows various material models to be included.

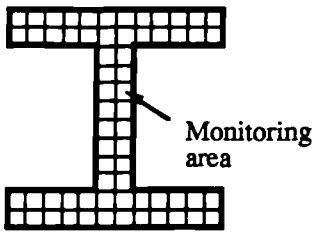


Figure. 1.3 Monitoring areas for an I-section

The cubic formulation can model the spread of plasticity within the cross-section and along the length, although at least six elements per member would be required to achieve accurate representation. In addition, this formulation is capable of modelling the variation of the elastic modulus over the cross-section, since each monitoring area can employ a different elastic modulus.

1.6 OBJECTIVES AND ORIGINALITY OF THE PRESENT WORK

This research aims at developing a computationally efficient environment for the integrated nonlinear analysis of steel frames subject to fire and explosion, and calibrating this tool against available experimental results, particularly those from the full-scale fire test carried out by the Building Research Establishment at Cardington. Once sufficient confidence in the efficiency and accuracy of this analysis tool is established, the analysis method may be employed in formulating new guidance for the design of fire and blast resistant structures. It is intended that the issues of accuracy, efficiency and integrated analysis for fire and explosion loading will be addressed through extending the nonlinear adaptive analysis program ADAPTIC (Izzuddin, 1991), developed at Imperial College.

The objectives of this work thus include extending the adaptive method to the analysis of steel frames under fire and explosion, enabling these two forms of loading to be considered in an integrated manner within the same analysis, and developing an appropriate representation of the steel decked composite slab and its influence on the overall and local structural response. The analysis tool thus developed will then be calibrated against the available experimental results, especially those from the BRE full scale fire test at Cardington. Parameteric studies will then be undertaken aimed at providing a better understanding of the structural behaviour under fire and blast, with particular consideration given to the influence of blast on the fire resistance of steel members and frames.

This work contributes to the field of analysis of steel framed structures under fire and explosion in four ways. Firstly, it leads to the development of an advanced nonlinear analysis tool capable of predicting, with sufficient accuracy and simultaneous efficiency, the behaviour of structures under fire and blast. Such a calibrated analysis tool will play an important role in the preparation of design guidance on the fire and blast resistance of multi-storey framed structures. In addition, an integrated environment is developed for analysing steel frames subject to the successive actions of explosion and fire. This enables the investigation of the influence of explosion on the fire resistance of steel structures. Thirdly, a new formulation is proposed for composite steel-deck slabs based on the finite element method. This slab formulation pioneers the modelling of geometrically orthotropic composite slab by utilising the concepts of two-level interpolation and of additional rib freedoms. Finally, this work has advanced the development of ADAPTIC, a nonlinear analysis program developed at Imperial College, by enhancing ADAPTIC with the aforementioned tools.

1.7 ORGANISATION OF THE THESIS

Following this introductory chapter, the thesis proceeds in Chapter 2 by presenting material models for the nonlinear material properties of steel at elevated temperatures. Two material models, namely the bilinear model and the elliptical model, are adopted and implemented into ADAPTIC. Examples are given to demonstrate their applicability in representing the nonlinear response of structural steel at elevated temperatures under general loading conditions.

In Chapter 3, the effect of creep is considered, and a creep model is developed and implemented within ADAPTIC. Numerical examples show the accuracy of the creep model on the material level, and illustrate the influence of creep on structural response at elevated temperatures.

Chapter 4 focuses on verifying the developed material models for steel at elevated temperatures against the experimental results available in the technical literature, and demonstrating their potential application. Verification is carried out against experiments on structural members and scaled frame tests, and the accuracy and efficiency of the developed models are illustrated.

An integrated procedure for explosion and fire analysis is developed in Chapter 5, which considers the response of a structure subjected to a loading scenario in which blast loading is followed by fire. This is an original contribution of this work, providing for the first time an integrated analysis tool for assessing the effect of explosions on the fire resistance of individual steel members, as well as steel framed structures.

In Chapter 6, an elastic formulation based on finite element method is proposed for modelling steel decked composite concrete slabs. To consider the different slab cross-sections in the two orthogonal directions, termed hereafter 'geometric orthotropy', a novel approach has been developed which employs the concepts of two-level interpolation and of additional rib freedoms. The first concept derives from the fact that the element response would be considerably over-stiff if conventional finite element interpolation is employed, and interpolation is proposed at the block level, coupled at the block boundaries to conventional interpolation at the element level. The second concept introduces additional transverse extension freedoms at the bottom of the ribs, thus providing an improved interpolation of displacements over the rib depth. These two concepts, which lead to a realistic slab element, form the first attempt to model a geometrically orthotropic composite slab.

In Chapter 7, the composite slab formulation is verified against the results of various simple theoretical problems. Since the element is formulated in a different manner in the two orthogonal directions, the verification is performed over both directions. More importantly, it is satisfactorily verified against available experimental results in the linear elastic range.

Calibration against the BRE full-scale fire test is reported in Chapter 8. In order to predict the structural response efficiently and realistically, a subassembly is so chosen to maintain the original structural characteristics. The subassembly consists of the fire compartment along with the direct adjacent structural members and composite slab. Temperature data recorded from the experiment are used in the analysis, and the measured displacements are compared with predictions of ADAPTIC using the developed models. Through employing various structural models and material properties, it is established that creep is of importance in the structural response under fire conditions, and that the deterioration of the material properties in the steel decking and the nonlinear material response of concrete must be realistically modelled.

Using the integrated analysis environment developed in this work, parameteric studies are carried out in Chapter 9 to investigate the influence of explosion on the fire resistance of steel members and framed structures. It is shown that blast can significantly affect the fire resistance of structures, and that ignoring the interaction between blast and fire can lead to unsafe design.

Finally, Chapter 10 concludes the thesis by summarising the work, outlining important conclusions, and providing suggestions for further work.

CHAPTER 2
MODELLING STEEL BEHAVIOUR AT ELEVATED TEMPERATURES

To consider the behaviour of a steel frame under fire, an appropriate understanding of the properties of steel at elevated temperatures is required. This chapter is concerned with modelling steel behaviour at elevated temperatures. The influence of elevated temperatures on the thermal strain and Poisson's ratio is first discussed. After a brief introduction to steel behaviour at elevated temperatures, discussion then focuses on the stress-strain relationship of steel. The stress-strain relationship at ambient temperature is discussed prior to its modification to account for high temperature. Two models for representing the stress-strain relationship at elevated temperatures are adopted, and their implementation within the nonlinear analysis program ADAPTIC are presented. The first is the bilinear model with kinematic strain-hardening, whereas the second is the elliptical model recommended by Eurocode 3 (1990). The first model is simple and computationally more efficient, while the second model represents more realistically the nonlinear behaviour of steel. The two material models are verified using a number of examples.

Since it is intended to investigate the structural behaviour assuming that the temperature profile in the structure is known, general thermal properties of steel at elevated temperatures are not discussed here, with the exception of the thermal expansion, a property responsible for thermal strain.

2.1 THERMAL STRAIN

The thermal strain (or thermal expansion) is commonly determined by heating unloaded steel specimens to various temperatures and measuring the increase in length.

When a solid material is heated it elongates according to the cubic function (Cooke, 1988):

$$L_t = L_0(1 + \alpha T + \alpha_1 T^2 + \alpha_2 T^3) \tag{2.1}$$

where L_0 is the length at the initial temperature, L_t is the length after a temperature rise of T, and α, α_1 and α_2 are coefficients of the thermal expansion.

For pure metals, the constants α, α_1 and α_2 have values of the order of 10^{-5}, 10^{-11} and 10^{-14}, respectively. Because α_1 and α_2 are small compared to the coefficient of linear thermal expansion α, the following alternative expression is adequate for most purposes:

$$L_t = L_0(1+\alpha T) \tag{2.2}$$

The National Physical Laboratory reported, for the British Iron and Steel Research Association (1953), data on precise determinations of the thermal movement of 22 different steels at elevated temperatures. For structural steel, α varies from a mean value of 12.18×10^{-6}/°C, in the range 0 - 100°C, to 14.81×10^{-6}/°C, in the range 0 - 1200°C. Over the range 0 - 550°C, the temperature range of main interest concerning the behaviour of structural steel in fire, the mean value is 14.17×10^{-6}/°C. It appears sensible to take a nominal value of 14×10^{-6}/°C, as in BS 5950: Part 8 (1990) and in a comprehensive set of recommendations by the European Convention for Constructional Steelworks (ECCS, 1983) for the design of steel structures exposed to the standard fire. However, effected by phase transformation, the coefficient of thermal expansion α, indeed varies with temperature (Cooke, 1988). Reflecting this, in Eurocode 3 (1993), the variation of the thermal strain of steel with temperature is given by a piece-wise relationship, as shown in Figure 2.1:

$$\left.\begin{array}{ll} \Delta l/l = 1.2\times10^{-5}T + 0.4\times10^{-8}T^2 - 2.416\times10^{-4} & \text{for } 20°C \le T \le 750°C \\ \Delta l/l = 1.1\times10^{-2} & \text{for } 750°C \le T \le 860°C \\ \Delta l/l = 2\times10^{-5}T - 6.2\times10^{-3} & \text{for } 860°C \le T \le 1200°C \end{array}\right\} \tag{2.3}$$

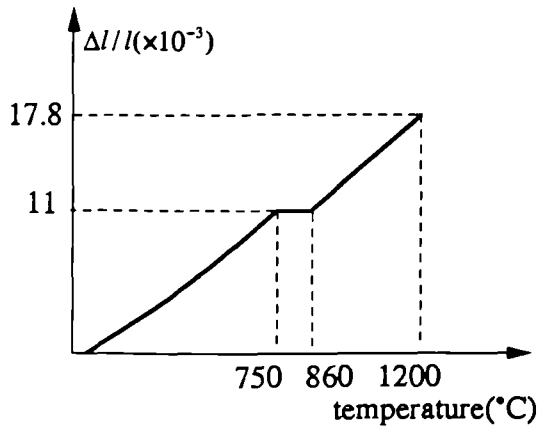


Figure 2.1 Thermal expansion of steel as a function of temperature (Eurocode 3, 1993)

Investigations published in literature indicate that the type of steel and its strength characteristics have no significant influence on its thermal expansion properties (Anderberg, 1988).

2.2 POISSON'S RATIO

When a prismatic bar is loaded in tension, the axial elongation is accompanied by lateral contraction. The ratio of the strain in the lateral direction to the strain in the axial direction is known as Poisson's ratio denoted by υ. BS 5950: Part 1:1985, which deals with the ambient temperature design of steel structures, recommends that a value of $\upsilon = 0.30$ should be used.

There appears to be a paucity of data on the variation of Poisson's ratio with temperature (Cooke, 1988). Clarke (1953) reported values up to a temperature of 650 °C for a mild steel containing 0.15% C, 0.46% Mn and 0.28% Si, and the variation is not great, as shown in Table 2.1.

Table 2.1 Variation of Poisson's ratio of steel with temperature

Temperature(°C)	20	95	205	425	595	650
Poisson's ratio	0.288	0.290	0.293	0.300	0.306	0.311

Stirland (1980), of the British Steel Corporation (BSC), reported a value of υ=0.34 at 1000°C, and has recommended that a value of 0.3 should be used for calculation purposes for all structural steel grades. This value has been adopted in BS 5950: Part 8 (1990) which deals with fire design of structural steel.

2.3 STEEL BEHAVIOUR

Figure 2.2 shows the typical behaviour of mild steel when subjected to a tensile test at ambient temperature. The response is linear elastic up to point A, referred to as the proportional limit. The slope of this straight line is the modulus of elasticity (E), also known as Young's modulus.

Increasing the applied stress beyond the proportional limit causes the strain to begin to increase more rapidly. At point B, the stress-strain curve becomes horizontal, beyond

which considerable elongation can occur, without noticeable increase in the stress. This is known as yielding of the material, and the corresponding stress at point B is referred to as the yield stress, f_y, which is the most significant property that differentiates various types of structural steel.

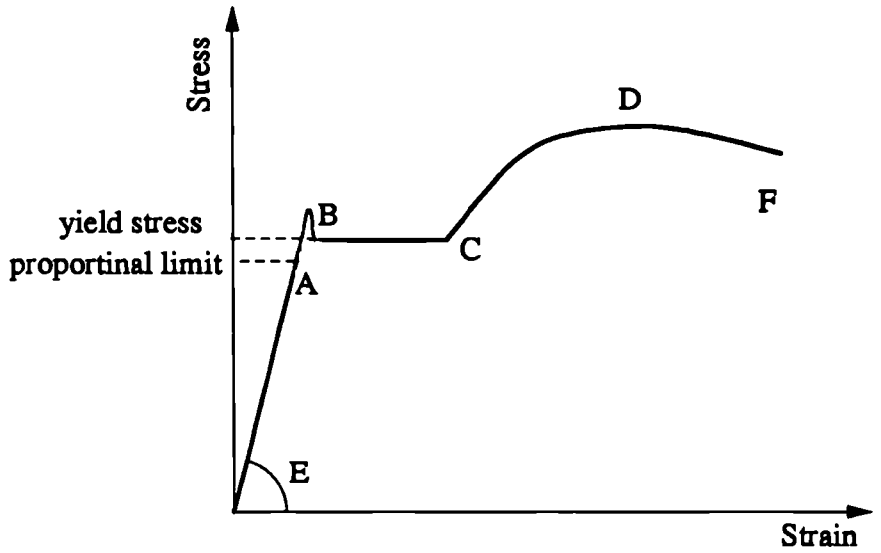


Figure 2.2 Typical stress-strain response for mild steel at ambient temperature

In the region from B to C, the material becomes perfectly plastic, sustaining considerable elongation without an increase in the applied stress. This elongation (strain) is typically 10 to 15 times the elongation (strain) corresponding to the proportional limit. Further elongation beyond C causes strain hardening, where the material undergoes changes in its atomic and crystalline structure, resulting in increased resistance. This increase in stress continues until point D, referred to as the ultimate stress. Further stretching is then accompanied by a reduction in the stress, and fracture finally occurs at F.

During a fire situation, the steel is normally subjected to transient processes with varying temperature and stress. As steel is heated above a temperature of about 150°C, its elastic modulus, as well as yield and ultimate stresses, reduce with further temperature increase. Figure 2.3, given by Harmathy and Stanzak (1970), shows a family of stress-strain curves for mild steel obtained at different temperatures.

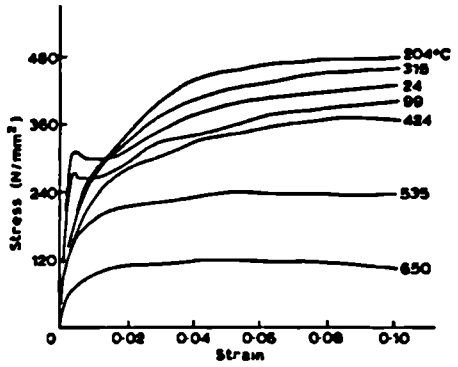


Figure 2.3 Stress-strain curves for an ASTM A36 steel at elevated temperatures (Harmathy and Stanzak, 1970)

Tests have been carried out to determine the mechanical properties of steel at elevated temperatures. Cooke (1988) and Anderberg (1988) summarised some of the works in this field. There exist a number of different test procedures. The three main test parameters are the heating process, application and control of load, and control of strain, as stated by Anderberg (1988). These can have constant values or be varied during testing, giving steady-state or transient-state conditions depending on the heating procedure.

To predict the structural behaviour under fire conditions, it is essential to model not only the stress-strain response, but also its variation with temperature. In the following sections, uniaxial material models are presented which account for variations of Young's modulus, yield stress, and strain hardening with temperature.

2.4 MATERIAL MODELLING

As stated previously, a mathematical representation of the stress-strain-temperature relationship is required for predicting structural behaviour at elevated temperatures. This section considers existing models and adapts them for their utilisation within a general nonlinear analysis procedure, which accounts for non-monotonic variation in strains and temperatures.

2.4.1 Stress-strain-temperature Relationship

2.4.1.1 Stress-strain at room temperature

Various models have been proposed to represent the stress-strain relationship of steel at ambient temperature based on curve-fitting techniques. Some of the important

models are summarised below.

Bi-linear and multi-linear models

The simplest stress-strain relationship is based on a bilinear model, as illustrated in Figure 2.4, which uses a straight line to represent the elastic range and another to represent the plastic range, with or without strain hardening. An extension of this model is to approximate the stress-strain response by a number of straight lines, i.e., the multi-linear model. These piece-wise linear models have been adopted by Kouhia etc. (1988), Corradi etc. (1990) in their work.

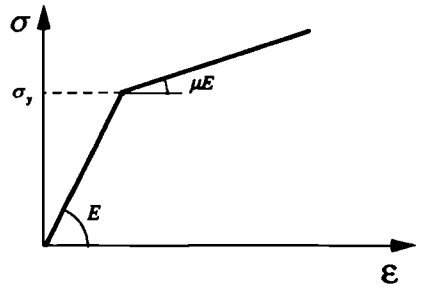


Figure 2.4 Bilinear stress-strain model

Linear-elliptic model

Douns and Golrang (1982) proposed an elliptic formulation to simulate the heavily nonlinear behaviour of the stress-strain response between the so called elastic-plastic regions. The whole stress-strain curve is represented by a straight line followed by an elliptic branch and a tangential straight line, as illustrated in Figure 2.5. The parameters α, β and ε_1 are dependent on the type of steel and the temperature level, and $\sigma_{f0.2}$ is 0.2% proof stress at temperature T. Anderberg (1988) adopted this model in structural analysis and gave analytical expressions for reinforcing and structural steel. Rubert and Schmann (1986) also used this model in their work.

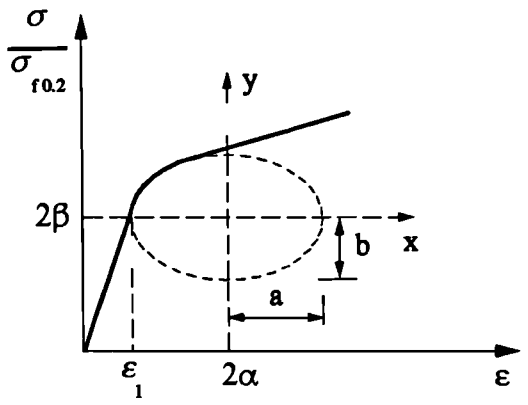


Figure 2.5 Linear-elliptic-linear stress-strain model

Ramberg-Osgood model

The Ramberg-Osgood formula (Ramberg & Osgood, 1943) expresses strain as a function of stress as below:

$$\varepsilon = \frac{\sigma}{E} + \alpha\left(\frac{\sigma}{E}\right)^{n} \tag{2.4}$$

where E is the initial tangent modulus, and α and n are material parameters determined from tests.

Various modified expressions of the Ramberg-Osgood equation have been widely used to model the stress-strain relationship of steel at elevated temperatures (Cheng & Mak, 1975; Cheng, 1983; Burgess et al., 1988, 1990, 1991; Showronski, 1988; Wang & Lennon, 1992; Saab & Nethercot, 1991).

2.4.1.2 Stress-strain at elevated temperatures

An analytical description of the stress-strain curve as a function of temperature can be provided in different ways. It can be assumed that the stress-strain response at elevated temperatures is similar to that at the ambient temperature, but with different mechanical properties/material parameters. Hence with appropriate consideration given to the elevated temperatures, the models in Section 2.4.1.1 would still hold. For example, a modified expression of the Ramberg-Osgood equation used by Magnusson (1974) has the following form:

$$\varepsilon_{\sigma} = \sigma / E(T) + 3/7 \times f_{0.2}(T) / E(T) \times (\sigma / f_{0.2}(T))^{m(T)} \tag{2.5}$$

where

$m(T)$ = material parameter in the range [6, 50],

$E(T)$ = Young's modulus at temperature T

$f_{0.2}(T)$ = 0.2% proof stress at temperature T.

The variation of Young's modulus and the 0.2% proof stress with temperature are required to determine the stress-strain response at a particular temperature.

2.4.2 Young's Modulus E

According to Cooke (1988), who gave a comparison between some existing *E-T* models, there is not, within Europe at least, a widely accepted model of the variation of elastic modulus with temperature. The ECCS (1983) defines the elastic modulus below 600 °C as:

$$E_T = E\left(1 - 17.2\times10^{-12}T^4 + 11.8\times10^{-9}T^3 - 34.5\times10^{-7}T^2 + 15.9\times10^{-5}T\right) \qquad (2.6)$$

where,

E_T = elastic modulus at elevated temperature, and

E = elastic modulus at room temperature.

But there is no definition of the elastic modulus for temperatures above 600°C. In Eurocode 3 (1993), the reduction factors for the elastic modulus, relative to its initial value at 20°C, are given at elevated temperatures up to 1200°C, as shown in Table 2.2. Linear interpolation is suggested for intermediate values of the steel temperature.

2.4.3 Effective Yield Stress

In ECCS (1983), the effective yield stress is approximated for all grades of steel by the following equations:

$$\frac{\sigma_{yT}}{\sigma_{y20}} = \begin{cases} 1 + \dfrac{T}{767\ln\dfrac{T}{1750}} & 0°C \le T \le 600°C \\ \dfrac{108\left(1 - \dfrac{T}{1000}\right)}{T - 440} & 600°C \le T \le 1000°C \end{cases} \qquad (2.7)$$

in which

σ_{yT} = effective yield stress at elevated temperature,

σ_{y20} = nominal yield stress at room temperature, and

T = steel temperature in °C.

In Eurocode 3, the reduction factors are tabulated for the yield strength and proportional limit at elevated temperatures up to 1200°C, as shown in Table 2.2.

Table 2.2 Reduction factors for the stress-strain relationship of steel at elevated temperatures (Eurocode 3, 1993)

Steel Temperature (°C)	Reduction factor for elastic modulus (relative to E)	Reduction factor for proportional limit (relative to σ_p)	Reduction factor for effective yield strength (relative to σ_y)
20	1.000	1.000	1.000
100	1.000	1.000	1.000
200	0.900	0.807	1.000
300	0.800	0.613	1.000
400	0.700	0.420	1.000
500	0.600	0.360	0.789
600	0.310	0.180	0.470
700	0.130	0.075	0.230
800	0.090	0.050	0.110
900	0.0675	0.0375	0.060
1000	0.0450	0.0250	0.040
1100	0.0225	0.0125	0.020
1200	0.0000	0.0000	0.000

2.4.4 Strain-hardening

With regard to the strain-hardening parameter (μ), Shen and Zhao (1995) described the following equations:

$$\mu = \begin{cases} 0 & T \le 200°C \\ 1.76 - 1.04\times10^{-2}T + 2.13\times10^{-5}T^2 + 1.47\times10^{-8}T^3 & 200°C < T \le 600°C \\ 0 & T > 600°C \end{cases} \quad (2.8)$$

This equation is discontinuous at T = 200°C and 600°C, nevertheless, it provides guidance on choosing μ if the bilinear/multilinear model is to be used.

In the present study, two material models, namely bilinear and elliptical models, are adopted for modelling the stress-strain relationship of steel at elevated temperatures. The following sections present the details of the two models, their implementations in ADAPTIC, and a number of illustrative examples.

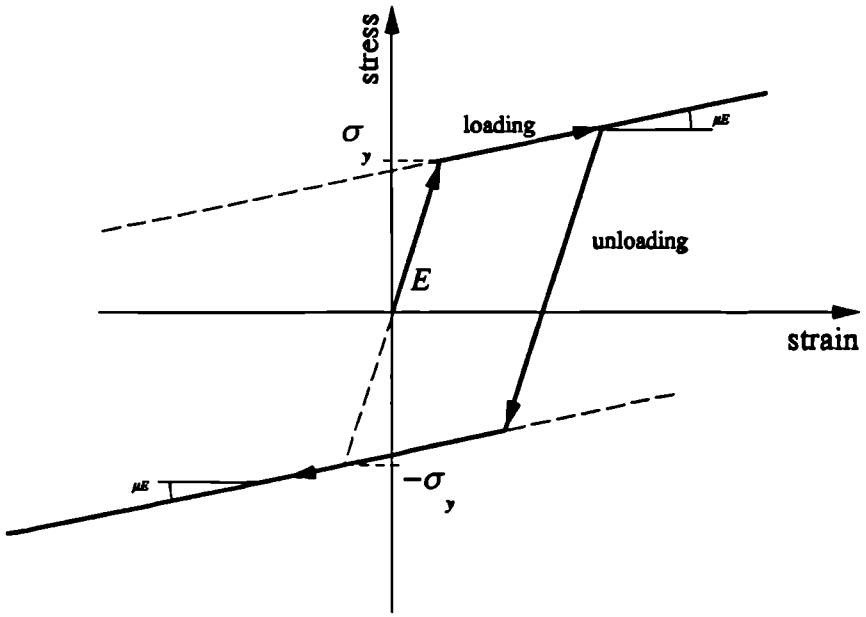


Figure 2.6 Loading and unloading path of bilinear model

2.5 BILINEAR MATERIAL MODEL

2.5.1 Basic Assumptions

The bilinear model with kinematic strain-hardening is illustrated in Figure 2.6. The model depends on three material parameters, namely Young's modulus, yield strength and strain hardening factor, and their variation with temperature. It assumes that the elastic range remains constant after plastic deformation, and adopts a hardening rule

which is a linear function of the increment of plastic strain. The variation of the elastic modulus (E) with temperature is represented by three segments over the considered temperature range, as illustrated in Figure 2.7. Trilinear functions are also used to represent the variation of the effective yield strength (σ_y) and the strain-hardening parameter μ with temperature. The parameters of the trilinear curves may be chosen based on the reduction factors for the elastic modulus and the proportional limit tabulated in the Eurocode 3 (1993), while the strain-hardening parameter μ is chosen according to the suggestion by Shen and Zhao (1995) to achieve a best representation of the nonlinear behaviour that can be provided by the elliptical model proposed by the code.

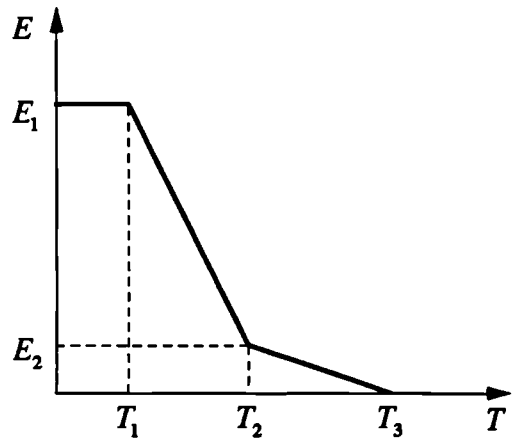


Figure 2.7 Trilinear model for the variation of elastic modulus with temperature

This model is approximate but its implementation is relatively straight forward. It is appropriate for cases of mild excursion into the nonlinear range (Elnashai & Izzuddin, 1993). It will be shown later, in the verification in Chapter 4, that this model is computationally efficient, yet the accuracy is still reasonable.

2.5.2 Details of Bilinear Material Model

The bilinear material model is developed for the elasto-plastic cubic formulation (Izzuddin & Elnashai, 1993), which requires the determination of the stress state corresponding to a given strain, as well as the tangent modulus reflecting the infinitesimal change of stress with strain at the current state. This is discussed in more detail hereafter.

2.5.2.1 Strain component

The total strain (ε_t) is assumed to consist of the thermal strain (ε_{th}) and the stress-induced strain (ε_σ) which includes the elastic strain (ε_e) and the plastic strain (ε_p). Let ε_0, ε_{p0} and σ_0 be the total strain, plastic strain and stress, respectively, at temperature T_0 and time t_0. Given an incremental temperature (ΔT_i), over the current time step (Δt_i), and a current total strain (ε_i), the current stress (σ_i), and tangent modulus are evaluated according to the following sections.

2.5.2.2 Determination of stress

The calculation of the stress (σ_i), corresponding to the strain level (ε_i), at time t_i involves the following steps:

i) Calculate the current thermal strain (ε_{th}) from the trilinear thermal strain-temperature relationship.

ii) Calculate the current tensile yield strength (σ_s) Young's modulus (E) and hardening factor (μ) at temperature T_i. The evaluation of σ_s is discussed in section 2.5.2.3.

iii) Assuming the stress-induced incremental strain is elastic, calculate the current stress (σ_i):

$$\sigma_i = E\left(\varepsilon_i - \varepsilon_{th} - \varepsilon_{p0}\right) \tag{2.9}$$

iv) If the stress obtained in the above step exceeds the tensile or the compressive yield strength then recalculate the stress according to the hardening rule given by:

$$\sigma_i = \mu E\left(\varepsilon_i - \varepsilon_{th}\right) \pm (1-\mu)\sigma_y \tag{2.10}$$

where the choice between (±) depends on whether the tensile or compressive stress is exceeded with the assumption of elastic response.

This procedure is illustrated in Figure 2.8.

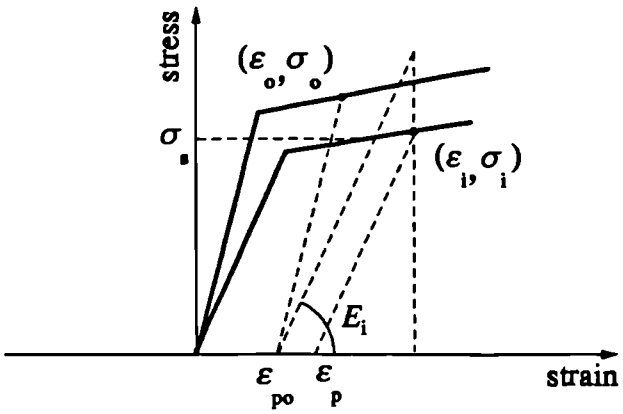


Figure 2.8 Determination of stress

2.5.2.3 Yield Strength

For a kinematic-hardening material model, the initial yield strength is a function of temperature. For a fixed temperature, the subsequent yield strength becomes a function of plastic strain. Given an incremental temperature within a time step, the current yield strength is calculated based on the plastic strain at the start of the step (ε_{p0}) and the initial yield strength at this temperature (σ_y). Mathematically, the tensile yield strength at temperature T can be expressed as:

$$\sigma_s = \sigma_y + \frac{\mu E \varepsilon_{p0}}{1-\mu} \tag{2.11}$$

where

σ_s = current tensile yield strength,

σ_y = initial yield strength at temperature T,

E = elastic modulus at temperature T,

μ = strain-hardening parameter at temperature T, and

ε_{p0} = plastic strain at the start of the current step.

2.5.2.4 Evaluation of plastic strain

Considering the incremental nature of the proposed model, the current plastic strain (ε_p) is required for establishing the tensile yield strength for the following step. Once the current stress (σ_t) is obtained, the plastic strain (ε_p) may be calculated from the following expression:

$$\varepsilon_p = \varepsilon_t - \varepsilon_{th} - \sigma_t / E \tag{2.12}$$

in which E is the elastic modulus for the current step.

2.5.2.5 Tangent modulus

The material tangent modulus must also be calculated to enable the calculation of the tangent stiffness of the elasto-plastic cubic element (Izzuddin & Elnashai, 1993). The determination of the tangent modulus depends on whether the current stress state is elastic or elasto-plastic, as given by the following expressions:

$$E_t = \begin{cases} E & \sigma_s - 2\sigma_y < \sigma_t < \sigma_s \\ \mu E & \sigma_t \geq \sigma_s - 2\sigma_y \text{ or } \sigma_i \geq \sigma_s \end{cases} \tag{2.13}$$

where σ_s is the current tensile yield stress, and $(2\sigma_y)$ is the size of the current elastic range.

2.5.3 Implementation into ADAPTIC

The above thermal material model, is incorporated within the cubic elasto-plastic formulation, which enables prediction of the response of steel frames under fire conditions.

The temperature profile in the cubic element is assumed to be known. It is also assumed that the temperature varies linearly both over the cross-section and along the length of the element. Temperature is specified as a time-dependent 'load' on the element level at the element nodes. This allows different temperatures to be specified at the same node connecting different elements. Since the cubic formulation is derived on the level of the constituent material rather than the stress resultants, the effect of elevated temperatures can be readily considered. The proposed thermal model is defined as material model *stl4* using 20 parameters, described in Appendix A. Figure 2.9 depicts the flow-chart of the thermal model within the ADAPTIC cubic formulation.

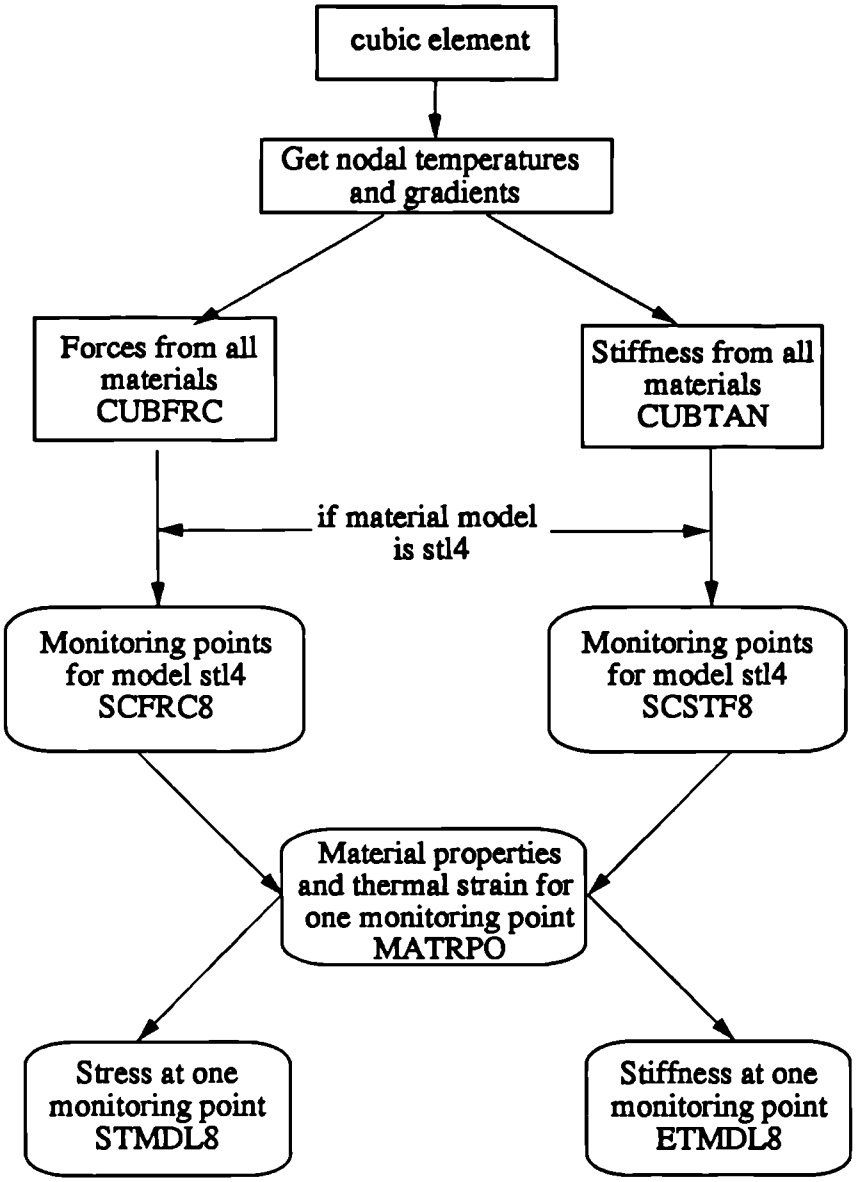


Figure 2.9 Main subroutines of thermal model

2.5.4 Examples

A column with a square cross section, shown in Figure 2.10, is modelled by one 2D cubic element with only one monitoring point at each Gauss section of the element.

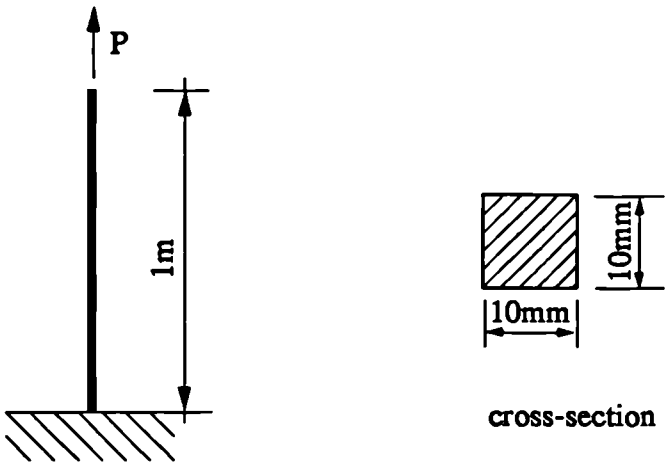


Figure 2.10 Column configuration and loading

The ambient temperature values of Young's modulus and yield strength are assumed to be 210 GPa and 310 MPa, respectively, The variation of the material properties with temperature is shown in Figure 2.11, which depicts the reduction factors for Young's modulus and the yield strength at elevated temperatures relative to their respective values at room temperature. The strain hardening parameter is assumed to be 0 at room temperature, with a maximum value of 0.08 at 400°C. The variation of the strain hardening parameter is also illustrated in Figure 2.11.

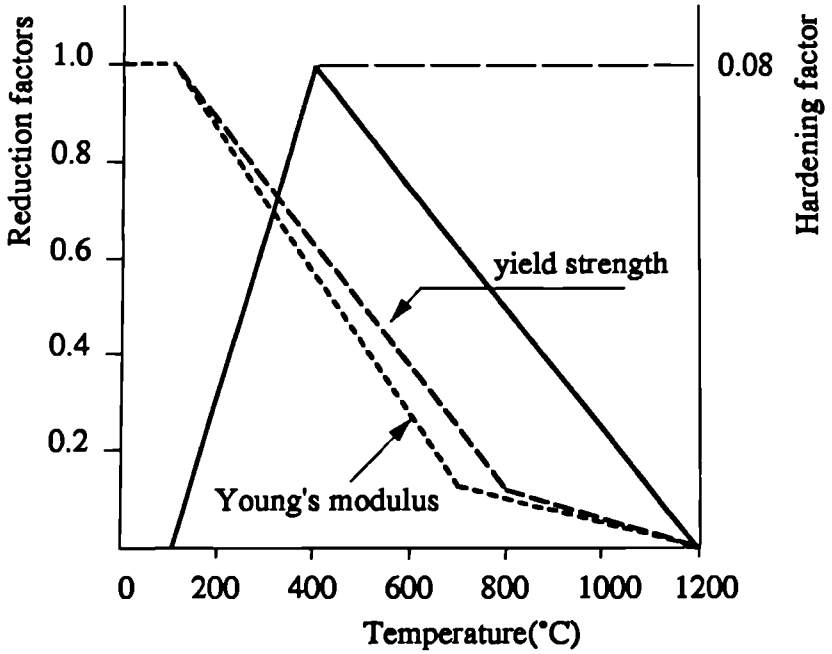


Figure 2.11 Material properties at elevated temperatures

The column is subjected to a uniform temperature rise, varying up to 600°C, before

applying a prescribed axial displacement at the top end. The temperature and prescribed displacement are applied in two different ways so that the stress-strain relationship at elevated temperature and the effects of loading and unloading can be examined, as discussed hereafter.

2.5.4.1 Stress-strain relationship at elevated temperatures

Firstly, a uniform temperature is applied as an initial load, at a value of 100°C, 200°C, 300°C, 400°C, 500°C or 600°C. The free end of the column is controlled to have an axial displacement of 10 mm, which gives a mechanical strain of 0.01. In order to check the bilinear variation of stress with mechanical strain holds the bilinear relationship, the thermal strain is excluded by assuming zero expansion. The stress-strain curves at different temperatures are shown in Figure 2.12, which indicates that the bilinear model gives a reasonable representation of the stress-strain relationship at elevated temperatures.

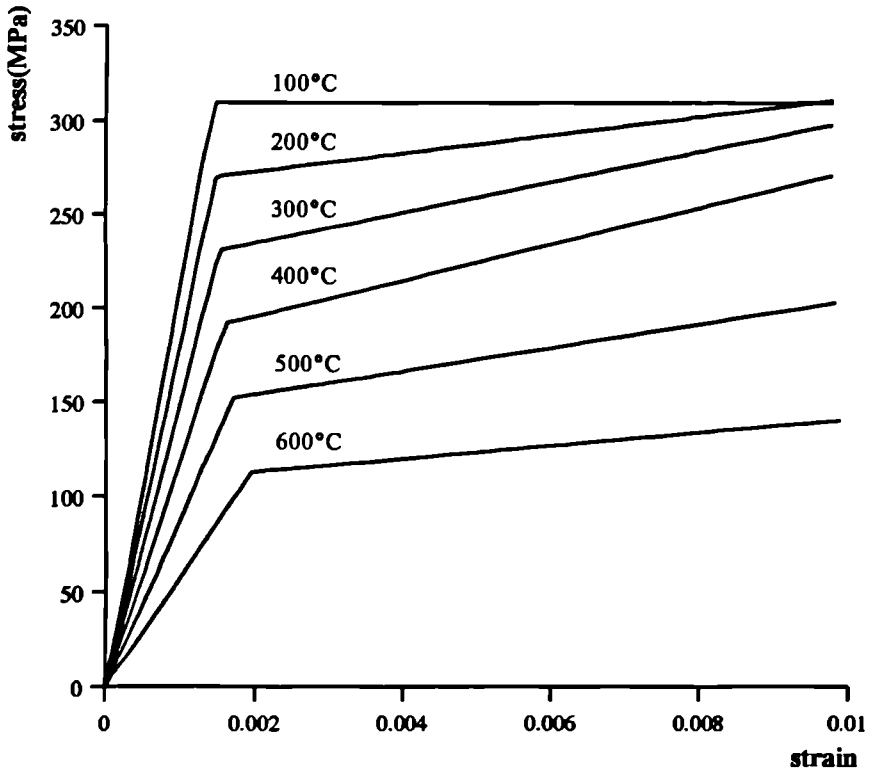


Figure 2.12 Stress-strain curves at elevated temperatures

2.5.4.2 Loading and unloading

For this case, the temperature is raised uniformly from 0°C to 600°C in 20 minutes. Over the following 5 minutes, the column is stretched by 10 mm and then compressed by 15 mm, so that both loading and unloading occur. The variations in temperature and free end displacement with time are shown in Figure 2.13. The thermal strain increases linearly to 0.011 at 750°C, and remains the same until the temperature rises to 860°C, when the thermal strain resumes its linear variation with temperature to 0.0178 at 1200°C.

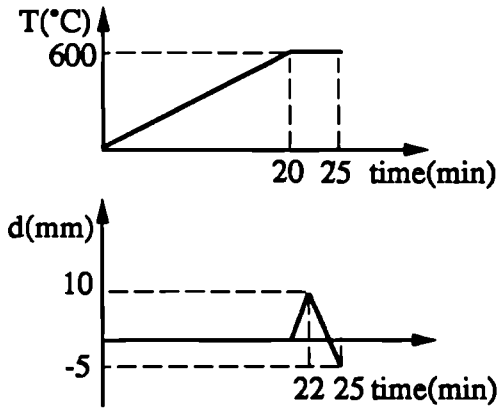


Fig 2.13 Temperature and load time history

The stress-time curve and the stress-strain curve are given in Figures 2.14 (a) and (b), respectively. During the heating stage, a compressive stress is induced , since the free end displacement is prescribed as a zero value. The stress increases rapidly with temperature and reaches the compressive yield strength of 310 MPa at about 106°C. At temperatures above 400°C, the stress decreases more significantly due to the deterioration of the Young's modulus and yield strength. Tensile stresses occur when the column is extended, and unloading occurs when the column is compressed by 15 mm into the compressive plastic range. The full loading and unloading stress-strain response is depicted in Figure2.14 (b).

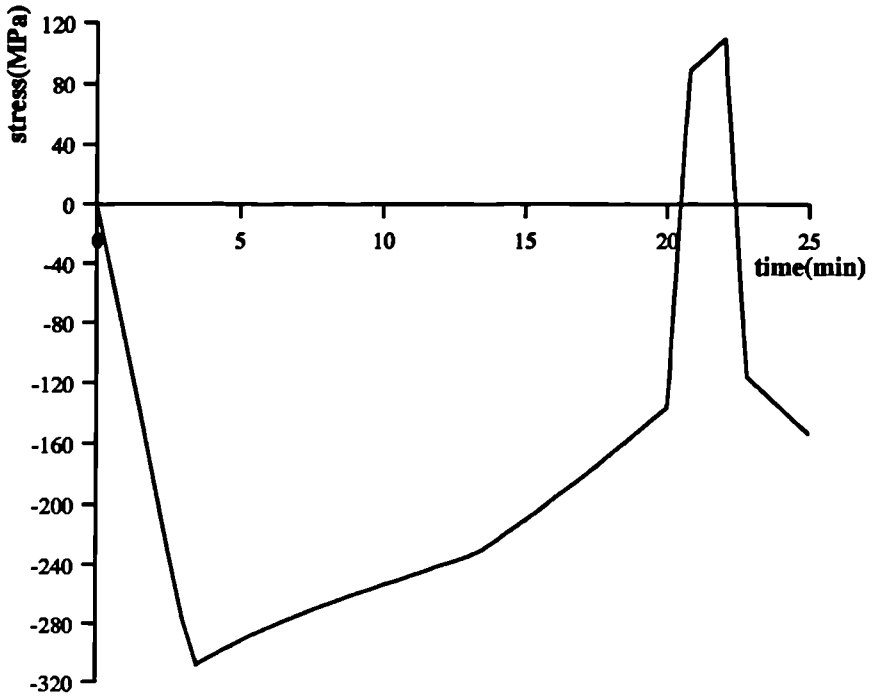


Figure 2.14 (a) Stress-time history of the column

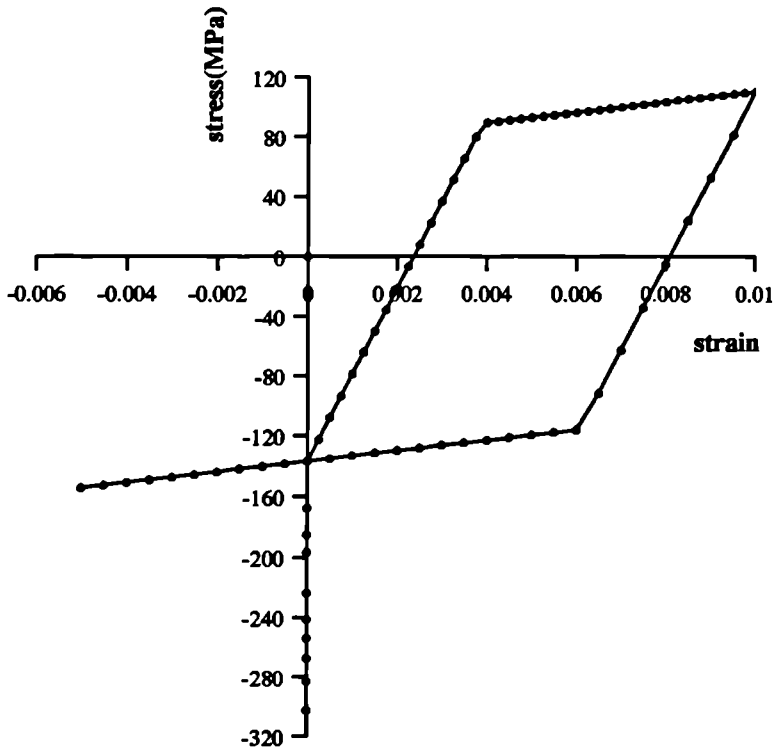


Figure 2.14(b) Stress-strain variation

2.6 ELLIPTICAL MATERIAL MODEL

2.6.1 Basic Assumptions

The elliptical model, shown in Figure 2.15, proposed by Eurocode 3 (1993), is characterised by an initially linear progression up to the proportional limit ($f_{p,T}$); followed by an elliptical progression up to the yield strength ($f_{y,T}$), and perfect plasticity is assumed thereafter, until the strain reaches the limiting strain for yield strength. The mathematical expressions representing the elliptical model are given in Table 2.3.

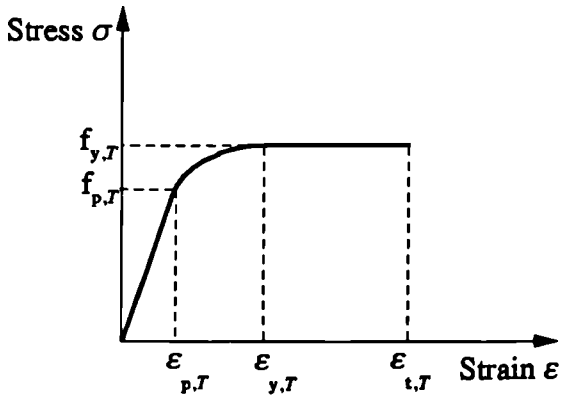


Figure 2.15 Stress-strain relationship

Table 2.3 Stress-strain relationship

Strain range	Stress σ	Tangent modulus
$\varepsilon \le \varepsilon_{p,T}$	$\varepsilon E_{a,T}$	$E_{a,T}$
$\varepsilon_{p,T} < \varepsilon < \varepsilon_{y,T}$	$f_{p,T} - c + (b/a)\left[a^2 - (\varepsilon_{y,T} - \varepsilon)^2\right]^{0.5}$	$\dfrac{b(\varepsilon_{y,T} - \varepsilon)}{a\left[a^2 - (\varepsilon - \varepsilon_{y,T})^2\right]^{0.5}}$
$\varepsilon_{y,T} < \varepsilon < \varepsilon_{t,T}$	$f_{y,T}$	0
Parameters	$\varepsilon_{p,T} = f_{p,T}/E_{a,T}$ $\quad \varepsilon_{y,T} = 0.02$ $\quad \varepsilon_{t,T} = 0.15$	
Functions	$a^2 = (\varepsilon_{y,T} - \varepsilon_{p,T})(\varepsilon_{y,T} - \varepsilon_{p,T} + c/E_{a,T})$ $b^2 = c(\varepsilon_{y,T} - \varepsilon_{p,T})E_{a,T} + c^2$ $c^2 = \dfrac{(f_{y,T} - f_{p,T})^2}{(\varepsilon_{y,T} - \varepsilon_{p,T})E_{a,T} - 2(f_{y,T} - f_{p,T})}$	

in which,

$f_{y,T}$ = the effective yield strength,

$f_{p,T}$ = the proportional limit,

$E_{a,T}$ = the slope of the linear elastic range,

$\varepsilon_{p,T}$ = the strain at the proportional limit,

$\varepsilon_{y,T}$ = the yield strain, and

$\varepsilon_{t,T}$ = the limiting strain for yield strength.

An isotropic strain-hardening rule is adopted for this model, as shown in Figure 2.16, so that the effects of stress reversals can be modelled realistically. The variation of elastic modulus ($E_{a,T}$) with temperature is defined as a piece-wise line with up to 5 segments, as illustrated in Figure 2.17. The same model is also used to represent the variation of the proportional limit ($f_{p,T}$) and the effective yield strength ($f_{y,T}$) with temperature. The parameters of these curves are chosen based on the reduction factors for the elastic modulus, proportional limit, and the effective yield stress provided in the Eurocode 3 (1993).

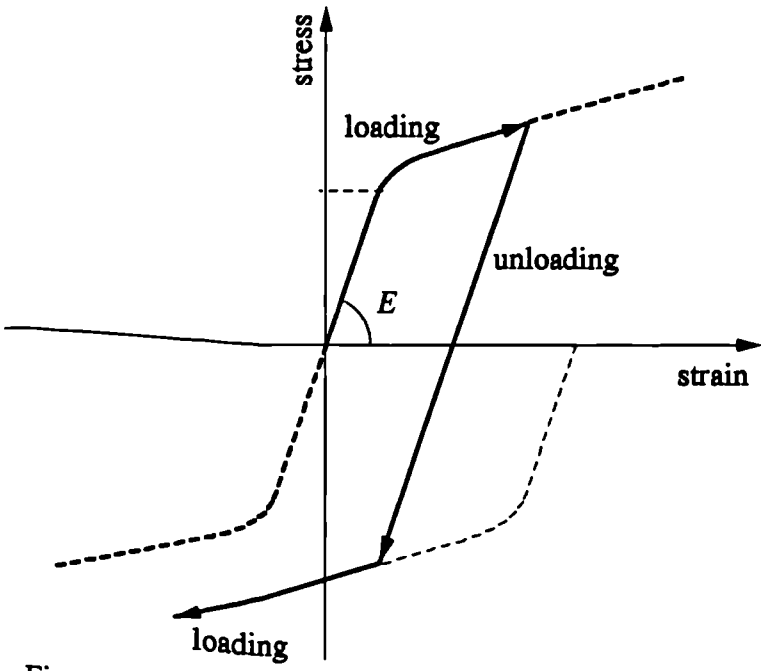


Figure 2.16 Loading and unloading path of elliptical model

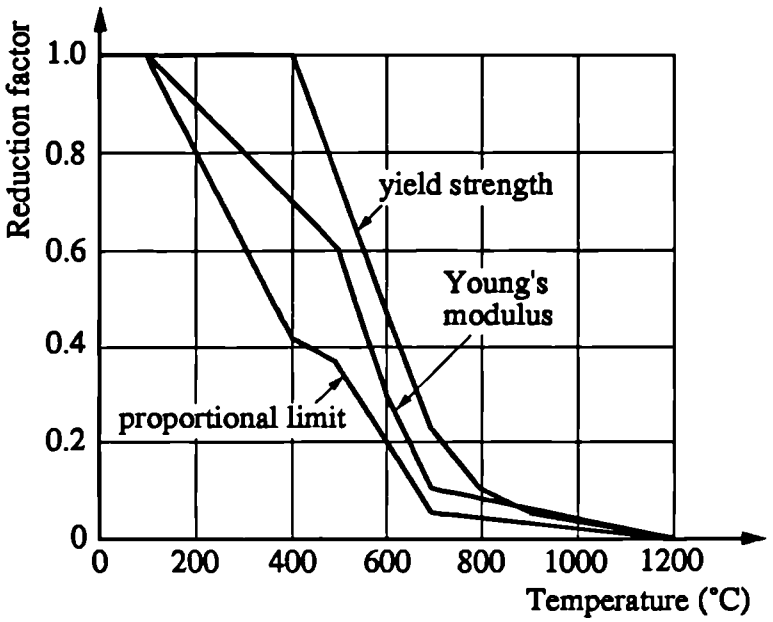


Figure 2.17 Material properties at elevated temperatures

2.6.2 Details of Model

2.6.2.1 Strain component

As with the bilinear model, the total strain (ε_i) is assumed to consist of thermal strain (ε_{th}) and stress-induced strain (ε_σ), which is referred to as the mechanical strain including elastic strain (ε_e) and plastic strain (ε_p). As mentioned previously, it is assumed that the material follows isotropic hardening. Suppose that ε_0, ε_{p0} and σ_0 are, respectively, the total strain, plastic strain and stress at time t_0. Given an incremental temperature (ΔT_i) over the time step (Δt_i) and a current total strain (ε_i), the current stress (σ_i) and tangent modulus are evaluated according to the following sections.

2.6.2.2 Determination of stress

The calculation of the stress (σ_i), corresponding to strain (ε_i) involves the following steps:

i) Calculate the current thermal strain (ε_{th}) from the given thermal strain-temperature relationship;

ii) Calculate the proportional limit (σ_p), the yield strength (σ_s) and Young's modulus (E), at current temperature (T_i);

iii) Assuming the stress-induced incremental strain is elastic, calculate the current stress from:

$$\sigma_i = E\left(\varepsilon_i - \varepsilon_{th} - \varepsilon_{p0}\right) \tag{2.14}$$

iv) If the stress obtained in the above step exceeds the current tensile or compressive proportional limit given in section 2.6.2.3, recalculate the stress according to the elliptical formula given in Table 2.3, with $(\varepsilon_i - \varepsilon_{th})$ replacing ε.

$$\sigma_i = \begin{cases} f_{p,T} - c + (b/a)\left[a^2 - (0.02 - (\varepsilon_i - \varepsilon_{th}))^2\right]^{0.5} & \varepsilon_i - \varepsilon_{th} \geq 0 \\ -f_{p,T} + c - (b/a)\left[a^2 - (0.02 + (\varepsilon_i - \varepsilon_{th}))^2\right]^{0.5} & \varepsilon_i - \varepsilon_{th} < 0 \end{cases} \tag{2.15}$$

If the mechanical strain exceeds $\varepsilon_{y,T}$, the stress will take the value of $f_{y,T}$.

2.6.2.3 Plastic strain

The current plastic strain is obtained from the stress state by:

$$\varepsilon_p = \varepsilon_i - \varepsilon_{th} - \sigma_i / E_{a,T} \tag{2.16}$$

The accumulated plastic strain, required for establishing the proportional limit according to the isotropic srain-hardening rule, is then determined from:

$$\bar{\varepsilon}_p = \bar{\varepsilon}_{po} + \left|\varepsilon_p - \varepsilon_{po}\right| \tag{2.17}$$

where ε_{po} is the plastic strain at the previous step.

2.6.2.4 Proportional limit

The initial proportional limit is a function of temperature as defined by appropriate reduction factors. However, due to isotropic strain-hardening, the subsequent proportional limit will be influenced by the accumulated plastic strain. Hence, the proportional limit (σ_p) is updated during the analysis from ($\bar{\varepsilon}_{po}$) the accumulated plastic strain at the start of each step, defined in Section 2.6.2.4.

The tensile yield strength at temperature T can be determined by the intersection of the line through $\bar{\varepsilon}_{po}$ on the strain axis with a slope of $E_{s,T}$, as illustrated in Figure 2.16. Mathematically, it may be expressed as:

$$\sigma_p = \frac{[2E_{s,T}^2[b^2(\bar{\varepsilon}_{po} - \varepsilon_{y,T}) - a^2E_{s,T}k]^2 - 4E_{s,T}^2(b^2 + a^2E_{s,T}) - b^2[a^2 - (\bar{\varepsilon}_{po} - \varepsilon_{y,T})^2] + a^2k^2]^{1/2}}{2(b^2 + a^2E_{s,T})}$$

$$+\frac{-2E_{s,T}[b^2(\bar{\varepsilon}_{po} - \varepsilon_{y,T}) - a^2E_{s,T}k]}{2(b^2 + a^2E_{s,T})}$$

in which,

$$d = a^2Ek + b^2(\bar{\varepsilon}_{po} - \varepsilon_{y,T})$$

$$k = f_{p,T} - c$$

and a, b and c were defined in Table 2.3.

Simplifying the above expression gives:

$$\sigma_p = \frac{2E_{s,T}d + \left[2E_{s,T}^2d^2 - 4E_{s,T}^2(b^2 + a^2E_{s,T}) - b^2(a^2 - (\bar{\varepsilon}_{po} - \varepsilon_{y,T})^2) + a^2k^2\right]^{1/2}}{2(b^2 + a^2E_{s,T})} \quad (2.18)$$

2.6.2.5 Tangent modulus

The tangent modulus for the elliptical model depends on the current stress state where three cases are considered, as follows:

$$E_t = \begin{cases} E_{s,T} & \text{if } |\sigma| \le \sigma_p \\ \dfrac{b(\varepsilon_{y,\theta} - \varepsilon_\sigma)}{a[a^2 - (\varepsilon_{y,\theta} - \varepsilon_\sigma)^2]^{1/2}} & \text{if } \sigma_p < |\sigma| < f_{y,\theta} \\ 0 & \text{if } |\sigma| = f_{y,\theta} \end{cases} \quad (2.19)$$

in which ε_σ represents the mechanical strain.

2.6.3 Implementation into ADAPTIC

The elliptical model is incorporated within the ADAPTIC cubic elasto-plastic formulation (Izzuddin & Elnashai, 1993), defined as material model *st10* with 36

parameters, presented in Appendix A. These parameters specify the reduction factors of Young's modulus, the proportional limit and yield strength, and the thermal expansion, allowing them all to be represented by 5 piece-wise linear segments, as illustrated in Figure 2.17. The implementation of the elliptical model, within the cubic formulation, is similar to that of the bilinear model.

2.6.4 Examples

For the purpose of testing the implementation of the elliptical model, the column described in section 2.2.4 is considered again. At room temperature, Young's modulus is assumed to be 210 GPa, and the proportional limit and yield strength are assumed to be 355 MPa. Table 2.4 gives the reduction factors for Young's modulus, proportional limit and yield strength at elevated temperatures relative to their values at room temperature, respectively.

Table 2.4 Reduction factors for material properties used in elliptical model

Young's modulus 210 GPa		Proportional limit 355 MPa		Yield strength 355 MPa	
Temperature (°C)	Reduction factor	Temperature (°C)	Reduction factor	Temperature (°C)	Reduction factor
100	1.0	100	1.0	400	1.0
300	0.8	200	0.9	700	0.2
500	0.6	300	0.6	800	0.13
700	0.4	500	0.5	900	0.06667
1000	0.0	700	0.0	1000	0.0

The column is subjected to a uniform temperature rise varying up to 700°C, before applying a prescribed axial displacement/force at the top end. Temperature and the prescribed displacement/force are applied in such a way that the stress-strain response at elevated temperatures, and the effects of loading and unloading, can be examined

2.6.4.1 Stress-strain relationship at elevated temperatures

Firstly, a uniform temperature is applied as an initial load, at values of 100°C, 200°C, 250°C, 400°C, 500°C and 600°C. The free end of the column is subjected to an axial displacement of 20 mm, so that the mechanical strain will reach 0.02. The thermal strain

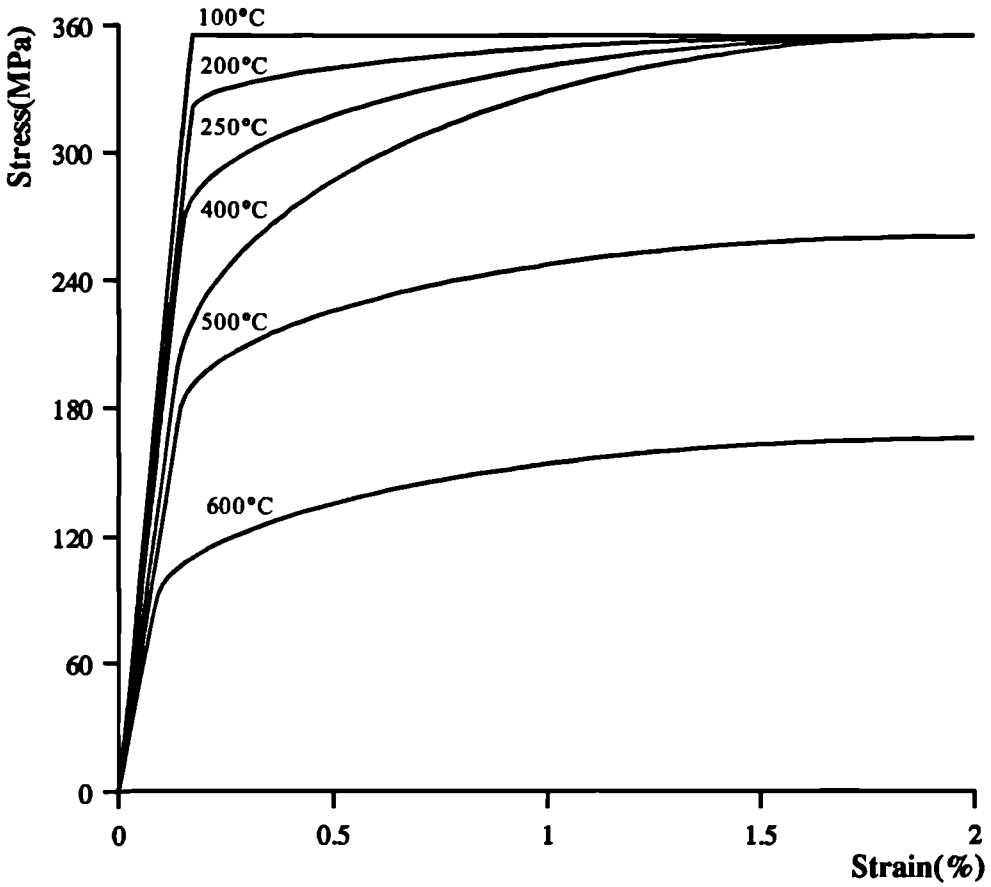


Figure 2.18 Stress-strain curves at elevated temperatures

is excluded by assuming zero expansion in order to check the stress-strain relationship. The stress-strain curves, at different temperatures, are shown in Figure 2.18, which indicates that the variation of the stress to strain follows the elliptical model at elevated temperatures.

2.6.4.2 Loading and unloading

A uniform initial temperature of 300°C is applied to the column, followed by an axial force varying as shown in Figure 2.19.

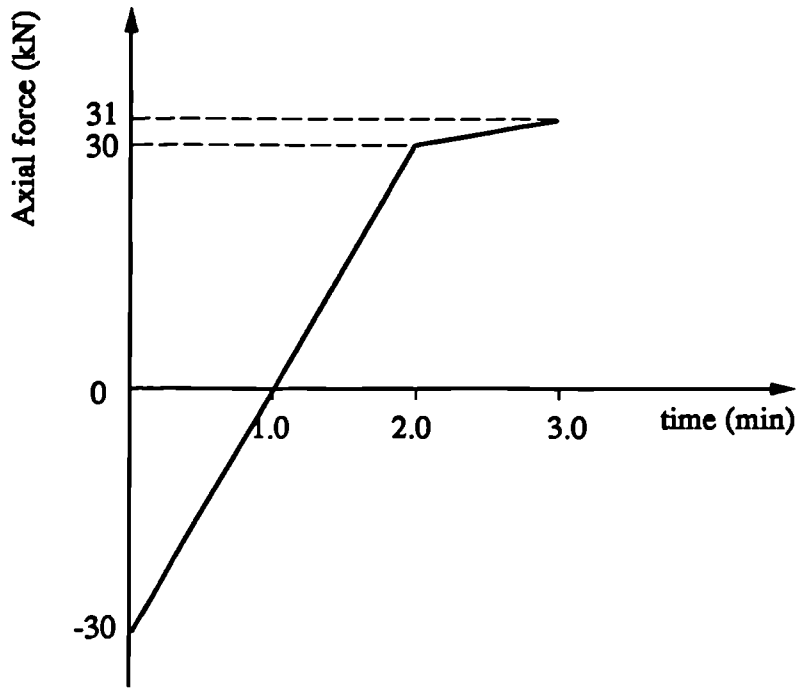


Figure 2.19 Temperature-time history and load history

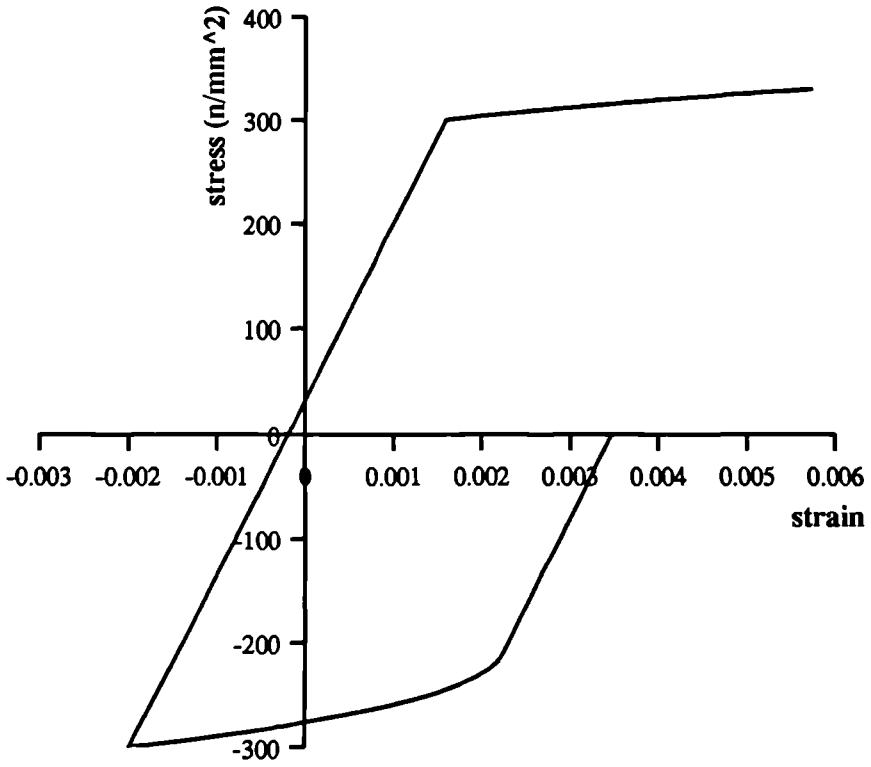


Figure 2.20 Stress-strain response of column at 300°C

The stress-strain response is given in Figure 2.20. At 300°C, the proportional limit is 213 MPa and the yield strength is 355 MPa. When a compressive force is applied, the stress varies linearly up to the proportional limit, and then follows the elliptical curve up to 300 MPa. Unloading occurs when the force is reversed. It can be seen from Figure 2.20 that the successive proportional limit becomes 300 MPa, above which the stress takes a continuation of the previous elliptical curve up to 310 MPa. This simple example demonstrates that the elliptical model, including the loading and unloading response, has been implemented correctly.

CHAPTER 3
MODELLING CREEP EFFECTS

Creep is a time-dependent strain that occurs when a material is subjected to a stress for a prolonged period of time. It is well known that metals creep at temperatures above $0.3T_m$, where T_m is the absolute melting temperature, and at temperatures around $0.5T_m$, creep strains can be substantial (Fessler & Hyde, 1978). On the other hand, Purkiss (1988) argued that creep in steel is negligible below 550°C and, thus, is only important at very high temperatures, which may not be reached by the material during a fire. Experimental observations, however, have shown that steel structures, exposed to fire, can undergo high temperatures above the creep threshold temperature, and for a long period of time (Lennon, 1995). It is therefore the objective of this chapter to study the creep of steel at elevated temperatures, and to develop an associated material model which can be used to investigate the influence of creep on steel structures subjected to fire.

Creep under steady and non-steady state are first discussed. The details of the adopted creep model are then presented, followed by its implementation within ADAPTIC (Izzuddin, 1991). Verifying examples are finally presented to demonstrate the accuracy of the creep model on the material level and to illustrate the influence of creep on structural response at elevated temperatures.

3.1 CREEP MODELS OF STEEL

Creep in steel under constant stress may be divided into three parts: an initial part of progressively decreasing creep strain rate called *primary creep*, a part of almost constant creep strain rate called *secondary creep*, and a final part of progressively increasing creep strain rate called *tertiary creep* which precedes fracture. The length of the primary range is usually stress-dependent. A typical variation of creep strain with time is shown schematically in Figure 3.1.

Creep behaviour is unique for every type of steel and a common description is hard to establish (Anderberg, 1986). This is due to the fact that the chemical composition and the degree of processing strongly influences the creep response. Furthermore, it was observed that the creep response is not related to the 0.2% proof stress or other strength characteristics at ambient temperature.

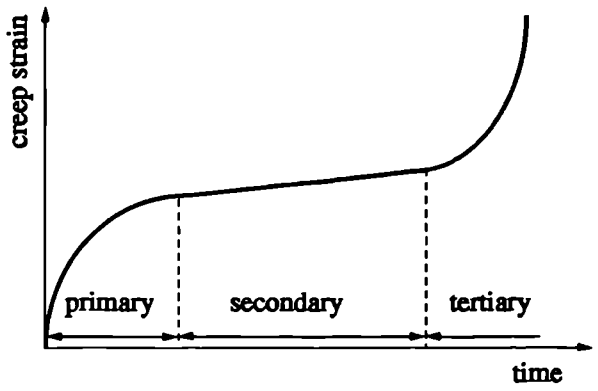


Figure 3.1 Variation of creep strain with time

Experimental testing has played an important role in studying the creep behaviour of steel. Creep tests are classified into two categories, i.e. steady state tests and transient (or non-steady) state tests. Steady state tests are characterised by a sustained constant load under isothermal conditions, while transient state tests are characterised by a varying temperature and/or a varying load. Creep strain can only be directly measured in steady state tests, moreover, the creep from steady state tests is of great importance in predicting the creep process in transient tests.

Creep models for steel at elevated temperatures, corresponding to the steady and transient conditions, are discussed hereafter.

3.1.1 Steady State Creep Response

Several uniaxial constitutive relations have been proposed to describe the creep response of steel at elevated temperatures under steady state (Conway, 1977). Since the temperature, stress level and time all affect the creep strain, it has been proposed that the creep response may be represented as the product of three independent functions of stress (σ), time (t), and temperature (T), at various constant temperatures (Fessler & Hyde, 1978; Boyle & Spence, 1983), for constant values of stress:

$$\varepsilon_c = f_1(\sigma) f_2(t) f_3(T) \tag{3.1}$$

The most commonly used *stress functions* are:

$$f_1(\sigma) = A_1 \sigma^n \tag{3.2a}$$

$$f_1(\sigma) = A_2 \sinh\left(\frac{\sigma}{\sigma_0}\right) \tag{3.2b}$$

$$f_1(\sigma) = A_3 \exp\left(\frac{\sigma}{\dot{\sigma}_0}\right) \tag{3.2c}$$

$$f_1(\sigma) = A_4[\sinh(\alpha\sigma)]^n \tag{3.2d}$$

$$f_1(\sigma) = A_5\left(\sigma - \sigma_0^*\right)^n \tag{3.2e}$$

where A_1, A_2, A_3, A_4, σ_0, $\dot{\sigma}_0$, σ_0^*, and α are material parameters determined from experimental data.

The *time function* is usually expressed as a polynomial, as first suggested by Andrade (1910):

$$f_2(t) = t^m + Ct + Dt^l \tag{3.3}$$

Where C and D are constants, m is a fraction often about 1/4, and l *is* an integer often assumed to be 3 (Fessler & Hyde, 1978). The three terms in this empirical expression are introduced to describe primary, secondary and tertiary creep, respectively. One or more of these terms can be omitted if a particular creep regime is to be neglected. For example, when primary creep is dominant, the usual expression for the creep strain under isothermal conditions is:

$$\varepsilon_c = A\sigma^n t^m \tag{3.4}$$

which combines Equation (3.2a) with the first term in Equation (3.3).

The *temperature function* is almost invariably assumed to be:

$$f_3(T) = \exp\left(\frac{-\Delta H}{RT}\right) \tag{3.5}$$

in which ΔH is the activation energy of creep (J/mol), R is the gas constant (J/mol K), and T is the absolute temperature (K).

The simplest secondary creep rate of the above would take the form:

$$\dot{\varepsilon}_c = A\sigma^n \exp\left(\frac{-\Delta H}{RT}\right) \tag{3.6}$$

This is the so called *power law*, which appears to provide an excellent description of steady state creep behaviour and is particularly useful in structural analysis (Boyle & Spence, 1983). However, at very high stress levels, the exponent (n) increases continuously with increasing stress. This increase is referred to as the *power law breakdown* (Evans & Wilshire, 1993), in which case the power law fails to represent creep behaviour realistically.

The representation of creep in Equation (3.1), using three decoupled functions, is analytically convenient. Nevertheless, the experimental observations show that expressions with separate stress and time functions are unlikely to lead to good predictions of component response (Fessler & Hyde, 1978).

Dorn (1954) proposed a creep model in which at some constant stress level, the creep strain is a unique function of the stress and of a temperature compensated time θ:

$$\varepsilon_c = f(\theta,\sigma) \quad \sigma = \text{constant} \tag{3.7}$$

where

$$\theta = \int e^{-\Delta H / RT} dt \tag{3.8}$$

in which t is time, and ΔH and R are the same as in Equation (3.5).

Temperature compensated time θ was introduced as a parameter to assist in the study of the creep process under constant stress but complex temperature history.

Based on Dorn's concept of temperature compensated time, Harmathy (1967) further developed a creep model in which the entire course of the creep curve of structural materials, excluding tertiary creep, is uniquely determined by two stress-dependent parameters, ε_{c0} and Z. An explicit expression for this creep process, within the primary phase, is:

$$\varepsilon_c = \frac{\varepsilon_{c0}}{\ln 2}\cosh^{-1}\left(2^{Z\theta/\varepsilon_{c0}}\right) \tag{3.9}$$

Z is Zener-Hollomon parameter and is related to the secondary creep rate $\dot{\varepsilon}_c$ as follows:

$$Z = \dot{\varepsilon}_c e^{\Delta H/RT} \tag{3.10}$$

Therefore, Z is also referred to as the temperature compensated secondary creep rate.

Due to the complexity of the Dorn-Harmathy creep formula, Plem (1975) proposed a modification so that a parabolic equation could be used for the primary phase and the secondary phase could be unchangingly represented by a straight line, as below:

$$\left.\begin{aligned} \varepsilon_c &= \varepsilon_{c0}\left(2\sqrt{Z\theta/\varepsilon_{c0}}\right) \quad 0 \le \theta \le \theta_0 \\ \varepsilon_c &= \varepsilon_{c0} + Z\theta \qquad\qquad \theta \ge \theta_0 \end{aligned}\right\} \tag{3.11a}$$

where

$$\theta_0 = \varepsilon_{c0}/Z \tag{3.11b}$$

is the point at which the transfer from the primary phase to the secondary phase occurs.

The following equations relate Z and ε_{c0} to the constant stress σ:

$$\varepsilon_{c0} = A\sigma^B \tag{3.12}$$

$$Z = \begin{cases} C\sigma^D & \text{if } \sigma \le \sigma_1 \\ G\exp(F\sigma) & \text{if } \sigma > \sigma_1 \end{cases} \tag{3.13}$$

where A, B, C, D, F, G and σ_1 are constants. The creep parameters used in the above creep model are shown in Table 3.1 for various structural steels.

3.1.2 Transient Creep Response

In reality, the creep response of steel structures under fire loading is generally transient with varying stresses and temperatures. Creep of metals under transient conditions of

Table 3.1 The values of $\Delta H / R$, Z and ε_{c0} as functions of the stress (kg/cm^2) for different structural steels at room temperature (Thor, 1973-b) (σ_y: yield stress)

Steel group	Steel	σ_y (kg/cm^2)	$\Delta H/R$ (K)	Z (hr^{-1})	ε_{c0}
Carbon steel	1312	2590	55800	$\begin{cases}\sigma \le 1100 & 4.89\times10^{3}\sigma^{7.808}\\ \sigma > 1100 & 8.3\times10^{24}e^{0.00567\sigma}\end{cases}$	$1.02\times10^{-7}\sigma^{1.722}$
	1411	3400	66000	$\begin{cases}\sigma \le 1200 & 1.37\times10^{6}\sigma^{8.4919}\\ \sigma > 1200 & 1.45\times10^{29}e^{0.00592\sigma}\end{cases}$	$2.82\times10^{-9}\sigma^{2.08}$
	A36-66	3100	38900	$\begin{cases}\sigma \le 1050 & 6.80\times10^{3}\sigma^{4.70}\\ \sigma > 1050 & 1.2\times10^{16}e^{0.0042\sigma}\end{cases}$	$7.00\times10^{-8}\sigma^{1.75}$
Carbon manganese	2172	3380	50000	$\begin{cases}\sigma \le 1100 & 3.00\times10^{6}\sigma^{5.38}\\ \sigma > 1100 & 6.50\times10^{20}e^{0.00438\sigma}\end{cases}$	$1.00\times10^{-10}\sigma^{2.30}$
	G40.12	3400	36100	$\begin{cases}\sigma \le 1050 & 1.50\times10^{6}\sigma^{3.25}\\ \sigma > 1050 & 3.70\times10^{14}e^{0.00313\sigma}\end{cases}$	$1.80\times10^{-6}\sigma^{1.00}$
Grain refined steel	with Al	3730	40900	$\begin{cases}\sigma \le 1300 & 2.10\times10^{1}\sigma^{5.78}\\ \sigma > 1300 & 8.00\times10^{16}e^{0.00455\sigma}\end{cases}$	$1.48\times10^{-9}\sigma^{2.15}$
	with Ni	4050	45000	$\begin{cases}\sigma \le 1250 & 5.03\sigma^{6.664}\\ \sigma > 1250 & 1.2\times10^{19}e^{0.00434\sigma}\end{cases}$	$4.78\times10^{-9}\sigma^{1.95}$

stress is rather complicated. Research on this problem has been concerned with predicting creep from the simple creep behaviour under steady-state stress conditions. A number of hypotheses have been proposed and the most general are the theories of *time-hardening, strain-hardening, work-hardening, life-fraction rule* and *state-variable* (Manson, 1961; Fessler & Hyde, 1978; Boyle & Spence, 1983).

3.1.2.1 Time-hardening

The time-hardening rule assumes that the creep rate depends on the current stress and time of loading. This is indicated in Figure 3.2(a), where the stress is increased at the end of various time intervals; i.e. points A and B. During any one interval, stress is assumed constant. When the stress is changed from σ_1 to σ_2 at point A, the new creep strain rate is determined by proceeding to point A′ immediately below A, according to the time-hardening rule. This implies that the level of creep strain induced in the prior history is not important.

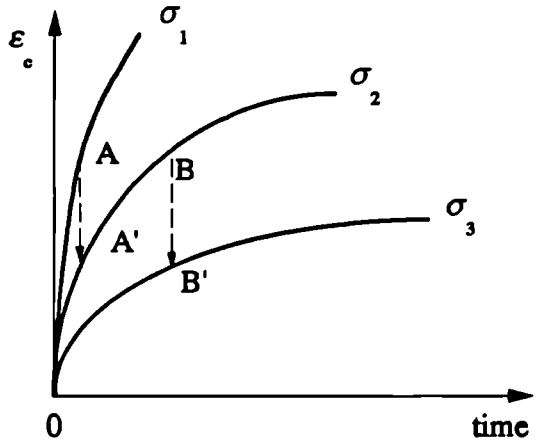


Figure 3.2(a) Time-hardening rule

3.1.2.2 Strain-hardening

The strain-hardening rule assumes that the creep rate depends on the current stress and creep strain, as illustrated in Figure 3.2(b). When stress is changed from σ_1 to σ_2 at point A, the new creep strain rate is determined by proceeding to point A′ immediately below A, corresponding to the same creep strain but at stress level σ_2.

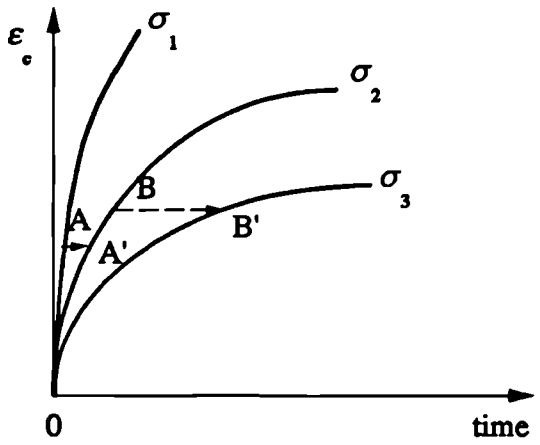


Figure 3.2(b) Strain-hardening rule

Some experimental programmes have been carried out to compare the time-hardening and strain-hardening theories. The test results show that the strain-hardening theory gives significantly better predictions than the time-hardening theory (Ohji & Marin, 1964; Marriott, 1964; Fessler & Hyde, 1978).

3.1.2.3 Work-hardening

The work-hardening rule assumes that the creep rate depends on the current stress and the work done in creep ($\int \sigma d\varepsilon_c$). The resulting prediction of the work-hardening theory is similar to that based on strain-hardening (Fessler & Hyde, 1978). More experimental data is required to support this hypothesis.

3.1.2.4 Life-fraction rule

The life-fraction rule assumes that the creep rate depends on the current stress and the time to rupture as shown in Figure 3.2(c), where A′ and A have the same fraction of the total time to rupture. According to the life-fraction rule, if a material has a certain fraction of its life left at a given stress and temperature, a change in stress and temperature will produce a new creep rate, corresponding to the point on the steady-state creep curve of the new stress and temperature, at which the same fraction of life is left. Robinson (1938) applied this rule to creep-rupture at constant stress but variable temperature. However, it was found by Miller (1954) and Caughey and Hoyt (1955) respectively that it does not successfully predict the influence of multiple overtemperature periods on the creep of Inconel.

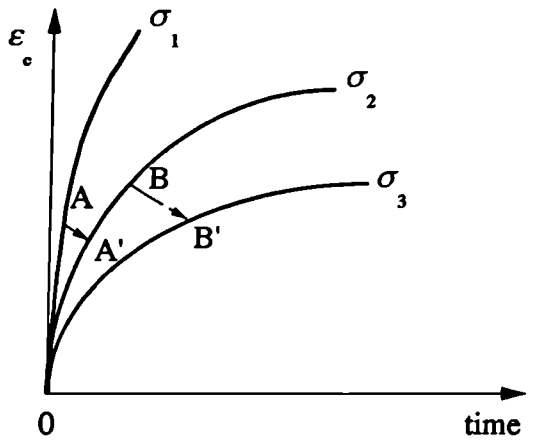


Figure 3.2(c) Life-fraction rule

3.1.2.5 State variable

The representations of material creep behaviour described above do not model well the recovery phenomenon for unloading. *State variable* theory has been suggested for this purpose, where the creep strain rate is expressed as:

$$\dot{\varepsilon}_c = f(\sigma, \alpha, R) \tag{3.14a}$$

where initially t =0, $\varepsilon_c = 0$, $\alpha = 0$ and $R = R_0$

The state variable α is usually called the *rest* stress and the variable R called the *drag* stress. Two competing mechanisms are assumed to govern the growth of the state variables: hardening and recovery, such that

$$\dot{\alpha} = f_1(\sigma, \alpha, R)\dot{\varepsilon}_c - f_2(\sigma, \alpha, R)\alpha \tag{3.14b}$$

$$\dot{R} = g_1(\sigma, \alpha, R)|\dot{\varepsilon}_c| - g_2(\sigma, \alpha, R)(R - R_0) \tag{3.14c}$$

The functions f_1, f_2, g_1 and g_2 assume different forms for different theories (Boyle & Spence, 1983). It is clear that a large number of material constants are required by these models. In order to identify the constants, tests other than simple constant load tests are necessary. With variable temperature, the testing programme could prove impractical.

3.2 ADOPTED CREEP MODEL

Figure 3.3 illustrates the general form of the steady-state creep model adopted in this work. The creep strain is assumed to be dependent on the magnitude of stress and on the temperature-compensated time. The primary phase is defined by a parabolic function, and the secondary phase defined by a straight line, while the tertiary creep leading to fracture is ignored. The change from the curved branch to the straight line, i.e. from primary to secondary phase, occurs at temperature compensated time (θ_0) and an associated creep strain ($2\varepsilon_{c0}$), with the slope of the secondary creep straight line denoted by Z.

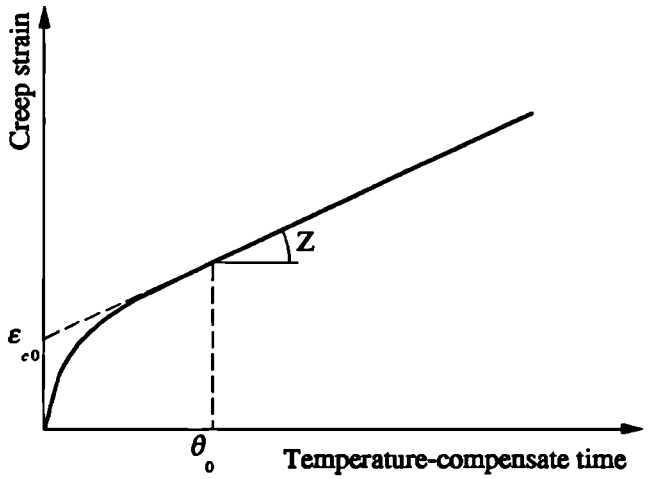


Figure 3.3 Adopted creep model

The governingequations of this steady state creep model are as follows:

$$\varepsilon_c = \begin{cases} \varepsilon_{c0}\left(2\sqrt{Z\theta/\varepsilon_{c0}}\right) & 0 \le \theta \le \theta_0 \\ \varepsilon_{c0} + Z\theta & \theta \gtrsim \theta_0 \end{cases} \tag{3.15}$$

where

$$\theta_0 = \varepsilon_{c0}/Z \tag{3.16}$$

$$\varepsilon_{c0} = A\sigma^B \tag{3.17}$$

$$Z = \begin{cases} C\sigma^D & \sigma \le \sigma_1 \\ G\exp(F\sigma) & \sigma > \sigma_1 \end{cases} \tag{3.18}$$

θ is temperature compensated time defined in Equation (3.8), and parameters *A, B, C, D, F, G* and σ_1 are all material constants.

The strain-hardening rule is used to predict creep strain under varying stress from the above steady state model. From Equation (3.15), the strain-hardening rule reduces to:

$$\dot{\varepsilon}_c = \begin{cases} \dfrac{2\varepsilon_{c0} Z}{\varepsilon_c} e^{-\frac{\Delta H}{RT}} & \varepsilon_c \le 2\varepsilon_{c0} \\ Ze^{-\frac{\Delta H}{RT}} & \varepsilon_c \ge 2\varepsilon_{c0} \end{cases} \tag{3.19}$$

In the analysis, the total strain (ε_t) consists of the thermal strain (ε_{th}), the stress inducing strain (ε_σ), and the creep strain (ε_c):

$$\varepsilon_t = \varepsilon_{th} + \varepsilon_\sigma + \varepsilon_c \tag{3.20}$$

To calculate the creep strain, temperature is assumed to be constant over each time step Δt, and the stress level at the start of the time step is used. ε_c^0, σ^0, T^0 are defined as the creep strain, stress and temperature, respectively, at the start of the time step. From Equation (3.8), the temperature-compensated time increment for the current step is:

$$\Delta\theta_c = e^{-\frac{\Delta H}{RT^0}} \Delta t \tag{3.21}$$

The temperature-compensated time (θ_c^0) corresponding to ε_c^0 on the steady state creep curve that corresponds to σ^0, can be obtained from Equation (3.15) as

$$\theta_c^0 = \begin{cases} \dfrac{\varepsilon_c^{0^2}}{4\varepsilon_{c0} Z} & \theta_c^0 \le \theta_0 \\ \left(\varepsilon_c^0 - \varepsilon_{c0}\right)/Z & \theta_c^0 > \theta_0 \end{cases} \tag{3.22}$$

The total temperature-compensated time θ_c at the end of the current time step is:

$$\theta_c = \theta_c^0 + \Delta\theta_c \tag{3.23}$$

The creep strain ε_c can be then obtained as in Equation (3.15) from:

$$\varepsilon_c = \begin{cases} \varepsilon_{c0}\left(2\sqrt{Z\theta_c/\varepsilon_{c0}}\right) & 0 \le \theta_c \le \theta_0 \\ \varepsilon_{c0} + Z\theta_c & \theta_c \ge \theta_0 \end{cases} \tag{3.24}$$

For the first step, ε_c is zero since the initial stress is zero. For the second and subsequent steps, ε_c is calculated according to the above procedure.

Once the creep strain is known, the procedure for calculating stress from strain is the same as that of the thermal models, discussed in the previous chapter, except that the thermal strain (ε_{th}) is replaced by the sum of thermal strain and creep strain ($\varepsilon_c + \varepsilon_{th}$).

3.3 IMPLEMENTATION INTO ADAPTIC

The creep model has been implemented into the cubic formulation within ADAPTIC (Izzuddin, 1991), with the flow chart shown in Figure 3.4. It is defined as material model *stl5* using 28 parameters, as described in Appendix A.

3.4 VERIFICATION EXAMPLES

Several examples are provided hereafter to test the implementation of the creep model and to demonstrate the significance of the creep effect. The material properties given in Table 3.2 are used in each of the examples in this section.

Table 3.2 Material properties and reduction factors at elevated temperatures

Young's modulus 210 GPa		Yield strength 355 MPa		Hardening factor	
Temperature (°C)	Reduction factor	Temperature (°C)	Reduction factor	Temperature (°C)	Value
100	1.0	100	1.0	400	0.0
700	0.13	800	0.11	600	0.08
1200	0.0	1200	0.0	1000	0.0

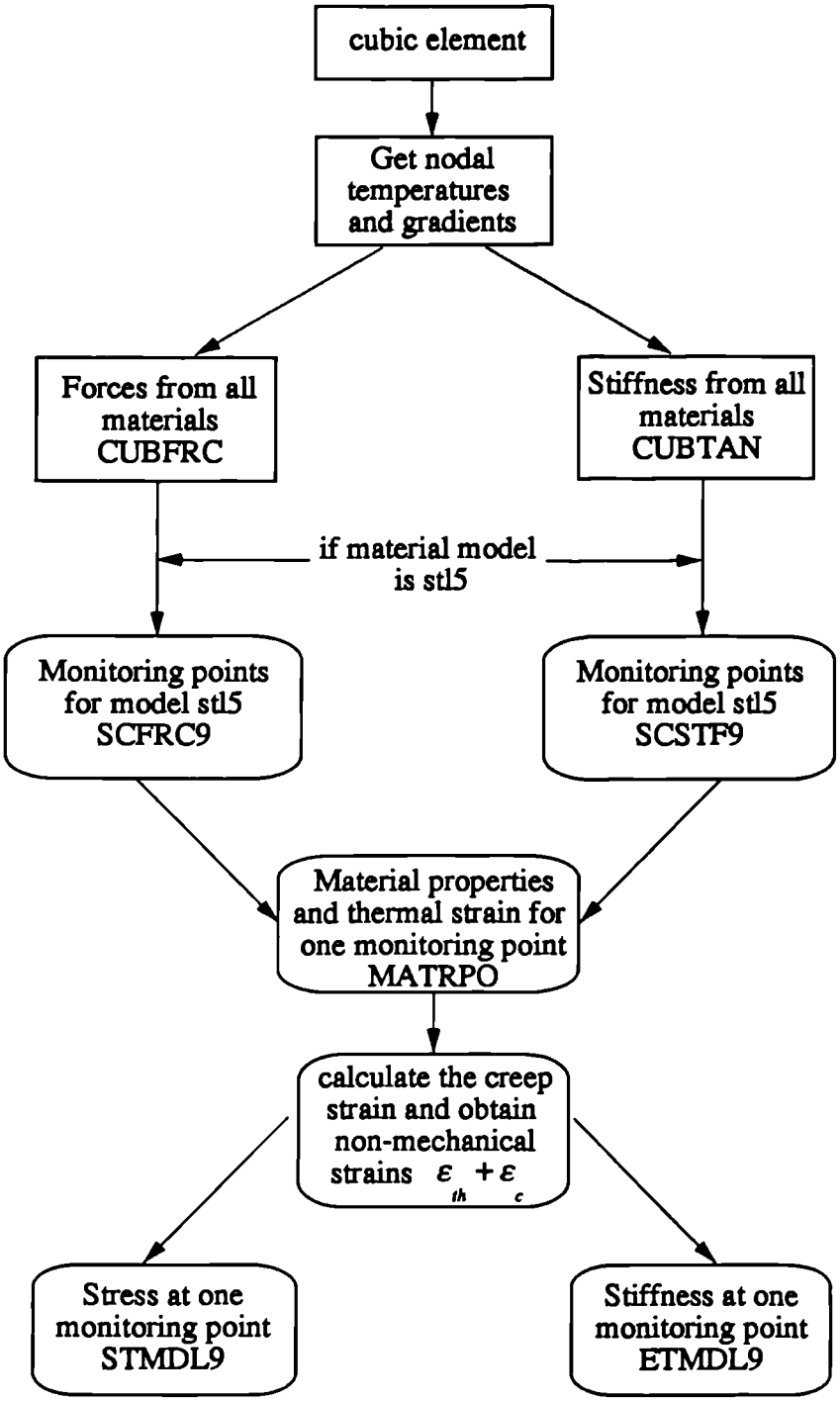


Figure 3.4 Main subroutines of creep model

3.4.1 Verification on Material Level

Creep strain is considered under two types of stress histories at constant temperature.

3.4.1.1 Linearly varying stress

Considering a stress history of a linearly increasing load with time as:

$$\sigma = \sigma_0 \frac{t}{t_1} \tag{3.25}$$

where t_1 is the time interval over which the creep is considered. 10 minutes duration is considered in this case.

A close form solution based on Equation (3.15) for creep under constant temperature and linearly varying stress expressed by Equation (3.25) can be obtained from the strain-hardening theory. Integrating Equation (3.19) gives:

$$\varepsilon_c = \left(4 \int_0^{t_1} \varepsilon_{c0} Z e^{-\frac{\Delta H}{RT}} dt \right)^{1/2} \tag{3.26}$$

Substituting Equation (3.25) into Equations. (3.17), (3.18) and rewriting Equation (3.26), the following is obtained:

$$\varepsilon_c = \left(\frac{4AC}{B+D+1} e^{-\frac{\Delta H}{RT}} t_1 \sigma_0^{B+D} \right)^{1/2} \tag{3.27}$$

For this problem, the parameters for carbon steel A36-66 in Table 3.1 are taken. Assuming σ_0 is 100 MPa and temperature is 600°C, substitution of these constants into Equation (3.27) renders the creep strain of 0.006952. The thermal and elastic strains can also be calculated as 0.0088 and 0.0017316, respectively. The total strain is, therefore, 0.017483 which compares well with the value 0.017419, obtained using ADAPTIC. This example shows that the creep model has been implemented correctly.

3.4.1.2 Stepped stress

A stress history shown in Figure 3.5(a) is considered. The variation of creep strain with time is given in Figure 3.5(b), along with the creep strain under three constant

stresses of 60, 80 and 100 MPa. It is shown in Figure 3.5(b) that at 60 minutes, when stress varies from 60 MPa to 80 MPa, the creep strain rate takes the slope at the point which has the same creep stain on the steady state creep curve of 80 MPa. When stress changes again at 90 minutes from 80 to 100 MPa, a similar observation is made, which again demonstrates the correct implementation of the creep model.

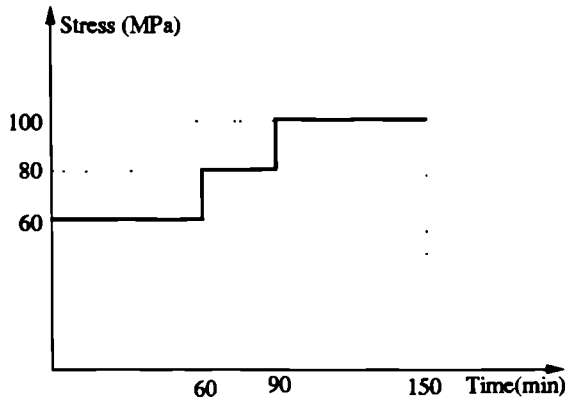


Figure 3.5 (a) Stress History

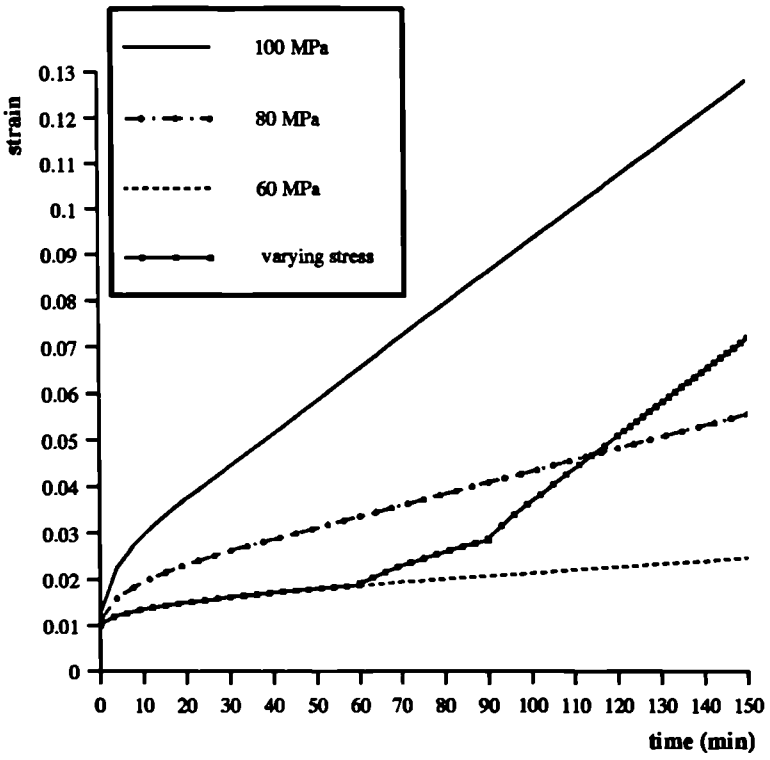


Figure 3.5(b) Creep under step stress history

3.4.2 Effect of Heating Rate

A simply supported beam, under a concentrated load applied at the mid-span, is considered. The dimensions of the beam are given in Figure 3.6. Load P is applied as an initial load. A uniformly distributed temperature is applied as a time history load. The beam is heated at three rates: 32 K/min, 5 K/min and 2K/min. To further demonstrate the creep effect, another case is studied in which creep is completely excluded from the analysis. The creep parameters for Carbon steel 1411 in Table 3.1 are taken.

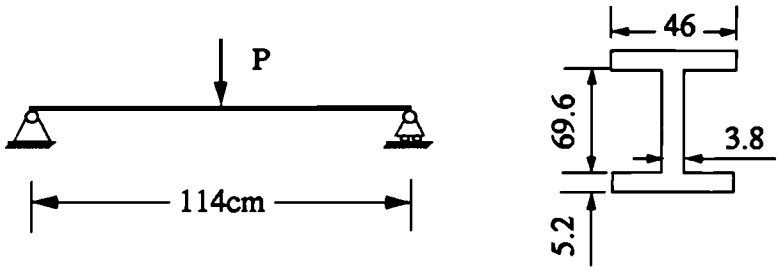


Figure 3.6 Simply supported beam with a single load at midspan

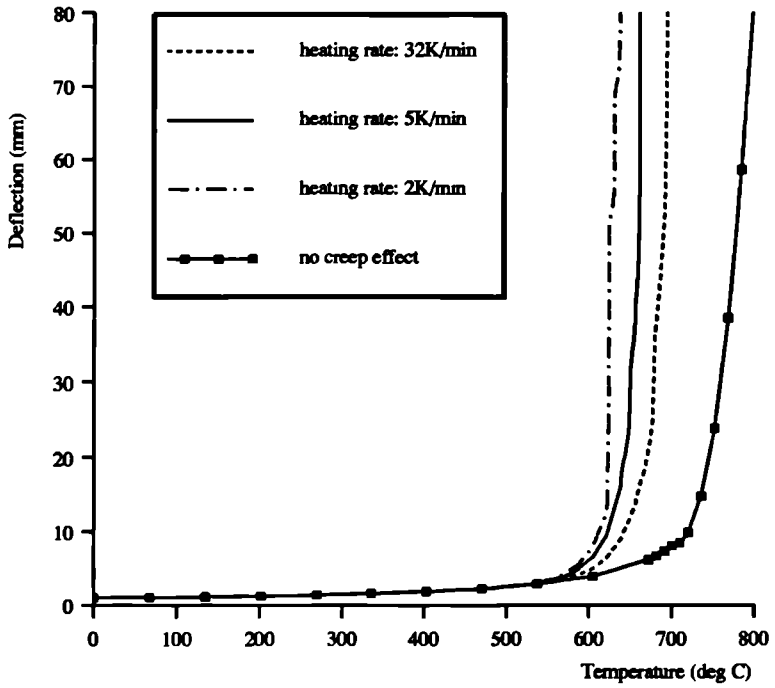


Figure 3.7 Effect of heating rate on limit temperature

The mid-span deflection is shown in Figure 3.7 for all four cases. The effect of creep on the beam response becomes significant when temperature exceeds 550°C. It is interesting to note that the limit temperature of the beam is dependent on the heating rate. For this particular case, when creep effect is not taken into account in the analysis, which implies that the heating rate is not considered, the limit temperature of the beam could be as high as 800°C, while for a slow heating rate of 2K/min it reduces to 636°C.

CHAPTER 4
ANALYSIS OF STEEL FRAMES UNDER FIRE CONDITIONS

In the previous two chapters, material models for steel at elevated temperatures, including the effect of creep, were presented, and their implementation within ADAPTIC was verified. With the incorporation of these models, ADAPTIC is capable of modelling the response of steel frames under fire conditions. This chapter is concerned with verifying the extended elevated temperature capabilities of ADAPTIC against available experimental results. Verification is undertaken on individual members, and on frames, where comparisons against experimental results are presented. Two illustrative examples are then provided to demonstrate the application of the program to realistic structures. The favourable comparison against experimental results and the applicability of the program justify the prospect of its application for predicting the response of steel frames to fire loading.

4.1 VERIFICATION AGAINST EXPERIMENTAL RESULTS

Numerous fire tests have been performed on steel members and frames (Wainman & Kirby, 1987; Latham et al., 1986; Cooke, 1987; Cooke and Latham, 1987; Rubert & Schumann, 1986), with some of the important experimental studies being summarised in Chapter 1. However, publications providing comprehensive details required for analysis, such as the temperature profile, are few. In the following, several analysis is performed to compare the program predictions against available test results. These cover various types of construction members, cross-sections, restraint conditions and temperature distributions.

4.1.1 Verification against Experiments on Individual Members

4.1.1.1 Members with uniform temperature

To study the temperature-dependent behaviour of steel under simultaneous external and thermal loading, several tests were carried out by Rubert and Schaumann (1986) on simply supported beams loaded at midspan, as shown in Figure 4.1. The beams, with cross-section IPE 80 and IPE 120 (DIN 1025-1), were subjected to a constant midspan load, and were then heated uniformly along their entire length. The parameter that was

varied in the test series was the load utilisation factor, which is the ratio of the actual load to the ultimate load carrying capacity at room temperature.

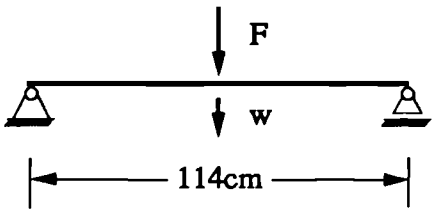


Figure 4.1 Simply supported beam with a single load at midspan

The various tested beams are simulated with ADAPTIC using 10 cubic elements, utilising both the bilinear and elliptical material models presented in Chapter 2. The reduction factors for Young's modulus, the proportional limit, the yield strength, and the strain hardening parameter at elevated temperatures, as well as their values at room temperature, are given in Tables 4.1(a) and (b) for the bilinear and elliptical model, respectively, and a constant coefficient of thermal expansion of 12.6×10^{-6} is adopted. The reduction factors for the elliptical model are taken from Rubert and Schaumann (1986). Importantly, the parameters used for the bilinear model are so chosen that the resulting stress-strain relationship at elevated temperatures provides a good fit to that represented by the elliptical model.

Table 4.1(a). Material properties and their reduction factors for the bilinear model

Young's modulus 210 GPa		Yield strength 399 MPa		Strain-hardening parameter μ	
Temperature (°C)	Reduction factor	Temperature (°C)	Reduction factor	Temperature (°C)	Value
100	1.0	200	1.0	100	0.0
1000	0.1	500	0.6	400	0.08
1200	0.0	700	0.0	700	0.0

Table 4.1(b). Material properties and their reduction factors for the elliptical model

Young's modulus 210 GPa		Proportional limit 399 MPa		Yield strength 399 MPa	
Temperature (°C)	Reduction factor	Temperature (°C)	Reduction factor	Temperature (°C)	Reduction factor
100	1.0	100	1.0	400	1.0
300	0.8	200	0.9	700	0.2
500	0.6	300	0.6	800	0.13
700	0.4	500	0.5	900	0.06667
1000	0.0	700	0.0	1000	0.0

The variation of the midspan deflection with temperature is shown in Figure 4.2 for load utilisation factors of 0.20, 0.50, 0.70 and 0.85, as obtained from the tests and from ADAPTIC using the bilinear and elliptical models. Favourable comparison is observed between ADAPTIC and the test results. It shows that the analytical results agree well with the test results, particularly for a utilisation factor of 0.7, for which both the bilinear and elliptical modes agree closely with the test results for the full fire duration.

It is noted that for a load utilisation factor of 0.85, the prediction of ADAPTIC using the elliptical model follows the measured points closely up to a temperature of 430°C. Beyond this temperature, the bilinear model provides a more accurate prediction, although it does not represent the variation in the displacement rate between 200°C and 430°C. The fact that the bilinear model approximates the nonlinear stress-strain relationship with two straight lines explains the above observation. From Figure 4.3, it can be seen that approximating the nonlinear stress-strain curve by a bilinear model over-estimates the material response, which explains the higher survival temperatures predicted by the bilinear model.

With regard to efficiency, the bilinear model is shown to be considerably more efficient than the elliptical model. The CPU time required to run the four cases with the bilinear model was 19.13s, 3.02s, 3.07s and 2.83s, respectively, compared with 35.2s, 17.58s, 36.63s and 47.93s, respectively, for the elliptical model.

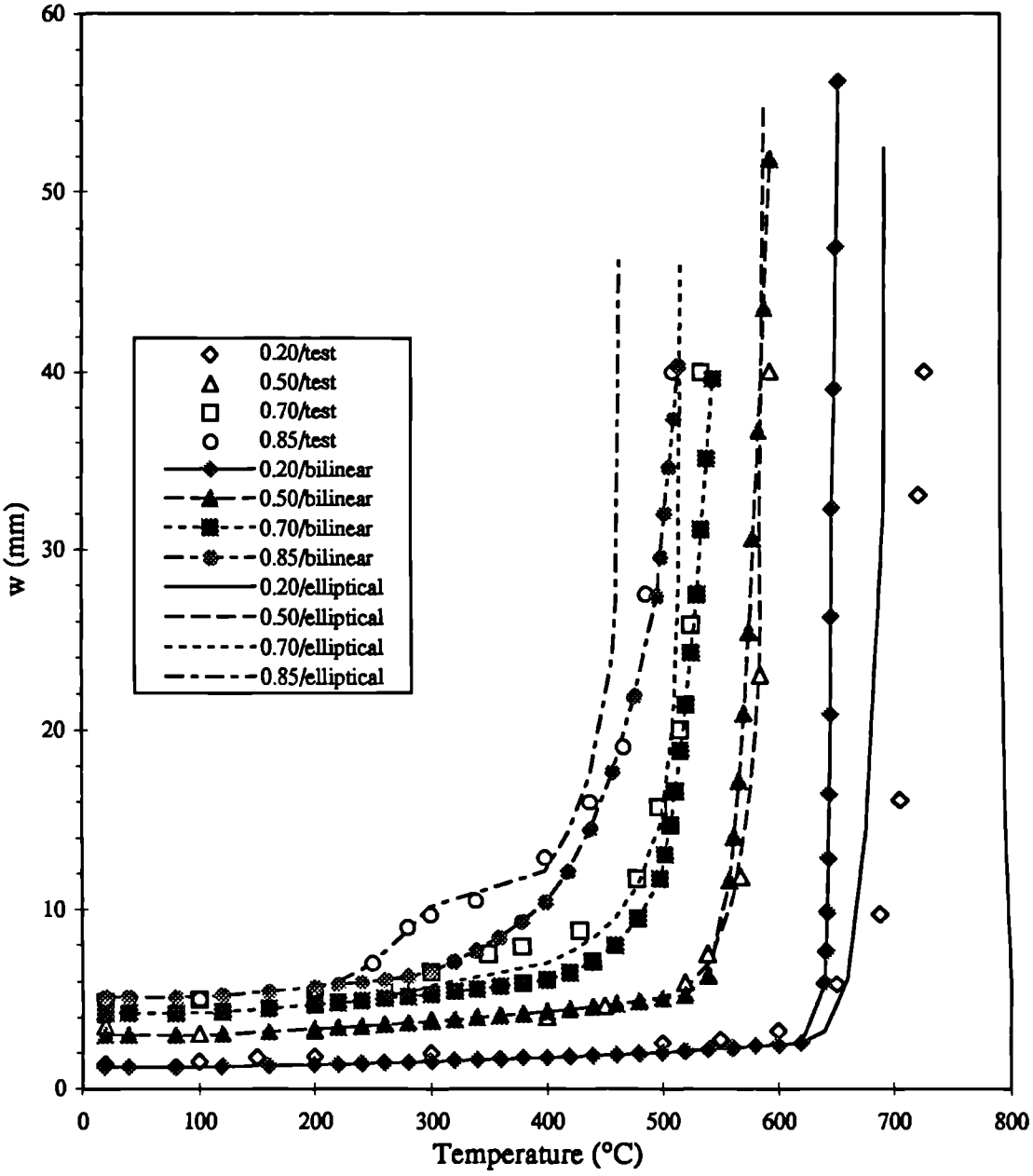


Figure 4.2 Temperature-displacement curves with different load factor

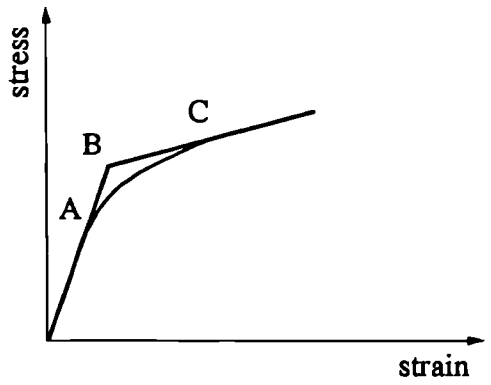


Figure 4.3 Comparison of bilinear and elliptical material models

4.1.1.2 Member with temperature gradient

Cooke (1987) carried out experiments to study the behaviour of beams subject to temperature gradient over the cross section. One of the tests is used herein to verify the material models for steel at elevated temperatures implemented within ADAPTIC.

The beam tested is 104 mm deep by 44 mm wide and 1500 mm long, of Grade 43. It has tapered flanges and a second moment of area about the major axis of 152.3 cm^4. During the test, the beam, unrestrained and load free, is heated along one flange over beam length, hence, the temperature profiles across the beam have curvilinear form, as illustrated in Figure 4.4. The thermocouples are located at 12 stations along the beam with a nominal distance of 128 mm. The numbers of the thermocouple at the centre of the web are given in Figure 4.4. The variation with time of temperatures at the top, middle and bottom of sections with thermocouple no. 3 and 28 are plotted in Figure 4.5.

A flange thickness of 5.97 mm, suggested by Cooke (1987), is adopted in the analysis. With this thickness, the calculated second moment of area of the section is 153.7 cm^4, which agrees well with the published value. As required by ADAPTIC, a linear temperature distribution, obtained from the temperature difference between the top and bottom of the member at each thermocouple station, is used as shown in Figure 4.4. Since the temperatures at the member ends are not available, they are assumed to be the same as those of the nearest stations.

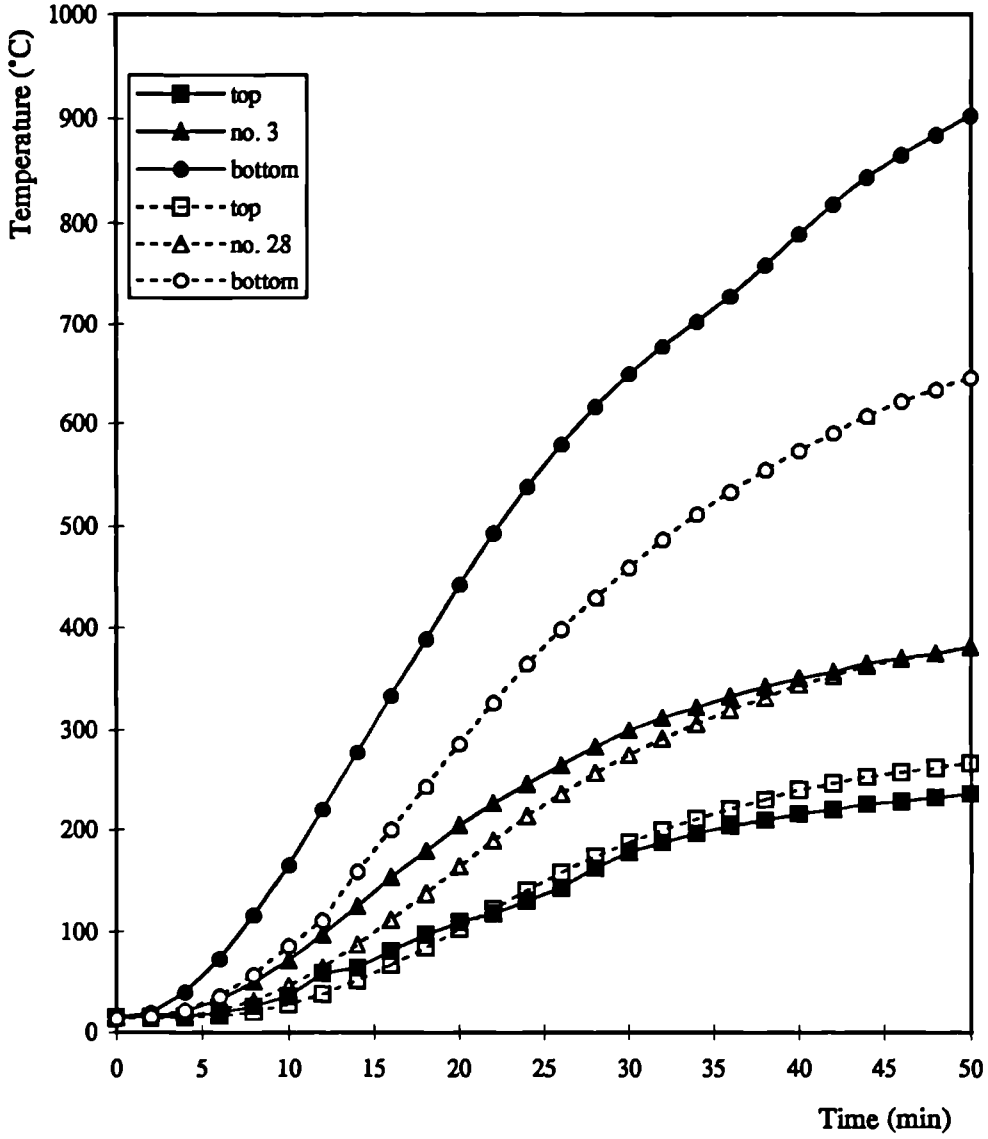


Figure 4.5 Temperatures at two thermocouple stations

Table 4.2. Material properties and their reduction factors at elevated temperatures

Young's modulus 210 GPa		Proportional limit 275 MPa		Yield strength 275 MPa	
Temperature (°C)	Reduction factor	Temperature (°C)	Reduction factor	Temperature (°C)	Reduction factor
100	1.0	100	1.0	400	1.0
500	0.6	200	0.9	700	0.2
600	0.31	300	0.6	800	0.13
700	0.13	500	0.5	900	0.06667
1200	0.0	1200	0.0	1200	0.0

The variation of the central displacement with time is shown in Figure 4.6. A favourable comparison is observed between ADAPTIC and the experimental results up to 30 minutes which corresponds to an average temperature of approximately 650°C. Thereafter, ADAPTIC overestimates the displacement in comparison with the experimental results. This disagreement is partially due to the assumption made in the analysis that the temperature distribution is linear through the member cross section. This assumption leads to higher temperatures in the web than in the test, and, consequently, to a larger displacement.

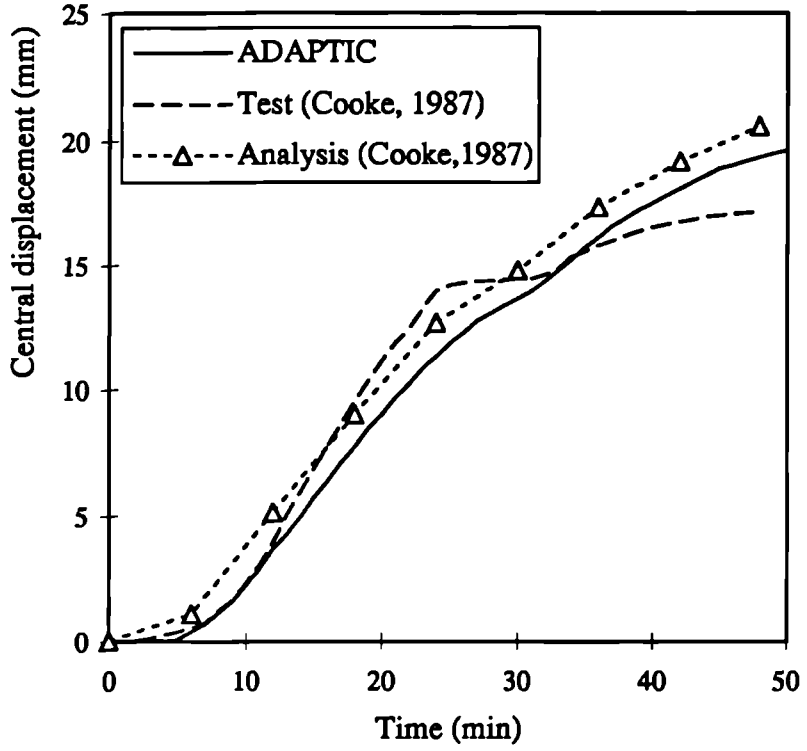


Figure 4.6 Comparison of analysis central displacement with experimental results

Considering the experimental results, it is observed that there is a depression between 26 and 36 minutes, with no increase in displacement over a period of 4 minutes. This phenomenon was explained by Cooke as being due to phase transformation and/or due to the reduction in the modulus of elasticity. The reduction in the modulus of elasticity is accounted for in the ADAPTIC model, it is concluded herein that phase transformation is responsible for this depression phenomenon.

4.1.2 Verification against Experiments on Frames

Series of tests was performed by Rubert and Schumann (1986) on 1/6-1/4 scale plane

steel frames at elevated temperatures. Three frame configurations, shown in Figure 4.7, were considered. Series EHR had two orthogonal members rigidly connected with pinned ends. Series EGR were rigidly connected portal frames with pinned bases. All members of the EHR and EGR series were heated uniformly using electrical devices. Series ZSR considered two-bay continuous portal frames with pinned bases. One bay was fully heated with the remaining two members left cold. The dimensions and loading used for each individual test, as well as the measured yield strength, are shown in Table 4.3.

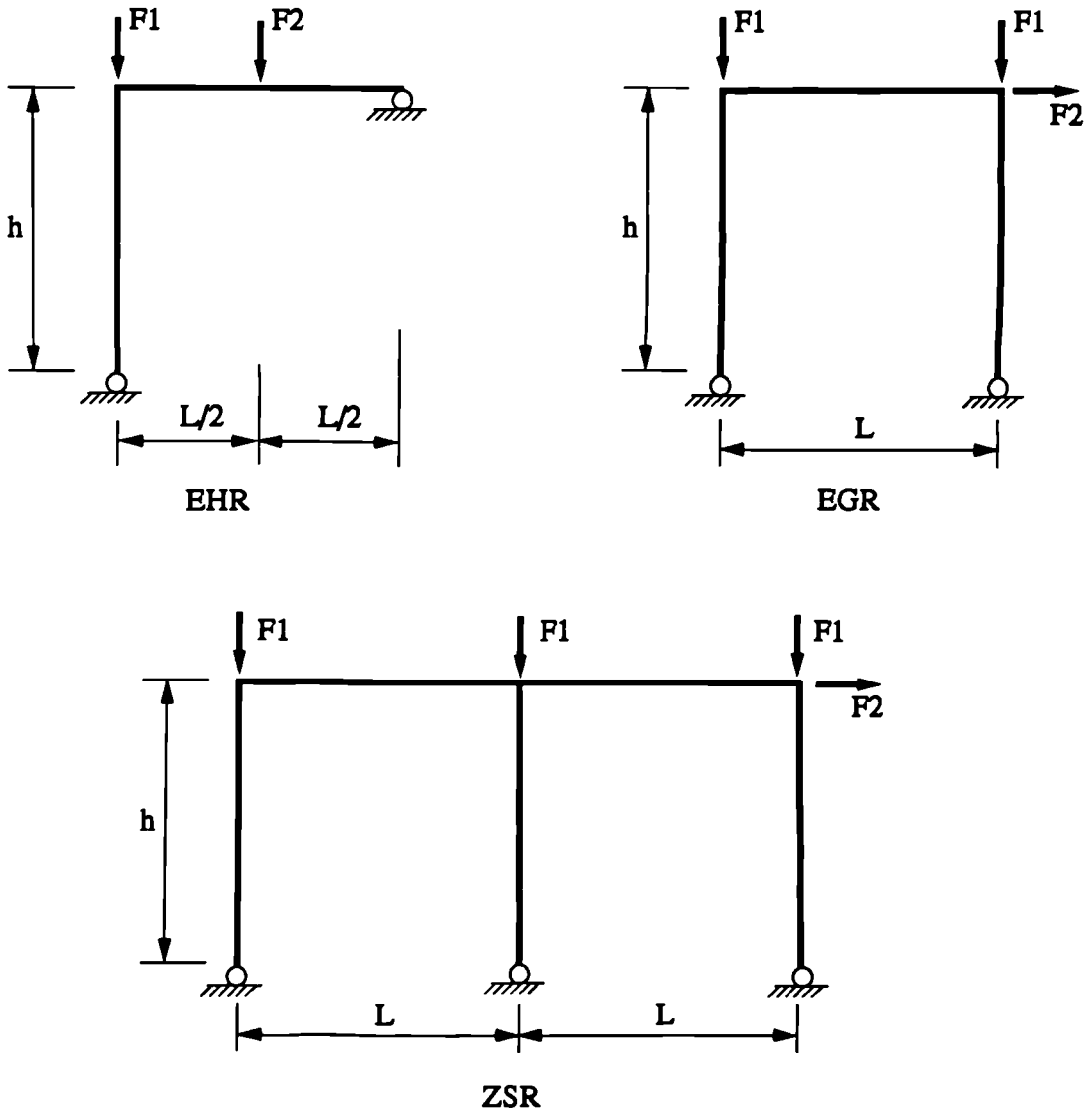


Figure 4.7 Medium-scale steel frame tests

The above tests are simulated with ADAPTIC utilising 10 cubic elements for each structural member, using the elliptical material model. Young's modulus is taken as 210

GPa, and the coefficient of thermal expansion assumes a constant value of 12.6×10^{-6}. The adopted reduction factors for Young's modulus, the proportional limit and the yield strength at elevated temperatures are given in Figure 4.8, as proposed by Rubert and Schumann (1986).

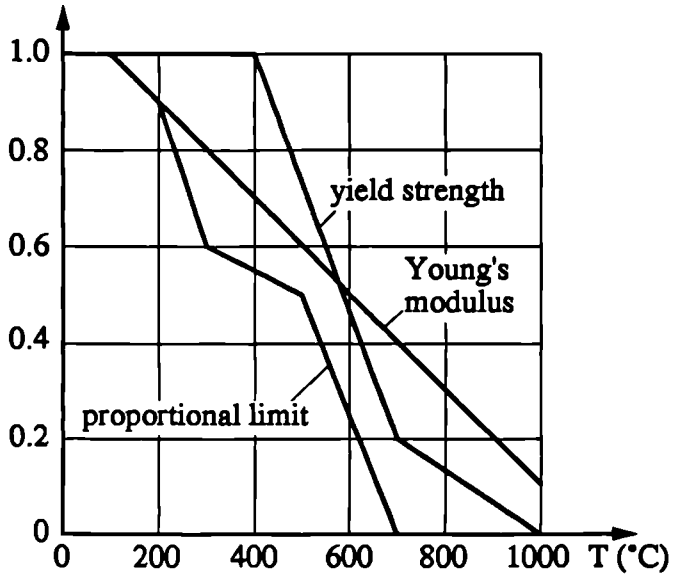


Figure 4.8 Reduction factors for material properties

The critical temperatures, predicted by ADAPTIC, are listed in Table 4.3, along with those reported by Rubert and Schumann (1986), where the critical temperature was taken as the steel temperature when a midspan deformation in the beam reaches *l*/60. Results from ADAPTIC show good agreement with the test results for all three configurations, with a discrepancy of less than 10% of the test results. In most of the cases, the predicted results are on the safe side, as illustrated in Figure 4.9.

The variation of displacements with temperature for three of the tests, namely EHR3, EGR1 and ZSR1 were also reported (Rubert & Schaumann, 1985), where comparisons against the results of ADAPTIC are shown in Figures 4.10, 4.11 and 4.12, respectively. The comparison with test ZSR1 is particularly good, with the prediction of ADAPTIC matching the test results closely up to the failure. The discrepancies for the other two tests are attributed to the uncertainty in material properties at elevated temperatures.

Table 4.3 Parameters and results for the frame tests (Rubert & Schumann, 1986)

System	l (cm)	h (cm)	β_s (kN/cm^2)	F1 (kN)	F2 (kN)	Critical Temperature Test(°C)	ADAPTIC(°C)
EHR1	119	117	39.5	56	14	600	620
EHR2	124	117	39.5	84	21	530	542
EHR3	124	117	38.2	112	28	475	452
EHR4	125	150	38.9	20	5	562	529
EHR5	125	150	38.9	24	6	460	471
EHR6	125	150	38.9	27	6.7	523	417
EGR1b	122	117	38.2	65	2.5	533	489
EGR1c	122	117	38.2	65	2.5	515	489
EGR2	122	117	38.5	40	1.6	612	599
EGR3	122	117	38.5	77	3.0	388	387
EGR4	122	117	41.2	77	3.0	424	417
EGR5	122	117	41.2	88	3.4	335	293
EGR6	122	117	41.2	88	3.4	350	293
EGR7	122	117	32.0	68.5	2.6	454	426
EGR8	122	117	38.5	77	3.0	464	423
EGR9	122	117	41.2	88	3.4	38.7 min	N/A
EGR10	120	113.5	43.2	82	3.1	609	593
ZSR1	120	118	35.5	74.0	2.85	547	514
ZSR2	120	118	38.0	84.5	3.25	479	464
ZSR3	120	118	43.2	68.5	2.64	574	579

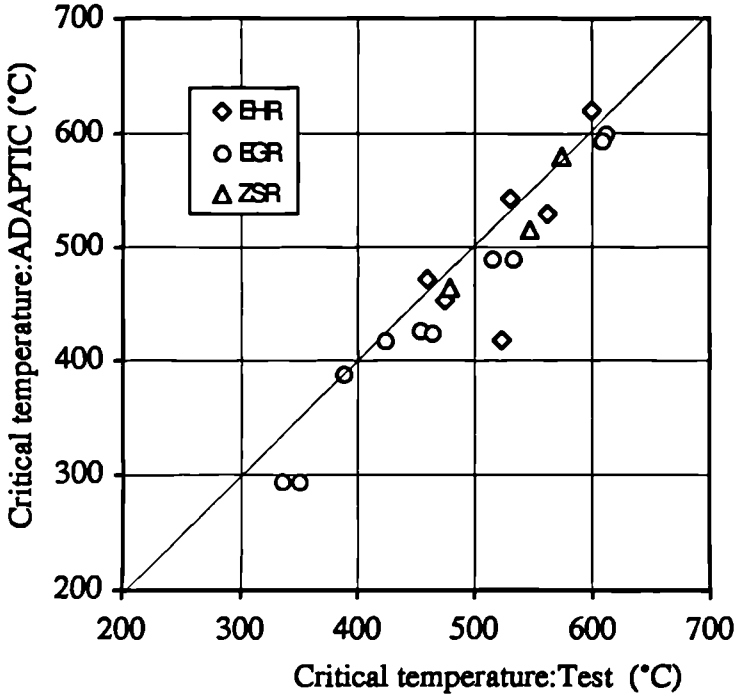


Figure 4.9 Critical temperatures for frame tests

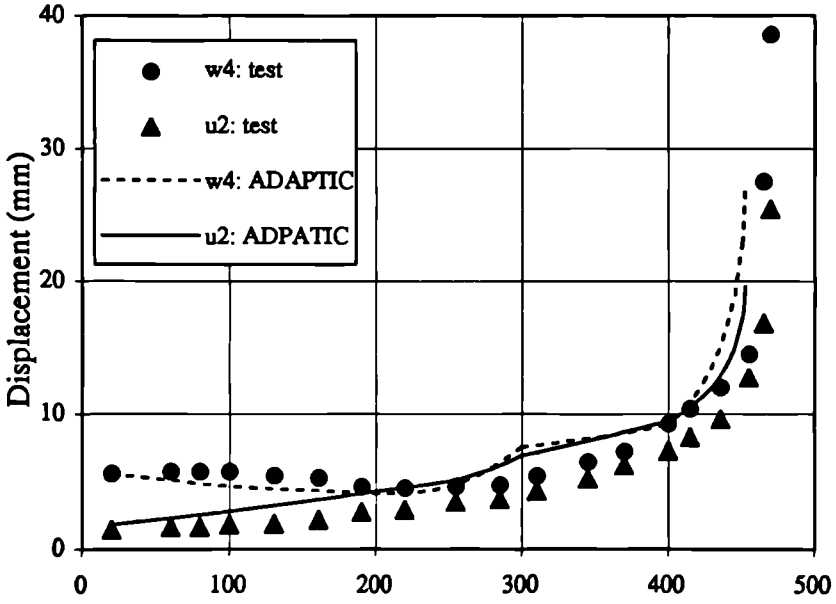


Figure 4.10 Displacement-temperature curves for test EHR3

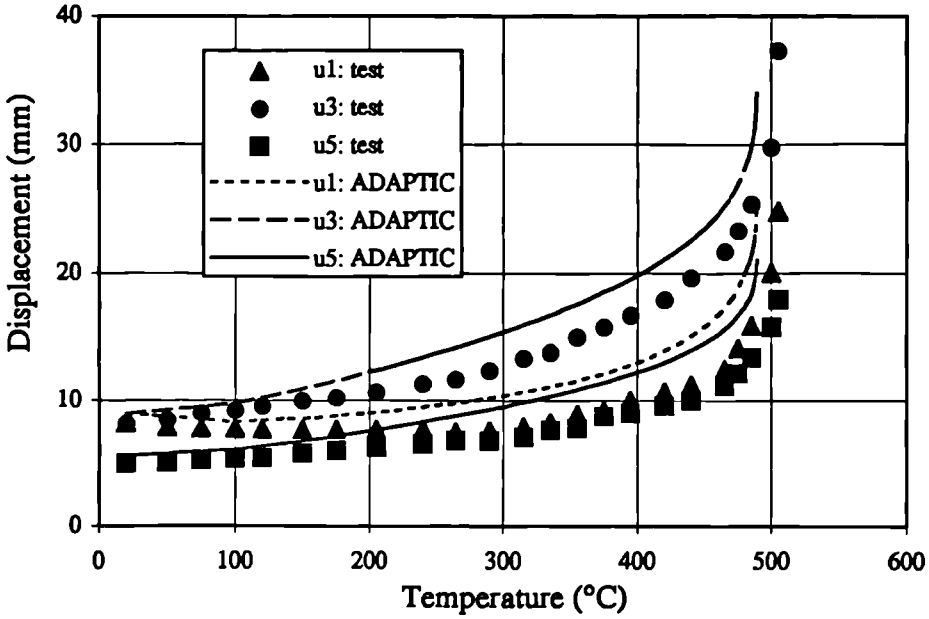


Figure 4.11 Displacement-temperature curves for EGR1

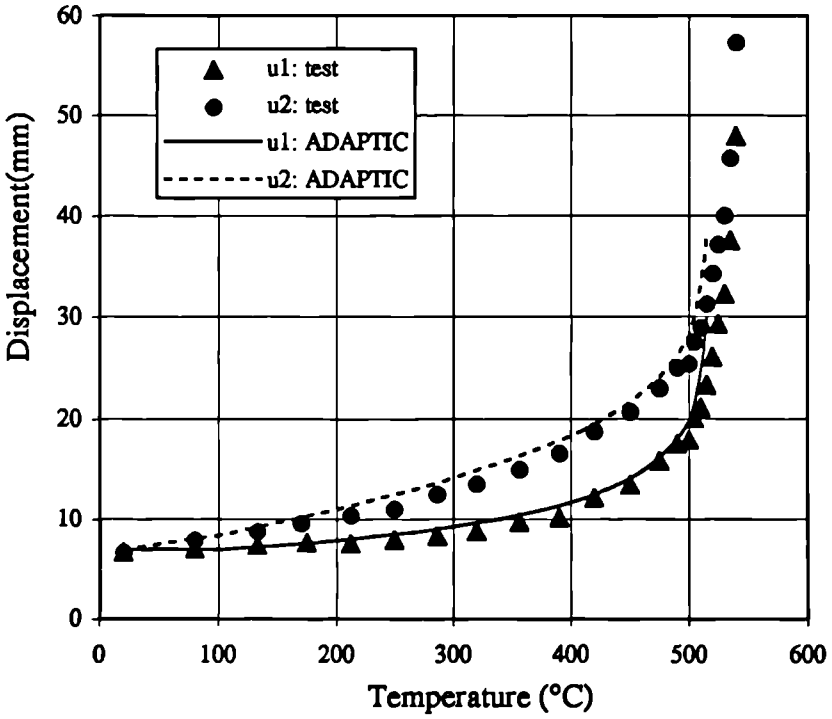


Figure 4.12 Displacement-temperature curves for ZSR1

4.2 ILLUSTRATIVE EXAMPLES

Two examples are presented hereafter to demonstrate the applicability of ADAPTIC for predicting the response of steel frames under fire conditions.

4.2.1 One Bay Frame

A one bay one storey frame with rigid connections and pinned bases is considered, with the geometric configuration and material properties at room temperature, as shown in Figure 4.13. After loads F1 and F2 are initially applied, the frame is heated completely and uniformly, with the temperature rising at the rate of 25°C/min.

The reduction factors for material properties at elevated temperatures, given in Table 4.4, and the creep parameters for steel A36, in Table 3.1, are used in the examples in Section 4.2. The thermal expansion assumes the values suggested in EC3 (1990).

Table 4.4. Reduction factors of material properties at elevated temperatures

Young's modulus		Yield strength		Strain-hardening parameter	
Temperature (°C)	Reduction factor	Temperature (°C)	Reduction factor	Temperature (°C)	Value
100	1.0	400	1.0	400	0.0
700	0.13	800	0.11	600	0.08
1200	0.0	1200	0.0	1200	0.0

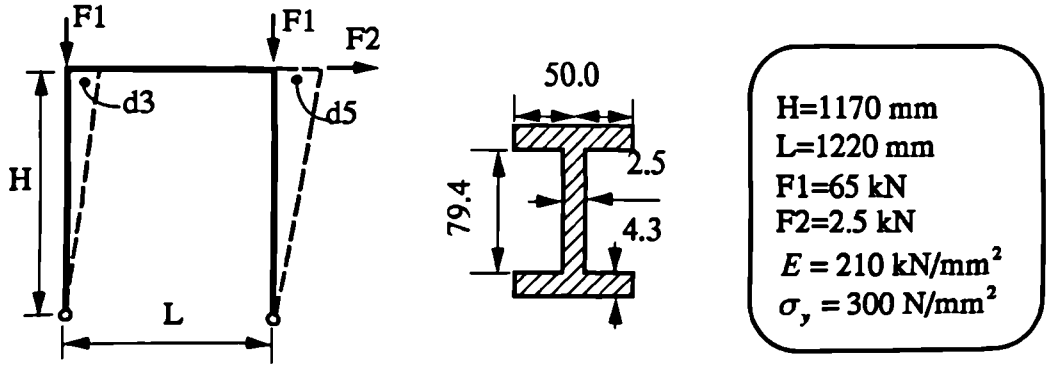


Figure 4.13 One-storey frame under fire condition

The deflection curves are shown in Figure 4.14. Under the initial load, the deflections at the top of the two columns, i.e. d3 and d5, are the same. When the temperature rises in the beam, d3 decreases while d5 increases due to the thermal expansion of the beam. At higher temperatures, d3 and d5 both increase rapidly due to the large deflections of the columns.

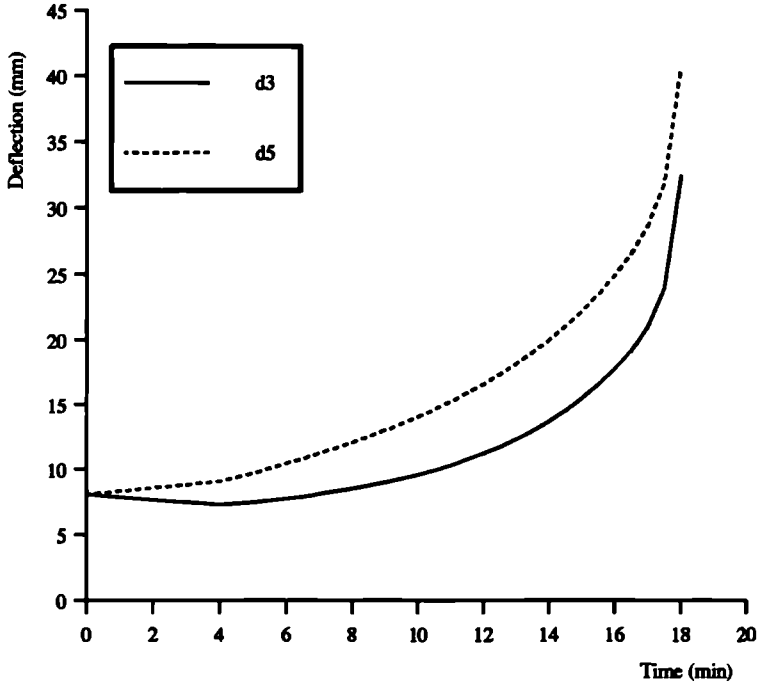


Figure 4.14 Horizontal displacements of one bay frame

4.2.2 Three Storey Frame

A three storey frame shown in Figure 4.15 is analysed using the bilinear material model with creep effects. Young's modulus and the yield strength at ambient temperature are assumed to be 210 GPa and 275 MPa, respectively, with the temperature reduction factors as 0.13, at 700°C, and 0.11, at 800°C. The concentrated loads are applied before the beams and columns are heated.

The fire is located in the left middle compartment only. Two fire protection schemes are considered: (i) columns (1) and (2) are unprotected with the beams fully protected, and (ii) beams (3) and (4) are unprotected with the columns fully protected. A uniform temperature is assumed throughout the members, rising linearly to 800 °C over 1 hour.

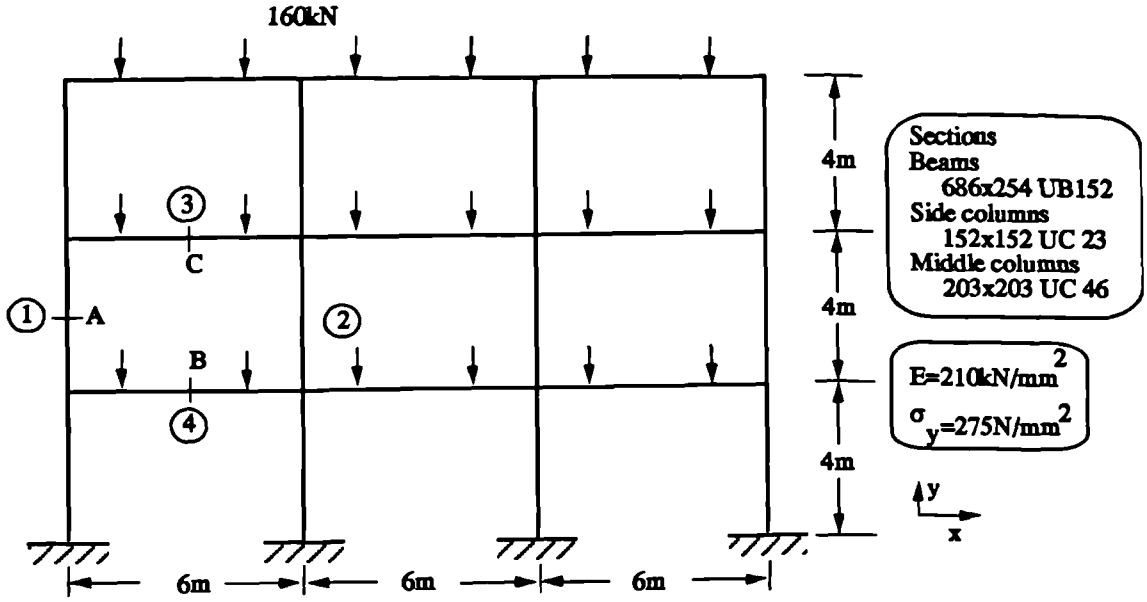


Figure 4.15 Three storey frame

For case (i), column (1) fails at 615 °C, whilst for case (ii) beam (4) fails at 797 °C. The displacements at point A, when the columns are heated, and at B and C, when the beams are heated, are shown in Figure 4.16.

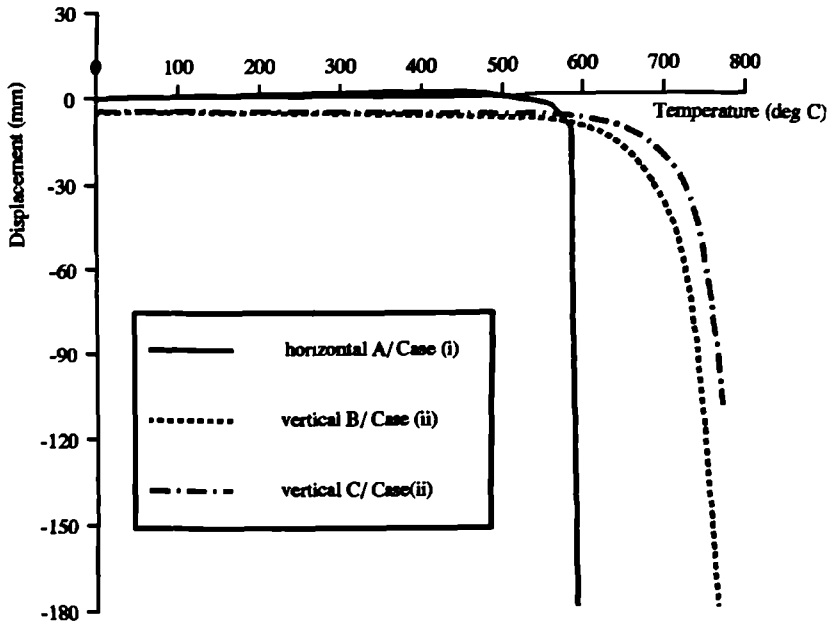


Figure 4.16 Deflections at points A, B and C

4.3 CONCLUSIONS

The main objective of this chapter is to verify the material models for steel at elevated temperatures, implemented within ADAPTIC, against available experimental results. A further objective is to illustrate the applicability of ADAPTIC to predicting the response of steel frames under fire conditions.

The comparison of the performance of the proposed material models against experimental results is satisfactory. The comparison of critical temperatures and displacement-temperature curves is made against those obtained from experiments. In all cases, the displacement-temperature curves predicted by ADAPTIC follow the test results closely, and the critical temperatures obtained from analysis compare satisfactorily with the experimental values by Rubert and Schumann (1986). Moreover, the illustrative examples on structural frames show the applicability of the proposed procedures to the analysis of realistic steel structures under fire conditions.

CHAPTER 5
INTEGRATED NONLINEAR ANALYSIS ENVIRONMENT FOR COMBINED EXPLOSION AND FIRE LOADING

In this chapter, a numerical approach is proposed, in the context of an *integrated environment*, to address the nonlinear response of steel frames subjected to explosion followed by fire. The nonlinear material response at high strain-rates in explosions and elevated temperatures in fire conditions, and geometric nonlinearity are considered.

This chapter begins by introducing the steel material response under high strain-rates and a number of rate-sensitive models. This is followed by a description of the adopted rate-sensitive model. The details of the proposed integrated analysis procedure are then provided. Results from preliminary numerical examples indicate that explosions can reduce considerably the fire resistance of steel frames, hence the importance of modelling the combined explosion-fire scenario.

This chapter also discusses the adaptive analysis procedure, which provides efficient modelling and nonlinear analysis, by maximising the use of inexpensive elastic elements in the nonlinear analysis. The three components associated with the adaptive procedure are introduced; namely, an elastic quartic, an elasto-plastic cubic formulation and a transitional procedure. The elastic quartic formulation is capable of representing imperfect beam-columns with one element per member, therefore one structural member can be modelled with only one element. This element is subsequently divided into a number of elasto-plastic cubic elements as this becomes necessary. The transitional procedure performs accuracy checking and automatically subdivides a quartic element into cubic elements, in pre-defined zones of the original quartic element, where inaccuracies are detected.

The benefits of the adaptive procedure are demonstrated through an example of a steel frame subjected to fire loading. In addition to the considerable modelling savings, it is shown that computational savings in excess of 80% can be achieved for real structures under realistic loading conditions.

5.1 MODELLING STEEL BEHAVIOUR UNDER EXPLOSION AND FIRE

It is well recognised that fire is often involved in the event of explosion. However, few

studies, both experimental and analytical, have thus far been presented on the structural response under combined explosion and fire loading scenarios.

The material properties of steel are significantly affected by high temperatures and strain-rates, both of which vary during fire and explosion scenarios, although the associated duration of the two types of loading are different by orders of magnitude. When exposed to fire, steel structures may be subject to a considerable reduction in stiffness and strength as a result of the deterioration in the material properties at elevated temperatures. On the other hand, high strain-rates associated with blast loading enhance the inelastic resistance of steel.

A summary of the properties of steel, pertinent to the development of a rate-sensitive model, is first presented, followed by a description of the adopted rate-sensitive model for this work.

5.1.1 Rate-sensitive Response of Steel

Several studies (Critescu, 1963; Symonds, 1984; Wakabayashi et al., 1980) have shown that for many types of loading, such as impact and blast loading, the effects of high strain-rates on the material behaviour can be significant. The most notable effect is the increase in yield stress with an increase in the strain-rate. It is hence important to establish what the implications of the strain-rate effect are on the structural response under explosion, so that realistic structural modelling can be achieved.

Critescu (1963) described a threshold strain-rate below which strain rate sensitivity is not observed. For steel, this threshold is of the order of 10^{-4} s^{-1}. For structures under impact and blast loading, maximum strain rates of the order of 10 s^{-1} may be expected. From the available experimental evidence, the following material response characteristics resulting from loading at significant strain-rates have been observed.

5.1.1.1 Elastic behaviour

It has been generally observed that the elastic behaviour of metals, both uniaxial and multiaxial, is unaffected by the rate of straining. Kolsky (1949) conducted tests on

copper and lead. Steel tests by several investigators, for example, Chang and Lee (1987) also confirmed this observation.

5.1.1.2 Plastic behaviour

Typical stress-strain curves from constant strain-rate tests on mild steel are shown in Figure 5.1 (Harding, 1983). It shows that both the upper and lower yield stresses increase as the strain-rate increases. The plastic plateau between the lower yield stress and the start of the work hardening region is observed to extend for higher strain rates. In the work hardening region, the steel exhibits less rate-sensitivity than in the plastic plateau region. Very often this behaviour is idealised by a family of stress-strain curves, illustrated in Figure 5.2, which imply a specific relationship between the overstress (X) and the strain-rate ($\dot{\varepsilon}$) at steady-state.

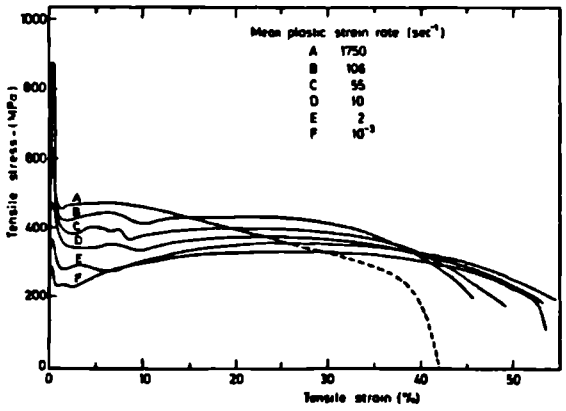


Figure 5.1 Monotonic stress strain curves at constant strain-rates (Harding, 1983)

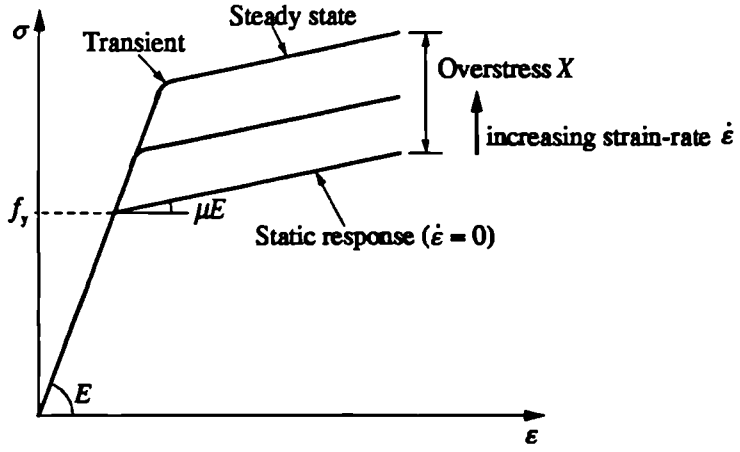


Figure 5.2 Idealised stress strain relationship at constant strain rate

5.1.1.3 Effect of temperatures

The effect of temperatures on material rate-sensitivity is considerable, and there is much evidence of an intrinsic relationship between loading at high strain-rates and the low temperature behaviour of steel. Harding (1989) describes some observations on the effects of temperatures and strain rates. At very low strain rates and very high temperatures, the plastic flow stress is independent of temperature and strain rate. This is the so called "athermal region". At higher strain rates and low temperatures, a linear relationship is generally found to apply between flow stress and the logarithm of the strain rate. The temperature effect on the rate-sensitive behaviour of steel is not considered in this work. Consideration is only given to a loading scenario in which explosion is followed by fire, which does not require the consideration of simultaneous elevated temperatures and high strain-rates.

5.1.2 Rate-sensitive Models

To quantify the strain rate effect, a number of constitutive models are formed in terms of a relationship between, either, the yield stress and the strain-rate, or between the plastic flow stress and the plastic strain-rate. Ludwick (1909) proposed a logarithmic relationship between plastic strain-rate ($\dot{\varepsilon}_p$) and the plastic flow stress for an elastic-perfectly plastic material, which has the form:

$$\sigma = \sigma_1 + \sigma_0 \ln\left[\frac{\dot{\varepsilon}_p}{\dot{\varepsilon}_{p0}}\right] \tag{5.1}$$

where

σ = the rate-sensitive plastic flow stress,

σ_1 = the static yield stress,

$\dot{\varepsilon}_p$ = the plastic strain rate,

σ_0 = material constants, and

$\dot{\varepsilon}_{p0}$ = the threshold strain rate, below which strain rate sensitivity does not occur.

The extension of Equation (5.1) to a monotonic static stress-strain relationship, with strain hardening, leads to the following expression:

$$\sigma = \sigma_1[\varepsilon] + A[\varepsilon]\ln(\frac{\dot{\varepsilon}_p}{\dot{\varepsilon}_{p0}}) \tag{5.2}$$

in which $\sigma_1[\varepsilon]$ is the static stress-strain relationship, and $A[\varepsilon]$ is a material function that models the variation of rate-sensitivity with strain, which is very often taken as a constant.

Malvern (1951) proposed a related expression for rate sensitivity represented by:

$$\sigma = g[\varepsilon] + S\ln(1 + b\dot{\varepsilon}_p) \tag{5.3}$$

which approaches equation (5.1) for high strain-rates and has the advantage of not requiring a threshold strain-rate.

The rate sensitivity relationships represented by Equations (5.1)-(5.3) describe a log-linear relationship between the plastic strain-rate ($\dot{\varepsilon}_p$) and the overstress ($\sigma - \sigma_1$) or ($\sigma - g[\varepsilon]$).

Another widely used rate-sensitive model is that of Symonds (Bodner & Symonds, 1960), who proposed the expression:

$$\frac{\sigma}{\sigma_y} = 1 + \left(\frac{\dot{\varepsilon}}{\dot{\varepsilon}_0}\right)^{\alpha} \tag{5.4}$$

where, for mild steel, the values $\dot{\varepsilon}_0 = 40\ s^{-1}$ and $\alpha = 0.2$ are commonly used.

5.1.2 Adopted Rate-sensitive Model

A rate-sensitive model for steel was developed and implemented in ADAPTIC by Manzocchi (1990), which allows for the strain rate effect. The adopted model is based on Malvern's visco-plastic equation (1951):

$$\left.\begin{aligned} E\dot{\varepsilon}_p &= f[X] \\ X &= \sigma - g[\varepsilon] \end{aligned}\right\} \tag{5.5}$$

where

E = Young's modulus,

$\dot{\varepsilon}_p$ = plastic strain-rate,

$f[X]$ = function of the overstress X,

$g[\varepsilon]$ = static stress-strain law, and

σ, ε = material stress and strain.

Under the steady-state conditions, the overstress (X) is related to the strain-rate by:

$$X = S \ln\left(\frac{\dot{\varepsilon}}{\dot{\varepsilon}_*} + 1\right) \tag{5.6}$$

Accordingly, the following function for $f[X]$ is employed:

$$f[X] = E\,\dot{\varepsilon}_*(1-\mu)\left(e^{X/S} - 1\right) \tag{5.7}$$

in which,

μ = strain-hardening parameter

$\dot{\varepsilon}$ = strain-rate

S, $\dot{\varepsilon}_*$ = model parameters, as illustrated in Figure 5.3.

The advantage of this model is that the integration of Equation (5.5), to evaluate the overstress due to an increment of material strain, can be obtained from a closed-form solution assuming constant strain-rate within each time-step. This leads to considerable computational savings in comparison with models based on numerical integration.

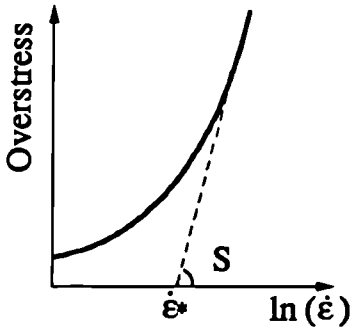


Figure 5.3 Strain rate sensitivity relationship

5.1.3 Thermal Model

The bilinear material model discussed in Chapter 2, representing the effect of elevated temperatures on steel in fire conditions, is used in conjunction with the rate-sensitive model discussed above to provide a material model for structural analysis when explosion and fire actions coexist. The thermal model has been described in detail in Chapter 2, but is as follows.

The bilinear model allows for the deterioration of the material properties of steel at elevated temperatures, with a kinematic bilinear model employed for the steady-state stress-strain relationship. The variation of the elastic modulus, yield stress and strain-hardening parameter with temperature assumed to follow a trilinear relationship. For each property, reduction factors are given to establish the corresponding trilinear curve over the temperature domain. The reduction factors can be chosen based on the relevant parameters recommended in Eurocode 3 (1990).

5.2 INTEGRATED ANALYSIS ENVIRONMENT

The previously discussed models have been incorporated within the nonlinear analysis program ADAPTIC. To address the combined scenario of explosion and fire loading on structures, an integrated analysis capability is provided by considering the modelling of material properties and the analysis procedure in two stages. The first stage is for structural analysis under explosion loading where the rate-sensitive model is employed, whereas the second stage is for analysis under fire loading in which the thermal model is utilised. Due to the different nature of explosion and fire loading, different time-integration steps are utilised in the two stages of analysis. The strategy, of employing two distinct but consecutive stages for explosion and fire analysis, is in view of the fact that the duration of explosion is so short that temperature variation during explosion, and strain-rate variation during fire, can be ignored.

5.3 ADAPTIVE EXPLOSION AND FIRE ANALYSIS

Generally, considerable effort is required for analysing a realistic building structure, especially when nonlinear behaviour is involved. This includes not only excessive computer resources, but also a great deal of data preparation.

This section describes the adaptive procedure provided by ADAPTIC for the nonlinear analysis of steel frames subject to fire and explosion. The adaptive approach,

originally proposed by Izzuddin and Elnashai (1993) for steel frames subject to static and dynamic loading, addresses the computational and modelling disadvantages of conventional nonlinear analysis through an adaptive process which maximises the use of inexpensive elastic elements within the structure, and employs more computationally demanding elasto-plastic elements only *when* and *where* necessary. The modelling advantages of the adaptive approach are significant, since a simple model of elements, often equivalent to that used in linear analysis, can be employed. More significantly, the computational saving of the approach has been shown to be considerable, often exceeding 80% with no loss in accuracy (Izzuddin, et al, 1995).

A considerable part of steel framed structures subject to explosion and fire loading conditions may remain elastic over the duration of loading, and hence it would be advantageous, when analysing such structures, to use inexpensive elastic elements for these parts. And the expensive elasto-plastic elements are applied only in regions which develop material plasticity as it occurs. Although explosion and fire are often localised spatially, plasticity could easily spread to other parts of the structure. Hence there is considerable benefit to be gained from an adaptive procedure which automatically modifies the model of elements to reflect the spread of plasticity. More precisely, such a procedure would utilise expensive elements only for those regions in the structure where the use of elastic elements would be inaccurate, and only when such inaccuracies are detected during analysis.

The three main components of the adaptive analysis procedure are described, with particular emphasis placed on the modelling of the effects of elevated temperatures associated with fire loading. The first component is an elastic formulation which is capable of modelling imperfect beam-columns in the geometrically nonlinear range using only one element per member. The second component is an elasto-plastic formulation based on the fibre approach, which includes the elasto-plastic rate-sensitive and thermal material models. The last component is the adaptive transitional procedure which modifies the current mesh by introducing a finer mesh of elasto-plastic elements instead of those elastic elements which become inaccurate during analysis.

5.3.1 Elastic Formulation

The elastic formulation is developed in a local Eulerian system (Izzuddin, 1991), where 8 local degrees of freedom are utilised, as shown in Figure 5.4. This allows quartic shape functions to be used for the transverse displacements $v(x)$ and $w(x)$, and linear

shape functions for the twist rotation $\alpha(x)$, with the constant axial force criterion employed instead of a shape function for the axial displacement $u(x)$ (Izzuddin, 1997). The quartic formulation models the geometrically nonlinear response of imperfect beam-columns accurately with only one element per member, where quartic functions are used to represent the initial transverse imperfections.

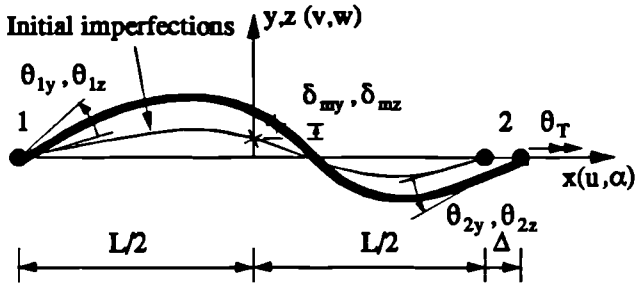


Figure 5.4 Local freedoms of quartic formulation (Izzuddin, 1997)

Variables associated with the centroidal temperature and temperature gradients are employed at the two ends of the quartic element and at its mid-length, thus allowing parabolic interpolation for these entities. The effect of temperature variation over the cross-section on thermal strains is accounted for using a constant coefficient of thermal expansion (γ), and therefore the change in (γ) at very high temperatures is not accounted for. Moreover, the quartic formulation is based on a constant elastic modulus (E) over the cross-section, and hence the effect of cross-sectional temperature gradients on (E) is not represented, although the variation of (E) with the centroidal temperature along the element length is modelled using a parabolic function (Izzuddin, 1997). Since the elastic modulus (E) of steel reduces at high temperatures (Cooke 1988, EC3 1993) which can be approximated by a decreasing curve above a threshold temperature (t_s), the assumption of a constant (E) over the cross-section would remain valid only if the temperature gradients are zero or if all the temperatures within the cross-section are below (t_s).

5.3.2 Elasto-plastic Formulation

The elasto-plastic formulation is also derived in a local Eulerian system (Izzuddin, 1991), where six degrees of freedom are employed. These are the same as those of the elastic quartic formulation without the two midside transverse freedoms. Therefore, cubic shape functions can be used for the transverse displacements $v(x)$ and $w(x)$, hence the name cubic formulation (Izzuddin & Elnashai, 1993). The element response

is assembled from contributions at two Gauss points where the cross-section is discretised into a number of monitoring areas, as illustrated in Figure 5.5 for an I-section. This formulation utilises a relationship between the direct material stresses and strains; therefore it allows various material models, for example the rate-sensitive and the thermal models described previously, to be utilised.

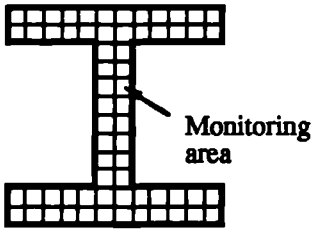


Figure 5.5 Monitoring areas for an I-section

The cubic formulation can model the spread of plasticity within the cross-section and along the length, although at least six elements per member would be required to achieve accurate representation. In addition, this formulation is capable of modelling the variation of the elastic modulus over the cross-section, since each monitoring area can employ a different elastic modulus.

5.3.3 Adaptive Procedure

The adaptive procedure is based on maximising the use of the computationally efficient elastic quartic elements, and replacing them by the more expensive elasto-plastic elements only as the quartic elements become inaccurate. In the context of an incremental iterative solution strategy, which is often adopted in nonlinear analysis, the adaptive procedure can be described by the following steps:

1. Start analysis with one quartic element per member.

2. Establish the loads, including temperatures, for the next increment.

   2.a. Perform iterations until convergence to equilibrium is achieved.

   2.b. Consider the quartic elements in turn:

   - Check accuracy of the current quartic element in pre-defined zones.

- If the quartic element is inaccurate in some of the pre-defined zones, introduce elasto-plastic cubic elements into these zones, keeping elastic quartic elements in the remaining zones of the original element.

2.c. If at least one quartic element has been modified, repeat from sub-step (2.a) with the new mesh.

3. Update the nodal and element variables, and repeat from step (2) until all increments have been applied.

The main difference between the adaptive procedure and standard nonlinear analysis procedures is in step (2.b), which includes accuracy checking and automatic subdivision of quartic elements, as discussed hereafter.

5.3.3.1 Accuracy checking

The accuracy of the quartic element is established at the Gauss points of potential elasto-plastic elements, by determining the axial force and bending moments at these points.

Considering that finite elements predict displacements better than displacement derivatives, or strains and stresses, the axial force and bending moments within the element are obtained from equilibrium considerations rather than through differentiation of displacement functions.

For thermal analysis, the quartic element is considered inaccurate at the current Gauss point of a potential elasto-plastic element if any of these conditions is detected at selected points within the cross-section:

1. The direct strain (ε) exceeds the yield strain, which depends on the temperature at the cross-sectional point under consideration.

2. The temperature exceeds the proportional limit of thermal strains, above which the coefficient of thermal expansion (γ) can no longer be considered constant.

3. The elastic modulus varies significantly between the various cross-sectional points due to temperature variation. A 10% variation is used as the maximum allowable variation.

The above conditions are checked at the two extreme fibres in plane frame analysis, whereas for space frame analysis the checks are made at selected points on the cross-section boundaries depending on the cross-section shape.

5.3.3.2 Automatic subdivision

The automatic subdivision process involves the removal of an original quartic element and the introduction of new cubic and quartic elements in the appropriate zones. New nodes are created at appropriate locations over the original element, which serve to specify the connectivity of the new elements. The displacements of the new nodes are obtained from the deflected shape of the original element at the end of the previous incremental step. It is important, however, in the calculation of nodal displacements that the nonlinear variation of the axial displacement is accounted for, which may be due to the variation of the elastic modulus along the original element length or due to the second order effect of transverse displacements.

The introduction of new quartic elements requires their connectivity, cross-sectional and material properties, applied distributed loads and subdivision zones to be defined. Similarly, new cubic elements require the definition of connectivity, cross-sectional monitoring areas, material properties and applied distributed loads. For both types of element, the characteristics of new elements can be readily determined from those of the original element.

5.4 ILLUSTRATIVE EXAMPLES

The proposed integrated analysis procedure implemented within ADAPTIC is used to study the response of a three-storey frame subjected to loading scenarios of explosion followed by fire. With this example and another example of a steel frame under fire conditions, the benefits of adaptive nonlinear analysis procedure are demonstrated.

5.4.1 Three-storey Frame under Explosion and Fire

The three-storey frame, shown in Figure 5.6, is considered under explosion and fire loading. The second level leftmost compartment is subjected to explosion, while the two columns in this compartment are also under fire loading applied as a uniform temperature which is increased at a rate of 22 °C/min. The explosion load is simulated by a triangular pressure pulse uniformly distributed on the beams and columns, where

the intensity is twice the static capacity of the left column with a rise-time of 0.001 sec and a duration of 0.05 sec.

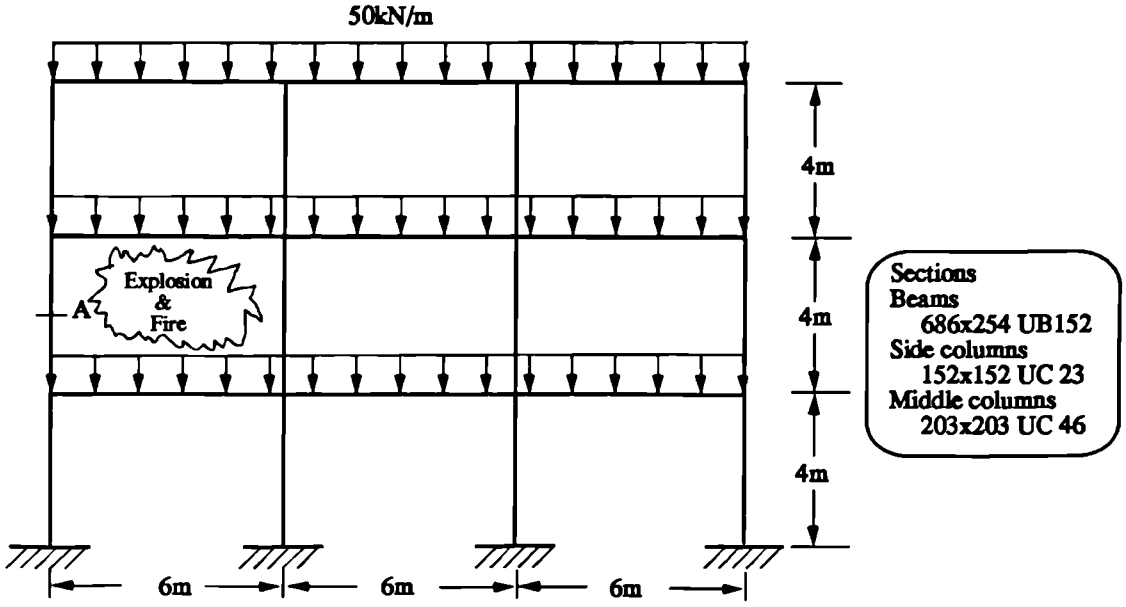


Figure 5.6 Three-storey frame subjected to explosion and fire loading

The parameters of the reduction factors for the trilinear curves are given in Table 5.1, for the elastic modulus, yield stress and strain hardening factor, whereas the parameters of the thermal strain curve are given in Table 5.2. As for the rate-sensitive model, S and $\dot{\varepsilon}_s$ assume a value of31.19 and 4.65×10^{-3}.

Table 5.1 Parameters of material trilinear curves

Property	t_1 (°C)	r_2	t_2 (°C)	t_3 (°C)
E (210 GPa)	100	0.13	700	1200
σ_y (275 MPa)	400	0.11	800	1200
μ (0.02)	400	0.50	600	1200

Table 5.2. Parameters of thermal strain trilinear curve

ε_{t1}	t_1 (°C)	t_2 (°C)	ε_{t3}	t_3 (°C)
0.011	750	860	0.0178	1200

The analysis is firstly run with an initially refined mesh using 10 cubic elements for each member. The horizontal displacements at mid height of the left column in the

compartment subjected to explosion and fire (node A) are shown in Figure 5.7. It is observed that at certain temperature, the deformation of the column becomes excessive, leading to instability. If the frame is subjected to fire conditions without being affected by explosion, the temperature at which the column fails is 656° C. However, for the same frame subjected to explosion and fire, this temperature is reduced to 581° C. This represents 11% reduction in the fire resistance of the frame in terms of the survival temperature.

To demonstrate its accuracy and efficiency, the adaptive procedure is then used by modelling the frame with one quartic element per member, and the results are compared to those of the initially refined mesh, as shown in Figure 5.7. These comparisons illustrate the accuracy of the nonlinear adaptive analysis, which is identical to that of the initially refined mesh. The deflected shape of the frame, at 581° C under explosion and fire, is given in Figure 5.8, where the mesh-refined zone is highlighted. In terms of computational requirements, the CPU time required for the adaptive analysis procedure in comparison with that for the initially refined mesh, is shown in Figure 5.9, where a saving of over 80% is observed.

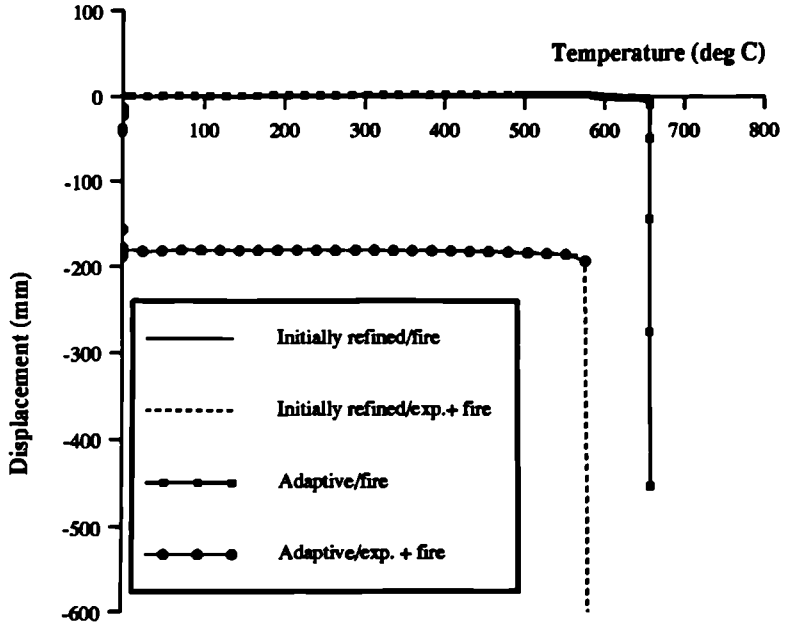


Figure 5.7 Horizontal displacement at nodes A.

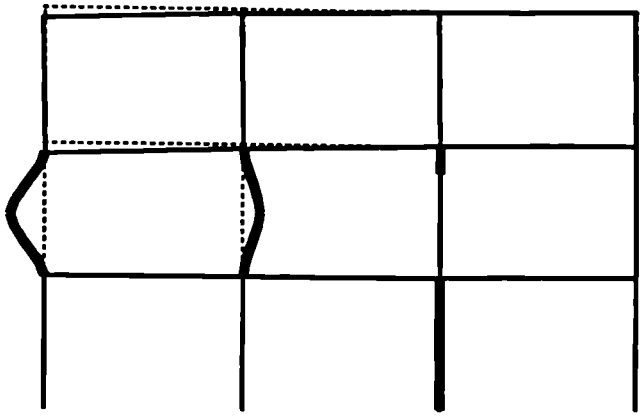


Figure 5.8 Deflected shape of the frame at 581°C under explosion and fire

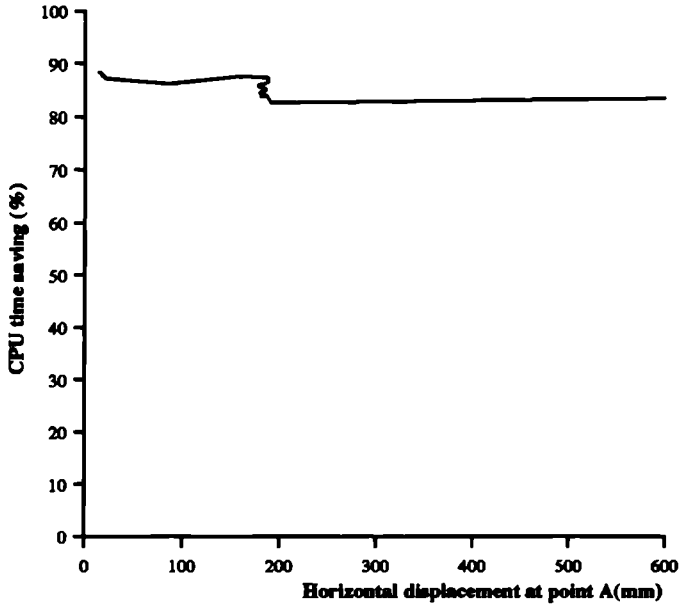


Figure 5.9 Comparison of the CPU time required in the analysis

5.4.2 Four Storey Frame under Fire Condition

A four-storey steel frame, shown in Figure 5.10, is used to illustrate the advantages of adaptive nonlinear analysis, where the frame is analysed under fire loading using

ADAPTIC. Transverse imperfections are introduced, which vary linearly over the height of the frame, reaching a maximum value of 1 cm at the fourth floor level. In addition, local imperfections of (L/1000) are assumed in the two internal ground floor columns.

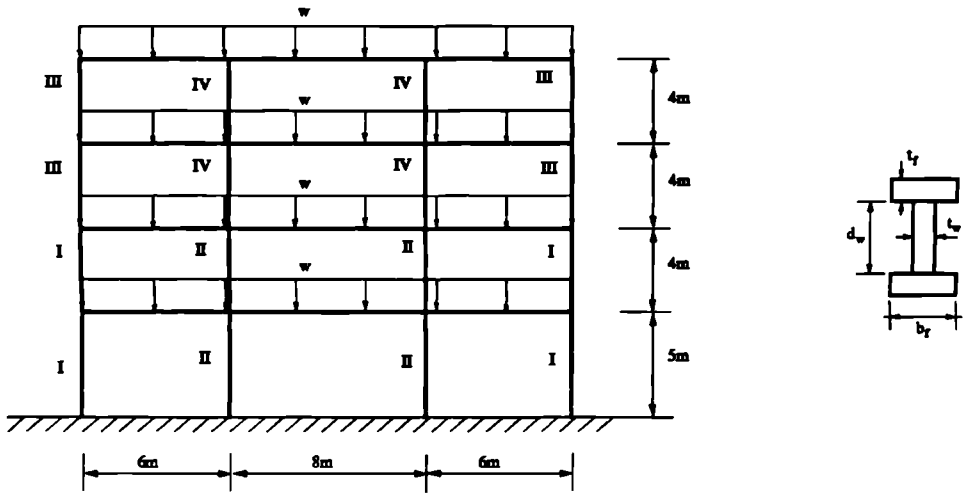


Figure 5.10 Geometric configuration of frame

Table 5.3. Cross-sectional dimensions of members

Section	b_f (mm)	t_f (mm)	d_w (mm)	t_w (mm)
Beam	311.5	31.4	570.2	18.6
I	254.0	14.2	225.6	19.2
II	264.5	31.7	225.6	19.2
III	154.4	11.5	138.8	8.1
IV	255.9	17.3	225.8	10.5

The cross-sectional dimensions of the frame members are given in Table 5.3. Two cases of uniformly distributed loading on the beams are considered; case (A) corresponds to w = 60 kN/m, whereas case (B) corresponds to w = 90 kN/m. The internal ground floor columns are subjected to fire loading simulated by uniform temperature along the length and over the cross-section of the columns, which is increased gradually at the rate of 60 °C/min. The parameters of the reduction factors

for the elastic modulus, yield stress and strain hardening factor, as well as the parameters of the thermal strain are the same to those assumed in the last example.

These two cases of vertical loading are considered with an initially-refined mesh and with the adaptive procedure. For loading case (A), the accuracy of the adaptive procedure is demonstrated in Figure 5.11, where identical results for the vertical displacement at the top of the left internal column are obtained using an initially-refined mesh of 10 elasto-plastic cubic elements per member. The modelling advantages of the adaptive procedure are evident in Figures 5.12(a) and (b), where cubic elements are required only in the affected columns up to 700 °C, with more cubic elements needed when 900 °C is reached.

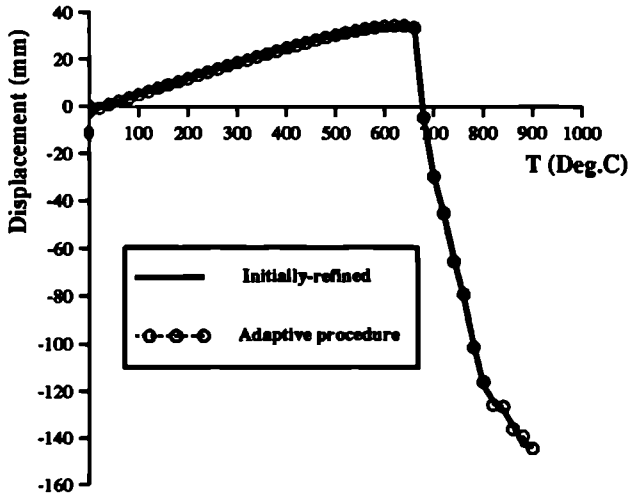


Figure 5.11 Vertical column displacement (Case A)

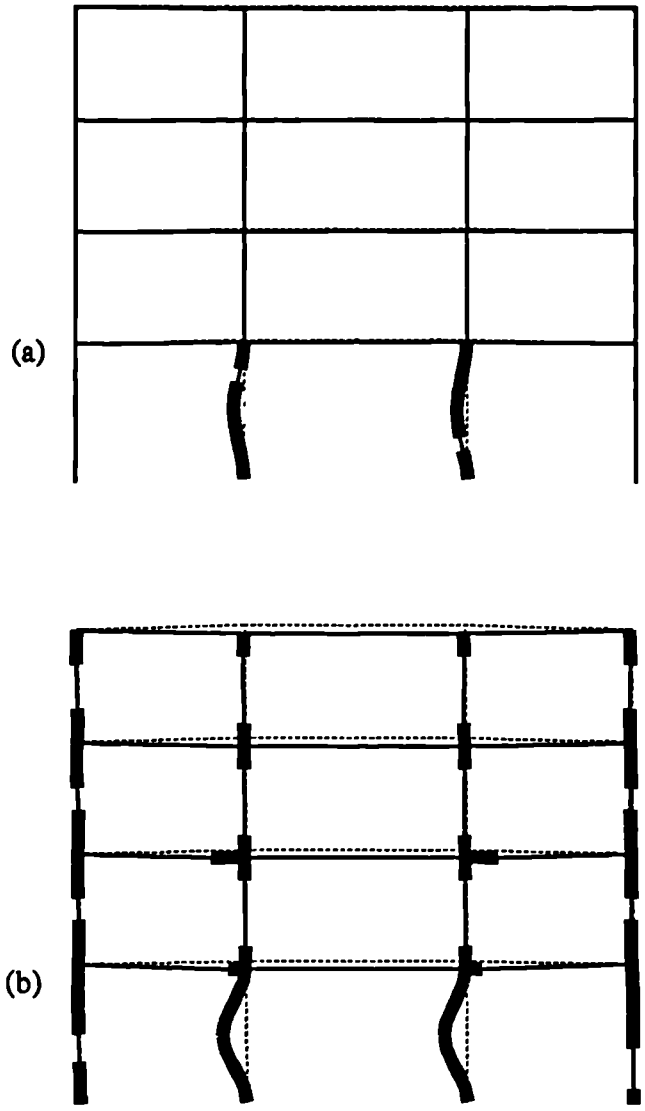


Figure 5.12 Cubic elements (Case A) (a) at 700 °C; (b) at 900 °C

For loading case (B), the accuracy of the adaptive procedure is again demonstrated in Figures. 5.13(a) and (b), where excellent comparison with an initially refined mesh is obtained for the vertical displacement at the top of the left internal column as well as for the horizontal sway displacement at the fourth floor level. The distribution of cubic elements with the adaptive procedure is shown in Figure 5.14 at 674 °C, which is the temperature at which overall lateral instability of the frame is initiated. This mode of frame collapse is due to the higher vertical loading which causes buckling in the ground floor columns as the stiffness of the internal columns deteriorates at high temperatures.

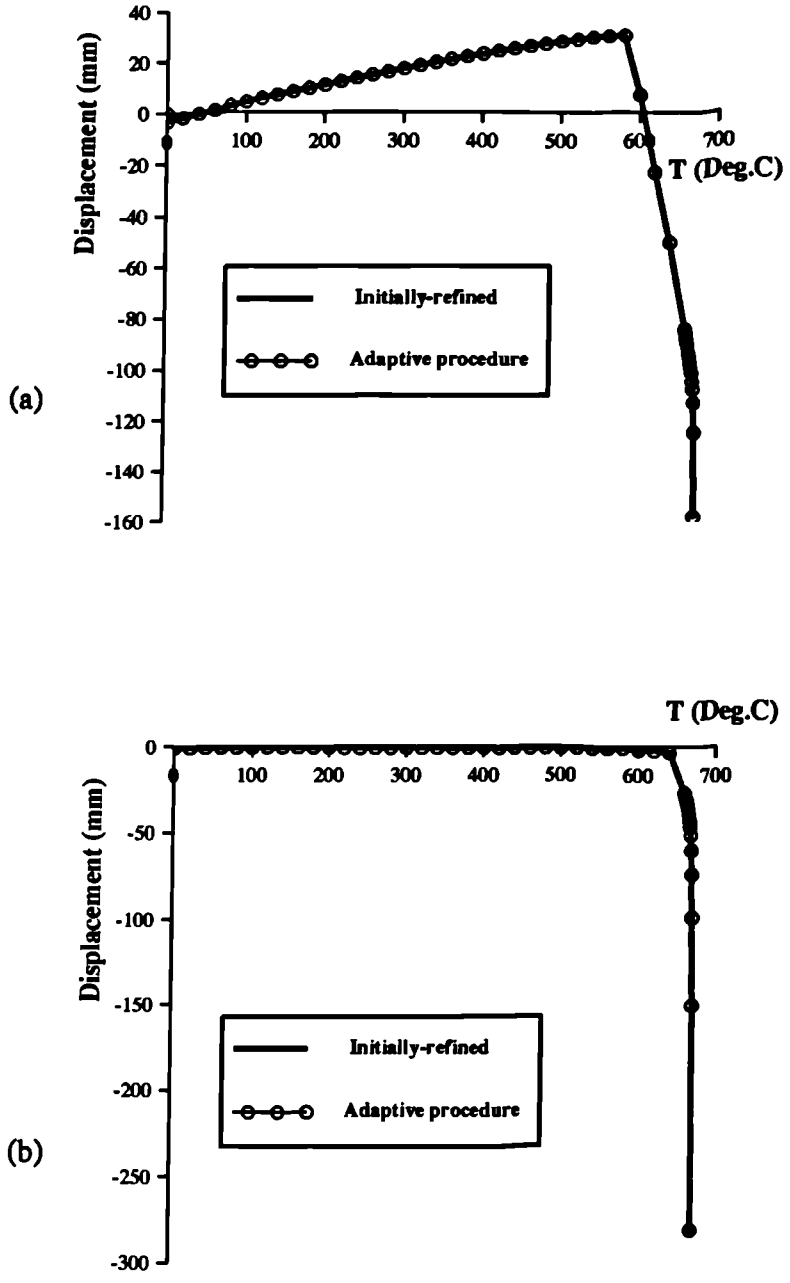


Figure 5.13 (Case B) (a) Vertical column displacement; (b) Sway displacement of frame

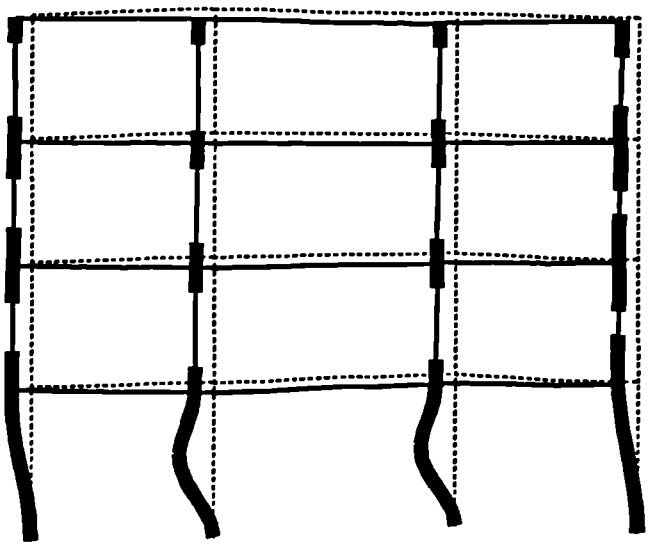


Figure 5.14 Cubic elements at 674 °C (Case B)

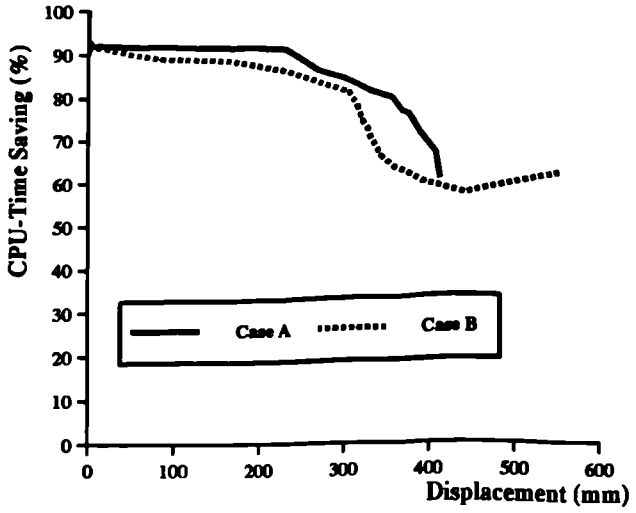


Figure 5.15. CPU savings of adaptive procedure

The efficiency of the adaptive procedure is illustrated in Figure 5.15, where CPU time savings are plotted against the mid-height horizontal displacement of the left internal column. Considerable reduction in the CPU consumption is achieved with the adaptive procedure in the early parts of analysis prior to the buckling of the left internal column, when only elastic quartic elements are necessary. For both loading cases, the CPU consumption rate increases with the adaptive procedure at temperatures when

elasto-plastic elements are introduced, although the rate is still less than that of the initially-refined mesh. It is shown that savings exceeding 80% are achieved with the adaptive procedure up to considerable column displacements (300 mm). At very large displacements, more elasto-plastic cubic elements are introduced, which increases the CPU consumption rate of the adaptive procedure, although savings exceeding 60% are still achieved for this example.

5.6 DISCUSSION

An analysis method is presented in this chapter for steel frames subjected to explosion followed by fire loading. To model the response of steel under explosion and fire conditions, a material model combining the thermal and rate-sensitive response is adopted. In the context of an *integrated environment*, the analysis procedure is considered in two stages for explosion and fire loading, where different time-integration steps are utilised. The nonlinear analysis program ADAPTIC, in which this procedure is implemented, was used to investigate the effect of explosion on the fire resistance of steel frames. The results show that explosion can significantly reduce the resistance of steel frames to fire. The reduction is affected by several factors, among which are the structural configuration and the nature of the explosion loading. The importance of considering the effects of explosion and fire within an integrated analysis environment is thus ascertained.

The adaptive analysis procedure and associated components provided by the nonlinear analysis program ADAPTIC are described. The adaptive process makes maximum use of the inexpensive elastic elements within the structure, and employs the more computationally demanding elasto-plastic elements only when and where necessary, hence achieving significant savings in both modelling and computing. A four-storey steel frame subject to fire is analysed using an adaptive procedure and the computational saving is shown to exceed 80% with no loss in accuracy.

CHAPTER 6
ANALYSIS OF COMPOSITE STEEL-DECKED SLAB

In the previous chapters, consideration has been given to the material modelling and the structural behaviour of skeletal steel frames under fire and explosion. This chapter will consider another major component of steel building structures; namely the steel-decked slab. Consideration is given in this chapter to concrete slabs with trapezoidal shaped steel decking and with mesh reinforcement.

Firstly, the historical back ground behind the development of the composite steel-decked slab is introduced, where attention is given to its structural advantages. Previous research work carried out on the slab is then reviewed and summarised.

Secondly, a linear formulation is proposed to model the behaviour of composite steel-deck concrete slabs, enabling the effect of the slab on the overall response of steel buildings to be taken into consideration. The formulation for steel-decked slabs with rectangular ribs is first discussed, based on which, a more general formulation for trapezoidal ribs is derived. A novel concept of two-level displacement interpolation is then introduced, so that the effect of the ribs on the slab response can be represented accurately without using very high order interpolation. Thermal effects are taken into consideration by including the equivalent thermal loading in the analysis.

6.1 INTRODUCTION

Composite floor systems have been under constant development over the last few decades. There is a growing opinion that the structural contribution of steel-decked floor systems is under-utilised in current design procedures, particularly for the fire limit state (Martin, 1995).

In this section, a historic background is given on the development of composite steel-decked slab systems. Research work carried out in this area is reviewed and the developments reached as part of this research are summarised.

6.1.1 Background

Nearly 60 years ago, engineers and designers realised that several advantages could be

gained by integrating the structural properties of concrete and cold-formed steel decking in the marriage of a new lightweight floor system for building structures (Schuster, 1976). This discernment was promoted by man's constant instinctive search for technological advancement, but also by several economic forces such as possible savings in foundation and steel frame costs. What seemed most attractive was the fact that the formed steel deck was capable of serving as both a form for the wet concrete fill and a working platform during the construction stage, thus replacing the forming operation of reinforced concrete. Interestingly, it soon became apparent that steel-deck floor systems possessed additional attributes in that electrical and communications wiring could be channelled through the ducting of the formed floor cells.

It was not until 1950 that the first composite steel-deck reinforced-concrete floor system appeared on the market. It soon became widely accepted in the USA and Canada. However, its adoption by the British construction industry was much later (Evans & Wright, 1988). Indeed, it is only in the last decade that its use has become widespread in UK. The development of an effective composite flooring deck system has greatly enhanced the competitiveness and effectiveness of steel-framed construction for high-rise buildings. At the present time, used in conjunction with steel frames, the composite steel-deck floor system is winning an increasing share of the high-rise construction market; its potential for refurbishment projects is also now being realised.

The rapid expansion in the use of this type of floor system may be attributed to its significant advantages. The most apparent and important advantages are (Schuster, 1976; Harding, 1986):

- The steel deck acts as permanent shuttering for the in-situ cast concrete slab, thus there is no need to erect and remove forms and falsework, with a consequent saving in time and labour. The decks, manufactured of light gauge sheet steel, are light in weight, hence resulting in easy handling and placing, as well as reducing installation time and on-site labour.

- The steel deck, once in position, immediately provides a platform to support construction loads and a safe, sturdy working surface. Since supporting false work is not required, finishing trades can operate on the flooring immediately below the one being constructed; this obviously facilitates the construction programme.

- The steel decking acts as the tensile reinforcement for concrete, thus eliminating the

time-consuming tasks of placing and fixing reinforcing bars for the slab.

- The steel deck geometry can result in a reduction of 30% in the amount of concrete fill required for the floor. The consequent reduction in dead weight leads to lighter superstructures and reduced foundation loads.

- The cellular geometry of the deck permits the formation of ducting cells within the floor so that services can be incorporated and distributed within the floor depth. This gives the possibility of increased headroom or a reduction in building height.

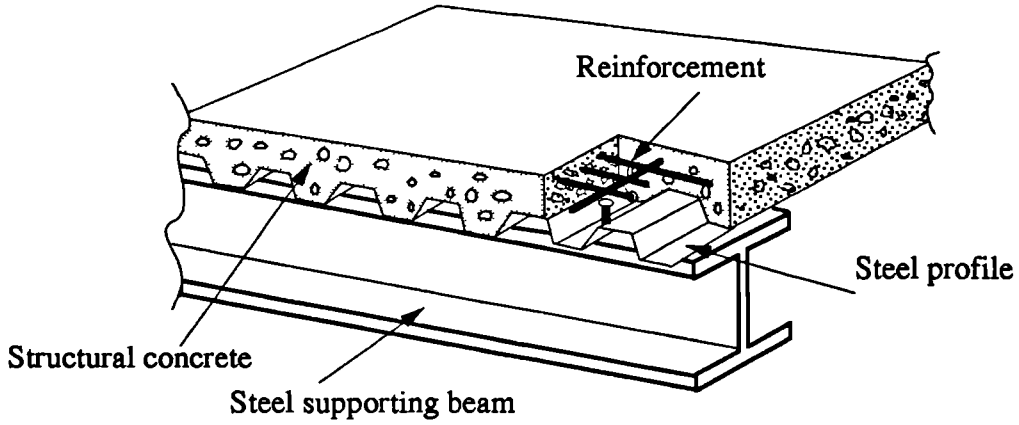


Figure 6.1 General view of the composite steel-decked slab system

Figure 6.1 gives a general view of a composite steel-decked slab system. Profile heights are usually in the range 38 to 75 mm, with sheet thickness between 0.8 to 1.5 mm. Spans of the order of 3.0-3.3 m between beams are common. Slab thickness is controlled by insulation requirements in fire: those above the profile of between 65 and 120 mm are sufficient to give a fire rating of 1-2 h, depending on the profile shape and concrete type (Lawson, 1983). The essential composite action between the steel deck and the concrete slab is provided by some form of interlocking device, capable of resisting horizontal shear and preventing vertical separation between the concrete and the deck. Some profiled sheets rely mainly on their geometry to ensure composite action; others, although less common, may make use of transverse wires welded to the upper flanges of the profile. However, the most common and satisfactory method is utilising a fixed pattern of indentations and/or embossments, rolled into the surface of the steel sheeting, which provide mechanical interlocking between the concrete and the deck against slip, as adhesive bonds deteriorate. The shape and the size of the steel

deck can vary considerably, with the trapezoidal shaped decks being the most popular.

6.1.2 Review of Previous Research Work

It appears that the first significant publication on the subject of the composite steel-decked reinforced concrete floor system was by Friberg in 1954. His work not only provided an understanding of the design of the particular steel deck tested, but also presented an excellent comparison of cost between the conventional concrete slab and the steel-deck slab. By 1967, extensive independent research had been carried out by each steel deck manufacturer, mainly due to the independent nature of product development (Schuster, 1976). Recognising the requirement for a standard design specification, the American Iron and Steel Institution (AISI) initiated a research project in 1967 at Iowa State University. An overview of experiments and analytical results of the research at Iowa State university is outlined by Porter and Ekberg (1971). From the review of published literature, it can be concluded that early research was undertaken mainly by means of full-scale testing. The emphasis was placed on:

- how composite action between the profiled steel sheeting and concrete, as well as between the slab and supporting members, can be achieved (Bryl, 1967; Robinson, 1967, 1969; Fisher, 1970; Winter, 1971);

- investigation of the ultimate load-carrying capacity (Ekberg & Schuster, 1968; Porter & Ekberg, 1971, 1972, 1976; Schuster, 1970, 1972; Porter, 1968, 1974); and

- the primary mode of failure, mechanisms and the pertinent factors (Bryl, 1967; Schuster, 1970).

The numerous test results led to a better understanding of the design characteristics of the composite steel-deck concrete slab system, giving rise to valuable guidance in the design and construction of composite steel-deck concrete slabs (Schuster, 1970; Luttrell & Davison, 1973; Porter & Ekberg, 1976; Luttrell, 1987). Later, full-scale experiments were performed to a wider coverage, such as multispan slabs (Roeder, 1981; Daniels & Crisinel, 1993-a, 1993-b) and different load conditions (Klaiber & Porter, 1981; Roeder, 1981). These experiments are much closer to actual conditions. However, most of these tests were limited to evaluating the performances of individual slabs.

The ultimate behaviour of composite slabs is controlled by a combination of friction,

bond and mechanical interlocking after initial slippage. Hence, the performance of a particular steel-decked slab system can only be assessed by testing (Dowling et al., 1988). However, tests can only be conducted once the slab has been constructed. A method of estimating composite slab capacity, without resorting to performance testing, would therefore be invaluable (Evans & Wright, 1988). Several researchers have attempted to provide such a method. In 1984, Presannan and Luttrell proposed an empirical formula to predict the capacity of any composite slab incorporating a trapezoidal sheet profile. The formula was based on the results of 79 full-scale tests, and was suggested to be applicable to any new composite steel-deck concrete slab. However, it was found that this empirical formula provided misleading results in some instances (Evans & Wright, 1988). As an alternative to full scale tests, Daniels and Crisinel (1993-a,1993-b) presented a procedure which combines shear-bond testing with numerical analysis to predict the behaviour and strength of composite slabs. However, this work essentially involved testing.

It has been widely recognised that the influence of in-plane effects on the steel-decked slab is significant (Long, 1994). However, in design, the steel-decked slab is generally treated as a simply supported one way slab. The cross-sectional area of the sheeting acts as conventional reinforcement at a lever arm determined by the centroid of the steel profile. On the other hand, the steel-decked slab together with the simple beam, over which the decking is placed, is considered to be a composite beam. The compressive force is developed in the slab, within the effective width, by use of shear-connector devices. In the European Recommendations (ECCS, 1981), the effective width of the slab is defined as being lesser of the 1/3 of the beam span or the distance between the beams. AISC Code (AISC, 1978) defines the effective width as the lesser of 1/4 of the span, or 16 times the slab thickness; and in CP117 (BS, 1965) as 1/3 of the span or 12 times the slab thickness. It is believed that giving appropriate consideration to the in-plane effect in a composite steel-decked slab could result in more economic design of a steel-decked slab system (Long, 1994).

Nevertheless, publications on modelling the two-way response of composite floor slabs can hardly be traced. The author is therefore strongly motivated to develop a numerical model to represent the two-way response of steel-decked composite slabs. To develop such a numerical model, the finite element method is chosen as it is one of the most powerful and versatile methods for structural analysis. Inherently possessing greater versatility than other procedures, in dealing with various structural configurations, loading and boundary conditions, the finite element method is especially suitable for performing parametric studies, which would be useful in the

formulation of empirical rules and provisions for design.

6.1.3 Overview of the Proposed Work

A linear formulation is proposed for modelling the composite steel-decked concrete slab with mesh reinforcement, which is based on the finite element method. The proposed element adopts cubic shape functions on the overall element level, but employs another level of displacement interpolation over the level of a repetitive block of ribs. The second level displacement interpolation is defined in a piece-wise manner over a typical rib block, where firstly rectangular ribs are considered, which is then extended to trapezoidal ribs. To address the shear locking effect, the transverse rotation is chosen to be of one order lower than the interpolation of lateral deflections.

Thermal effects present in a fire condition are taken into consideration by including the equivalent nodal forces in the analysis. The numerical integral for generating the equivalent nodal forces of the thermal effects, as well as the distributed load, is presented.

With this new element, the effect of the slab elastic stiffness on the overall response of a steel building structure can be taken into consideration, so that its implications on the fire and explosion resistance of the overall structure can be studied. It is worth noting that the proposed formulation is linear, and cannot be used to model slabs which undergo large displacements and considerable material nonlinearities. Therefore, its utility in the context of the present work is with regard to the effect of the slab stiffness, outside the fire or explosion compartment, on the overall response.

6.2 ELEMENT FORMULATION

6.2.1 Basic Assumptions

As mentioned previously, the steel-decked composite flooring system consists of a profiled steel sheeting, a concrete cover slab and normally mesh reinforcement. It is assumed initially that the bending deformation follows the Mindlin hypothesis; therefore, a straight line normal to the plane of the slab before deformation remains straight, but not necessarily normal to the deflected slab surface. As a result, the stresses and strains over the element may be related to displacements at the mid-surface of the slab. Since the ribs are disposed asymmetrically with respect to the middle plane of the slab, this plane is no longer a neutral surface under bending, and

hence coupling exists between the membrane and bending actions. The Mindlin hypothesis is later modified by the introduction of rib freedoms, which imply different orientations of the normals in the rib and the slab cover.

For convenience, one repetitive portion of the slab is termed a *block* and each of the three parts within a block is termed a *unit*, as shown in Figure 6.2. The definitions of *block* and *unit* are important for the discussion of displacement interpolation and the derivation of the element stiffness matrix, presented in later sections.

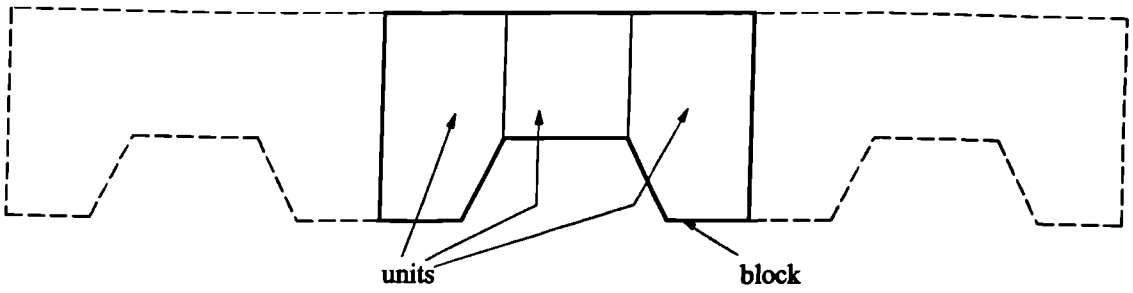


Figure 6.2 block and units

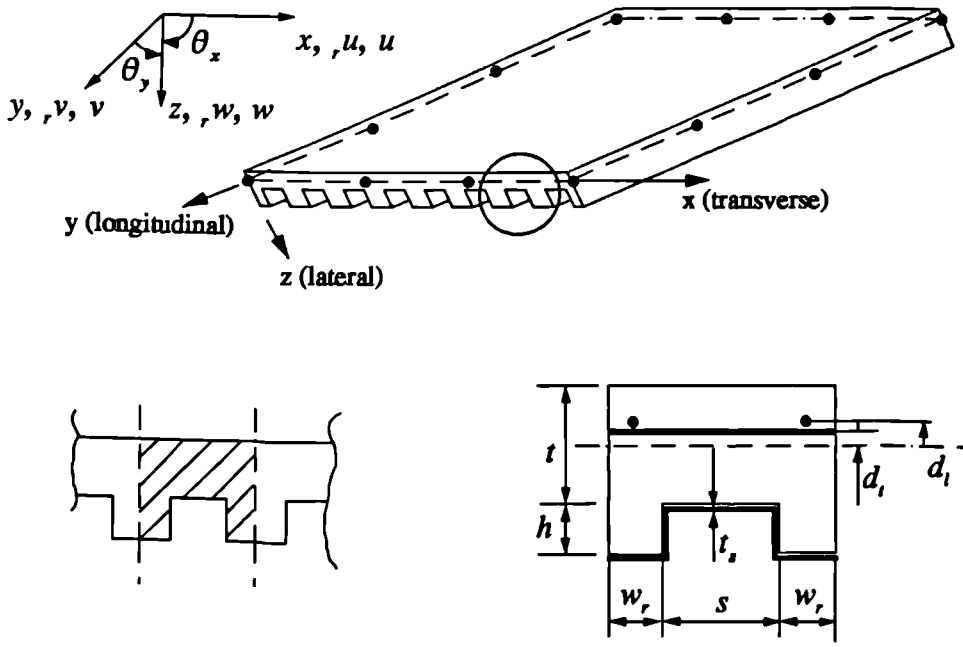


Figure 6.3 Geometric configuration of the slab element

6.2.2 Element Geometry

The reference plane of the slab element is defined as the mid-surface of the concrete cover above the ribs. The cross-sectional geometry of the element is defined by the thickness of the concrete slab (t), the depth of the ribs (h), the thickness of the steel decking (t_s), the width of ribs (w_r), the spacing of ribs (s), the position of mesh reinforcement (d_t) and (d_t), and the reinforcement areas per unit width, as illustrated in Figure 6.3.

6.2.3 Kinematics for Rectangular Ribs

The proposed element consists of a variable number of blocks, and employs 12 nodes, as illustrated in Figure 6.3, thus enabling cubic shape functions. The cubic element is chosen, instead of other linear or quadratic elements, so that appropriate accuracy can be achieved, even when a relatively coarse mesh is used. The reference plane of the slab, before deflection, defines the local x and y axes, with the positive direction of the z-axis being downwards. The displacements along the reference plane of the slab in the x, y and z directions are designated by ${}_r u$, ${}_r v$ and ${}_r w$, and the rotations in the xz and yz planes by θ_x and θ_y, respectively, as shown in Figure 6.3.

These five displacements/rotations are interpolated independently; therefore, five local degrees of freedom are considered at each node. One of the most important aspects of finite element formulation is the interpolation of the displacement field. Serendipity shape functions are adopted for this element, and an isoparametric formulation is assumed. In other words, the same shape functions used to express the element geometry in terms of nodal coordinates are adopted to define the displacement field in terms of nodal displacements. For an element shown in Figure 6.3, the displacement interpolation can be expressed as:

$$\begin{Bmatrix} {}_r u \\ {}_r v \\ {}_r w \\ {}_r \theta_x \\ {}_r \theta_y \end{Bmatrix} = \tilde{\mathbf{N}} \begin{Bmatrix} \mathbf{d}_1 \\ \mathbf{d}_2 \\ \vdots \\ \mathbf{d}_{12} \end{Bmatrix} \tag{6.1}$$

where $({}_r u, {}_r v, {}_r w, {}_r \theta_x, {}_r \theta_y)^T$ is the displacement vector at any point on the reference plane; $\mathbf{d}_i = \{u^i \quad v^i \quad w^i \quad \theta_x^i \quad \theta_y^i\}^t$ (i=1,2, ..., 12), is the displacement vector at node i; and $\tilde{\mathbf{N}}$ is a 5×60 shape function matrix expressed in terms of the natural coordinates

ξ and η.

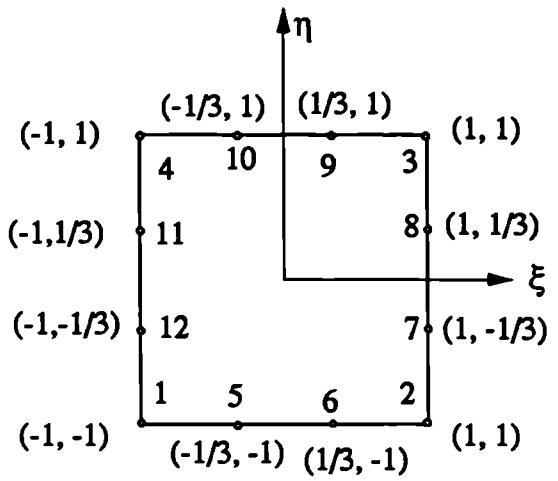


Figure 6.4 Element with natural coordinates

Methods for generatingisoparametric shape functions for various types of element can be found in several text books on finite elements (e.g. Zienkiewicz & Taylor, 1989; Cook et al., 1989). Using the natural coordinate system shown in Figure 6.4, the shape functions for this element can be shown to have the following form:

$$N_i = \frac{1}{32}(1+\xi_i\xi)(1+\eta_i\eta)\left[-10+9(\xi^2+\eta^2)\right] \quad \text{corner nodes } (i = 1, 2, 3, 4) \quad (6.2.a)$$

$$N_i = \frac{9}{32}(1+\xi_i\xi)(1-\eta^2)(1+9\eta_i\eta) \quad \text{side nodes } (i = 7, 8, 11, 12) \quad (6.2.b)$$

$$N_i = \frac{9}{32}(1+\eta_i\eta)(1-\xi^2)(1+9\xi_i\xi) \quad \text{side nodes } (i = 5, 6, 9, 10) \quad (6.2.c)$$

where (ξ_i, η_i) are the natural coordinates of node (i).

6.2.3.1 Two level displacement interpolation

Since the ribs are disposed on only one side of the slab, the reference plane is no longer a neutral plane under bending. Consequently, the in plane response is coupled to the bending response. The geometric composition of a ribbed slab also suggests that it exhibits different elastic properties in the longitudinal and transverse directions. While the homogeneity of bending stiffness is ensured in the longitudinal direction of the ribs,

the bending stiffness is not evenly distributed in the transverse direction (see Figure 6.3). Therefore, it is conceivable that the variation of vertical displacements along the transverse direction is more complex than that in the longitudinal direction.

To model the variation of the strains along the transverse direction accurately, a very high order of polynomial interpolation may be required, which could lead to extensive computational requirements. Additionally, in some cases, high order polynomials show unexpectedly large derivatives from a smooth curve (Gerald & Wheatley, 1992). This effect could hinder their application within the finite element method, in which the accuracy is more dependent on how well the strain field is represented, rather than the displacement field.

In this work, the problem is addressed by performing displacement interpolation within a block using piece wise polynomials. In this respect, a novel concept of two-level displacement interpolation is proposed. The element cubic shape functions, defined in Section 6.2.3, represent the *first level* of displacement interpolation. It is assumed that in the transverse x direction, only the ends of the repetitive blocks follow the first level displacement interpolation. In other words, the element shape functions may be used to calculate longitudinal displacement ($_{r}v$) and rotation (θ_y) at any point, and to calculate displacements associated with the transverse and lateral directions ($_{r}u$) and ($_{r}w$) and the transverse rotation (θ_x) at the ends of each block. The field for $_{r}u$, $_{r}w$ and θ_x will be interpolated over the block domain by another set of shape functions, defined accordingly as the *second level* of displacement interpolation.

6.2.3.2 Displacement interpolation over block domain

The second level of displacement interpolation is considered in the transverse direction x, where only displacements $_{r}u$, $_{r}w$ and θ_x are of direct relevance. Since the second level interpolation is proposed to account for the effect of ribs, it is performed on the block level. Displacements $_{r}u$, $_{r}w$ and θ_x in a block are defined in a piece-wise manner, in terms of 15 degrees of freedom, as shown in Figure 6.5, with $_{r}u$ and θ_x interpolated linearly, and $_{r}w$ interpolated parabolically.

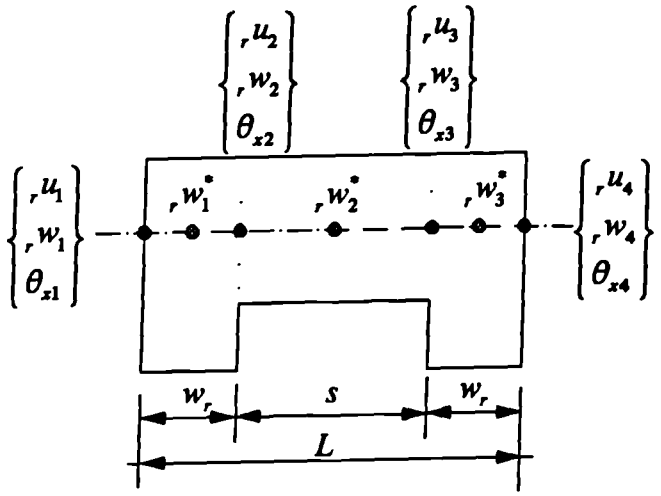


Figure 6.5 Degrees of freedom for second level interpolation

The displacement field in unit (1) is given by:

$$ {}_r u = \mathbf{H}_u \begin{Bmatrix} {}_r u_1 \\ {}_r u_2 \end{Bmatrix} = \begin{bmatrix} N_{s1} & N_{s2} \end{bmatrix} \begin{Bmatrix} {}_r u_1 \\ {}_r u_2 \end{Bmatrix} \tag{6.3.a} $$

$$ \theta_x = \mathbf{H}_\theta \begin{Bmatrix} \theta_{x1} \\ \theta_{x2} \end{Bmatrix} = \begin{bmatrix} N_{s1} & N_{s2} \end{bmatrix} \begin{Bmatrix} \theta_{x1} \\ \theta_{x2} \end{Bmatrix} \tag{6.3.b} $$

$$ {}_r w = \mathbf{H}_w \begin{Bmatrix} {}_r w_1 \\ {}_r w_2 \\ {}_r w_1^* \end{Bmatrix} = \begin{bmatrix} \overline{N}_{s1} & \overline{N}_{s2} & \overline{N}_{s3} \end{bmatrix} \begin{Bmatrix} {}_r w_1 \\ {}_r w_2 \\ {}_r w_1^* \end{Bmatrix} \tag{6.3.c} $$

where N_{si} and $\overline{N}_{si}$ are shape functions having the following form:

$$ N_{s1} = \tfrac{1}{2}\left(1 - \overline{\xi}\right) \tag{6.4.a} $$

$$ N_{s2} = \tfrac{1}{2}\left(1 + \overline{\xi}\right) \tag{6.4.b} $$

$$ \overline{N}_{s1} = \tfrac{1}{2}\left(-\overline{\xi} + \overline{\xi}^2\right) \tag{6.4.c} $$

$$ \overline{N}_{s2} = \tfrac{1}{2}\left(\overline{\xi} + \overline{\xi}^2\right) \tag{6.4.d} $$

$$ \overline{N}_{s3} = 1 - \overline{\xi}^2 \tag{6.4.e} $$

in which $\bar{\xi}$ designates the natural co-ordinate, for unit (1), parallel to the x-axis.

Since the interpolation of θ_x is one order lower than that of ${}_r w$, shear locking would be effectively prevented (Cook et al., 1989). This method of interpolation fits the local irregularities in the variation of ${}_r u$, ${}_r w$ and θ_x with an overall smooth interpolation over the element domain. The significance of this property will be illustrated by the example presented in the next chapter.

Having established the two levels of displacement interpolation, the displacements of a point in the element reference plane can be calculated as follows:

1. Given the coordinates at one end of a block in the element as (ξ_n, η_j), the displacements at this point may be determined from Equation (6.1) as:

$$\begin{Bmatrix} {}_r u \\ {}_r v \\ {}_r w \\ \theta_x \\ \theta_y \end{Bmatrix}_n = \tilde{\mathbf{N}}(\xi_n, \eta_j) \begin{Bmatrix} \mathbf{d}_1 \\ \mathbf{d}_2 \\ \vdots \\ \mathbf{d}_{12} \end{Bmatrix} \tag{6.5}$$

   Since the dimensions of block are known, the coordinates (ξ_{n+1}, η_j) at the other end of the block can be readily obtained, and the displacements at this point can be determined from an equation similar to (6.6) evaluated at (ξ_{n+1}, η_j).

2. To define the block displacement field, 15 displacements are required among which only 6 displacements (u_1, w_1, θ_{x1}, u_4, w_4, θ_{x4}) are given as a result of the previous step (see Figure 6.5). The other 9 displacements (internal displacements) can be estimated from the known 6 displacements by solving a plane strain problem. A general analytical solution for the plane strain problem of a general block geometry is rather difficult to obtain, however, a numerical solution is feasible. A simplified method is employed in this study, with details presented in Appendix B. Basically, the three units in a block are considered as beams allowing transverse shear. Using a procedure of static condensation and recovery, the 9 internal displacements can be expressed in terms of the external displacements (Figure 6.5) as:

$$\tilde{\mathbf{d}}_i = \mathbf{T}\, \tilde{\mathbf{d}}_e \tag{6.6}$$

in which,

$$\tilde{\mathbf{d}}_t = \{u_2 \quad w_2 \quad \theta_{x2} \quad u_3 \quad w_3 \quad \theta_{x3} \quad w_1^* \quad w_2^* \quad w_3^*\}^T \tag{6.7}$$

$$\tilde{\mathbf{d}}_e = \{{}_r u_1 \quad {}_r w_1 \quad \theta_{x1} \quad {}_r u_4 \quad {}_r w_4 \quad \theta_{x4}\}^T \tag{6.8}$$

3. Once all 15 displacements are available, the displacements $({}_r u, {}_r w, \theta_x)$ at any point on the element reference plane can be determined from Equations (6.3) and (6.4). As mentioned previously, the displacements ${}_r v, \theta_y$ at any point (ξ, η) can be determined from Equation (6.1).

Through the above procedure, the displacement field along the reference plane is established. The displacement of an arbitrary point over the element domain will be further discussed in Section 6.2.5.

6.2.3 Rib Freedoms

The strict application of the Mindlin hypothesis to the proposed composite slab element can lead to an overstiff response, as illustrated in the next chapter. The principal reason is that enforcing this hypothesis over the full depth of the slab, including the ribs, can lead to excessive transverse strains in the lower zones of the ribs. This shortcoming is addressed in this work through modifying the Mindlin hypothesis. A further field (Δ) expresses the departure from the Mindlin displacements at the lower face of the ribs, as shown in Figure 6.6. This field is evaluated at the centre line of the ribs (ξ_n, η), and is interpolated in terms of 12 additional nodal freedoms (Δ_i):

$$\Delta(\xi_n, \eta) = \tilde{\mathbf{N}}(\xi_n, \eta) \begin{Bmatrix} \Delta_1 \\ \Delta_2 \\ \vdots \\ \Delta_{12} \end{Bmatrix} \tag{6.9}$$

The proposed relative displacement field (Δ) influences only the transverse displacements in the ribs. Its effect on the material strain is discussed in Section 6.2.5.

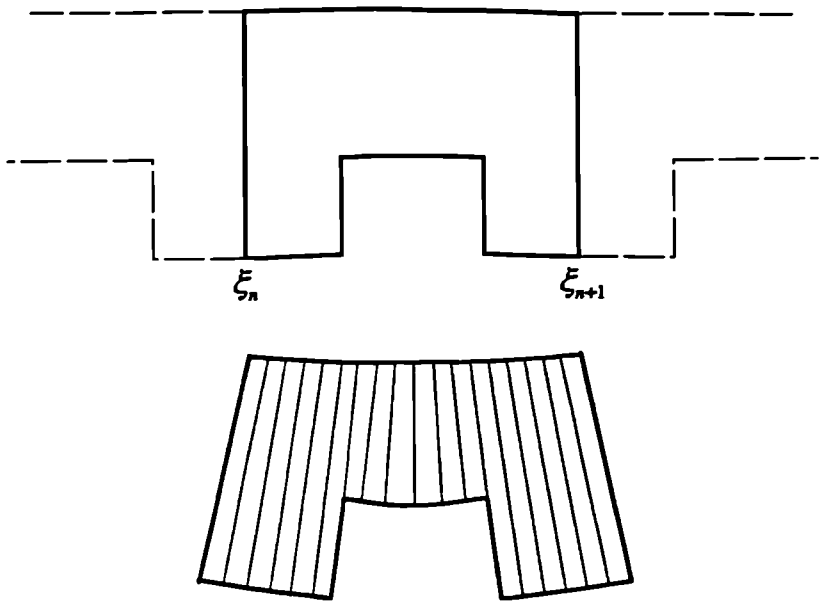
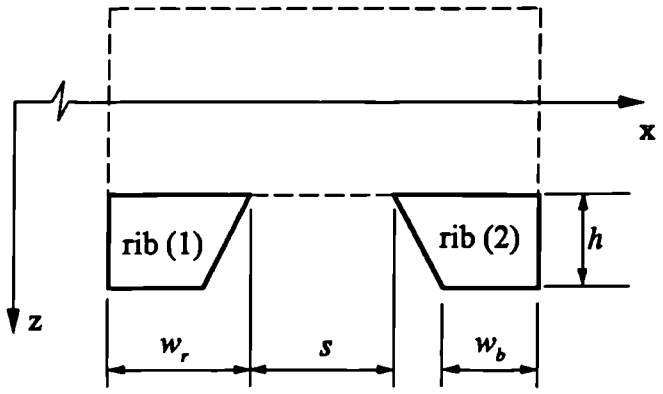


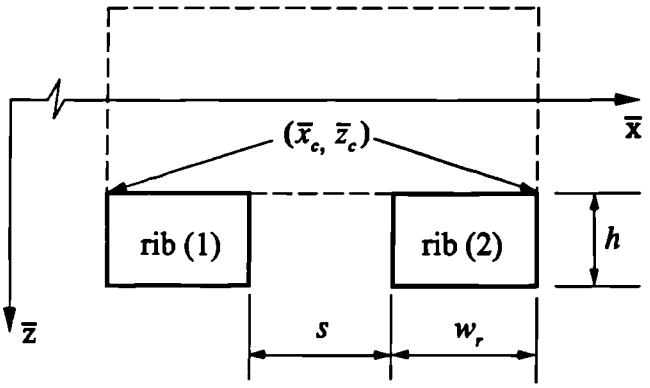
Figure 6.6 Additional rib freedoms

6.2.4 Kinematics for Trapezoidal Ribs

The displacement field is now completely defined for a slab element with rectangular decking. Generally, however, the steel decking has a trapezoidal shape, as it is more economical in terms of covering length. In the following, a procedure for formulating the slab element with trapezoidal decking is discussed, which is based on the formulation of the slab element with rectangular shaped decking. More precisely, the trapezoidal shape is mapped to a rectangular shape in a similar way to isoparametric mapping applied to irregular element shapes.



Real trapezoidal rib domain



Reference rectangular rib domain

Figure 6.7 Transform action from trapezoidal ribs to rectangular ribs

To establish this mapping, a block is considered in the real trapezoidal rib form and in the reference rectangular rib form, as shown in Figure 6.7. The reference form is assumed to have the same top width and depth for the ribs as the real trapezoidal form.

Considering the different shapes and positions for ribs (1) and (2), they have different mapping operations. However, if $(\bar{x}_c, \bar{z}_c)$ denotes the coordinates of the upper corner on the block edges, the following general mapping relationship can be used for both rib units:

$$\begin{cases} x = \bar{x}_c + (\bar{x} - \bar{x}_c)\left(1 - \dfrac{(1-r)(\bar{z} - \bar{z}_c)}{h}\right) \\ z = \bar{z} \end{cases} \tag{6.11.a}$$

in which,

$$r = \frac{w_b}{w_r} \tag{6.11.b}$$

where (x, z) are the coordinates of a point in the real trapezoidal domain, and $(\bar{x}, \bar{z})$ are the coordinates in the reference rectangular domain.

Accordingly, the derivatives with respect to the reference coordinates $(\bar{x}, \bar{z})$ can be transformed to derivatives with respect to the real coordinate system (x, z) through the Jacobian:

$$\mathbf{J}_r = \begin{bmatrix} \dfrac{\partial x}{\partial \bar{x}} & \dfrac{\partial z}{\partial \bar{x}} \\ \dfrac{\partial x}{\partial \bar{z}} & \dfrac{\partial z}{\partial \bar{z}} \end{bmatrix} = \begin{bmatrix} 1 - \dfrac{(1-r)}{h}(\bar{z} - \bar{z}_c) & 0 \\ -\dfrac{(1-r)}{h}(\bar{x} - \bar{x}_c) & 1 \end{bmatrix} \tag{6.12}$$

The two level displacement interpolation is applied to determine the block displacement fields over the reference block with rectangular ribs, through the use of Mindlin hypothesis as modified by the proposed additional rib freedoms. These fields are mapped directly to the real block with trapezoidal ribs, using the coordinate mapping established above. The implication of this mapping on the evaluation of material strains is discussed in the following section.

6.2.5 Strains

The construction of the element stiffness matrix requires the determination of the material strain field associated with the element freedoms. Since the evaluation of strains is directly related to the displacement fields which are defined using two level interpolation, the following discussion is made within reference to a single block over which the two level displacement interpolation is established. Within one block, the numerical evaluation of the strain is considered in the concrete slab cover, concrete rib and steel decking, for each of the three units, as illustrated by Figure 6.8. However, general expressions for the strains can be established for the concrete slab cover,

concrete rib and steel decking independent of the particular unit under consideration.

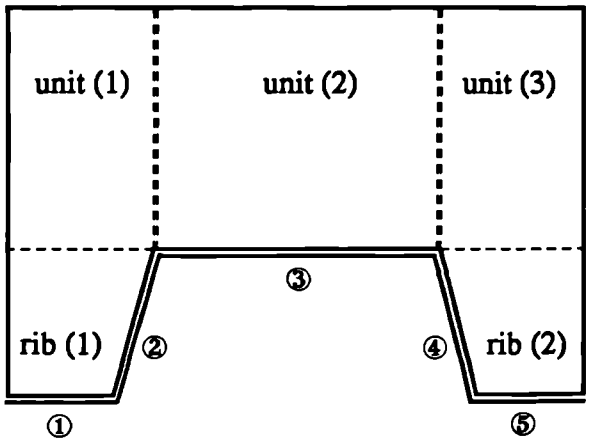


Figure 6.8 Partitioning of one block for strain evaluation

6.2.5.1 Concrete slab cover

The strains of an arbitrary point in the concrete slab cover are related to the displacements of that point (u, v, w) by the following expression:

$$\begin{Bmatrix} \varepsilon_x \\ \varepsilon_y \\ \gamma_{xy} \\ \gamma_{xz} \\ \gamma_{yz} \end{Bmatrix} = \begin{Bmatrix} \dfrac{\partial u}{\partial x} \\ \dfrac{\partial v}{\partial y} \\ \dfrac{\partial u}{\partial y} + \dfrac{\partial v}{\partial x} \\ \dfrac{\partial u}{\partial z} + \dfrac{\partial w}{\partial x} \\ \dfrac{\partial v}{\partial z} + \dfrac{\partial w}{\partial y} \end{Bmatrix} \tag{6.13}$$

where, according to the Mindlin's hypothesis, the displacement (u, v, w) can be related to the reference plane displacement $\{{}_r u, {}_r v, {}_r w, \theta_x, \theta_y\}^t$ by:

$$\begin{Bmatrix} u \\ v \\ w \end{Bmatrix} = \begin{Bmatrix} {}_r u \\ {}_r v \\ {}_r w \end{Bmatrix} - z \begin{Bmatrix} \theta_x \\ \theta_y \\ 0 \end{Bmatrix} \tag{6.13.b}$$

where z is the distance from the material point to the element reference plane. Therefore, the strains can be related to the reference plane displacement field by:

$$\begin{Bmatrix} \varepsilon_x \\ \varepsilon_y \\ \gamma_{xy} \\ \gamma_{xz} \\ \gamma_{yz} \end{Bmatrix} = \begin{Bmatrix} \frac{\partial(_r u)}{\partial x} \\ \frac{\partial(_r v)}{\partial y} \\ \frac{\partial(_r u)}{\partial y} + \frac{\partial(_r v)}{\partial x} \\ \frac{\partial(_r w)}{\partial z} - \theta_x \\ \frac{\partial(_r w)}{\partial z} - \theta_y \end{Bmatrix} - z \begin{Bmatrix} \frac{\partial \theta_x}{\partial x} \\ \frac{\partial \theta_y}{\partial y} \\ \frac{\partial \theta_x}{\partial y} + \frac{\partial \theta_y}{\partial x} \\ 0 \\ 0 \end{Bmatrix} \tag{6.14.a}$$

Assuming full compatibility between the steel reinforcement and the concrete, the direct strain in the transverse and longitudinal reinforcement are obtained from the expression below:

$$\varepsilon_x = \frac{\partial(_r u)}{\partial x} + d_t \frac{\partial \theta_x}{\partial x} \qquad \text{(transverse reinforcement)} \tag{6.14.b}$$

$$\varepsilon_y = \frac{\partial(_r v)}{\partial y} + d_l \frac{\partial \theta_y}{\partial y} \qquad \text{(longitudinal reinforcement)} \tag{6.14.c}$$

As the displacement fields are defined in the natural coordinate system (ξ, η), the derivatives in Equation (6.14) are not immediately available. Therefore, the derivatives with respect to ξ and η are first established, and the derivatives with respect to x, y and z are then obtained from:

$$\begin{Bmatrix} \frac{\partial}{\partial x} \\ \frac{\partial}{\partial y} \end{Bmatrix} = \mathbf{J}^{-1} \begin{Bmatrix} \frac{\partial}{\partial \xi} \\ \frac{\partial}{\partial \eta} \end{Bmatrix} \tag{6.15}$$

where the Jacobian matrix **J** is defined by:

$$\mathbf{J}=\begin{bmatrix}\frac{\partial x}{\partial \xi} & \frac{\partial y}{\partial \xi}\\ \frac{\partial x}{\partial \eta} & \frac{\partial y}{\partial \eta}\end{bmatrix}=\begin{bmatrix}\sum\frac{\partial N_i}{\partial \xi}x_i & \sum\frac{\partial N_i}{\partial \xi}y_i\\ \sum\frac{\partial N_i}{\partial \eta}x_i & \sum\frac{\partial N_i}{\partial \eta}y_i\end{bmatrix} \tag{6.16}$$

6.2.5.2 Concrete ribs

The displacements (u, v, w) of a material point in the concrete ribs consist of two parts:

$$\begin{Bmatrix}u\\ v\\ w\end{Bmatrix}=\begin{Bmatrix}{}_{,}u\\ {}_{,}v\\ {}_{,}w\end{Bmatrix}-\bar{z}\begin{Bmatrix}\theta_x\\ \theta_y\\ 0\end{Bmatrix}+\begin{Bmatrix}{}_{\Delta}u\\ 0\\ 0\end{Bmatrix} \tag{6.17}$$

The last term represents the modification of Mindlin hypothesis through the additional rib displacement field (Δ) and is given by:

$${}_{\Delta}u=\frac{(\xi-\xi_n)}{(\xi-\xi_n)}\frac{(\bar{z}-t/2)}{h}\Delta(\xi_n,\eta) \tag{6.18}$$

The material strains are defined, as for the slab cover, by:

$$\begin{Bmatrix}\varepsilon_x\\ \varepsilon_y\\ \gamma_{xy}\\ \gamma_{xz}\\ \gamma_{yz}\end{Bmatrix}=\begin{Bmatrix}\frac{\partial u}{\partial x}\\ \frac{\partial v}{\partial y}\\ \frac{\partial u}{\partial y}+\frac{\partial v}{\partial x}\\ \frac{\partial u}{\partial z}+\frac{\partial w}{\partial x}\\ \frac{\partial v}{\partial z}+\frac{\partial w}{\partial y}\end{Bmatrix} \tag{6.19}$$

Since the displacement fields (u, v, w) are already established in terms of ($\xi,\eta,\bar{z}$), two transformations are needed to determine the derivatives of these fields with respect to x, y and z in Equation (6.19), from the corresponding derivatives with respect to ξ, η and $\bar{z}$:

$$\begin{Bmatrix} \frac{\partial}{\partial x} \\ \frac{\partial}{\partial z} \end{Bmatrix} = \mathbf{J}_r^{-1} \begin{Bmatrix} \frac{\partial}{\partial \bar{x}} \\ \frac{\partial}{\partial \bar{z}} \end{Bmatrix} \tag{6.20}$$

$$\begin{Bmatrix} \frac{\partial}{\partial \bar{x}} \\ \frac{\partial}{\partial \bar{z}} \end{Bmatrix} = \mathbf{J}^{-1} \begin{Bmatrix} \frac{\partial}{\partial \xi} \\ \frac{\partial}{\partial \eta} \end{Bmatrix} \tag{6.21}$$

where $\mathbf{J}$ and $\mathbf{J}_r$ are the Jacobain at the element and rib levels defined by equations (6.16) and (6.12), respectively.

6.2.5.3 Steel decking

Full compatibility is assumed between the steel decking and the concrete rib, so that the material strains in the steel decking can be evaluated at corresponding positions in the concrete rib, following the procedure established in the above section. However, since the steel decking is very thin, generally about 1 mm, only the in-plane strains are considered in the various parts of the decking. It should be noted that the shear strain in the web of the steel decking can not be exactly evaluated by use of the shear strain in the concrete rib, as the web plane is inclined. Nevertheless, the shear stiffness in the web of the steel decking is not significant, thus such an approximation is considered acceptable.

6.2.6 Element Stiffness

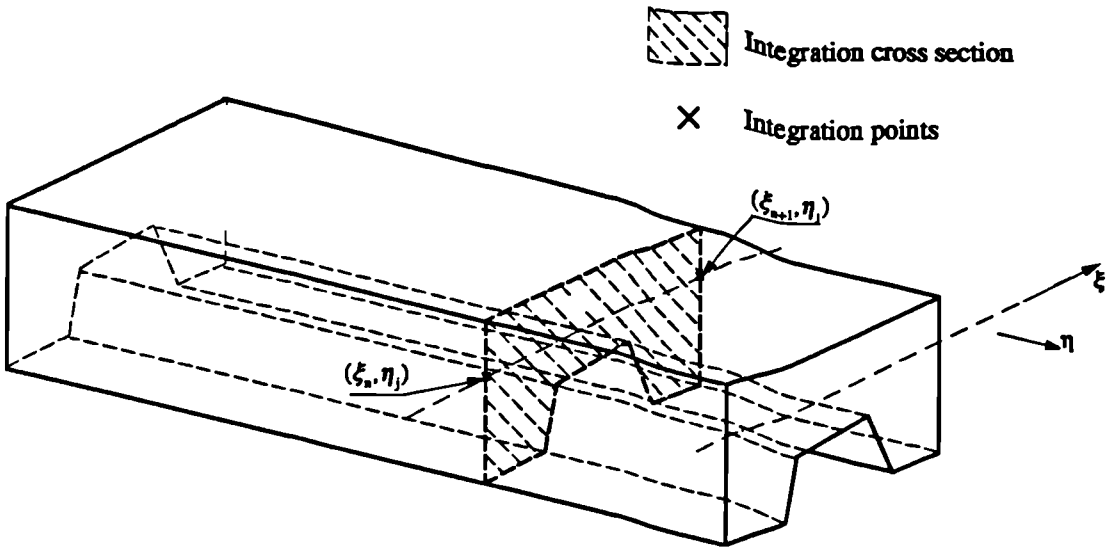
The element stiffness can be expressed as:

$$\mathbf{k} = \int_v \mathbf{B}^T \mathbf{D}\, \mathbf{B} dv \tag{6.22}$$

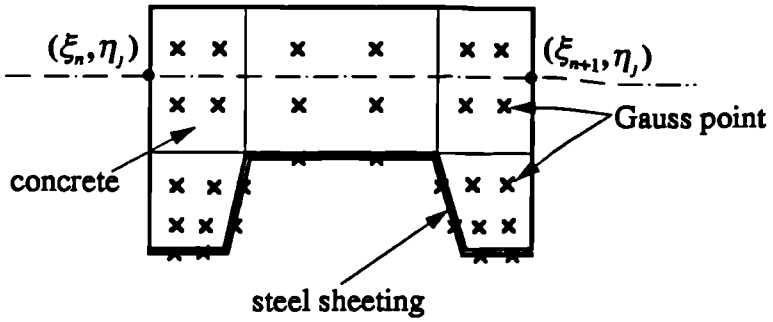
where $\mathbf{B}$ is the strain-displacement matrix, such that the following relationship holds:

$$\{\varepsilon\} = \begin{pmatrix} \varepsilon_x & \varepsilon_y & \gamma_{xy} & \gamma_{xz} & \gamma_{yz} \end{pmatrix}^T = \mathbf{B}\{\mathbf{d}_1, \cdots, \mathbf{d}_{12}, \Delta_1, \cdots \Delta_{12}\}^T \tag{6.23}$$

Hence, $\mathbf{B}$ can be determined, with the procedure established in Section 6.2.5, for the concrete slab cover, steel reinforcement, concrete ribs and steel decking.



(a) longitudinal integration



(b) Integration on block cross section

Figure 6.9 Integration cross section and integration points

Due to the irregularities in the geometric domain and the introduced assumptions about the strain distribution, the integration of (6.24) is most conveniently carried out numerically. The integration procedure is accomplished block by block within one element, and the contribution from each block is assembled by summation. Thus, Equation (6.24) may be expressed as:

$$\mathbf{k} = \sum_{n=1}^{Num} \int_{v_b} \mathbf{B}^T \mathbf{D}\, \mathbf{B}\, dv_b \tag{6.24}$$

in which *Num* is the number of blocks in the element, and v_b is the volume of block n. To perform the numerical integration over one block, J Gauss integration sections are employed along the longitudinal direction, where, in the present implementation, 4

Gauss sections are employed ($J = 4$). For a specific Gauss cross-section, integration is carried out using Gauss points along the length and through the depth, as illustrated in Figure 6.9. For the steel reinforcement and the steel decking, the stresses and strains are considered to be constant throughout the steel thickness, hence, 2D numerical integration is carried out.

Therefore, the element stiffness matrix can be written in this form,

$$\mathbf{k} = \sum_{n=1}^{Num} \sum_{j=1}^{J} \sum_{i=1}^{3} [\mathbf{k}_u]_{nji} \tag{6.25}$$

where,

$[\mathbf{k}_u]_{nji}$ = stiffness contribution from one unit,

n = block number,

j = cross-section number,

i = unit number.

For the side units ($i = 1$ or 3), $[\mathbf{k}_u]_{nji}$ is given by,

$$\begin{aligned}
[\mathbf{k}_u]_{nji} = W_j \mathrm{Det}(\mathbf{J}) \left(\xi_{n,i+1} - \xi_{n,i}\right) \Bigg(& \sum_k \sum_m \mathbf{B}_s^{\mathrm{T}} \mathbf{D}_s \mathbf{B}_s W_k W_m \frac{t}{2} \\
& + \sum_k \sum_m \mathbf{B}_r^{\mathrm{T}} \mathbf{D}_r \mathbf{B}_r W_k W_m \mathrm{Det}(\mathbf{J}_r) \frac{h}{2} \\
& + \sum_k \sum_m \mathbf{B}_{dh}^{\mathrm{T}} \mathbf{D}_{dh} \mathbf{B}_{dh} W_k \mathrm{Det}(\mathbf{J}_r) t_s \\
& + \sum_k \sum_m \mathbf{B}_{dw}^{\mathrm{T}} \mathbf{D}_{dw} \mathbf{B}_{dw} W_m \mathrm{Det}(\mathbf{J}_r) h \frac{t_s}{w_r} \\
& + \sum_k \sum_m \mathbf{B}_{ml}^{\mathrm{T}} E \, \mathbf{B}_{ml} W_k t_{ml} \\
& + \sum_k \sum_m \mathbf{B}_{mt}^{\mathrm{T}} E \, \mathbf{B}_{mt} W_k t_{mt} \Bigg)
\end{aligned} \tag{6.26}$$

in which,

$\xi_{n,i}$, $\xi_{n,i+1}$ = natural coordinates at the ends of unit i of block n (see Figure 6.9),

k, m = the Gauss point number,

$\mathbf{J}$ = Jacobian on element level defined by Equation (6.16),

$\mathbf{J}_r$ = trapezoidal rib Jacobian defined by Equation (6.12),

W_j, W_k, W_m = weighting coefficients, and

$\mathbf{B}_s, \mathbf{B}_r, \mathbf{B}_{dl}, \mathbf{B}_{dw}, \mathbf{B}_{ml}$ and $\mathbf{B}_{mt}$ are the strain-displacement matrices for the concrete slab

cover, concrete rib, horizontal part of the decking, the decking web, and the longitudinal and transverse mesh reinforcement, respectively.

For the inner unit ($i = 2$), the stiffness contribution is obtained in an identical manner to the outer units in (6.28), but excluding the second and forth summations associated with the ribs, and assigning the determent of $\mathbf{J}_r$ to be 1.

6.3 THERMAL EFFECT

When the slab is subjected to fire conditions, thermal effects are introduced. Given the temperature field within the element, the effect of thermal expansion is dealt with by means of equivalent nodal forces.

A general expression for the nodal forces required to model the initial stresses is given by:

$$\{\mathbf{r}_e\} = \int_{V_e} [\mathbf{B}]^T \{\sigma_0\} dV \tag{6.27}$$

in which $\{\sigma_0\}$ is the initial stress, V_e is the volume of the element and $\{\mathbf{r}_e\}$ is the nodal forces.

Considering the thermal stress as an initial stress, the equivalent nodal forces for the thermal effect can be derived from the above expression. With the same reason as for generating the stiffness matrix, the integration in Equation (6.27) is carried out numerically, block by block on each Gauss section along the longitudinal direction. On one Gauss section, the integration is then performed within one unit on all the Gauss points throughout the depth and along the transverse direction. Therefore, the contribution of one unit within a block on a particular Gauss section is first considered. Such a contribution to the equivalent nodal force, from unit i of block n on the j-th Gauss section, may be expressed as:

$$
\begin{aligned}
[\mathbf{R}_u]_{nji} = W_j \mathrm{Det}(\mathbf{J})\left(\xi_{\eta n,i+1} - \xi_{\eta n,i}\right)\Bigg(& \sum_k \sum_m \mathbf{B}_s^T \{\sigma_s\} W_k W_m \frac{t}{2} \\
& + \sum_k \sum_m \mathbf{B}_r^T \{\sigma_r\} W_k W_m \mathrm{Det}(\mathbf{J}_r) \frac{h}{2} \\
& + \sum_k \sum_m \mathbf{B}_{dh}^T \{\sigma_{dh}\} W_k \mathrm{Det}(\mathbf{J}_r) t_s \\
& + \sum_k \sum_m \mathbf{B}_{dw}^T \{\sigma_{dw}\} W_m \mathrm{Det}(\mathbf{J}_r) h \frac{t_s}{w_r} \\
& + \sum_k \sum_m \mathbf{B}_{ml}^T \{\sigma_{ml}\} W_k t_{ml} \\
& + \sum_k \sum_m \mathbf{B}_{mt}^T \{\sigma_{mt}\} W_k t_{mt} \Bigg)
\end{aligned}
\tag{6.28}
$$

In Equation (6.28), all matrices and constants are known, as in the element stiffness, except the thermal stresses, which will be discussed in Section 6.3.2.

6.3.1 Temperature Field

The temperature field within a slab element is defined by the nodal temperature and temperature gradients through the element interpolation defined in Equation (6.2). It is assumed that temperature varies linearly in the concrete slab cover through the depth, and the temperature in a concrete rib is uniformly distributed, being the same as that at the bottom of the concrete slab cover.

6.3.2 Thermal Stresses

As the thermal expansion through the slab depth is not considered, the thermal stresses used in Equation (6.28) have two non-zero components, which are the thermal stress in the transverse and longitudinal directions:

$$
\{\sigma\} = \begin{Bmatrix} \sigma_{x,th} & \sigma_{y,th} & 0 & 0 & 0 \end{Bmatrix}^T \tag{6.29}
$$

The transverse component of the thermal stresses can be determined for a block which is fully restrained at two ends against axial and rotational movement. Considering one block in a slab element (see Figure 6.5), it is assumed that the temperatures and temperature gradients at the block ends are T_1, $dT_{x,1}$ and T_2, $dT_{x,2}$, respectively. If the block is fully restrained at the left hand side and allowed to expand freely at the right hand side, the free end will deform according to the following, with linear variation of the temperature assumed along the reference plane within the block:

$$
\left.
\begin{aligned}
{}_{r}u_4 &= \int_o^L \alpha\left(T_1 + \frac{(T_2 - T_1)x}{(2w_s + s)}\right)dx \\
{}_{r}w_4 &= \int_o^L \alpha\left(dT_{x,1} + \frac{(dT_{x,2} - dT_{x,1})x}{(2w_s + s)}\right)xdx \\
\theta_{x4} &= \int_o^L \alpha\left(dT_{x,1} + \frac{(dT_{x,2} - dT_{x,1})x}{(2w_s + s)}\right)dx
\end{aligned}
\right\} \tag{6.30}
$$

To enforce full restraint, displacements equal in magnitude but opposite in sign to the above displacements are applied to the right end of the block. Through the procedure described in Appendix C, the internal displacements can be obtained for these block end displacements. Once all the 15 displacements in the block are established, the transversal component of the thermal strain can be calculated according to Section 6.2.5 Then stress can be calculated by using an appropriate stress-strain relationship.

The evaluation of the longitudinal component of the thermal stress is relatively easy since the material strain in the longitudinal direction is directly linked to nodal degrees of freedom at the element level. Therefore, the longitudinal component of the thermal strains (ε_{th}) can be expressed in terms of the temperature (T) by:

$$\varepsilon_{th} = \alpha T \tag{6.31}$$

where α is the thermal expansion coefficient of concrete or steel as appropriate.

It should be noted that in the mesh reinforcement, uniaxial stress state is considered; and in the decking web, only longitudinal stress is considered.

6.4 UNIFORMLY DISTRIBUTED LOADING

The equivalent nodal forces corresponding to a uniformly distributed load on the slab element are given by:

$$\{r_{wd}\} = \int_{S_e} \mathbf{N}^T \mathbf{w}\, dS \tag{6.32}$$

where $\mathbf{w} = \{w_x, w_y, w_z, 0, 0, 0\}^T$ is a uniformly distributed load on the element, and $\mathbf{N}$ is the element shape function defined in Equation (6.2).

This integral is performed numerically on the element reference surface according to:

$$\{r_{sd}\}_{km} = \sum_k \sum_m \mathbf{N}^T \mathbf{w}\, W_k W_m \det(\mathbf{J}) \tag{6.33}$$

in which, W_k, W_m and $\mathbf{J}$ are the same as that in Equation (6.26).

6.5 APPLICABILITY OF PROPOSED ELEMENT

A new slab element formulation, based on the finite element method, is derived in this chapter to model the elastic behaviour of composite steel-decked slabs. It must be noted, however, that from a structural point of view, the behaviour of a steel-decked slab can be considerably nonlinear due to the following effects (Lawson, 1983; O'leary et al., 1987; Jolly et al., 1987):

- concrete cracking
  At increased load, the tensile strength of concrete is exceeded and cracks form in the tensile zone.

- breakdown of shear bonds
  As the load is further increased, the shear bond between the steel sheeting and the slab breaks down and slippage occurs. The ultimate bond resistance is generally determined experimentally since its behaviour is affected by a combination of friction and mechanical interlocking after initial slip.

- partially composite and failure
  Yielding of the cold-formed trough takes place. The whole section may be considered partially effective. Any additional load is carried by the strength tensile reinforcement, which will yield under further increased load. Finally the ultimate capacities of the steel and the concrete are reached.

More importantly, when subjected to fire, a composite slab is much likely to experience large displacements leading to geometric nonlinearity, not considered in this slab formulation. However, the proposed element can be utilised effectively for modelling the continuity effects imposed by composite slabs which experience moderate effects of thermal expansion without considerable deterioration in stiffness and strength. Moreover, the work undertaken here lays a good foundation for the future formulation of a more comprehensive element.

CHAPTER 7
VERIFICATION OF THE SLAB ELEMENT

In this chapter, the proposed element formulation and its implementation are verified against theoretical and experimental results. The verification at the element level is firstly undertaken on a slab with uniform thickness, then a ribbed concrete slab, where a single element is used. Examples are given to demonstrate the significance of employing two level displacement interpolation and the benefit of introducing additional rib freedoms in the element formulation. The capability of the slab formulation to represent the two way response of a ribbed slab is illustrated. The thermal effect is verified on a steel-decked concrete slab with reinforcement, where consideration is given to a uniformly distributed temperature, over the slab, and a uniform temperature gradient, through the slab thickness. Numerical results are then provided to demonstrate that reasonable accuracy can be achieved even with a relatively coarse mesh in the analysis. This is followed by parametric studies where both single and continuous spanned slabs are considered. Finally, the slab formulation is satisfactorily verified against available experimental results.

7.1 UNIFORM SLAB

Since the slab element formulation is intended to reflect the different slab responses in the longitudinal and transverse directions, it is essential that numerical tests are undertaken in both directions. The first verification example is carried out on a uniform slab. The slab considered has a uniform thickness of 50 mm, and measures 3 m in both length and width. It is completely restrained at one edge and is therefore expected to behave as a cantilever beam. Loading is applied along the free edge opposite to the restraints. Three load cases are considered; 1) axial force, 2) vertical load, and 3) moment. To compare with the analytical beam results, Poisson's ratio ν is assumed to be zero for simplicity. The modulus of elasticity E is assumed to be 42 GPa.

A single element is employed to model this slab. It is assumed that there are 20 blocks in the element along the length, in which $w_r = 37.5$ mm and $s = 75$ mm. The rib depth h is set to zero in order to enforce uniform thickness.

7.1.1 Axial Force

When an axial force is applied, the slab will have axial displacement as follows:

$$u = \frac{Fx}{EA} \tag{7.1}$$

in which F is the applied force, x is the distance from the fixed end, and A is the area of the slab cross-section.

The Computed displacements for $F = 10^4$ kN , as well as the analytical results, are given in Table 7.1.1. The designation T and L in the last column, and hereafter, indicate verification in the transverse and longitudinal directions, respectively. Analytical and numerical results show excellent agreement.

Table 7.1.1 Deflections under axial load

(T-Transverse, L-Longitudinal)

Positions	Deflection (mm)	
x	Analytical	Numerical (T/L)
L/3	1.5873	1.5873 / 1.5873
2L/3	3.1746	3.1746 / 3.1746
L	4.7619	4.7619 / 4.7619

7.1.2 Vertical Load

A vertical load is applied as shown in Figure 7.1. Consideration of the shear effects yields the following expression for the beam deflection:

$$\begin{cases} w = \dfrac{Px^2(3L-x)}{6EI} + \dfrac{kPx}{GA} \\ \theta_x = \dfrac{Px(2L-x)}{2EI} + \dfrac{kP}{GA} \end{cases} \tag{7.2}$$

in which k is the form factor for shear.

In Table 7.1.3, the numerical results, from this analysis for M=1000 Nm, are compared with the analytical results, and excellent agreement is established.

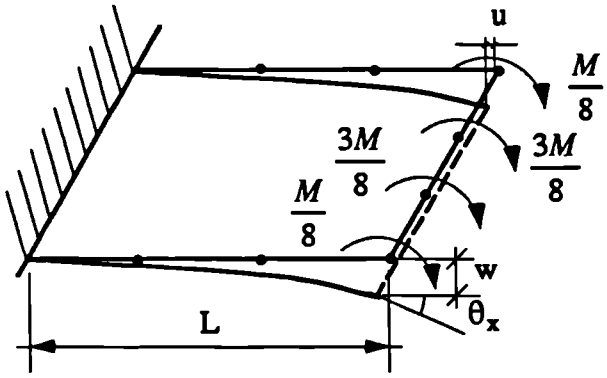


Figure 7.2 Deflection of slab subject to edge moment

Table 7.1.3 Deflections due to edge moment (T-Transverse, L-Longitudinal)

Positions	Deflections ($\times 10^{-1}$ mm)		Rotations ($\times 10^{-3}$)	
x	Analytical	Numerical (T/L)	Analytical	Numerical (T/L)
L/3	0.3810	0.38095 / 0.38095	0.7619	0.7619 / 0.7619
2L/3	1.5238	1.5238 / 1.5238	1.5238	1.5238 / 1.5238
L	3.4286	3.4286 / 3.4286	2.2857	2.2857 / 2.2857

This example was also considered with different numbers of blocks, where satisfactory comparisons were achieved. However, it should be noted that if the slab is modelled with an element consisting of only one block, numerical difficulties arise. This phenomenon is attributed to the nature of this element formulation, which states that no stiffness terms would be associated with the transverse internal nodes. As the internal displacements in the block are determined only by those degrees of freedom at the block end, a virtual displacement given at one of the two transverse internal nodes will not cause any virtual strains within the element. A minimum of three blocks is therefore required with this element to avoid a spacious mechanism.

7.2 SIGNIFICANCE OF TWO LEVEL DISPLACEMENT INTERPOLATION

As described in Chapter 6, one of the important features of this slab element is that it utilises two-level displacement interpolation in the transverse direction. The following examples illustrate that better accuracy is achieved by utilising two level interpolation than by using the conventional one level displacement interpolation.

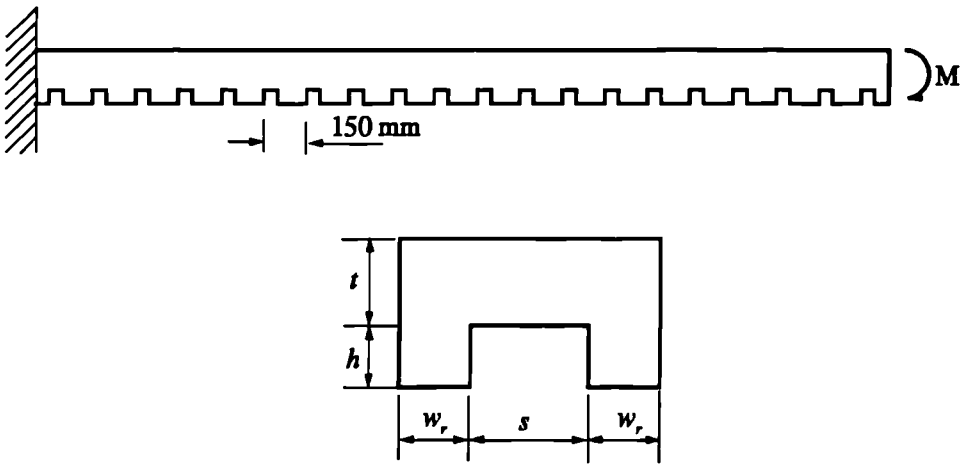


Figure 7.3 Ribbed beam under bending

A 3 × 3 m ribbed concrete slab with a total thickness of 90 mm and with 40 mm high ribs, as shown in Figure 7.3, is considered. The modulus of elasticity of concrete is assumed to be 42 GPa. Poisson's ratio is assumed to be 0, and the rib freedoms Δ are restrained in order to simplify the slab as a cantilever beam. The slab is restrained and loaded with a moment M=1000 Nm in the transverse direction, since in this case the behaviour in this direction is of major interest.

Analytically, the rotation of a cantilever under pure bending should be:

$$\theta = \int_0^x \kappa dx \tag{7.4}$$

where $\kappa_i = \frac{M}{EI_t}$, M is the applied moment, E is Young's modulus, and I is the moment of inertia.

w_r is taken as 37.5, 25, 10, and 5 mm, respectively, while the length of one block is kept constant at 150 mm. Rotations were calculated from both one and two level interpolation, as given in Table 7.2, also illustrated in Figure 7.4. The value immediately following the rotation for each position is the ratio of that computational rotation to

the analytical result. An examination of the computational rotations shows that those based on two level displacement interpolation have excellent agreement with theoretical results. Those results based on one level interpolation are consistently stiffer for all cases although the slab formulation appears to perform better when w_r becomes extremely short.

Table 7.2 Rotation under pure bending in transversal direction

w_r	Rotation($\times 10^{-3}$)		
(mm)	analytical	one level interpol.	two level interpol.
37.5	1.33882	0.56673 / 0.4233	1.33882 / 1.0000
25	1.65445	0.71051 / 0.4294	1.65445 / 1.0000
10	2.03321	1.13993 / 0.6890	2.03321 / 1.0000
5	2.15946	1.49756 / 0.6935	2.15946 / 1.0000
1	2.26046	2.06029 / 0.9114	2.26046 / 1.0000

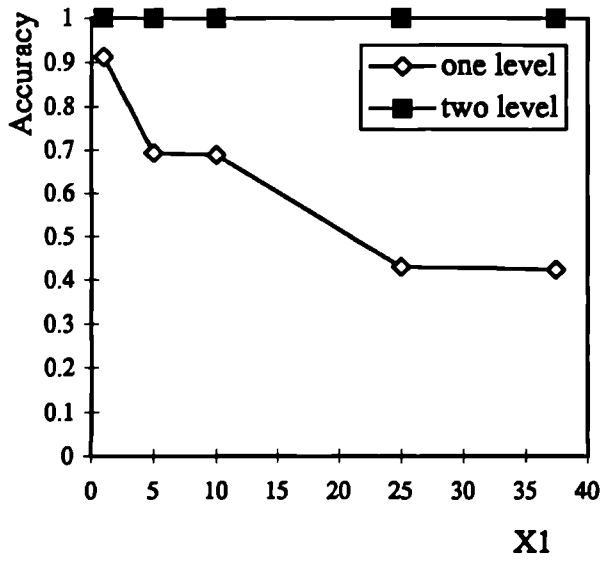


Figure 7.4 Accuracy comparison of one and two level interpolation

7.3 RIBBED CONCRETE SLAB —LONGITUDINAL DIRECTION

The slabs considered throughout Sections 7.3 to 7.5 have the same dimensions, cross sectional geometry and modulus of elasticity, as that in Section 7.2 unless stated otherwise.

The slab was analysed with a prescribed displacement field and applied vertical load. For each case, two values of Poisson's ratio υ, 0 and 0.2, are considered. As far as the longitudinal behaviour is concerned, theoretical beam results are available for comparison in the case of a zero Poisson's ratio. To evaluate the effect of the additional variable delta, comparison was also made between the results of considering the delta effect and those obtained when the effect of delta was not considered. Accordingly, there are four cases for each test.

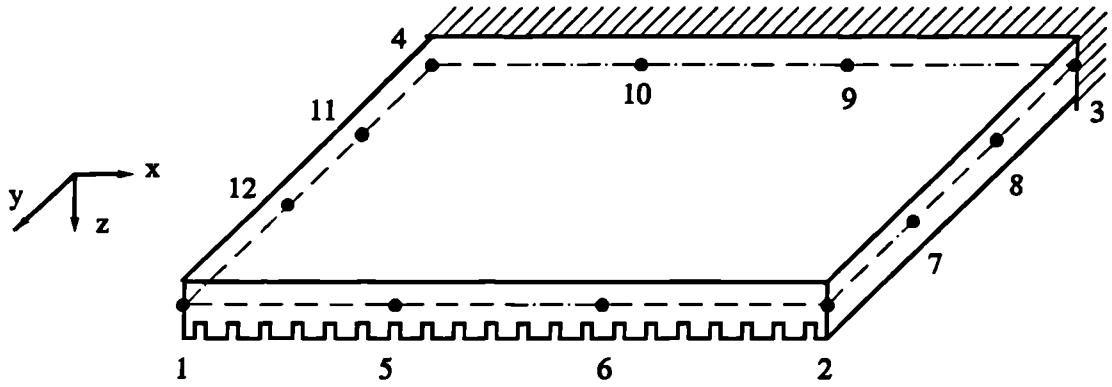


Figure 7.5 Slab clamped longitudinally

7.3.1 Prescribed Displacement Field

The slab is subjected to a prescribed displacement field. Nodes 1, 2, 5 and 6 (shown in Figure 7.5) are given an axial displacement of 10 mm, nodes 7 and 12 a displacement of 20/3 mm, nodes 8 and 11 a displacement of 10/3 mm, and nodes 3, 4, 9 and 10 no displacement. This prescribed displacements are considered such that they have a uniform expansion with $\varepsilon_y = 1/300$. The computed resultants at each node are given in Table 7.3.1.1.

From this displacement field, the following force and moment can be obtained analytically:

$$F_y = EA\varepsilon_y = 2.94 \times 10^7 \text{ N}$$

$$M_y = -20X1\ E\varepsilon_y \int_{-25}^{65} z dz = -3.78 \times 10^5 \text{ Nm}$$

F_y and M_y have the same value as the summation of resultants from nodes 1, 2, 5 and 6.

It is found, as expected, that when Poisson's ratio is assumed to be zero, consideration of the delta effect makes no difference. Resultant nodal forces and moments, for the case of Poisson's ratio of $\upsilon = 0.2$, are listed in Table 7.3.1.2. It can be seen that the resultant force and moment at edge 1-5-6-2 is about 4.2% higher than the corresponding force and moment for $\upsilon = 0$. With the effect of Poisson's ratio, the overall stiffness of the slab is stronger, hence the higher resultants for the same displacement field. It is noted that results are unaffected by possible consideration of the delta effect. This is due to the fact that the transverse deformation is so small, the effect of delta becomes negligible.

Table 7.3.1.1 Nodal resultants ($\upsilon = 0$)

Node	Restrained Δ_i		Unrestrained Δ_i	
No.	F_y (kN)	M_y(Nm)	F_y(N)	M_y(Nm)
1	3702.5625	-47604.3746	3702.5625	-47604.3746
2	3702.5625	-47604.3746	3702.5625	-47604.3746
5	10997.4377	-141395.6272	10997.4377	-141395.6272
6	10997.4377	-141395.6272	10997.4377	-141395.6272
Total	29400	-378000	29400	-378000

Table 7.3.1.2 Nodal resultants (υ=0.2)

Node	Restrained Δ_i		Unrestrained Δ_i	
No.	F_y(kN)	M_y(Nm)	F_y(kN)	M_y(Nm)
1	3856.8359	-49587.8902	3823.7773	-47879.8621
2	3856.8359	-49587.8902	3823.7773	-47879.8621
5	11455.6640	-147287.1086	11357.4726	-142213.8860
6	11455.6640	-147287.1086	11357.4728	-142213.8890
Total	30625	-393750	30362.5	-380187.5

7.3.2 Vertical Edge Load

A vertical load P = 10 kN is applied along edge 1-2, distributed to the nodes as shown in Figure 7.1. The computed displacements of the slab at the loaded edge are given in Table 7.3.2 for various depths of the ribs and checked against the analytical results, which have the following expression for a zero Poisson's ratio (υ=0.0):

$$\begin{cases} w = \dfrac{PL^3}{3EI} + \dfrac{kPL}{GA} \\ \theta_x = \dfrac{PL^2}{2EI} + \dfrac{kP}{GA} \end{cases} \tag{7.5}$$

It is found that the computed deflections are in good agreement with the theoretical values; the largest difference is less than 0.03%. It is also shown that the deflections are unaffected by the restraint of Δ_i, when υ=0.0.

For the case of υ=0.2, the deflections are less than for the case when υ=0.0. This is expected, due to the stiffening effect of a non-zero Poisson's ratio, particularly close to the built-in edge 3-4 where transverse strains are prevented. It is also observed that the deflections are slightly increased when the rib freedoms Δ_i are unrestrained, since further transverse rib expansion would then be possible.

Table 7.3.2 Deflection of mid-edge nodes under a vertical load of P = 10 kN

			Computed			
h	Deflection	Analytical	Restrained (Δ_i)		Unrestrained (Δ_i)	
(mm)			υ=0.0	υ=0.2	υ=0.0	υ=0.2
10	w (mm)	4.9105	4.9104	4.7104	4.9104	4.7533
	θ_x ($\times 10^{-3}$)	2.4551	2.4547	2.3562	2.4547	2.3774
20	w (mm)	3.4091	3.4089	3.2716	3.4089	3.3251
	θ_x ($\times 10^{-3}$)	1.7044	1.7041	1.6363	1.7041	1.6630
30	w (mm)	2.3816	2.3813	2.2877	2.3813	2.3352
	θ_x ($\times 10^{-3}$)	1.1906	1.1904	1.1443	1.1904	1.1681
40	w (mm)	1.7010	1.7007	1.6359	1.7007	1.6736
	θ_x ($\times 10^{-3}$)	0.85037	0.85011	0.81837	0.85011	0.83728

7.4 RIBBED CONCRETE SLAB —TRANSVERSE DIRECTION

In the last section, verification of the element response for a ribbed concrete slab was performed in the longitudinal direction. Further verification in the transverse direction is presented in this section. As no direct theoretical results are available for comparison, two extreme cases of a slab with exceedingly thin ($w_r \rightarrow 0$) and exceedingly thick ($s \rightarrow 0$) ribs are considered. The other dimensions of the slab remain the same as those in the previous section. The load is applied along the edge opposite the built-in edge as axial force, vertical load, or moment for each geometric configuration of the slab.

7.4.1 Case A: ($w_r \rightarrow 0$)

Starting with 37.5 mm, four additional widths of the rib w_r are considered: 10 mm, 1 mm, 0.1 mm and 0.001 mm. When the width of the rib becomes extremely small, that is ($w_r \rightarrow 0$), as illustrated in Figure 7.6, the effect of the ribs should become negligible, and the deformation of the slab should converge to that of a uniform slab with a thickness of 50 mm.

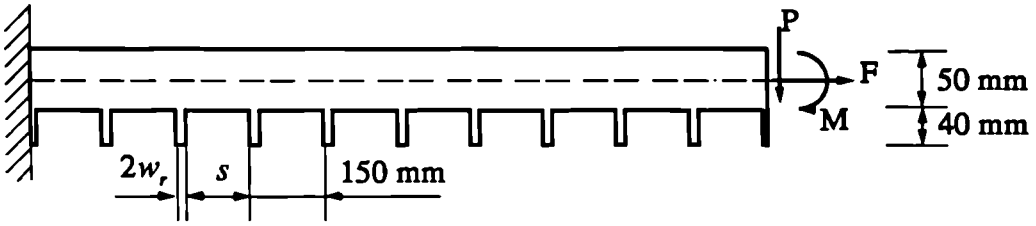


Figure 7.6 Slab with very thin ribs

The theoretical deflections of a 50 mm thick uniform slab (υ=0) are given in Table 7.4.1.1 for the considered loading. For various widths of rib, the computed deflections along the edge where the load is applied are shown in Tables 7.4.1.2 to 7.4.1.4, for the three load cases.

Table 7.4.1.1 Deflections of uniform slab with a thickness of 50 mm

Displacements	Load applied		
& Rotation	axial ($F=10^4$ kN)	vertical (P=1 kN)	moment ($M=10^3$ Nm)
u (mm)	4.7619	0.0	0.0
w (mm)	0.0	6.85794	3.42857
θ_x	0.0	3.42884×10^{-3}	2.28571×10^{-3}

Table 7.4.1.2 Deflections under an edge axial force of $F = 10^4$ kN

w_r	Deflections	Computational			
		Restrained (Δ_i)		Unrestrained (Δ_i)	
(mm)	(mm)	υ=0.0	υ=0.2	υ=0.0	υ=0.2
	u	4.4876	4.4661	4.4894	4.4664
37.5	w	58.789	55.670	56.715	54.551
	θ_x ($\times 10^{-2}$)	3.9193	3.7511	3.7810	3.6861
	u	4.6887	4.7009	4.6892	4.7010
10	w	15.677	14.779	15.160	14.617
	θ_x ($\times 10^{-2}$)	1.0451	0.9992	1.0106	0.9926
	u	4.7546	4.7829	4.7546	4.7829
1	w	1.5680	1.4766	1.5166	1.4660
	θ_x ($\times 10^{-2}$)	0.1045	0.0999	0.1011	0.0997
	u	4.7612	4.7913	4.7612	4.7913
0.1	w	0.1568	0.1476	0.1517	0.1467
	θ_x ($\times 10^{-2}$)	0.01045	0.0009	0.0101	0.00998
	u	4.7619	4.7912	4.7619	4.7922
0.001	w	0.00002	0.0016	0.0001	0.0001
	θ_x ($\times 10^{-2}$)	0.0001	0.0001	0.0001	0.0001

The results in Table 7.4.1.2 show that when subjected to the transverse axial force F, the ribbed slab does not only undergo transverse axial deflection u but also lateral deflection w and rotation θ_x. Indeed, the lateral deflection is more significant compared to the axial deflection when the rib width is so large that the effect of eccentricity is considerable. However, the lateral deflection decreases significantly, when w_r is reduced, becoming negligible when w_r approaches zero. Simultaneously, the transverse deflection converges to that of a uniform slab when w_r approaches zero. The results for the case of υ=0.2, show that the deflections have the same trend, and also converge, as $w_r \rightarrow 0$, but to a value slightly different from that of the case of υ=0.

It should be noted that in Tables 7.4.1.2 to 7.4.1.4, the given deflections are those at the internal edge nodes of the slab element. Generally, there exists differences in the

numerical values of the axial displacements, at the four nodes along the edge, with the displacement at the corner nodes being smaller than those at the internal nodes. For the case of υ=0.2, this difference is greater than for the case of υ=0. Although the displacement for υ=0.2 is larger than that of υ=0 for the internal edge nodes, it is smaller for the corner nodes, ensuring that the case of υ=0.2 maintains a stiffer response in comparison with the case of υ=0.

Comparing the results of restrained and unrestrained rib freedoms Δ_i, it is found that when Δ_i is unrestrained for a specific rib width w_r, the transverse deflection is greater than that for the restrained Δ_i, for both υ=0.2 and υ=0, as would be expected. These differences disappear when the slab becomes uniform ($w_r \rightarrow 0$), for which the effect of the additional rib freedoms vanishes.

Table 7.4.1.3 Deflections under a vertical force of P = 1 kN

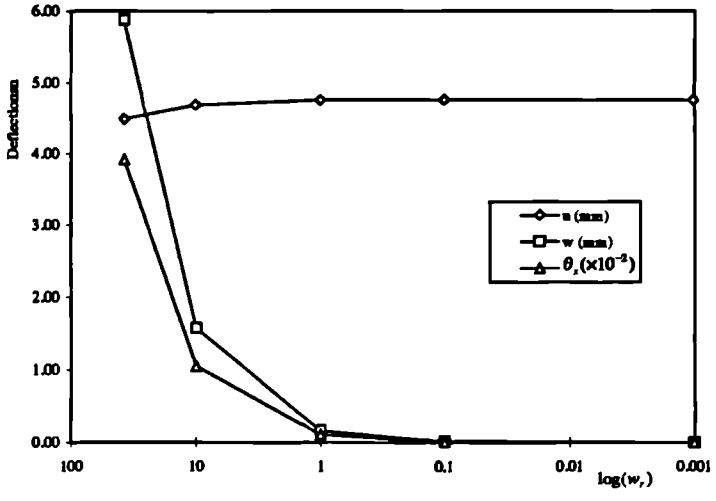
		Computed			
w_r	Deflections	Restrained (Δ_i)		Unrestrained (Δ_i)	
(mm)	(mm)	υ=0.0	υ=0.2	υ=0.0	υ=0.2
	u ($\times 10^{-3}$)	5.8789	5.6451	5.6715	5.4575
37.5	w	4.0156	3.8494	4.3311	4.1543
	θ_x ($\times 10^{-3}$)	2.0082	1.9270	2.1658	2.0786
	u ($\times 10^{-3}$)	1.5677	1.5078	1.5159	1.4625
10	w	6.0972	5.8474	6.1759	5.9233
	θ_x ($\times 10^{-3}$)	3.0498	2.9269	3.0891	2.9645
	u ($\times 10^{-3}$)	0.1567	0.1509	0.1516	0.1466
1	w	6.7783	6.5015	6.7861	6.5090
	θ_x ($\times 10^{-3}$)	3.3907	3.2542	3.3946	3.2579
	u ($\times 10^{-3}$)	0.0157	0.0151	0.0152	0.0147
0.1	w	6.8464	6.5669	6.8472	6.5677
	θ_x ($\times 10^{-3}$)	3.4248	3.2869	3.4252	3.2873
	u ($\times 10^{-3}$)	0.0002	0.0002	0.0002	0.0001
0.001	w	6.8539	6.5741	6.8539	6.5741
	θ_x ($\times 10^{-3}$)	3.4285	3.2905	3.4285	3.2905

When subjected to the vertical load P, the ribbed slab undergoes lateral deflection w, rotation θ_x, and transverse deflections u, as shown in Table 7.4.1.3. However, the transverse deflection decreases significantly when w_r is reduced, while the lateral deflection and rotation increase, and converge to the values of a uniform slab. Again, due to the effect Poisson's ratio, the lateral displacements for υ=0.2 are less than for the case of υ=0. Considering the effect of additional rib freedoms Δ_i, it is found that when Δ_i is unrestrained for a specific width w_r, the lateral deflection is greater than that for when Δ_i is restrained. Again, these differences become negligible when the slab becomes sufficiently close to a uniform slab for which the effect of the additional rib freedoms disappears.

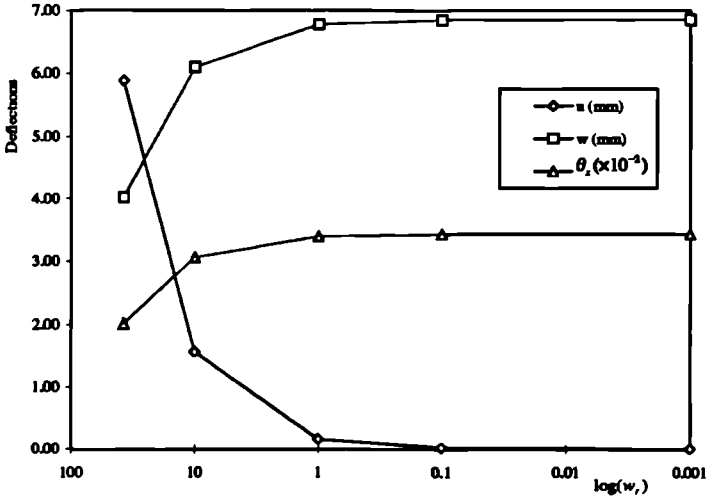
Table 7.4.1.4 Deflections under an edge moment of M= 1 kNm

		Computed			
w_r	Deflections	Restrained (Δ_i)		Unrestrained (Δ_i)	
(mm)	(mm)	υ=0.0	υ=0.2	υ=0.0	υ=0.2
	u ($\times 10^{-3}$)	3.9193	3.7640	3.7810	3.7481
37.5	w	2.0082	1.9220	2.1658	2.0748
	θ_x ($\times 10^{-3}$)	1.3388	1.2844	1.4439	1.3853
	u ($\times 10^{-3}$)	1.0451	1.0062	1.0106	1.0125
10	w	3.0498	2.9216	3.0891	2.9596
	θ_x ($\times 10^{-3}$)	2.0332	1.9510	2.0594	1.9759
	u ($\times 10^{-3}$)	0.1045	0.1007	0.1011	0.1018
1	w	3.3907	3.2491	3.3946	3.2528
	θ_x ($\times 10^{-3}$)	2.2605	2.1691	2.2630	2.1716
	u ($\times 10^{-3}$)	0.0104	0.0101	0.0101	0.0102
0.1	w	3.4248	3.2818	3.4252	3.2822
	θ_x ($\times 10^{-3}$)	2.2832	2.1910	2.2834	2.1912
	u ($\times 10^{-3}$)	0.0001	0.0001	0.0001	0.0001
0.001	w	3.4285	3.2854	3.4285	3.2854
	θ_x ($\times 10^{-3}$)	2.2857	2.1934	2.2857	2.1934

When subjected to the moment M, the ribbed slab undergoes lateral deflection w, rotation θ_x, and transverse axial deflections u, as shown in Table 7.4.1.4. When w_r is reduced, the lateral deflection and the rotation increase and converge to the values of a uniform slab, while the transverse deflection decreases significantly and approaches zero. Considering the Poisson's ratio effect, it is observed that the rotation for υ=0.2 is less than that for the case of υ=0, as expected. Considering the effect of additional rib freedoms, it is observed that when Δ_i is unrestrained for a specific width w_r, the rotational deflection is greater than that when Δ_i is restrained, before the differences disappear as the slab becomes uniform.

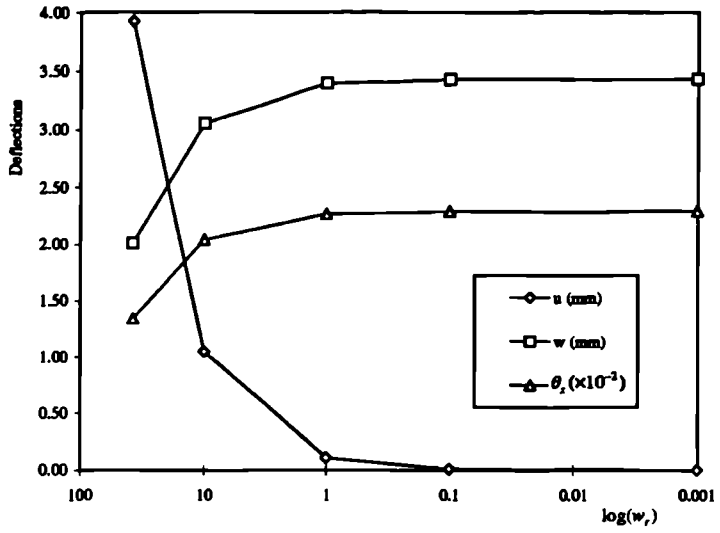


(a) under axial load



(b) under vertical load

Figure 7.7 Variation of deflections with rib width



(c) under moment

Figure 7.7 Variation of deflections with rib width (continued)

The deflections are plotted against $\log(w_r)$ in Figure 7.7 for the case of $\upsilon=0$ and unrestrained Δ_i. The graphs show that the deflections converge to the theoretical predictions of a uniform slab as $w_r \rightarrow 0$, in which case the effect on the eccentric rib becomes negligible.

7.4.2 Case B: ($s \rightarrow 0$)

When the width of the slab rib increases, such that the clear space between the ribs becomes excitedly small, $s \rightarrow 0$, as illustrated in Figure 7.8, the deformation of the slab is expected to assume that of a slab with a uniform thickness of 90 mm.

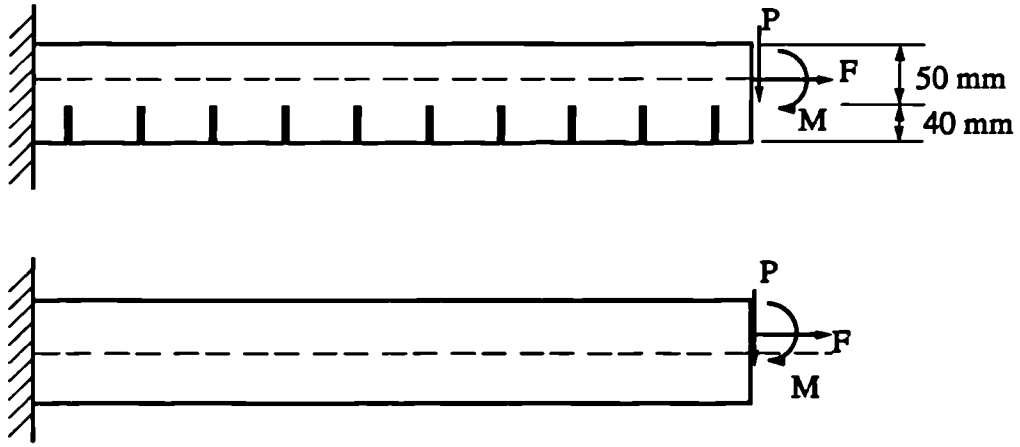


Figure 7.8 Slab with thick ribs and the corresponding uniform slab

For a 90 mm thick uniform slab with υ=0.0, the theoretical deflections at the free end, for the loads shown in Figure 7.8, are as given in Table 7.4.2.1. For various widths of ribs, the deflections at the nodes at the mid edge, where the load is applied are given in Tables 7.4.2.2 to 7.4.2.4 for the three load cases.

Table 7.4.2.1 Deflections at reference surface of a 90 mm thick uniform slab

Deformation	F (10^3 kN)	P (1 kN)	M (1 kNm)
u (mm)	0.4213	11.7607×10^{-3}	7.8385×10^{-3}
w (mm)	11.758	1.17622	0.587889
θ_x ($\times10^{-3}$)	7.8386	0.588036	0.31926

Table 7.4.2.2 Deflections under an axial force of $F = 10^3$ kN

		Computed			
s	Deflections	Restrained (Δ_r)		Unrestrained (Δ_r)	
(mm)	(mm)	υ=0.0	υ=0.2	υ=0.0	υ=0.2
	u	0.4488	0.4466	0.4489	0.4466
75	w	5.8789	5.5670	5.6715	5.4551
	θ_x $\times10^{-3}$)	3.9193	3.7511	3.7810	3.6861
	u	0.4350	0.4314	0.4354	0.4315
37.5	w	8.8183	8.3729	8.4626	8.1374
	θ_x ($\times10^{-3}$)	5.8789	5.6301	5.6417	5.4841
	u	0.4232	0.4185	0.4240	0.4193
5	w	11.366	10.812	10.401	9.9709
	θ_x ($\times10^{-3}$)	7.5772	7.2597	6.9340	6.7077
	u	0.4214	0.4165	0.4232	0.4187
0.1	w	11.750	11.181	9.5867	9.1081
	θ_x ($\times10^{-3}$)	7.8333	7.5055	6.3912	6.1247
	u	0.4213	0.4165	0.4233	0.4187
0.01	w	11.757	11.188	9.5303	9.0495
	θ_x ($\times10^{-3}$)	7.8380	7.5104	6.3536	6.0852

Similar observations to those described in Section 7.4.1, are made. When subjected to the axial force F, the ribbed slab undergoes lateral deflection w, rotation θ_x, and transverse axial deflection u due to the eccentricity of the force, as shown in Table 7.4.2.2. When s is reduced, the lateral deflection and the rotation increase and converge to the values of a uniform slab. Considering the effect of Poisson's ratio, it is found that the deflections for υ=0.2 are less than those for the case of υ=0. Considering the additional rib freedoms, it is observed that for a certain width of w_r, when Δ_i is unrestrained, the transverse deflection is greater than that when Δ_i is restrained while the lateral deflection and the rotation are less.

Despite of the fact that when $s \rightarrow 0$, the response of the ribbed slab becomes similar to that of a uniform slab, the ribbed slab is slightly more flexible than the uniform slab due to the discontinuity between the ribs. However, the formulation with restrained Δ_i cannot effectively represent this discontinuity as the displacement in the rib is predominated by the displacement in the slab. On the other hand, with the additional rib freedoms, the expansion of the ribs is possible, hence more flexible response of the ribbed slab is achieved.

Similar conclusions can be drawn from the results given in Tables 7.4.2.3 and 7.4.2.4. For the same reason, when Δ_i is unrestrained, the lateral deflections and the rotations for the case of vertical load P and moment M are larger than those for the case of restrained Δ_i.

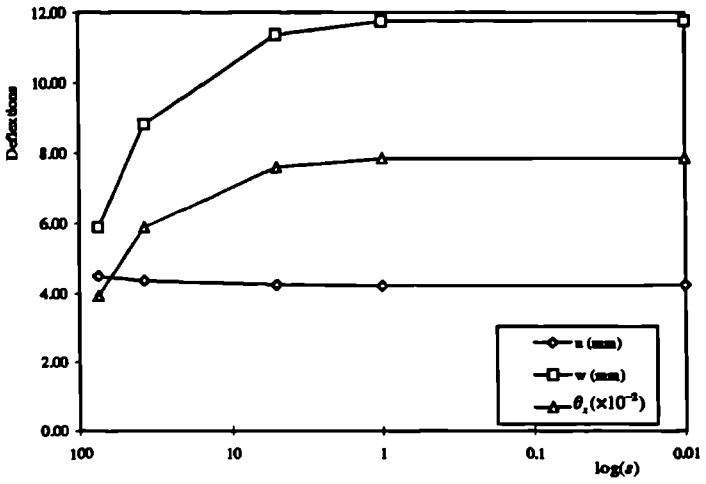
Table 7.4.2.3 Deflections under a vertical force of $P = 1$ kN

s	Deflections	Computed			
		Restrained (Δ_r)		Unrestrained (Δ_t)	
(mm)	(mm)	υ=0.0	υ=0.2	υ=0.0	υ=0.2
	u ($\times 10^{-3}$)	5.8789	5.6451	5.6715	5.4575
75	w	4.0156	3.8494	4.3311	4.1543
	θ_x ($\times 10^{-3}$)	2.0082	1.9270	2.1658	2.0786
	u ($\times 10^{-3}$)	8.8183	8.4625	8.4626	8.1370
37.5	w	2.5962	2.4872	3.1371	3.0098
	θ_x ($\times 10^{-3}$)	1.2981	1.2454	1.5684	1.5058
	u ($\times 10^{-3}$)	11.366	10.900	10.401	9.9928
5	w	1.3659	1.3065	2.8302	2.7147
	θ_x ($\times 10^{-3}$)	0.6826	6.5455	1.4159	1.3591
	u ($\times 10^{-3}$)	11.750	11.266	9.5867	9.1936
0.1	w	1.1804	1.1285	4.4508	4.2679
	θ_x ($\times 10^{-3}$)	0.5898	5.6548	2.2338	2.1437
	u ($\times 10^{-3}$)	11.758	11.272	9.5303	9.1383
0.01	w	1.1769	1.1252	4.5427	4.3560
	θ_x ($\times 10^{-3}$)	0.5881	5.6384	2.2803	2.1884

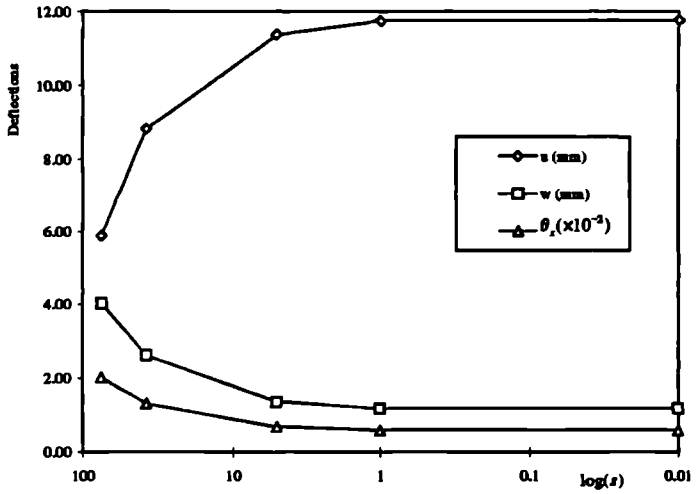
Table 7.4.2.4 Deflections under an edge moment of M =1 kNm

		Computed			
s	Deflections	Restrained (Δ_t)		Unrestrained (Δ_t)	
(mm)	(mm)	υ=0.0	υ=0.2	υ=0.0	υ=0.2
	u ($\times 10^{-3}$)	3.9193	3.7640	3.7810	3.7481
75	w	2.0082	1.9220	2.1658	2.0748
	θ_x ($\times 10^{-3}$)	1.3388	1.2844	1.4438	1.3853
	u ($\times 10^{-3}$)	5.8789	5.6407	5.6417	5.5639
37.5	w	1.2981	1.2407	1.5684	1.5027
	θ_x ($\times 10^{-3}$)	0.8654	0.8299	1.0456	1.0036
	u ($\times 10^{-3}$)	7.5772	7.2628	6.9340	6.7754
5	w	0.6826	0.6503	1.4159	1.3560
	θ_x ($\times 10^{-3}$)	0.4550	0.4361	0.9439	0.9058
	u ($\times 10^{-3}$)	7.8333	7.5055	6.3912	6.1370
0.1	w	0.5898	0.5612	2.2338	2.1395
	θ_x ($\times 10^{-3}$)	0.3932	0.3767	1.4892	1.4289
	u ($\times 10^{-3}$)	7.8385	7.5100	6.3536	6.0944
0.01	w	0.5881	0.5596	2.2803	2.1841
	θ_x ($\times 10^{-3}$)	0.3920	0.3756	1.5202	1.4587

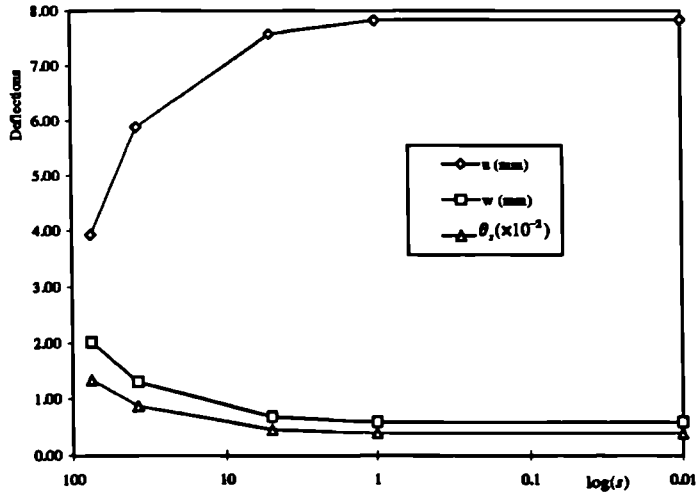
It can be seen that the computational results based on a zero Poisson's ratio compare very well with the theoretical results when s is sufficiently close to zero and Δ_t are restrained. Deformations versus log(s) are shown in Figures 7.9 (a-c), for υ=0.0 and restrained Δ_t, which clearly demonstrate this tendency.



(a) under axial force



(b) under vertical load



(c) under moment

Figure 7.9 Variation of deflections with s

7.5 EFFECT OF RIB DEPTH ON LONGITUDINAL AND TRANSVERSE RESPONSE

A ribbed slab exhibits different elastic properties in the longitudinal and transverse directions due to its 'orthotrpic' geometry. To demonstrate the capability of the proposed element to model this characteristic, a square ribbed slab is modelled by one element, and analysed as a cantilever in both the longitudinal and transverse directions, shown in Figure 7.10. The height of the ribs, h, is varied from 0 to 60 mm with a step of 10 mm. Poisson's ratio υ is taken as 0.2. The other dimensions of the slab and the material properties are the same as in Section 7.2. Two cases of applied loading, consisting of a moment M and a vertical force P distributed along the free edge, are considered. The computed deflections are given in Table 7.5.

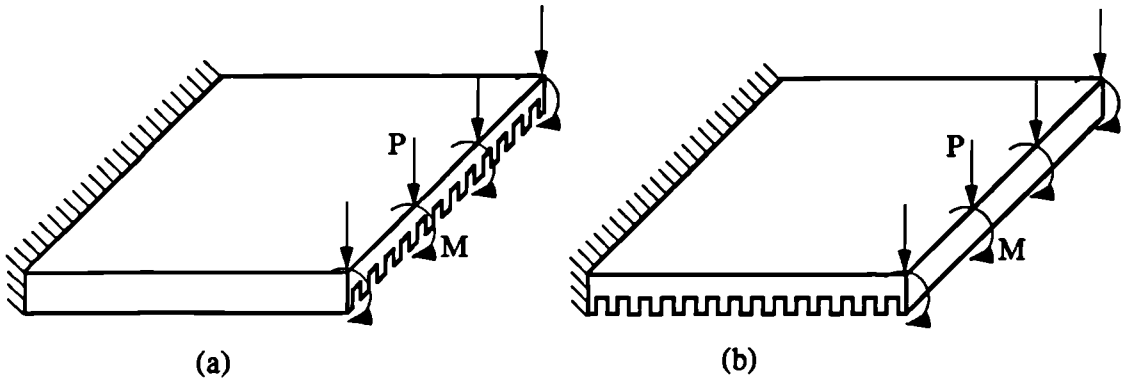


Figure 7.10 Ribbed slab with a built-in edge
(a) longitudinal response, (b) transverse response

The variation of the edge vertical deflection with the depth of the ribs can be clearly seen in Figure 7.11. It is noted that deeper ribs lead to a stiffer response, both longitudinally and transversely. The results also indicate that increasing the height of the ribs has more effect in the longitudinal direction than in the transverse direction. More interestingly, the effects have different characteristics for longitudinal and transverse loading. After h reaches 40 mm, the deflections keep reducing under longitudinal loading for a further increase in h, but reach an asymptotic value for the slab with transverse loading. This implies that once the ribs reach a certain depth, a further increase in their depth does not make a significant contribution to the transverse flexural rigidity, although it considerably affects the longitudinal flexural rigidity. In fact, when the value of h is very large, the rib becomes similar to a rigid link in the transverse direction. The ribbed slab may then be considered as a chain structure in the

transverse direction, with one rigid element and one flexible element connected sequentially. In such a structure, the flexible part is more responsible for the overall behaviour.

Table 7.5 Effect of rib depth on the vertical slab deflection

Test direction	h (mm)	Computational deflection			
		Vertical load		Moment	
		Restrained (Δ_r)	Unrestrained (Δ_r)	Restrained (Δ_r)	Unrestrained (Δ_r)
T	0	6.5622	6.5662	3.2740	3.2740
	10	5.1842	5.8391	2.5859	2.9134
	20	4.4816	5.0660	2.2363	2.5287
	30	4.0874	4.5149	2.0403	2.2543
	40	3.8494	4.1543	1.9220	2.0748
	50	3.6973	3.9175	1.8465	1.9569
	60	3.5956	3.7580	1.7961	1.8776
L	0	6.5793	6.5793	3.2862	3.2862
	10	4.7104	4.7534	2.3525	2.3742
	20	3.2716	3.3251	1.6339	1.6612
	30	2.2877	2.3352	1.1428	1.1670
	40	1.6359	1.6736	0.8174	0.8366
	50	1.2011	1.2300	0.6004	0.6150
	60	0.9048	0.9269	0 4524	0.4636

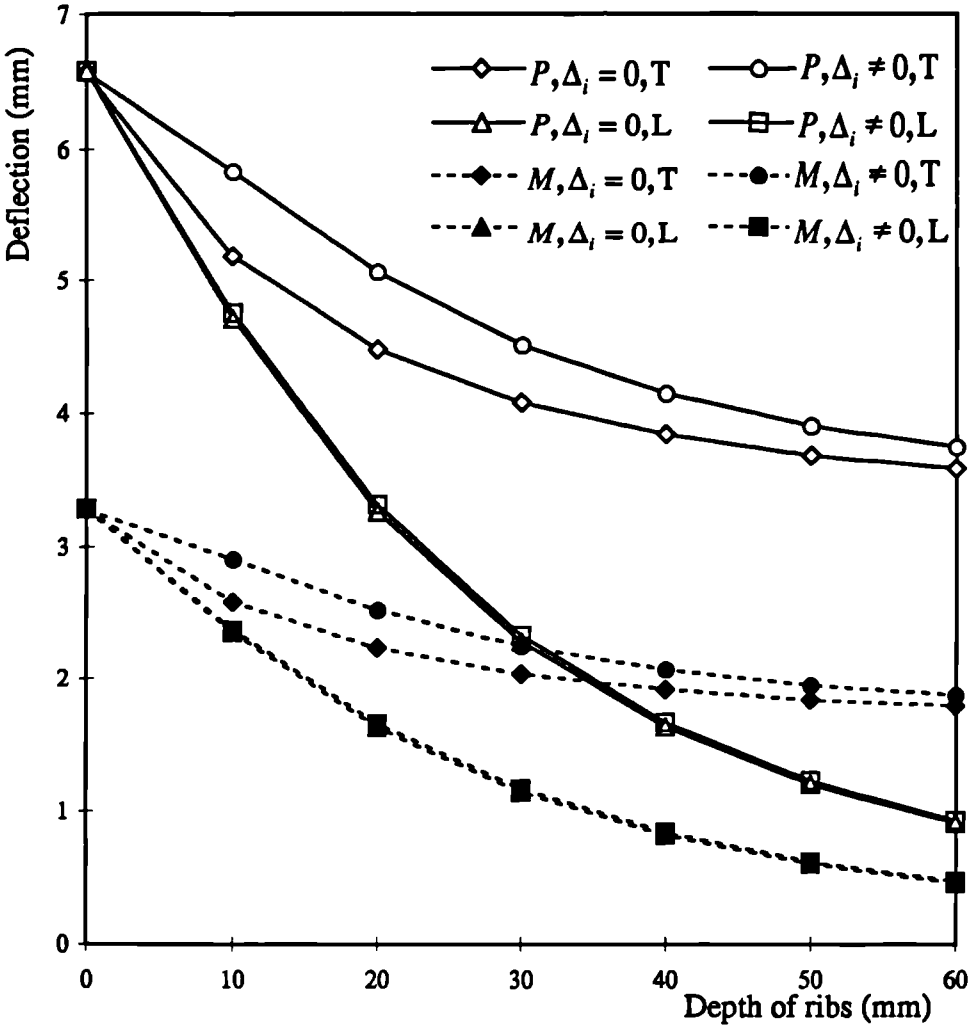


Figure 7.11 End deflections of the slabs with different rib depth

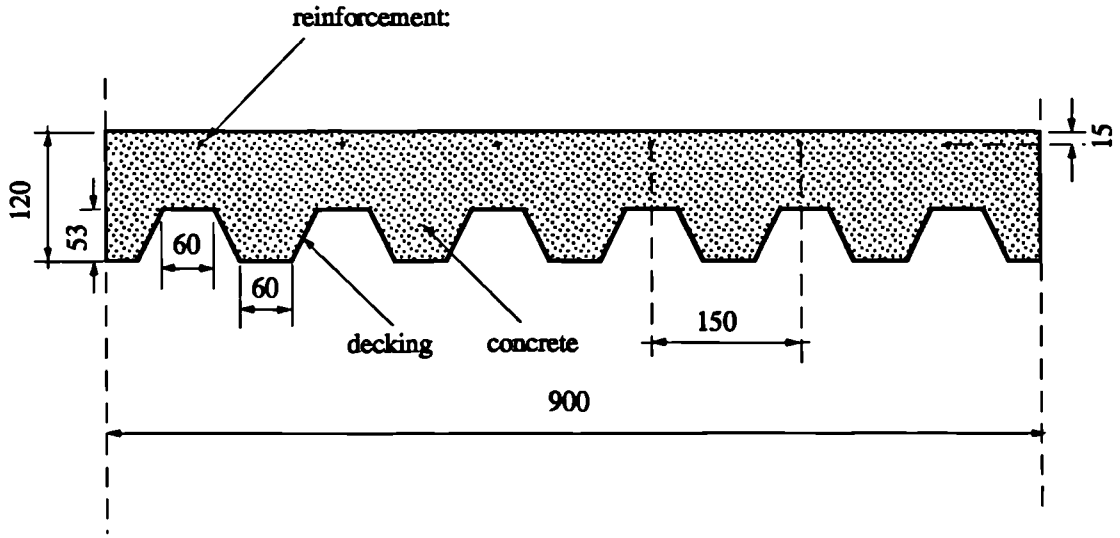
This particular example also demonstrates the advantage of utilising two level displacement interpolation in the element formulation. If the element is formulated by adopting global shape functions, as is the case with the conventional finite element method, increasing the rib depth would cause an increase in the overall transverse stiffness of the element, unless very high order shape functions are used. Using the proposed slab formulation, the local behaviour is represented by the second level displacement interpolation, hence providing a more accurate model forthe ribbed slab.

In addition to the above, the benefit of having additional rib freedoms in the element formulation is clearly illustrated. It is observed, in Figure 7.11, that the transverse response is much stiffer when the rib freedoms are excluded from the element formulation, although their effect on the longitudinal response is not significant.

7.6 THERMAL EFFECTS

The cross-sectional geometry of the example composite slab used for verifying the thermal effects is illustrated in Figure 7.12. The slab is 0.9 m wide and 5 m long. A mesh reinforcement, consisting of 8 mm diameter wire at 150 mm spacing (335.1 mm^2/1000 mm), has been provided 15 mm below the top of the slab. The steel decking consists of 53 mm high ribs at 150 mm spacing. The thickness of the cold-formed steel sheet, from which the decking is formed, is 0.75 mm. The upper and lower flanges of the decking are 60 mm wide.

The three materials used for the slab are thin walled, cold-formed steel sheeting, wire mesh reinforcement, and normal weight concrete. Young's modulus of steel is taken as 210 GPa and the modulus of elasticity of concrete is 30 GPa. Poisson's ratio is assumed to be 0.2 and 0.3 for steel and concrete respectively, and a thermal coefficient of 1.24×10^{-5}/°C is assumed for both steel and concrete.



Dimensions in (mm)

Figure 7.12 Cross-sectional geometry of steel decked slab with reinforcement

7.6.1 Uniform Expansion

To test uniform expansion, the slab is subjected to a uniformly distributed temperature of 100°C. As illustrated in Figure 7.13, along the left edge, nodes 1, 9, 10 and 5 are restrained against x and z displacements, with the front corner node 1 restrained also in the y direction. Nodes 2, 3 and 4 are restrained against movement in the y and z

directions and Node 8 is restrained in only the z direction. Under these restraint conditions, the slab is free to expand uniformly without inducing any reactions at the supports.

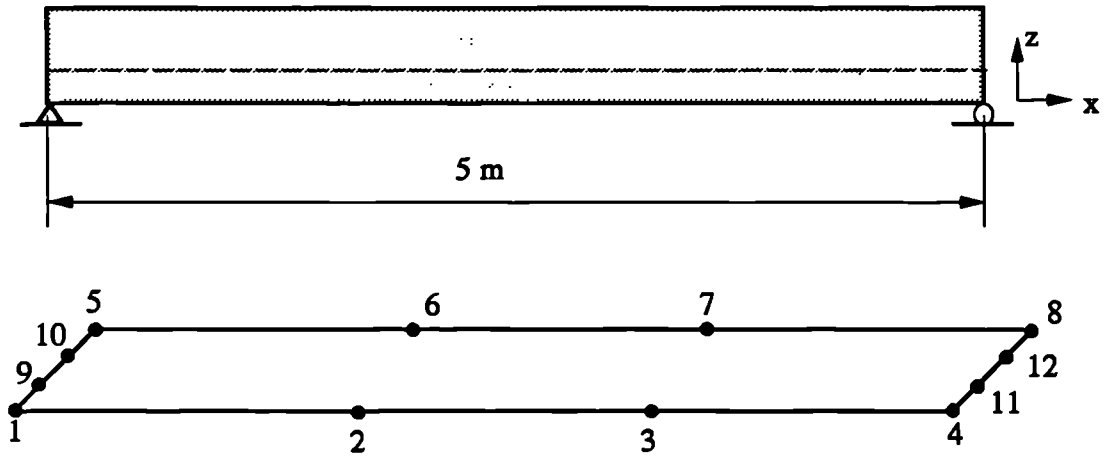


Figure 7.13 Slab subject to uniformly distributed temperature

From the computed results given in Table 7.6.1, it can be seen that displacement on all nodes matches the theoretical expansion of 1.24 mm/m. The reaction forces and moments at all supports are in the order of 10^{-5}, which is negligible. Therefore, free expansion is predicted.

Table 7.6.1 Slab with uniform expansion

Node No.	Displacement-x (cm)	Displacement-y (cm)
8	0.62	0.1116
6	0.4133	0.1116
7	0.2067	0.1116
11	0.62	0.0744
12	0.62	0.0372

7.6.2 Thermal Gradient

In this example, the temperature at each node is assumed to be 40°C, with a gradient of 100°C/m through the slab depth. The same restraints as described in the previous

section are applied. Since it is assumed in the element formulation that the temperature is uniform throughout the rib, having the same value as that at the slab bottom, the temperature distribution is nonlinear, as shown in Figure 7.14.

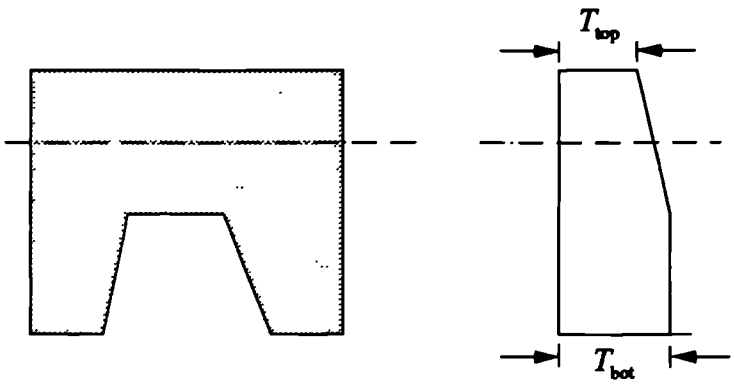


Figure 7.14 Temperature and strain distribution over the cross section

Theoretically, the rotation in a one dimensionalmember with a temperature gradient of 100°C/m through its depth will follow the expression:

$$\theta = \alpha \int_0^{L/2} T_g dx \tag{7.6}$$

where T_g is the temperature gradient, and α is the thermal coefficient, which is 1.24×10^{-5}/°C in this example. Applying the above expression to the slab and assuming a constant gradient through the depth, the rotation will be 0.0031 along edges 1-9-10-5 and 4-11-12-8, and 0.00058 alongedges 1-2-3-4 and 5-6-7-8.

Table 7.6.2 Computed rotations of the slab with temperature gradient

Position	without ribs		with ribs	
(Node No.)	Rotation-x	Rotation-y	Rotation-x	Rotation-y
1	0.0031	0.000558	0.001887	0.000594
2	0.001033	0.000558	0.0.00063	0.000594
9	0.0031	0.000186	0.001887	0.000198

Table 7.6.2 gives the computed rotations for the slab with and without consideration of the ribs. It can be seen that the rotations of the uniform slab agree with the theoretical results. The deflected shape of such a uniform slab is shown by dashed lines in Figure 7.15, whereas the solid line shows the deflected reference surface of the slab with ribs.



Figure 7.15 Deflected shape of the slab with thermal gradient

7.7 EFFECT OF NUMBER OF ELEMENTS ON ACCURACY

7.7.1 Cantilever

The slab in this example is a steel decked concrete slab, without reinforcement, subjected to a uniformly distributed load of 3 kN/m^2. The slab is 6.16 m by 3.66 m, with a total depth of 111 mm. The dimensions of the slab cross section are shown in Figure 7.16. The decking consists of 39.4 mm high ribs, at 152.4 mm spacing, having 24 repetitive blocks in the slab along the transverse direction. One edge parallel to the rib direction is fixed.

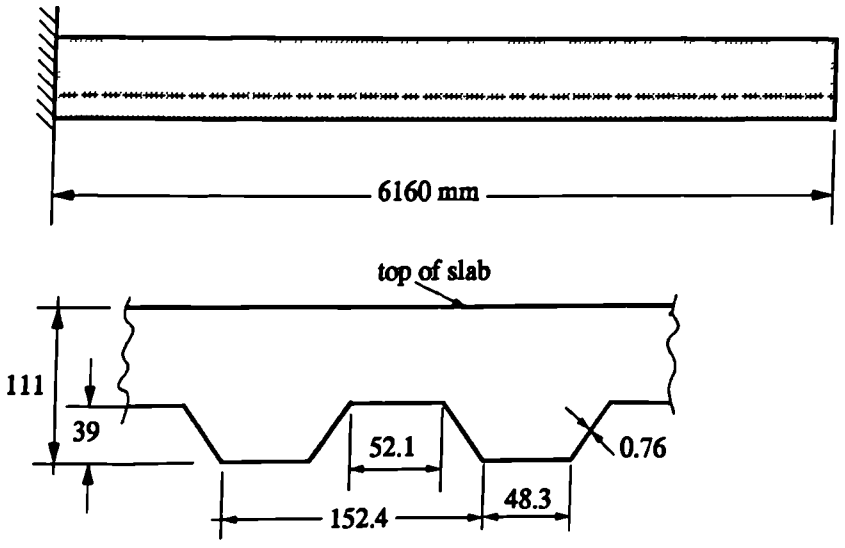


Figure 7.16 Cantilever slab

Young's modulus of the steel is assumed to be 210 GPa and the modulus of elasticity of concrete is assumed to be 30 GPa. Poisson's ratio is 0.2 and 0.3 for steel and concrete, respectively.

Starting with one element, the number of elements in the transverse direction is then increased to 2, 3, 4, 6 and 8. The cantilever slab is also analysed with a refined mesh in both directions, that is using a mesh of 2×2, 3×3, 4×4, 6×6 and 8×8 elements.

The deflection at the centre of the free edge is plotted, in Figure 7.17, against the number of elements in the transverse direction. Convergence is achieved at a mesh of 4×4 elements. Nevertheless, the deflection calculated using one element is only 0.88% different from that calculated using an 8×8 mesh of elements.

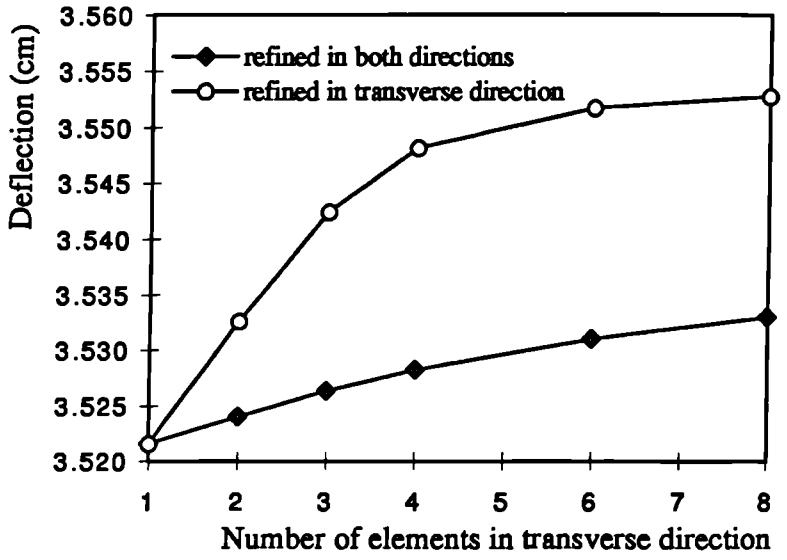


Figure 7.17 Convergence of displacement with refined mesh

7.7.2 Slab Supported on Steel Beams

A 9 m long slab, supported on beams (356×171UB51) along its 4 edges, is loaded by a small uniformly distributed load of 5 kN/m^2. The cross-sectional geometry of the slab is the same as that used in Section 7.6, but without reinforcement. Two span lengths of 5 m and 6 m are considered. The number of elements utilised in the analysis is 2×2, 4×4 and 6×6. The slab mid-span deflection, against the number of elements along one edge, is plotted in Figure 7.18.

For the case of a 5 m longitudinal span, the mid-span deflection obtained from a 2×2 mesh is 93.6% of the deflection obtained from a 6×6 mesh, with the deflection obtained from a 4×4 mesh representing a 99.9% ratio. For the case of a 6 m longitudinal span, the mid-span deflection obtained from a 2×2 mesh is 87.8% of the deflection obtained from a 6×6 mesh, with the deflection obtained from a 4×4 mesh being 99.6%.

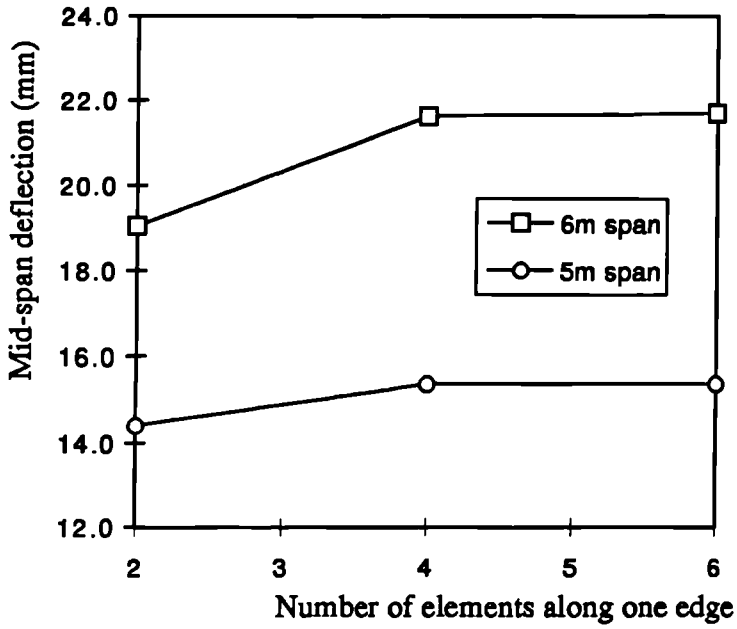


Figure 7.18 Effect of element mesh on slab mid-span deflection

7.8 EFFECT OF RIB DEPTH ON LOAD DISTRIBUTION

The slab considered in this section, and Section 7.9, is of the same cross-sectional geometry, and materials, as used in Section 7.7. The parameters which are varied are the depth of ribs and the span length. Four rib depth have been chosen — 0 mm, 26 mm, 40 mm and 53 mm, whereas two span lengths are investigated — 3 m and 5m. The ratio of the longer span to the shorter span is 3 for the 3 m slab and 1.8 for the 5 m slab.

When a slab is supported on all four sides it effectively spans in both directions. The extent of bending in each direction will depend on the ratio of the two spans, and the conditions of restraint at each support. If a uniform slab is square, and the restraints are identical along the four sides, the load will be distributed equally in both directions to the supporting beams. If the uniform slab is rectangular, more than one-half of the load

will be carried in the stiffer, shorter direction, and less in the longer direction. In designing a slab with a uniformly distributed load, the loads on the supporting beams may be apportioned approximately according to Mosley (1990), as shown in Figure 7.19:

$$R_1 = R_3 = \frac{1}{4} w l_x^2$$

$$R_2 = R_4 = \frac{1}{2}(k - \frac{1}{2}) w l_x^2$$

where w is the intensity of the uniformly distributed load per unit area; R_1, R_2, R_3, R_4 are the total load carried by each supporting beam; and

$$k = \frac{l_y}{l_x} = \frac{\text{Longer span}}{\text{Shorter span}}$$

Applying this approximation, to the ribbed slab, leads to about 72% of the total load being carried in the shorter direction for the 5 m spanned slab. If one span is much longer than the other, a large proportion of the load will be carried in the shorter direction, and the slab may as well be designed as spanning in only one direction.

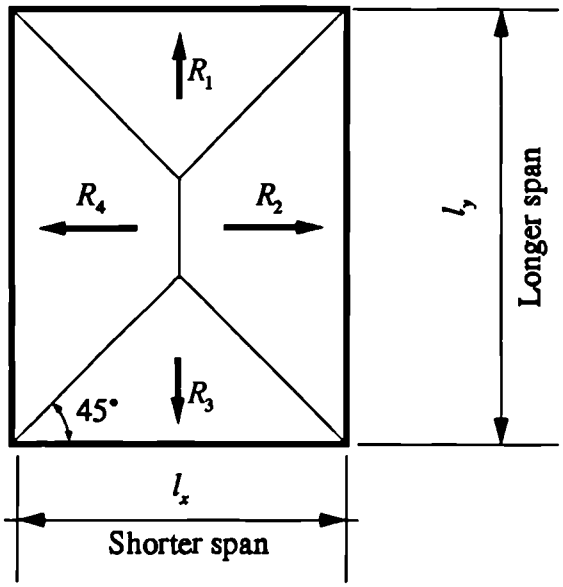


Figure 7.19 Loads carried by supporting beams

Analysis is undertaken with a 2x2 element to compare with the above approximate procedure. It is found that the 5m span is associated with a smaller transfer in the

shorter direction, in comparison to 3m slab as expected. The effect of increasing the rib depth is to increase the proportion of the load transferred in the shorter span direction, again as expected. Results indicated that this approximate procedure cannot reflect the effect of the rib depth, and is not realistic for decked slab. This is shown in Figure 7.19.

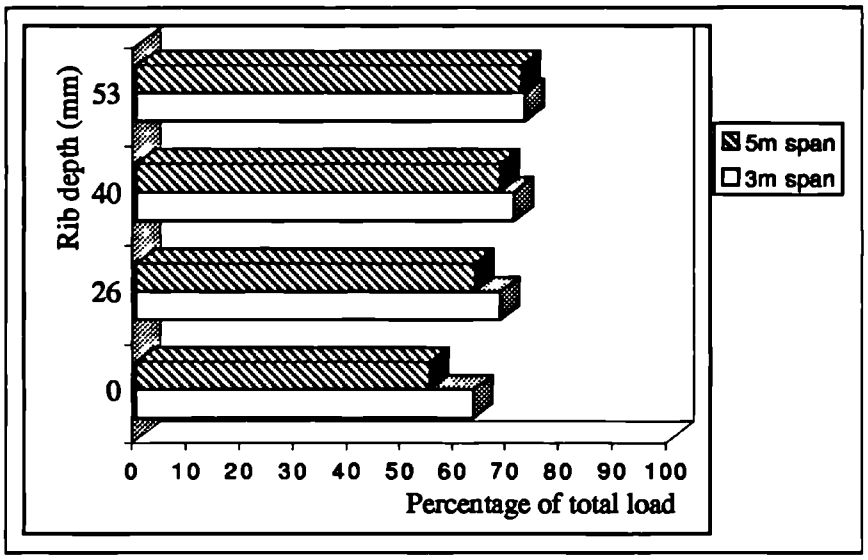


Figure 7.19 Effect of rib depth on load transfer in the short direction

7.9 CONTINUOUSLY SPANNED SLAB

A continuously spanned slab is supported by four beams along the outer edges, and an internal secondary beam, as illustrated in Figure 7.20. The slab has the same cross-sectional configuration as used in Section 7.7.

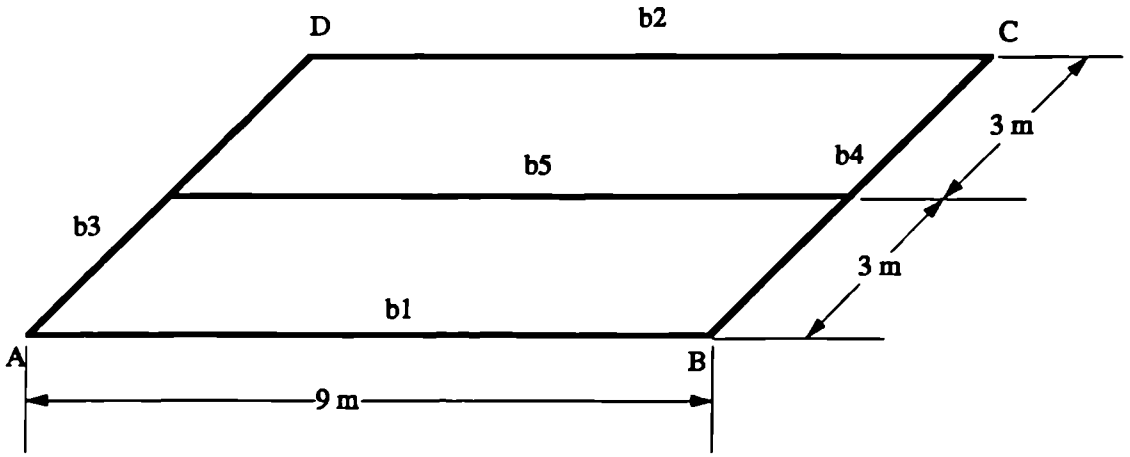


Figure 7.20 Beams supporting a continuously spanned slab

To evaluate the effect of the beam rigidities on the slab behaviour, beams of different dimensions are used, with the chosen cross-sectional dimensions given in Table 7.9.1. Four cases of supporting beam size are considered, as given in Table 7.9.2.

Table 7.9.1 Beam cross-sectional dimension

Beam	b_f (mm)	t_f (mm)	d_w (mm)	t_w (m)
254x102x28	102.1	10.0	240.4	6.4
356x171x51	171.5	11.5	332.6	7.3
610x305x170	370.0	23.6	570.3	14.1

(Note: b_f and t_f are flange width and thickness ; d_w and t_w are web depth and thickness.)

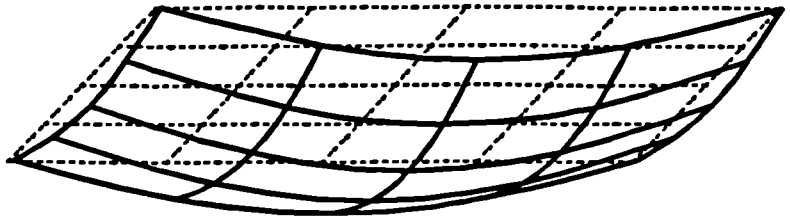
Table 7.9.2 Beam configuration

Case	b1 & b2	b3 & b4	b5
I	356x171x51	356x171x51	356x171x51
II	254x102x28	254x102x28	356x171x51
III	610x305x170	610x305x170	610x305x170
IV	254x102x28	610x305x170	610x305x170

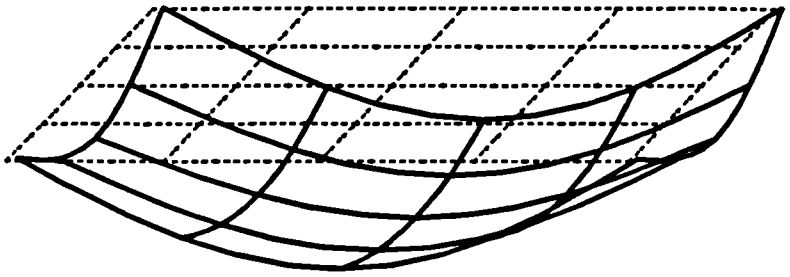
The slab is analysed using a mesh of 4x4 elements. The deflections at the midspan of beams b1 and b5 are given in Table 7.9.3. The deflected shapes of the slab are shown in Figure 7.21.

Table 7.9.3 Midspan deflections at of beams b1 and b5

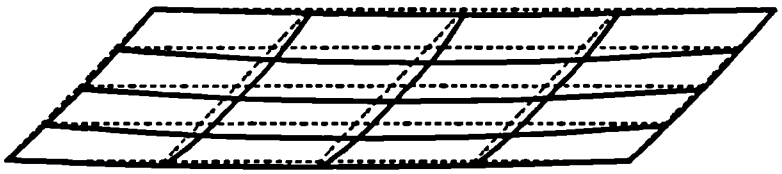
Deflections (mm)	Case I	Case II	Case III	Case IV
Beam b1	7.6	16.1	0.8	7.1
Beam b5	12.3	19.4	2.3	3.4



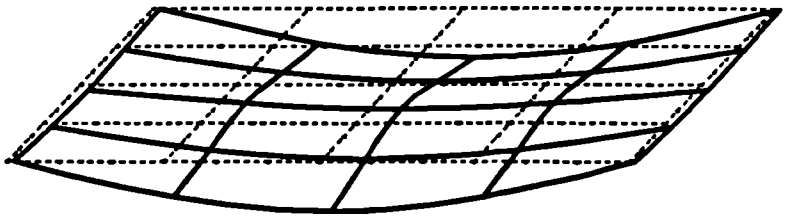
(a)Case I (Scale 50,000)



(b) Case II (Scale 50,000)



(c) Case III (Scale 50,000)



(d) Case IV (Scale 50,000)

Figure 7.21 Deflected shapes

Comparing with Case I, the results show that both the edge beam and the inner beam have a larger deflection in Case II. Since the edge beams in Case II are less stiff, the midspan deflection in Case II is more than twice that in Case I. The larger deflection of the inner beam is due to the reduction in the overall support stiffness. In Case III, all beams are much stiffer than those in Case I, although their relative rigidity remains the same. As expected, the deflections of the beams are much smaller. Case IV is particularly designed to investigate the behaviour of a continuously spanned slab when its supporting beams have different relative rigidity. In this case, the inner beam and the beams supporting the shorter edges are relatively rigid, while the beams along the longer edges are more flexible. It is found that the inner beam b5 deflects less than the edge beam b1. Furthermore, it can be seen from the deflected shape in Figure 7.21, that the slab displays largely a hogging response in the short span direction.

7.10 VERIFICATION AGAINST EXPERIMENTAL RESULTS

Klaiber and Porter (1981) reported a series of tests on steel decked concrete slabs. Originally, the tests were purposely developed to substantiate the assumption that a simply supported slab, with concentrated loads at quarter points, behaves in a similar manner to the same slab with uniform loading. Some of these tests are used to verify the proposed slab formulation.

7.10.1 Description of Test

Slab specimen were constructed with nominal depths and width of 3/8 in (111.1 mm) and 24.25 in (616 mm), respectively. Two of the slab specimens were 8 ft (2.44 m) long, and two were 12 ft long (3.66 m). Each slab specimen was constructed with a single panel width of steel decking, having a depth of 39.4 mm. The average measured thickness of the steel was 0.76 mm, and the modulus of elasticity was assumed to be 29,500 ksi (203 GPa). The deck had an average yield strength of 38.7 ksi (266 MPa), as determined by the manufacturer. The 8 ft long specimens were cast with supports at the ends only. The 12 ft specimens were cast with supports at both ends, and at the midspan to simulate shoring.

The slab specimens were tested under concentrated line loads and uniform load. The concentrated loads were applied by two hydraulic cylinders at quarter span points. Due to the nature of the test setup, the weight of the loading system was applied first. Load was next applied in increments of 500 lb (2,224N) for the first portion of the test. When a large increase in deflection occurred, the loading increment was reduced to 200

lb (889N). The uniform load was applied by inflating a plastic bag, which was confined by the top surface of the test specimen and an inverted rigid box. To start loading, the air bag was firstly sufficiently inflated to lift the confinement box from the end supports. Thus the weight of the confinement box, and the remaining tie-down equipment, became the first increment of loading. Then the load was increased in a manner similarly to that used in applying the concentrated loads. An illustration of the support conditions and applied loading is given in Figure 7.22 for a 8 ft slab.

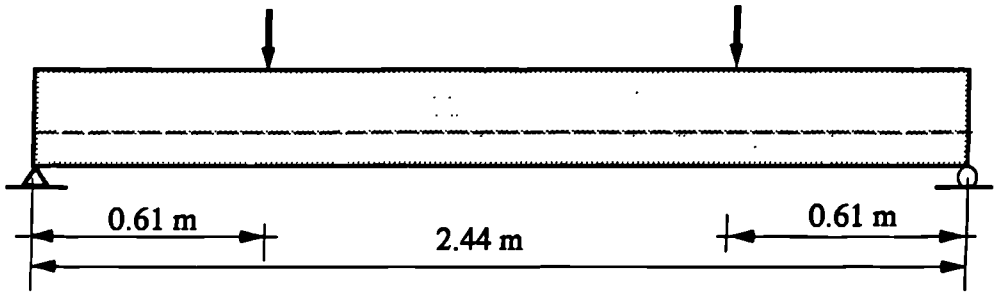


Figure 7.22 Support conditions and applied loading of the 8 ft slab

Vertical deflections at midspan and at quarter-span points were measured on the specimen throughout each of the tests. However, only the midspan deflections were reported.

The reported midspan deflections and the corresponding loads are given in Table 7.10. The specimen designation in the first column of Table 7.10 indicates, respectively, the length of specimen, shear span, and type of loading. For example, the slab designation 12-35-C indicates a 12 ft (3.66 m) long specimen, a 35 in (0.89 m) shear span, and concentrated loading. Uniform loading is indicated by the letter U.

Table 7.10 Measured deflection at 1/2 P_u

Slab Specimen	Applied Load (lb)	Measured deflection (inch)	Calculated deflection (inch)
8-23-U	3570	0.058	0.05393
8-23-C	3275	0.053	0.05445
12-35-U	2445	0.26	0.1293
12-35-C	2012.5	0.23	0.1171

Note: 1 in = 2.54 cm 1 lb = 4.45 N

7.10.2 Analysis of the Tested Slabs

The four slab tests described above are simulated here by the developed slab element. For the case of uniform loading, two slab elements are employed. For the concentrated line loading, four elements are utilised simply because the loading is at the two quarter-span position.

The slab is taken as 2.337 m and 3.556 m in length for the 8 ft and 12 ft specimens, respectively. It was reported that the tested slab was 0.616 m in width. However, when this width is used to calculate the number of blocks in the slab, it does not derive an integer. The width is therefore taken as 0.61 m in analysis. The other cross-sectional dimensions used in the analysis are:

Concrete slab depth: $t = 0.0717$ m
Rib depth: $h = 0.0394$ m
Rib width: $w_r = 0.05207$ m
Rib crest width: $s = 0.05207$ m
Width ratio: $r = 0.829$
Thickness of steel decking: $t_s = 0.00076$ m.

The modulus of elasticity of the concrete is assumed to be 30 GPa and Young's modulus for the steel decking is taken as 203 GPa. Poisson's ratio is assumed to be 0.2 and 0.3 for concrete and steel, respectively.

The reported deflection is that measured at half of the ultimate loading ($0.5P_u$). For the uniform loading case, this value is 15.89 kN(3,570 lb) for the 8 ft slab and 10.88 kN (2,455 lb) for the 12 ft slab, resulting in a uniform intensity of 11.15 kPa and 5.02 kPa,

respectively. The concentrated line loading used in analysis is 14.37 kN (3,275 lb) for the 8 ft slab and 8.95 kN (2,012.5 lb) for the 12 ft slab. This is applied as a nodal load, at the quarter-span nodal positions.

The computed midspan deflections are given in the last column of Table 7.10. The computed results are given in inches for direct comparison with the experimental results. The load-deflection response of the slab is shown in Figure 7.23, which provides a clear picture regarding the comparison between the analytical and the experimental results. For the 8 ft slabs, for which the response is mostly linear, the agreement between experimental and computational results is very good up to $0.5P_u$. For the 12 ft slabs, the computed results compare favourably with the initial slopes of the experimental load-deflection curves. However, the discrepancy between the computed deflections and the experimental deflections increases as the load increases due to the nonlinear nature of the slab behaviour.

Consideration of Figure 7.23 shows that the computed deflections, for a specific level of concentrated loading, are higher than those for an equivalent level of uniform loading, as is confirmed by linear elastic beam theory. These observations are also confirmed by the experimental results, particularly those obtained for the 12 ft slab.

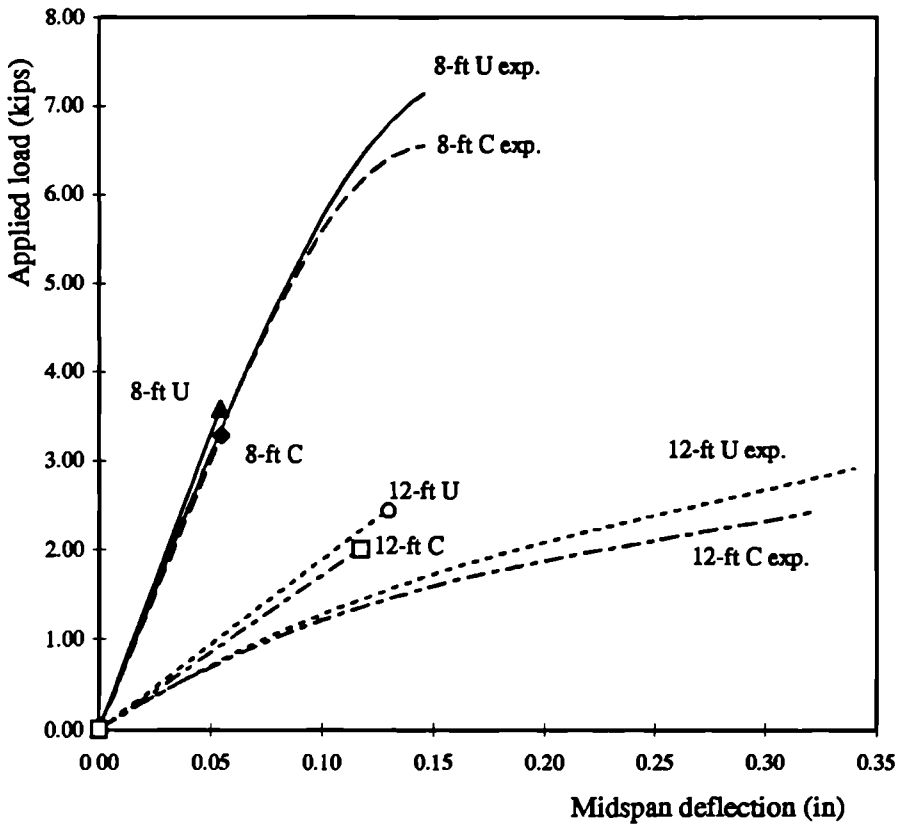


Figure 7.23 Load-deflection curves

7.11 SUMMARY

In this chapter, the slab element formulation described in Chapter 6 is verified using a number of examples. The following general observations can be made:

1) The numerical results of the proposed element provide excellent agreement with the theoretical results for both uniform and ribbed slabs;

2) Two-level displacement interpolation gives better representation of the displacement field in the transverse direction, accounting for the effect of the ribs on the overall response of slab, and hence improving accuracy;

3) Examples show that better accuracy is achieved, through introducing additional rib freedoms, especially for bending in the transverse direction;

4) Numerical results indicate that the proposed slab formulation is capable of representing the two-way property of steel-decked concrete slabs;

5) The thermal effect is verified for a slab with uniformly distributed temperature and with uniform temperature gradient throughout slab thickness;

6) Numerical results demonstrate that reasonable accuracy can be achieved even with a relatively coarse element mesh;

7) The depth of ribs has considerable effect on the distribution of loading when the slab is supported on all four sides. The deeper the rib, the more of the total load would be transferred to the beams orthogonal to the ribs; and

8) The proposed slab formulation is satisfactorily verified in the elastic range against a set of experimental results.

CHAPTER 8
CALIBRATION AGAINST CARDINGTON FULL-SCALE FIRE TEST

In this chapter, the developed nonlinear analysis tool is calibrated against the full-scale test conducted by the Building Research Establishment at Cardington. The tested structure is first analysed as a bare steel subframe formed by extending the fire compartment by one adjacent bay and storey. Then the steel decked concrete slab is modelled using the slab formulation presented in Chapter 6. To accommodate the nonlinearity under fire conditions, not considered in the current slab element, the nonlinear slab response in the fire compartment is simulated by means of reinforced concrete beams and concrete beams in the longitudinal and transverse directions, respectively. A parametric study is carried out to investigate how the structural behaviour is influenced by the effective width of the concrete beams, the slab adjacent to the compartment, creep effects and the temperature in the compartment slab. By comparing the measured displacements with the analytical predictions, the applicability, of the developed nonlinear analysis tool, to predicting the behaviour of steel building structures in fire is established.

8.1 THE FULL-SCALE TEST

8.1.1 Compartment Configuration

On the 23rd October, 1995, the Building Research Establishment (BRE) conducted a corner compartment fire test in a steel framed building with composite floors within its Large Building Test Facility at Cardington. The tested building is eight storeys high, five bays long and three bays wide, having a rectangular area of approximately 945 m^2.

The fire took place on the second floor of the building in a corner compartment bounded by grid line E to F and 3 to 4, as shown in a typical floor plan of the building in Figure 8.1. The objective was to investigate the response of the slab and beams on the floor above i.e. the third floor. Figure 8.2 gives a three dimensional view of the compartment.

Temperatures in steel members, as well as the deflection of the concrete slab, were recorded at 2 minute intervals throughout the two and a half hours duration of the fire. With this essential information, the experiment provides a great opportunity to study

the behaviour of a multi-storey steel framed building subjected to natural fires, and, more importantly, to calibrate the developed analytical models described in the previous chapters.

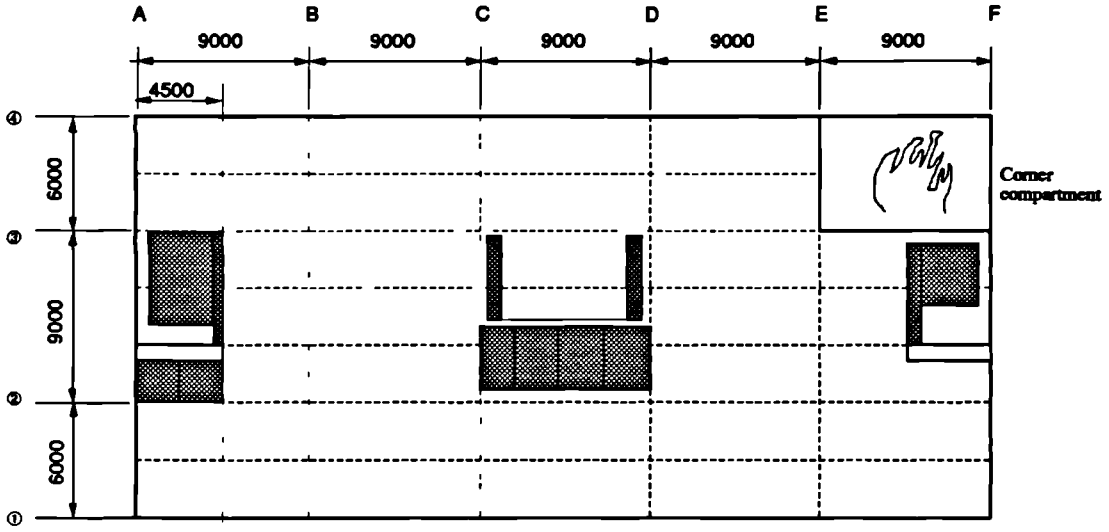


Figure 8.1 BRE corner compartment test

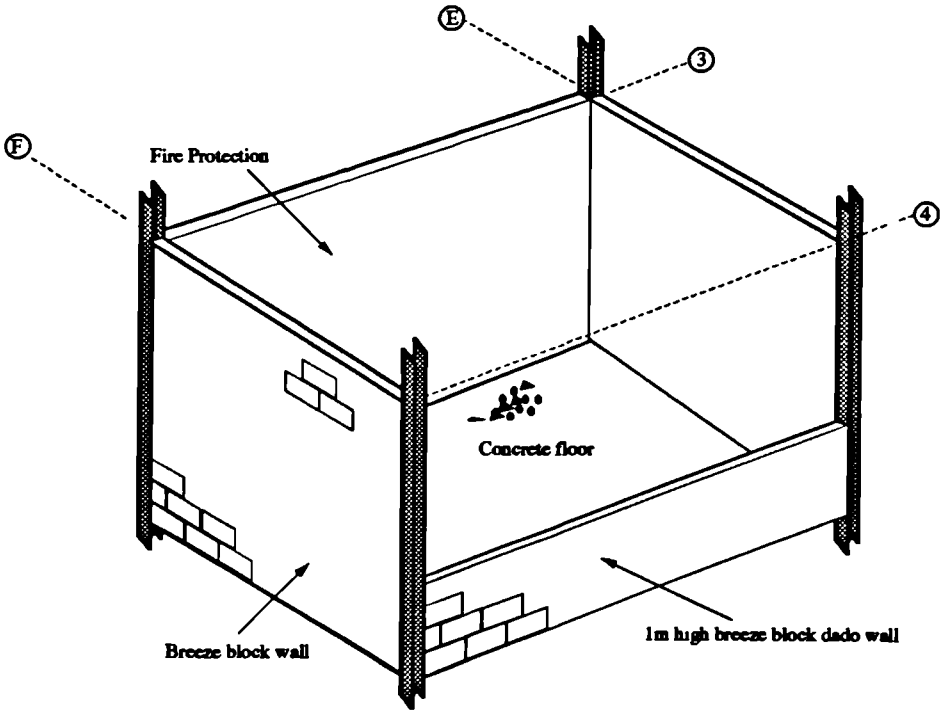


Figure 8.2 3D view of corner Compartment

8.1.1.1 Beams and Columns

For ease of reference, the main steel members, forming the boundaries of the compartment, are identified according to the schematic shown in Figure 8.3. The dimensions of the members in, and adjacent to, the compartment are shown in Figure 8.4, with the cross-sectional dimensions and grade of steel listed in Table 8.1.

Table 8.1 Member dimension (in mm)

Type	Grade	D	B	t_f	t_w
356x171UB51	50	352	171.0	9.7	6.9
305x165UB40	43	303.8	165.1	10.2	6.1
610x228UB110	43	602.4	227.6	14.8	10.6
305x305UC137	50	320.5	308.7	21.7	13.8
254x254UC89	50	260.4	255.9	17.3	10.5

(Note: D - overall depth, B - flange width, t_f - flange thickness, t_w- web thickness)

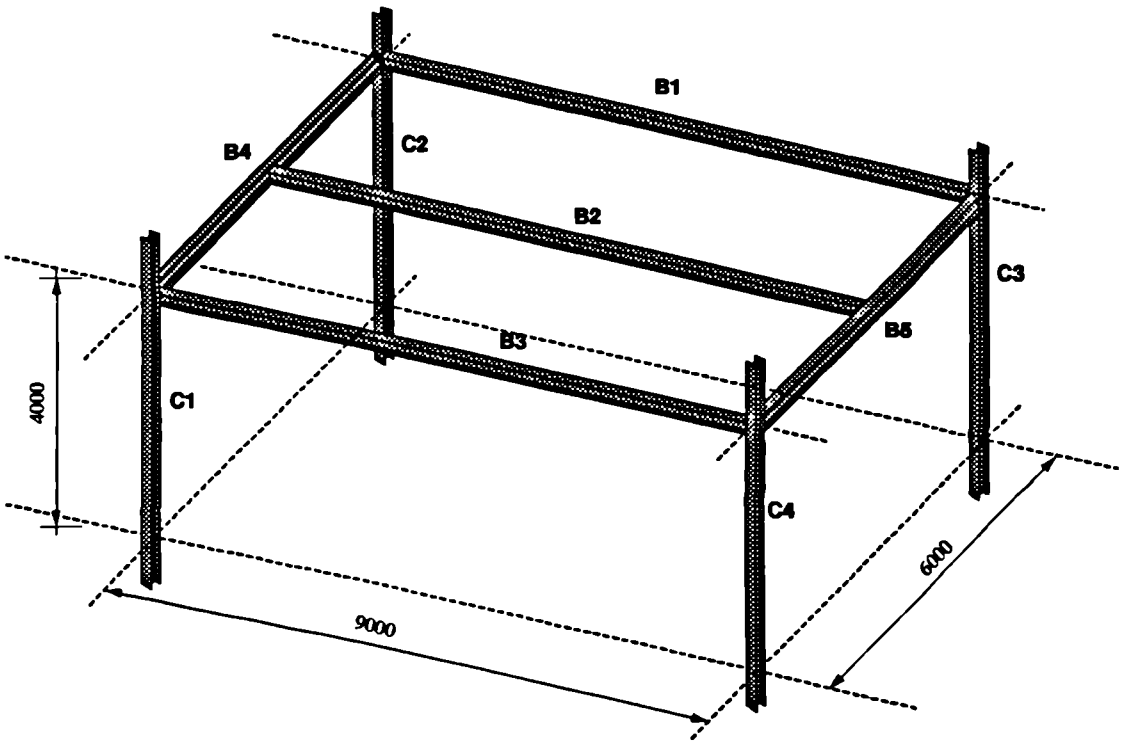


Figure 8.3 Location of beams and columns

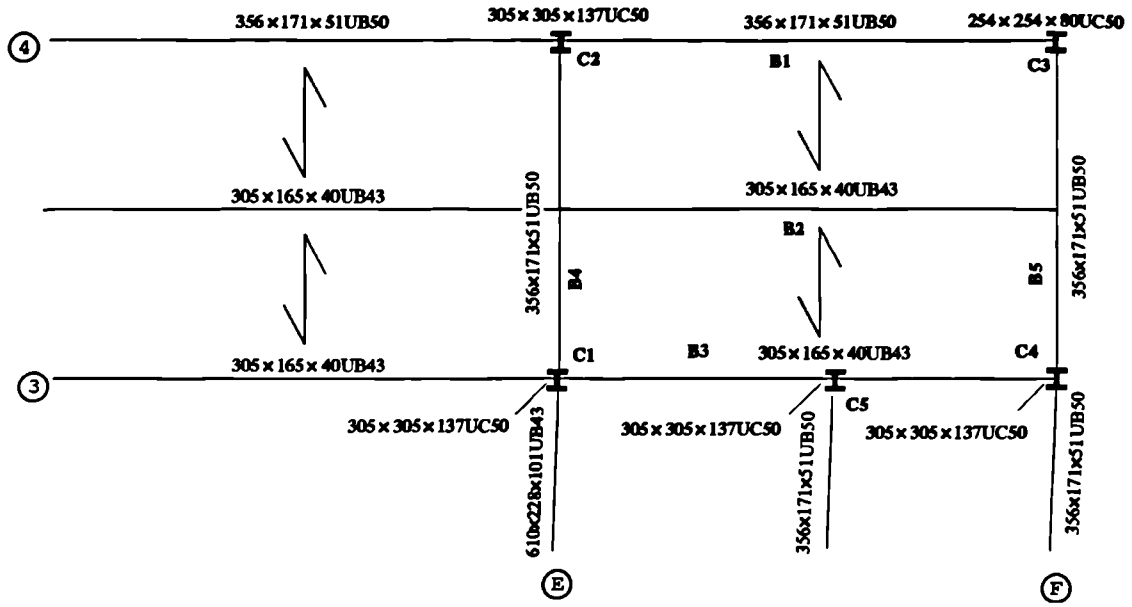


Figure 8.4 Plan of the corner compartment

8.1.1.2 Slab

The composite steel decked slab considered is of lightweight aggregate concrete with a density of 1900 kg/m^3, in strength class c25/30, with an overall thickness of 130 mm. The depth of concrete above the sheeting is 60 mm, as shown in Figure 8.5. The steel fabric supported on the top surface of the sheeting is 6 mm wire, spaced at a distance of 200 mm (A = 142 mm^2/m). The sheeting has a nominal thickness of 0.9 mm, with nominal width of 900 mm. The mean width of the trapezoidal troughs of the sheeting is 162 mm.

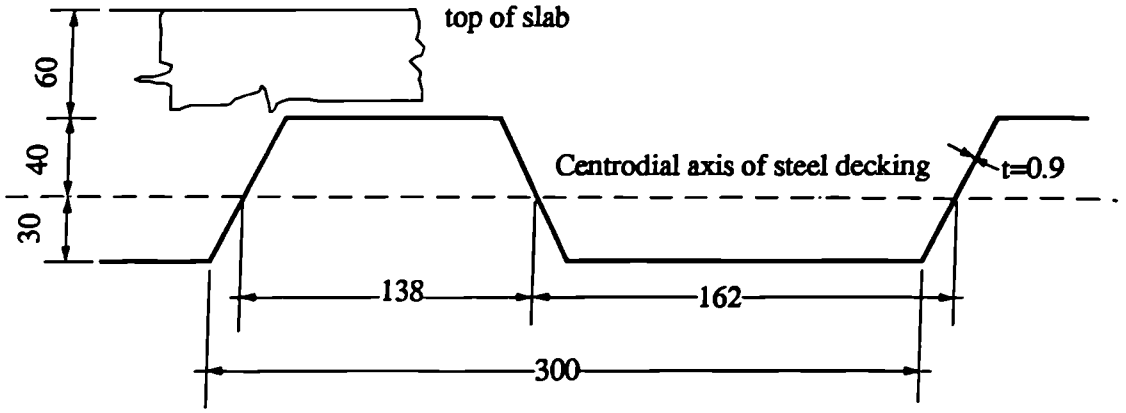


Figure 8.5 Cross section of the composite slab

8.1.2 Compartment Temperatures

8.1.2.1 Columns

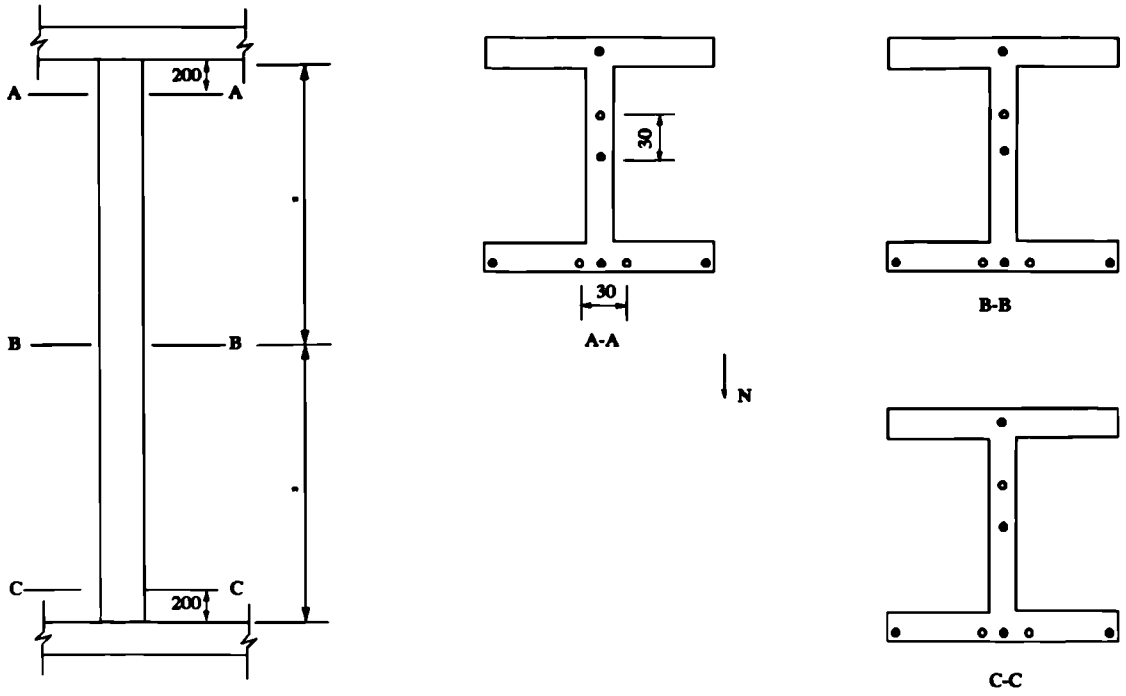
The columns in the compartment, protected to ensure structural integrity, were extensively instrumented. The locations of thermocouples on columns C1, C2, C3, C4 and C5 are illustrated in Figure 8.6(a)-8.6(d). The dots, both solid and hollow, indicate the positions of thermocouples at each cross-section. As the columns were protected, temperatures in the columns remained below 200°C for a large part of each member, with the highest temperature measured at the top of Column C2 in the flange, reaching 359°C, 120 minutes after the fire commenced.

8.1.2.2 Beams

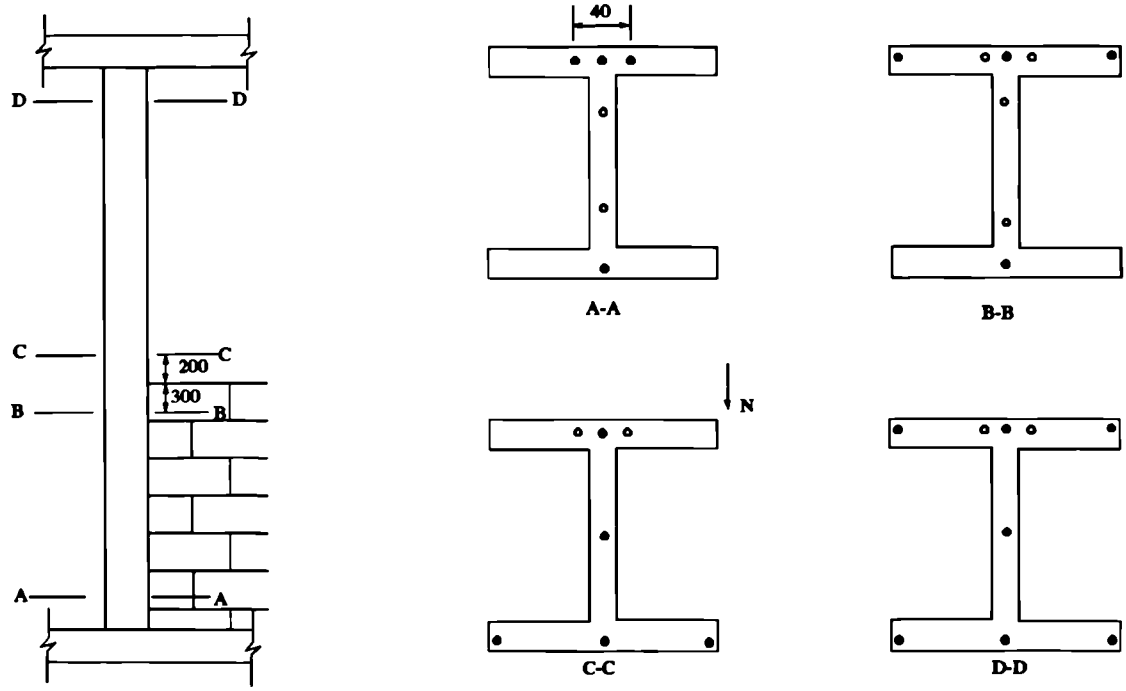
The locations of thermocouples on beams B1 and B2, are shown in Figure 8.7(a), where three sections along the length of the beams were instrumented. Figures 8.7(b) to 8.7(d) show the positions of thermocouples on beams B3, B4 and B5. Beams are the members heated the most in the compartment, with temperatures rising by up to 900°C. The average temperature in beam B2 was above 700°C.

8.1.2.3 Slab

The temperature through the depth of the concrete slab was monitored with a total of 22 thermocouples. The details of the locations of the cut-outs, and the instruments, can be found in the BRE test report (Lennon, 1995). The measured temperatures within the concrete were below 250°C, although the temperatures at the decking reached as high as 751°C.

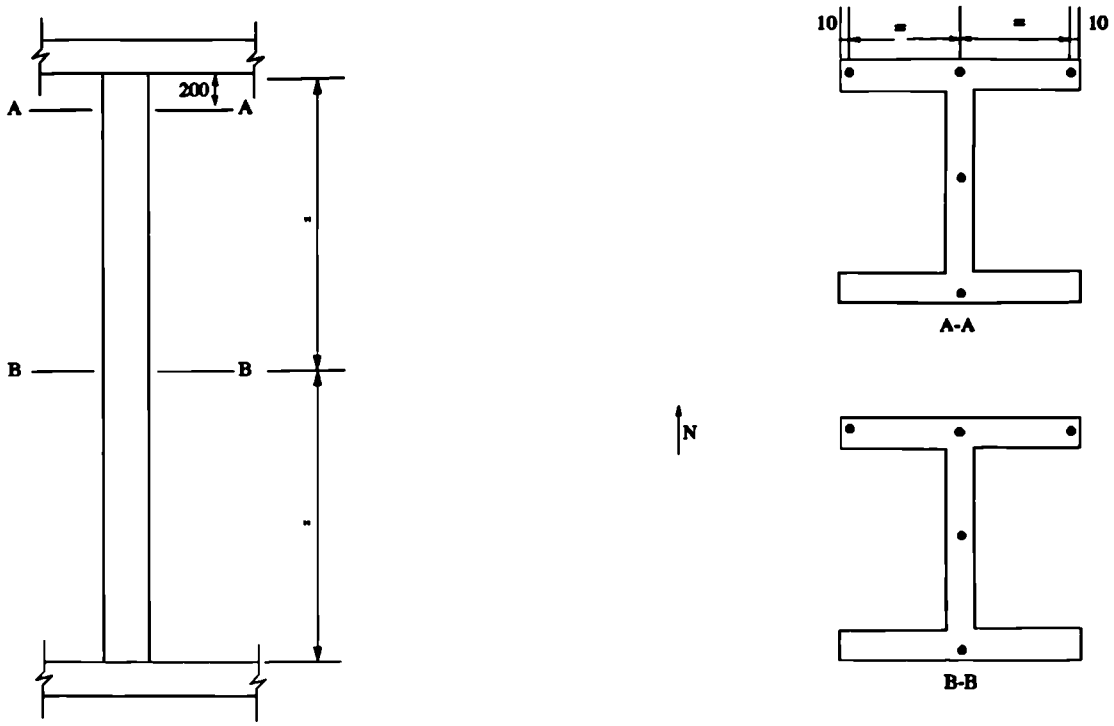


(a) Column C1

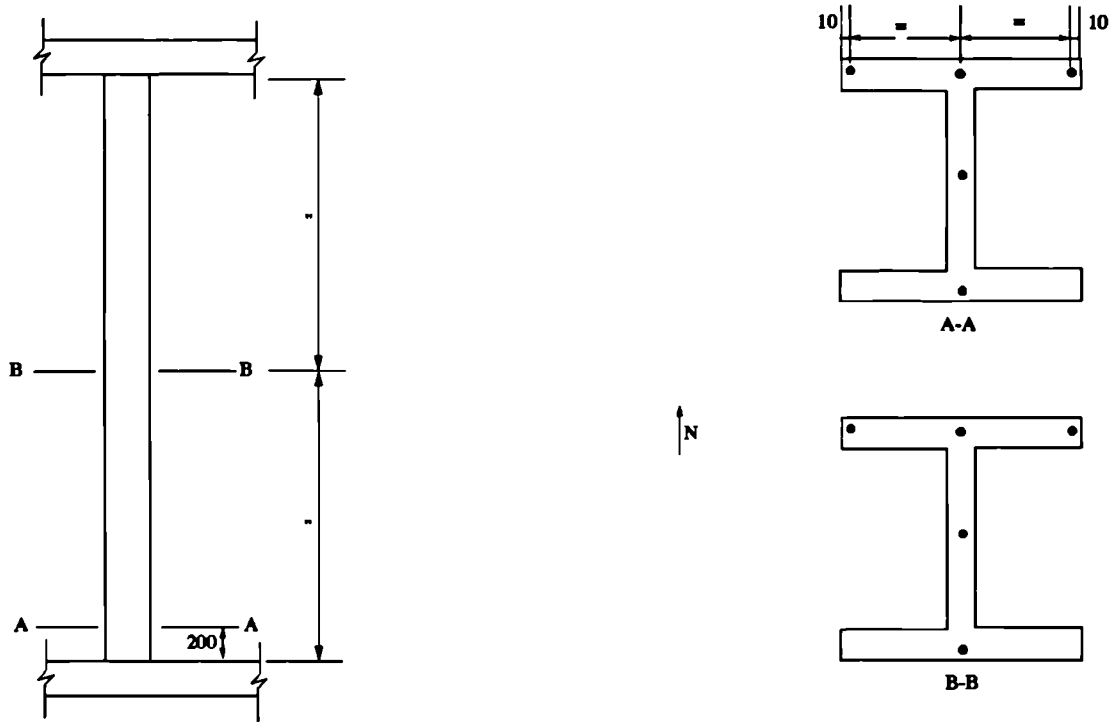


(b) Column C2 and C3

Figure 8.6 Locations of thermocouples on the compartment columns

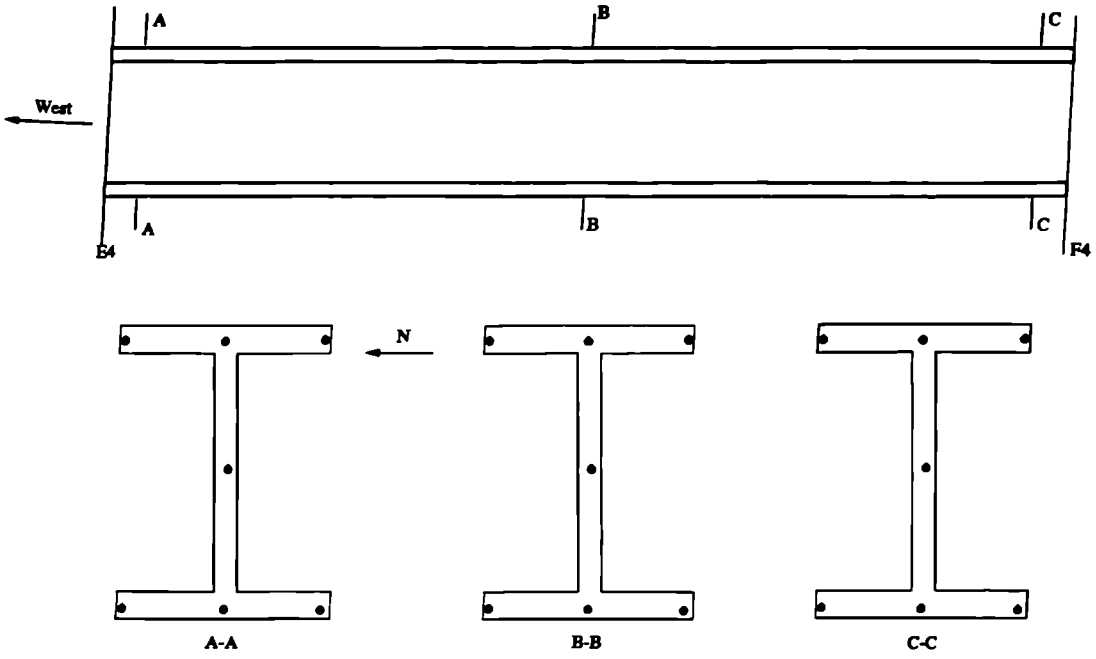


(c) Column C4

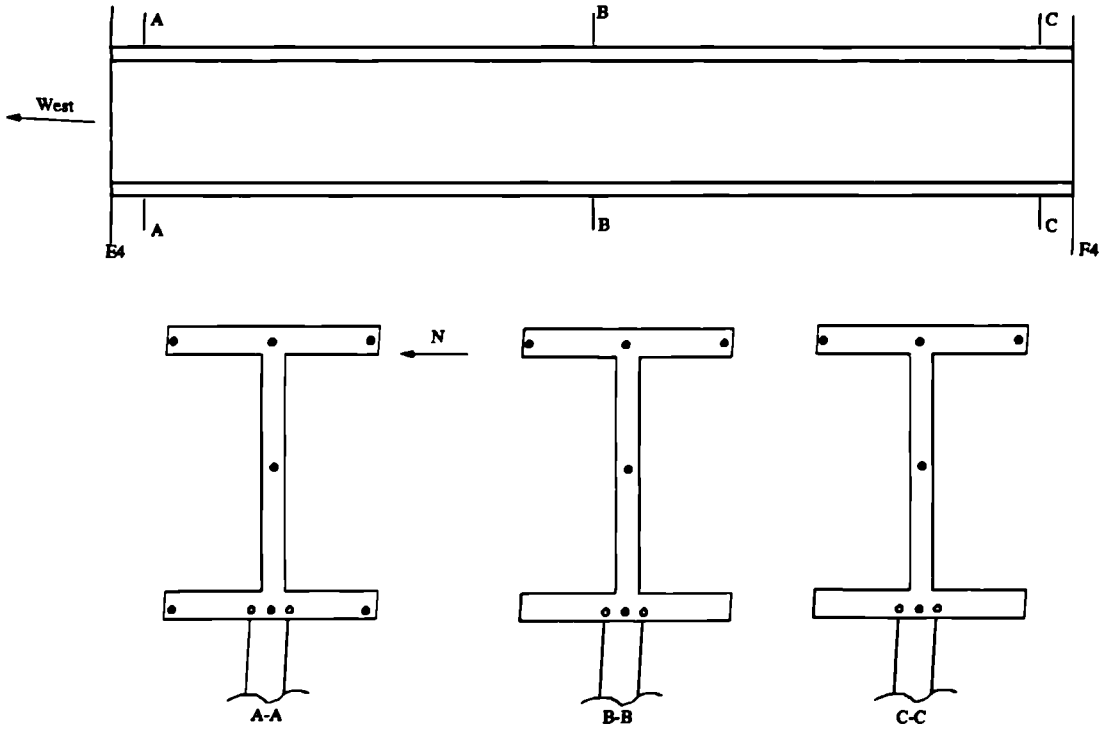


(d) Column C5

Figure 8.6 Locations of thermocouples on the compartment columns (continued)

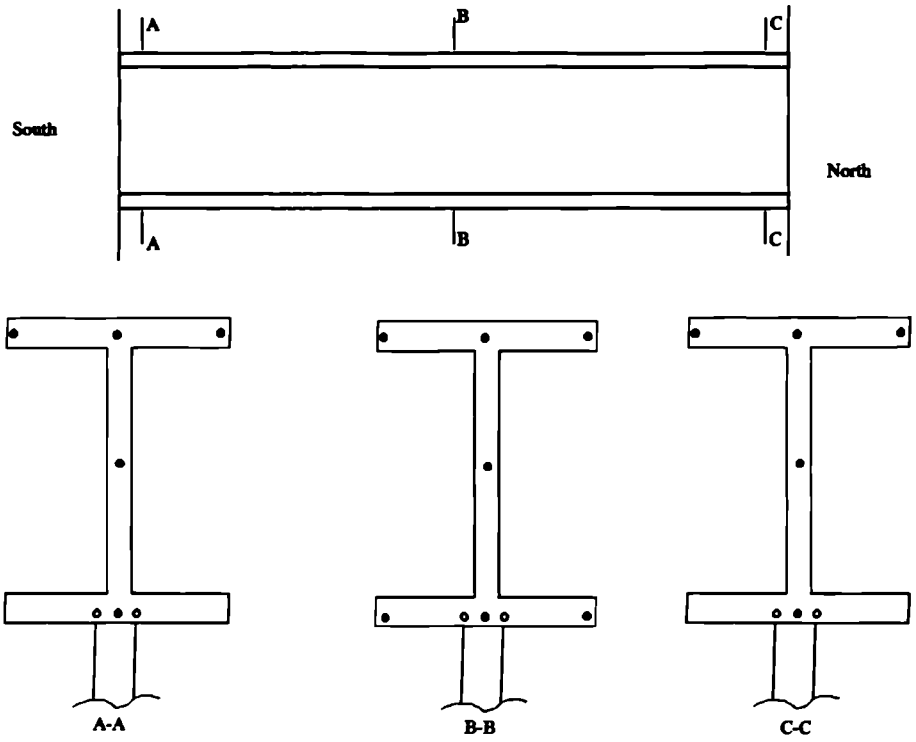


(a) Beams B1 and B2

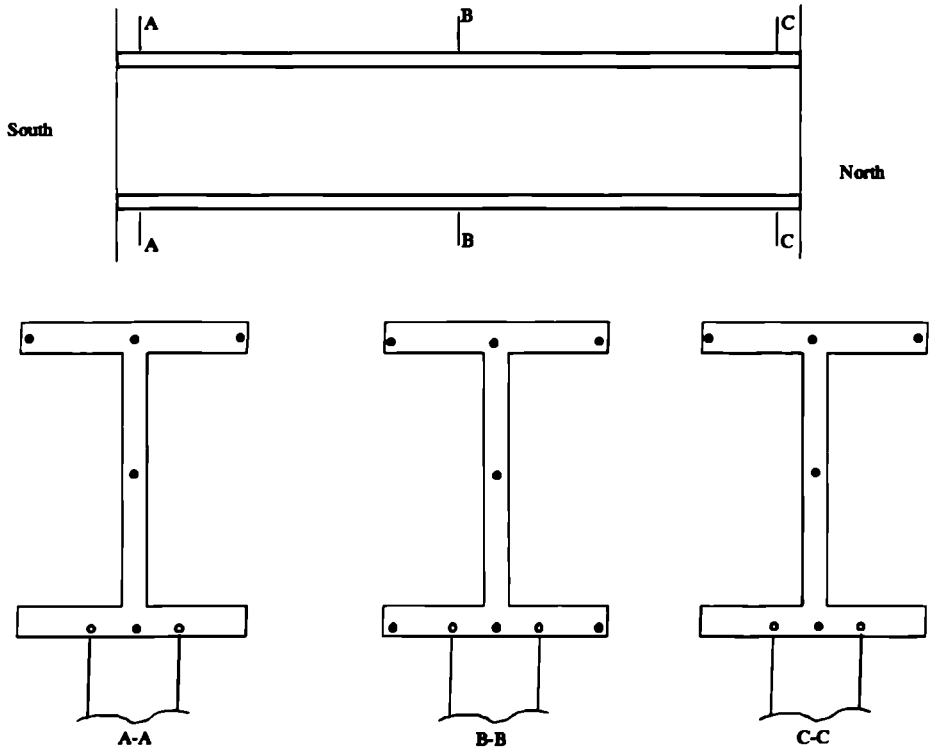


(b) Beam B3

Figure 8.7 Locations of thermocouples on the compartment beams



(c) Beam B4



(d) Beam B5

Figure 8.7 Locations of thermocouples on the compartment beams (continued)

8.1.3 Displacement Response

A total of 23 displacement transducers were used to monitor the deflection of the concrete slab. Their locations are shown in Figure 8.8. The largest deflections were observed at the middle of the slab, with a value of 269 mm occurring after 130 min.

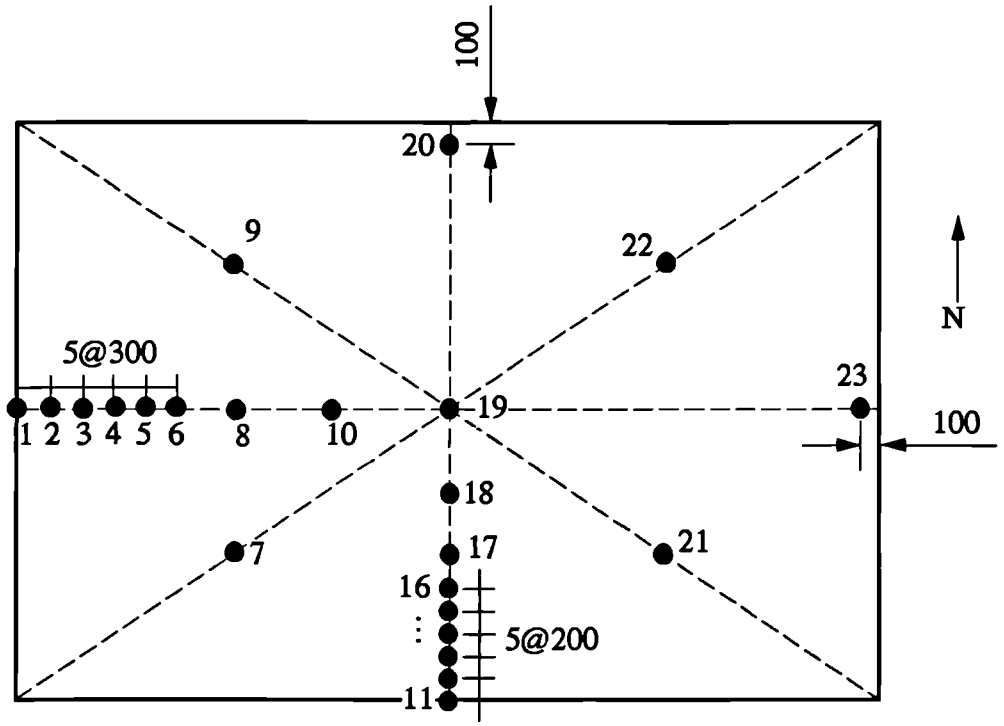


Figure 8.8 Locations of displacement transducers

8.2 MODELLING THE COMPARTMENT TEST

A skeletal steel frame of the tested 8 storey building is illustrated in Figure 8.9. It consists of over 1000 beams and 300 columns. To analyse the entire building would require not only a great deal of tedious data preparation, but also enormous computing time. Considering the fire is restricted to one compartment, and that the majority of the frame stays unheated, a 3D subframe, formed by extending the fire compartment by one adjacent bay and storey, is studied. In this section, the material properties used in the analysis are presented, followed by a description of the structural models analysed.

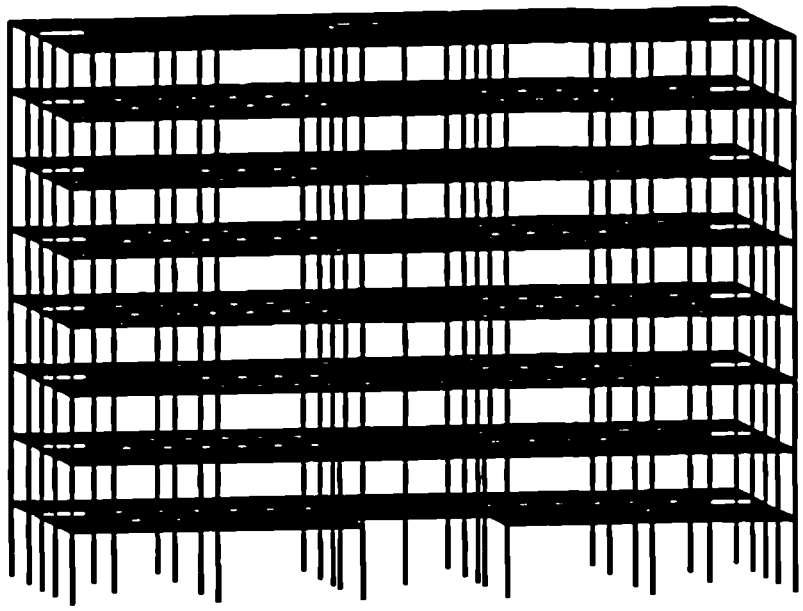


Figure 8.9 Steel frame of the Cardington building

8.2.1 Material Properties

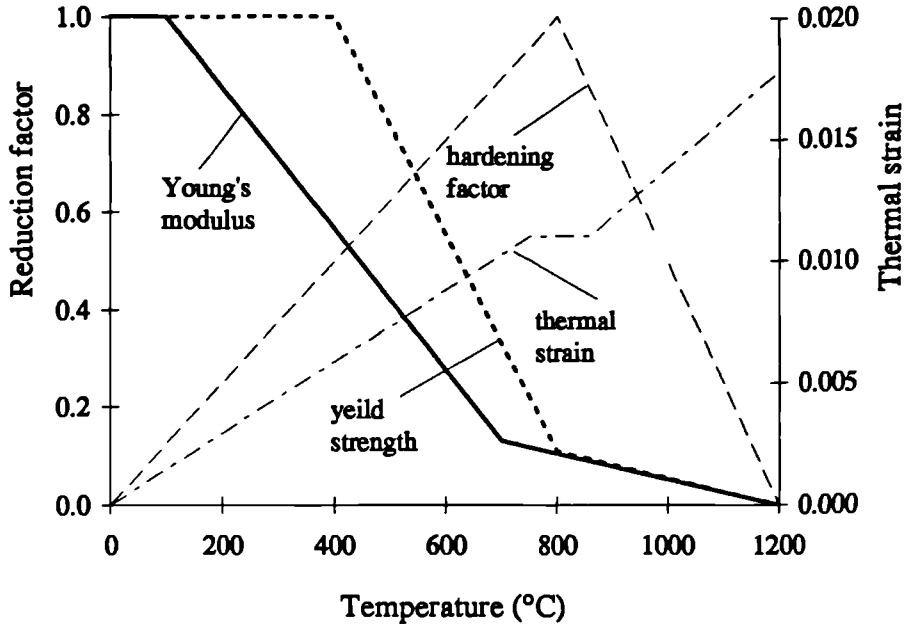
8.2.1.1 Steel

The Young's modulus of steel is taken as 210 GPa at room temperature. The following values of yield strength (Table 8.2) are used, as given in BS5950:

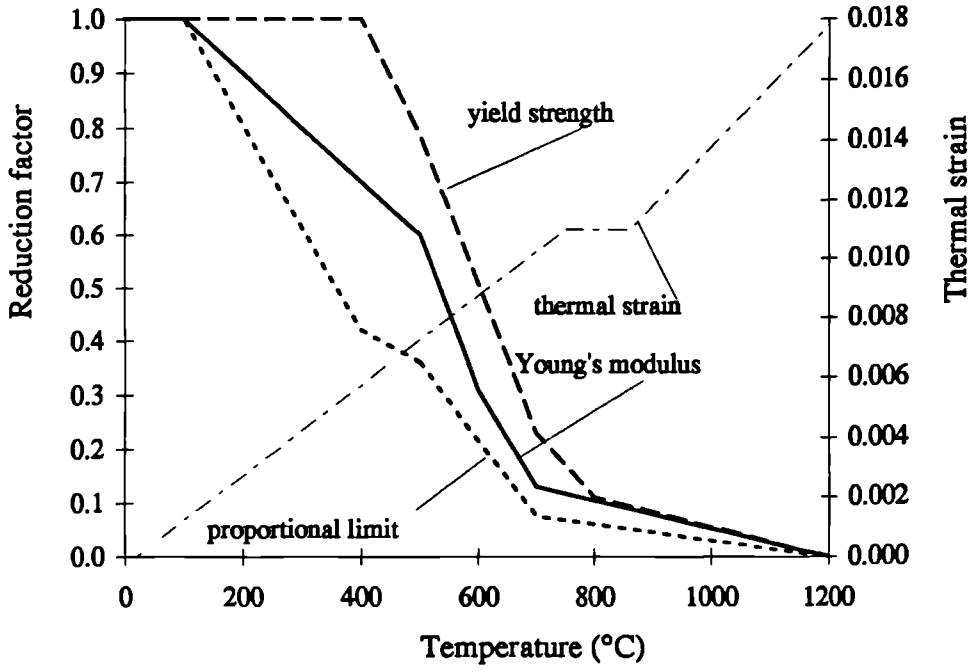
Table 8.2 Yield strength

BS4350 Grade	Thickness (mm) less than or equal to	Strength (N/mm^2)
43	16	275
50	16	355
	63	340

To model the steel properties at elevated temperatures, the bilinear and elliptical models (cf. Chapter 2) are employed in different analysis, with the reduction factors shown respectively in Figures 8.10 (a) and (b). These factors are chosen as a best fit to those given in Eurocode 3 part 1.2, as discussed in Chapter 2. The creep properties taken in the analysis are that for Carbon steel 1411, as given in Table 3.1.



(a) Reduction factors used in bilinear model



(b) Reduction factors used in elliptical model

Figure 8.10 Reduction factors for material properties at elevated temperatures

8.2.1.2 Concrete

The uniaxial concrete model developed by Madas (1993) is used for modelling nonlinearities in the composite beam representation of the composite slab. The elastic modulus of the concrete is taken as 20,000 MPa. The crushing strength f_c is taken as 25 MPa, with a crush strain ε_{∞} of 0.002. The tensile strength is ignored. Figure 8.11 illustrates the stress-strain relationship of the adopted uniaxial concrete model.

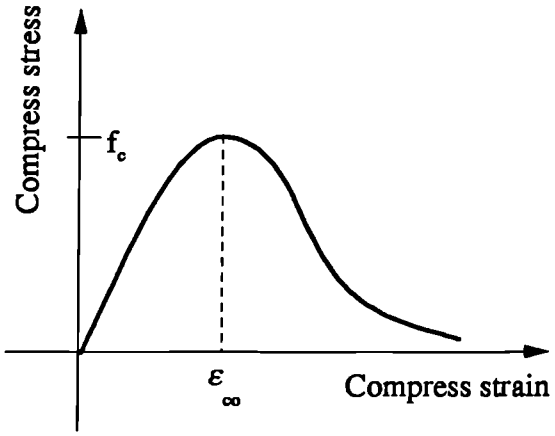


Figure 8.11 Concrete material model

8.2.2 Structural Model

8.2.2.1 Bare steel frame model

A bare steel subframe, including the compartment beams and columns, is considered first, with the beams in the adjacent span in both directions, as shown in Figure 8.12, illustrating in which the boundary conditions. To study the effect of the beams adjacent to the fire compartment, a model without the adjacent beams is also considered.

The loading, which will be further discussed in Section 8.2.4, is assumed to be taken directly by the secondary beams, as illustrated in Figure 8.12. Each of the beams is modelled by 12 elements.

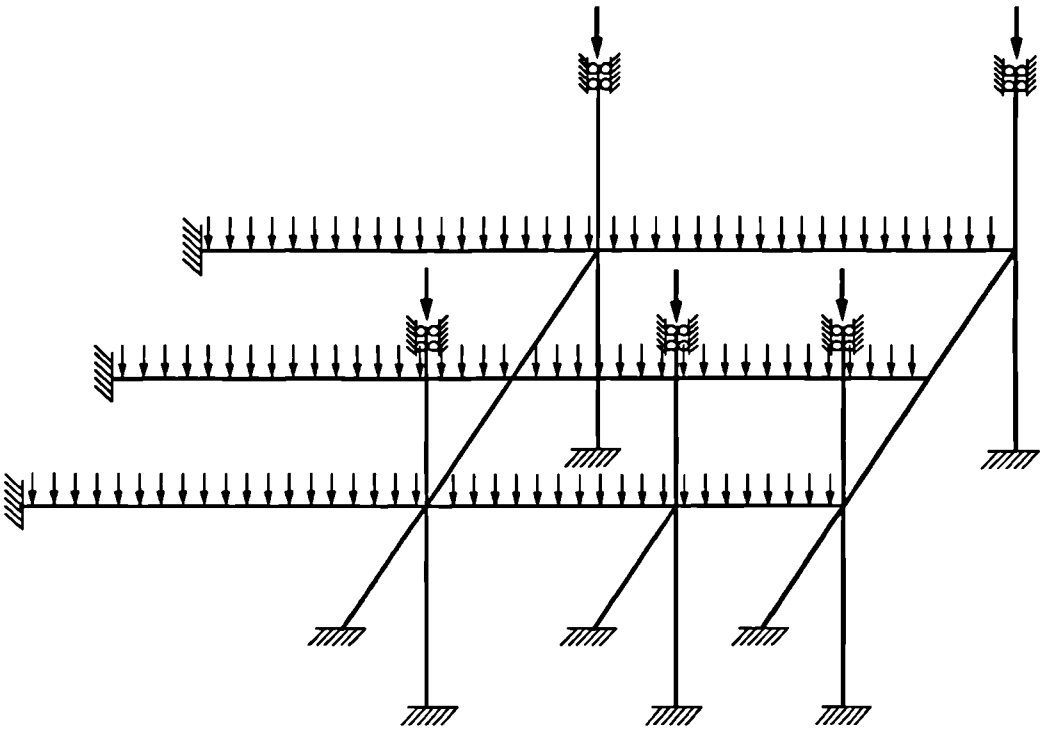


Figure 8.12 Bare steel frame model

8.2.2.2 *Steel frame with slab*

To simulate the effect of the composite floor, the slab is modelled with the developed slab formulation. The reinforcing steel mesh is modelled as a layer of steel, positioned 29 mm below the centre of the concrete slab, with a thickness of 0.142 mm in both longitudinal and transverse directions.

4 slab elements are used to model the compartment slab between grid lines E and F, and between 3 and 4. The extension between grid lines D and E is modelled by 2 slab elements, while extension in the other direction is modelled by one slab element. The slab element nodes were set 145.5 mm above the secondary steel beam nodes underneath, where rigid links are provided to enforce compatibility between the beam nodal displacements.

8.2.2.3 *Compartment slab represented by beams*

As the slab formulation is linear elastic, it could not accommodate the large displacement which occurred in the fire. Therefore, an alternative structural model is considered in which the composite slab in the fire compartment is represented by reinforced concrete beams with a T-section over the short span, and concrete beams

with a rectangular section acting compositely with the secondary beams, as illustrated in Figure 8.13. Figure 8.14 gives a 3D view of this structural model.

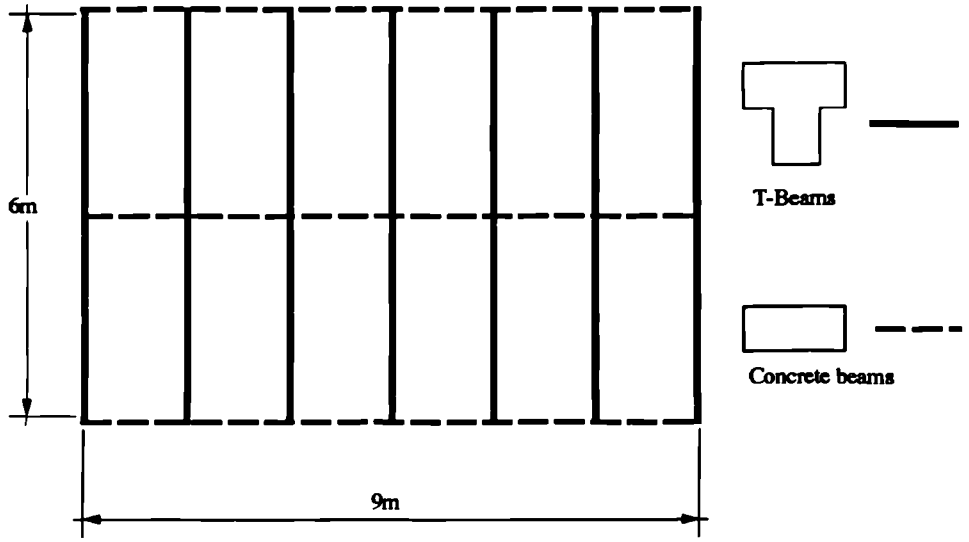


Figure 8.13 Beams representing slab effect in the fire compartment

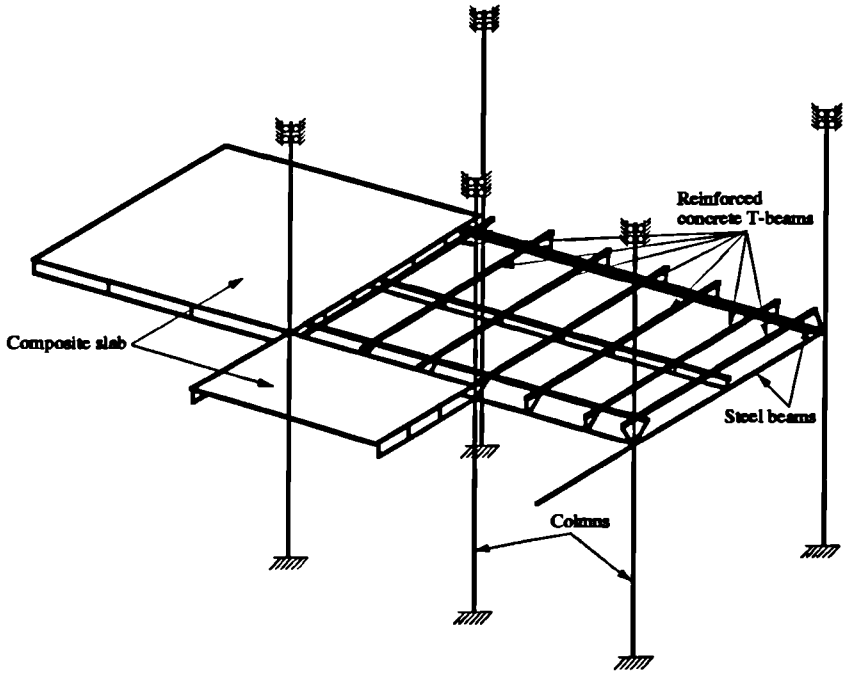


Figure 8.14 3D view of the fire compartment model

The sections of the beams are chosen so that they provide reasonable representation of the effect of the slab in the elastic range. Seven T beams are used in the short span. The cross-sectional dimensions of the T beams are given in Figure 8.15, where A_p is an

equivalent area of steel representing the deck. If Young's modulus of the steel is assumed to be 10 times that of the concrete, the elastic central axis of the T beam is 69.8 mm from its bottom fibre. Therefore, the reinforced concrete beams are placed 243 mm above the central line of the steel beams.

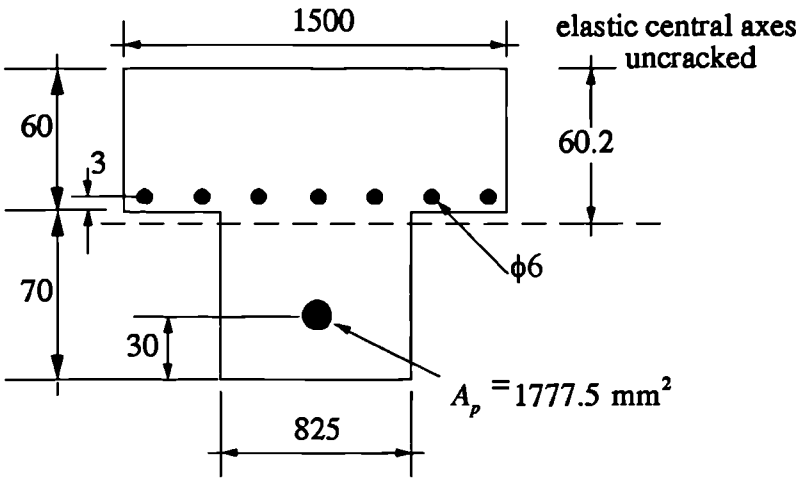


Figure 8.15 Cross-section of reinforced concrete T-beams

In the transverse direction, rectangular concrete beams are placed above the secondary steel beams to represent the composite action. These concrete beams are assumed to have a depth of 60 mm, which is the same depth of the concrete above the steel decking trough. The width of the cross-section is one of the parameters varied in the analysis. Two values of effective width are considered, equal to the full slab span and to half the slab span in the short direction, respectively.

8.2.3 Temperature Profile Used in Analysis

The structural members which are not in the fire compartment are assumed to remain at ambient temperature. The temperatures in the compartment beams, columns and the composite slab are discussed in the following sections.

8.2.3.1 Temperature along member length

For the purpose of analysis, it is assumed that along each structural member, beams and columns, the temperature-time history is known at three positions: the two ends and the mid span of the member. Assumptions are made accordingly, if temperatures were not recorded at any of these positions. For example, at columns C4 and C5, the temperature was measured at only two sections. The following assumptions are then made:

1) the temperature at the bottom section of column C4 is the same as that measured at the bottom section of column C5; and

2) the temperature at the top section of column C5 is the same as that measured at the top section of column C4, except that the temperature gradient along the flanges is assumed to be zero, as column C5 is not a middle of the partition.

The end sections, where thermocouples are located, are spaced from the actual joint with a nominal distance of 200 mm. As the steel has high thermal conductivity, the temperatures at the joints are assumed to be the same as measured by the nearest thermocouple.

8.2.3.2 Temperature over cross section

Constant temperature gradients are assured in the two orthogonal directions over a cross section. However, it is observed that at some cross sections, for example the mid-span section of Beam B5, the temperature gradients virtually have different signs along the top and bottom flanges. Therefore, from the measured temperatures, least-squares approximation (Gerald & Wheatley, 1992) is adopted in determining the centroidal temperature and the two temperature gradients over a cross section. This procedure is outlined as follows:

1) Choose representative temperatures from the thermocouple measurements over each cross section.

2) Let T_{mi} represent an experimental temperature, and let T_i be a value from the constant gradient equation:

$$T_i = T_0 + \frac{\partial T}{\partial y} y_i + \frac{\partial T}{\partial z} z_i \tag{8.1}$$

where T_0, $\partial T/\partial y$ and $\partial T/\partial z$ are the centroidal temperature, and the temperature gradients over the cross section, respectively.

Let $e_i = T_i - T_{mi}$, represent the error between the measured and assumed temperatures. The objective is then to determine the best values for T_0, $\partial T/\partial y$ and $\partial T/\partial z$ so that the sum of the squares of the errors is minimised; that is,

$$F(e) = \sum_{i=1}^{m} e_i^2$$
$$= \sum_{i=1}^{m} (T_0 + \frac{\partial T}{\partial y} y_i + \frac{\partial T}{\partial z} z_i - T_m)^2 \quad (8.2)$$

is to be minimised. At a minimum for $F(e)$, the three partial derivatives with respect to the three unknowns will be zero. Solving these three equations simultaneously gives the values for centroidal temperature and the two temperature gradients for each section at a given time.

The applied temperature profile is established by processing the measured temperatures using this method. In Figures 8.7 and 8.8, the locations where the temperatures have been used in this process are marked with solid dots while the hollow dots represent those which have not been used.

8.2.3.3 Temperature-time history

At each thermocouple, the temperature was recorded at 2 minute intervals. Examining the measured temperature-time history, it is noted that the temperature variation with time is nonlinear. However, to simplify the simulation, the temperature profiles were approximated for the purpose of analysis by piece-wise linear curves.

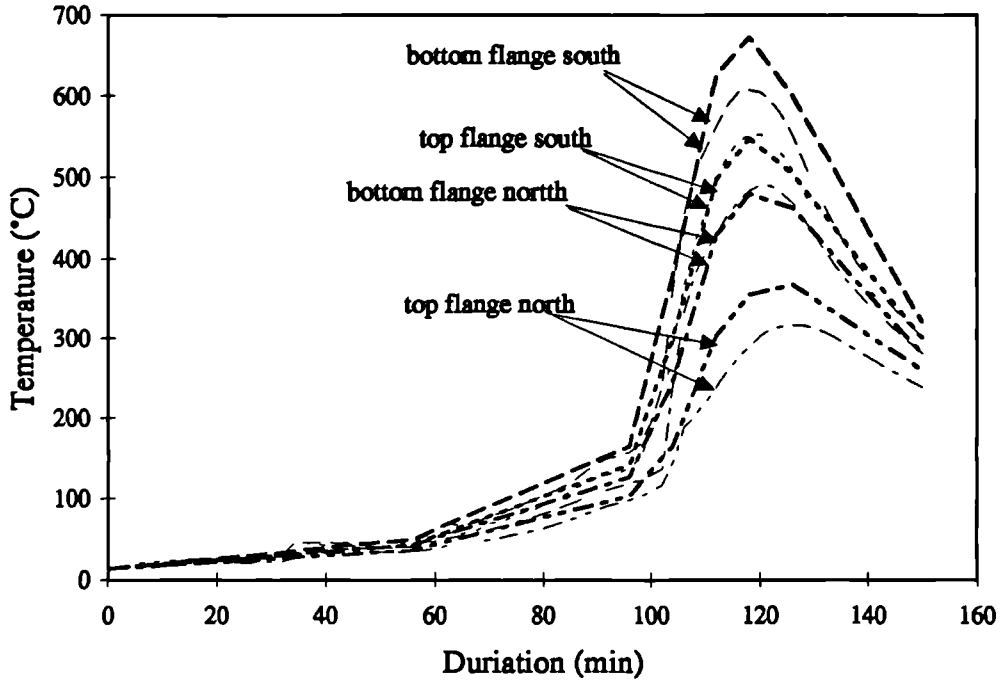
8.2.3.4 Temperature in slab

Since the measured temperatures are not as comprehensive as required for an accurate description of the slab temperature profile, great simplification is made in the representation of slab temperatures. As the change of the concrete properties with temperature is not currently modelled, the temperature variation in the concrete has been neglected, firstly because the nonlinear uniaxial model of concrete (Madas, 1993) does not account for elevated temperature, and secondly since the average temperatures in the concrete are low in comparison with steel at around 700°C. Elevated temperatures are considered, however, in the reinforcement mesh and steel decking, but the temperature distribution over the slab plane is assumed to be uniform.

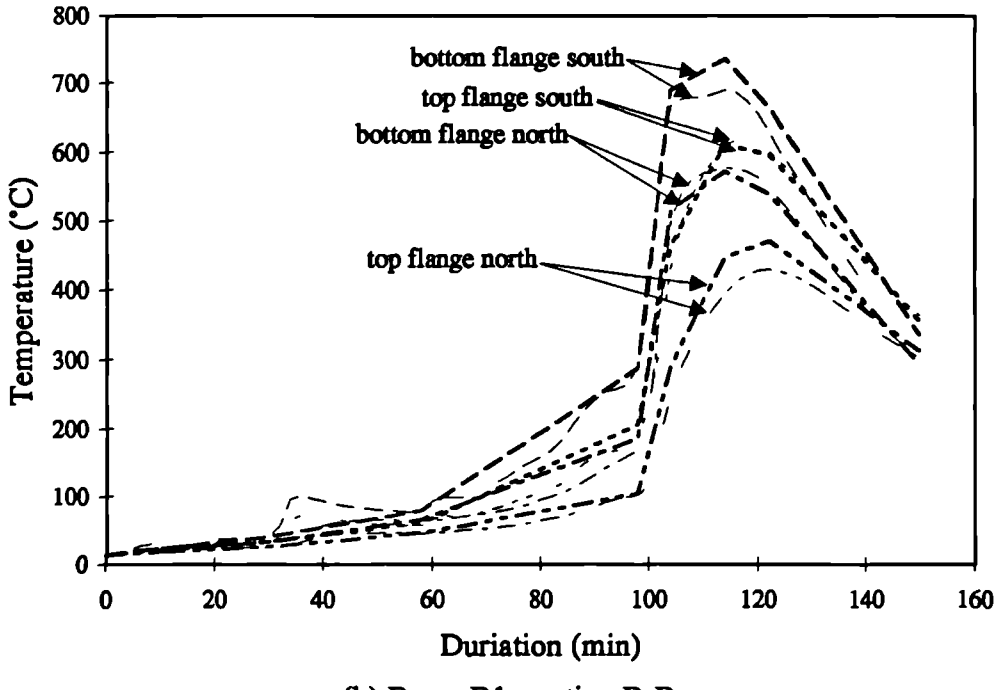
8.2.3.5 Comparison between applied and measured temperature

Beams in the compartment are the most heated members and are considered to have a significant effect on the overall structural behaviour. In Figure 8.16, the temperature

profiles used in the analysis are compared to the measured temperature for each of the four corners of the three cross sections of beams B1 and B2 (see Figure 8.7), where favourable comparisons can be observed.

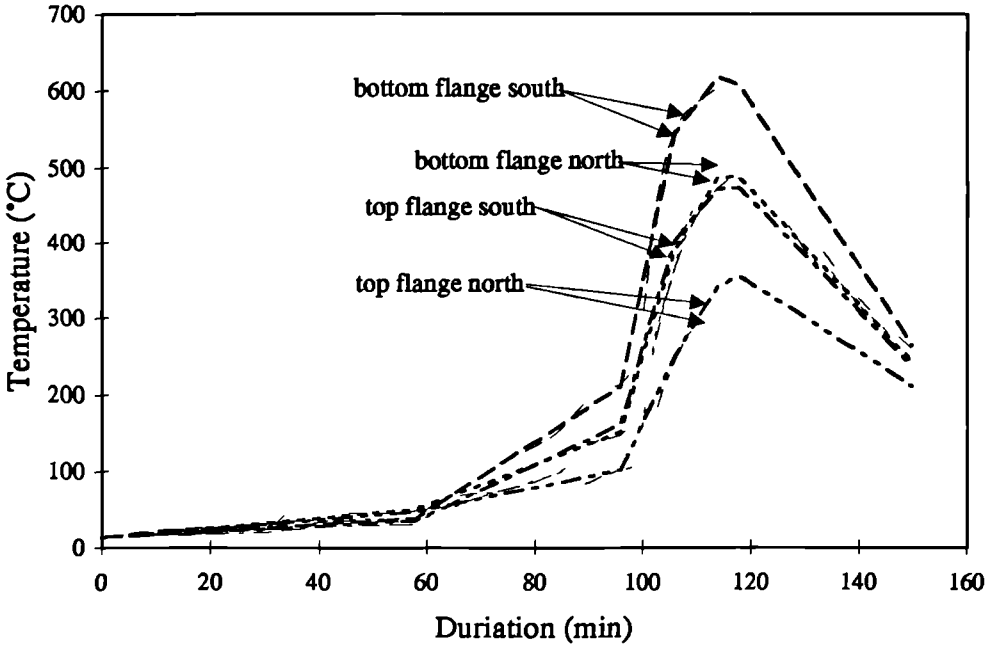


(a) Beam B1: section A-A

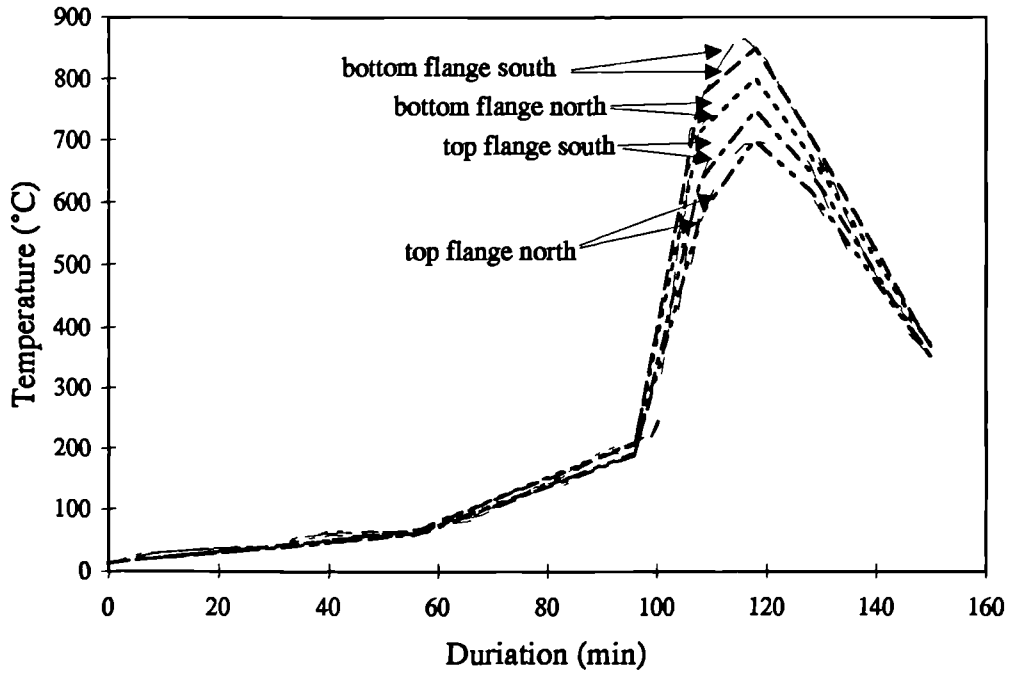


(b) Beam B1: section B-B

Figure 8.16 Comparison of measure and applied temperatures in beams B1 and B2

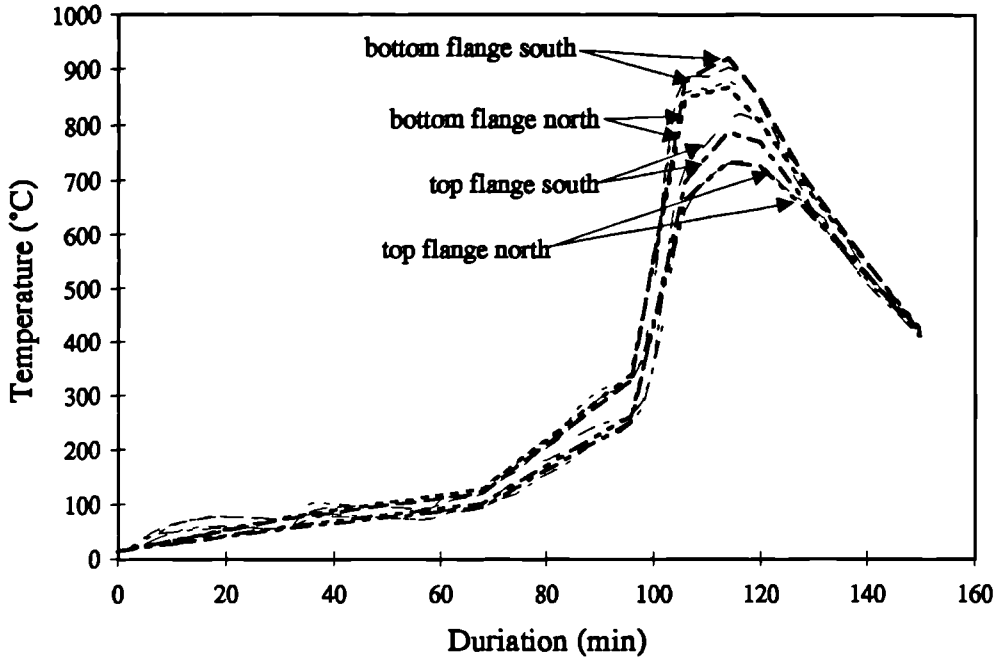


(c) Beam B1: section C-C

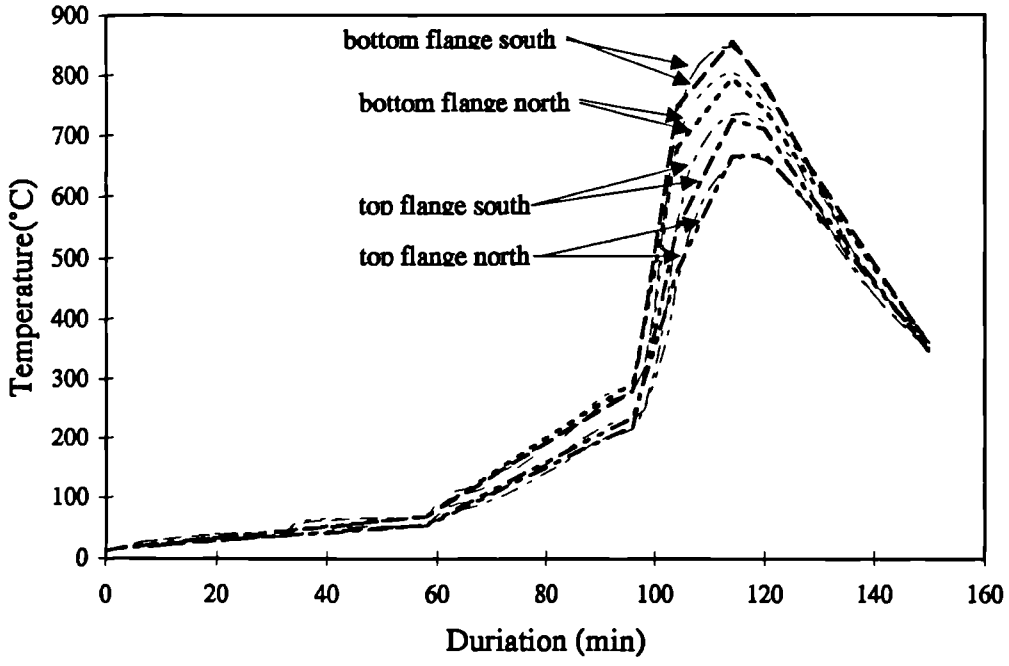


(d) Beam B2: section A-A

Figure 8.16 Comparison of measure and applied temperatures in beams B1 and B2 (continued)



(e) Beam B2: section B-B



(f) Beam B2: section C-C

Figure 8.16 Comparison of measured and applied temperatures in beams B1 and B2 (continued)

The measured and applied temperatures in the steel decking are compared in Figure 8.17.

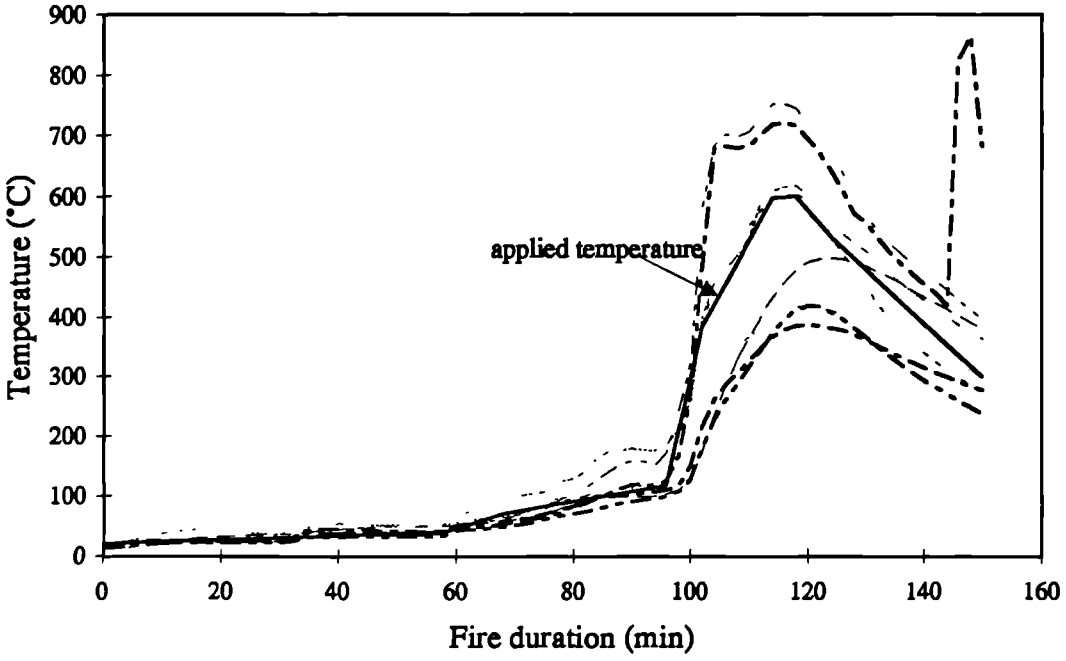


Figure 8.17 Comparison of applied and measured temperatures in steel decking

8.2.4 Loading

As well as the temperature loading, the design loads on the frame are considered in the analysis, as discussed below.

8.2.4.1 Distributed load on beam/slab

For a given fire and condition of steel work, the failure temperature will depend on the applied load. The design loads are given in Table 8.3. Specified in the Steel Construction Institute report (1995), it was the intention of BRE to supply a basic loading of a third of the design imposed load in addition to the full loads due to the raised floor, partitions, ceiling and services, as given in Table 8.4. The total of the supplied load and the floor dead load is 5.48 kN/m^2, which is the level of loading applied to the slab in the analysis.

Table 8.3 Design loads

Floor dead load		
	Slab weight	2.6
	Raised floor	0.4
	Services	0.25
	Ceiling	0.15
	Steel beam	0.25
	Total	3.65 kN/m^2
Floor live load		
	Imposed	2.5
	Partitions	1.0
	Total	3.5 kN/m^2

Table 8.4 Applied load in fire test

Floor dead load		
	Slab weight	2.6
	Steel beam	0.25
	Total	2.85 kN/m^2
Supplied basic load		
	Imposed	0.83
	Raised floor	0.4
	Services	0.25
	Ceiling	0.15
	Partitions	1.0
	Total	2.63 kN/m^2

Since the 9 m wide composite slab has a short span of 3 m, the distributed load is considered to transfer to the secondary beams by sharing equally the load on the slab area enclosed between the beams. This leads to a uniformly distributed load of 8.22 kN/m on beams B1 and B3, and 16.44 kN/m on beam B2.

8.2.4.2 Loads on columns

As the fire test was carried out on the 2nd floor, there are 5 loaded floors above the tested compartment. Assuming that columns C1 to C5 carry the load acting directly above the compartment, the load applied on the top of these five columns is determined as in Table 8.5.

Table 8.5 Applied load on the columns

Columns	C1	C2	C3	C4	C5
Load (kN)	684	760	281	191	400

8.3 CONDUCTED ANALYSES

8.3.1 Skeletal Steel Frame

The frame shown in Figure 8.12 is analysed by two quartic elements along each beam and column using the adaptive nonlinear analysis procedure. The bilinear material model is adopted in the analysis. At around 90 minutes after the start of the fire, the midspan vertical deflection of beam B2 becomes excessive, which indicates that the bare steel frame is not able to resist the applied load long before the temperature approaches its highest level. This structural model is designated as BS in the discussion of results.

8.3.2 Compartment Slab Represented by Beams

A series of studies are performed on the model, with the corner slab represented by reinforced T-beams in the span direction and rectangular concrete beams in the transverse direction, as described in Section 8.2.2.3. The slab outside the fire compartment is modelled by means of the developed slab formulation. Since the steel decking is represented by a steel reinforcement, positioned 30 mm above the bottom fibre of the T-beam, the temperature gradient over the cross-section is specified in such a way that the temperature at this reinforcement level has the appropriate temperature profile of the steel decking.

The parameters considered here are (1) the width of the rectangular concrete beams with either half span, FW1 or quarter span, FW2; (2) the temperature in the steel decking, FST; (3) the absence of the adjacent slab, FNS; and (4) the absence of the creep effect, FNC.

Since the span of the slab is 3 m, the concrete beams above the secondary steel beams B1 and B3 take a width of 1.5 m or 0.75 m, while the one above B2 takes a width of 3 m or 1.5m, respectively for analysis FW1 and FW2.

8.4 RESULTS

The mid-span deflections of beams B1 and B2 obtained from all the analyses conducted are shown over the fire duration in Figures 8.18(a)-(b).

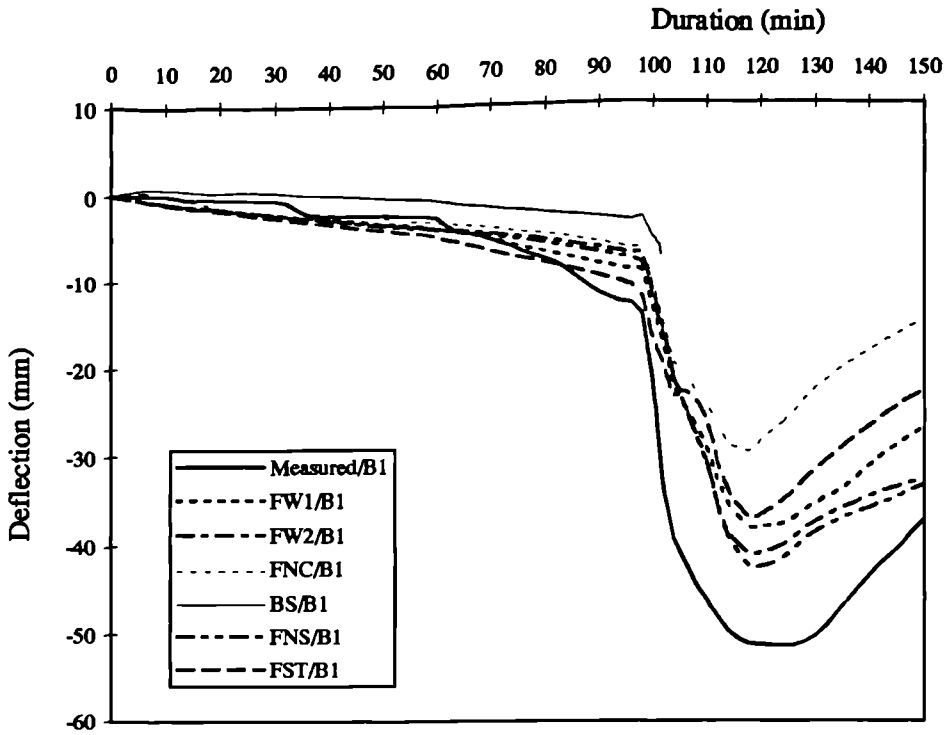
The simplest structural model analysed is the bare steel frame, which predicted premature failure at a fire duration of 102.2 minutes when the deflections became excessive.

The closest analysis prediction came from FW2, in which the maximum deflection of beam B2 went to 270.35 mm at 118.3 minutes of fire duration, comparing well with the measured deflection of 269.4 mm at 130 minutes. However, between 70 and 96 minutes, the variation of the measured deflection was greater than that from the analysis. Several facts can be responsible for this discrepancy. Firstly, the measured temperature profile in the compartment slab was inadequate, hence a uniformly distributed temperature was assumed in the analysis over the plane of the slab and the temperatures in the concrete were ignored. Secondly, the connections in the fire compartment were unprotected during the fire test. It is believed that connections are affected by the fire condition and this could influence the overall behaviour of the test structure.

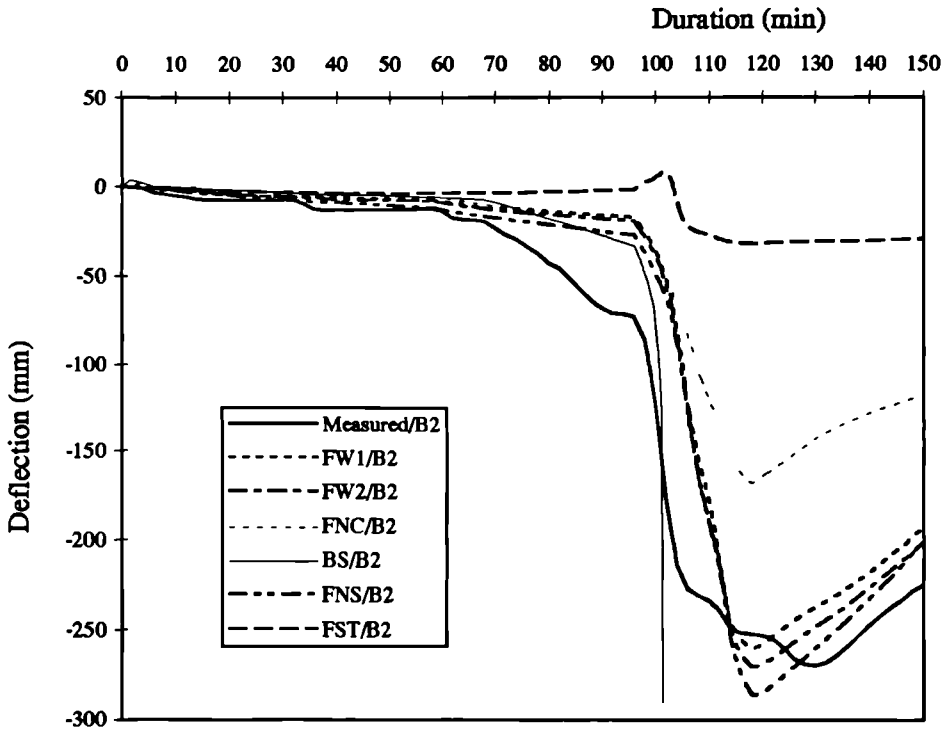
Examining the result of analysis FNC, it is noted that when the creep effect is excluded from the analysis, the maximum deflection of beam B2 becomes 167.4 mm at 118.2 minutes of fire duration. Comparing analyses FW2 and FNC, it is established that the creep effect is considerable for structures under fire condition, which claims 38% of the total deflection for this particular case.

The difference between FW2 and FNS, in which the slab in the adjacent compartment is not considered, shows that the contribution from the adjacent slab to the structural integrity is of some importance. Moreover, the contribution of the composite slab to the bending stiffness of the secondary beam is shown to be moderately important, as evidenced by the result from analysis FW1, in which the effective width of the concrete beams was assumed to be half the span.

It is worth noting that the deterioration of the steel decking stiffness and strength has a great effect on the structural behaviour at elevated temperatures. This can be seen from analyses FST, in which the temperature variation in the steel decking was not taken



(a) Deflection of beam B1



(b) Deflection of beam B2

Figure 8.18 Verification against BRE full-scale corner compartment fire test

into account, and consequently, only small displacements were predicated for beams B1 and B2. Interestingly, the deflection of the internal beam from FST has a different trend from the measured curve at approximately 90 to 100 minutes of fire exposure. During this period of time, both the temperature and temperature gradient over the cross section of beam B2 increase in value, with the beam experiencing dramatic loss of strength and stiffness. As the temperature difference at the top and bottom of the beam flange becomes great, a bowing effect is introduced, which is responsible for the hogging of the beam.

8.5 CONCLUSIONS

The developed analysis tool for the behaviour of structural steel frameworks under elevated temperatures is validated against the results of the fire test undertaken by the BRE in corner compartment of the full-scale building at Cardington. The favourable comparison between the analysis prediction and the test results demonstrates that the behaviour of a real multi-storey steel framed building under a natural fire can be simulated by the proposed analytical approach. From the verification and parametric studies carried out, the following conclusions can be drawn:

1) The bare steel frame analysis prediction of a complete collapse of the internal beam, after 102 minutes of fire exposure, shows that the load bearing member will fail if its load-carring capacity is reduced by fire to such an extent that it cannot sustain the applied loading.

2) The difference between the response of the bare steel model and the other models including slab emphasises the importance of accounting for the role of the composite slab in maintaining structural integrity under fire.

3) Modelling the deterioration of the material properties at elevated temperature is important for an adequate representation of the structural behaviour. Moreover, the influence of the creep effect in steel at elevated temperatures is found to be significant.

4) The applicability of using subframes to predict the behaviour of structures in fire is established by achieving a favourable comparison between the measured displacements in the full-scale test and those obtained from a subframe analysis. Considering the enormous effort required to analyse the fire response of a

complete frame, it is important to use the minimum representative model wherever possible.

5) Using reinforced concrete beams and orthogonal concrete beams appears to represent the nonlinear behaviour of the composite slab under fire conditions with reasonable accuracy. It should be emphasised that appropriate consideration must be given to the effect of the deterioration in the response of the steel decking at elevated temperatures, the cracking and crushing of concrete, as well as the effect of large displacements. However, the inability of such a model to reflect the in-plane stiffness of a composite slab results in a situation where the predicted response is less stiff than the true behaviour. This highlights the necessity of developing a more advanced slab formulation which accounts for both material and geometric nonlinearities.

CHAPTER 9
PARAMETRIC STUDY ON STRUCTURES UNDER FIRE AND EXPLOSION

The analytical tools developed in this work were calibrated in the previous chapter, against available experimental results. Other examples were provided to demonstrate both the efficiency and accuracy of the integrated adaptive analysis method. One of the advantages of the analytical method lies in its versatility in parametric study. In this chapter, the advanced analysis tool is applied to carry out a parametric study on the response of steel structures to the successive actions of explosion followed by fire.

The investigation focuses on the effect of blast on the fire resistance of steel structures. The study is first carried out on an axially loaded column subjected to a blast loading followed by a fire. The column is considered under different values of axial force, overpressure from explosion and temperature distribution due to fire. The parametric study shows that the effect of blast on the fire resistance of a steel column can be significant. Interestingly, this effect could sometimes be beneficial, although, in the majority of cases, the explosion reduces the fire resistance of the column.

A plane steel frame representing a typical 8 storey office block is examined. In this frame, the effect of different blast locations is examined. It is found that blast indeed reduces the fire resistance of the steel structure and this effect varies with the location of the blast even for the same blast loading.

9.1 COLUMN UNDER BLAST AND FIRE

Columns are important load bearing members in a building structure. The column under consideration is illustrated in Figure 9.1. The column has a designated universal column section 254x254UC89. Two lengths are considered: 3m and 5.2 m. The load carrying capacity of the column can be approximated as the lesser of the plastic squash load or the elastic buckling load at elevated temperatures. Therefore, the failure of long columns is governed by elastic buckling, while short columns are governed by plasticity. Medium length columns buckle inelastically. At elevated temperatures, both of the plastic squash load and the elastic buckling of a column reduce, as a result of the deterioration the strength and Young's modulus. However, the Young's modulus and the strength of a material do not vary in the same manner with temperature. Hence, failure mode is not only dependent on temperature, but also on temperature-time

history. This is further complicated by the presence of the initial imperfection and residual stress and strain produced by a blast loading.

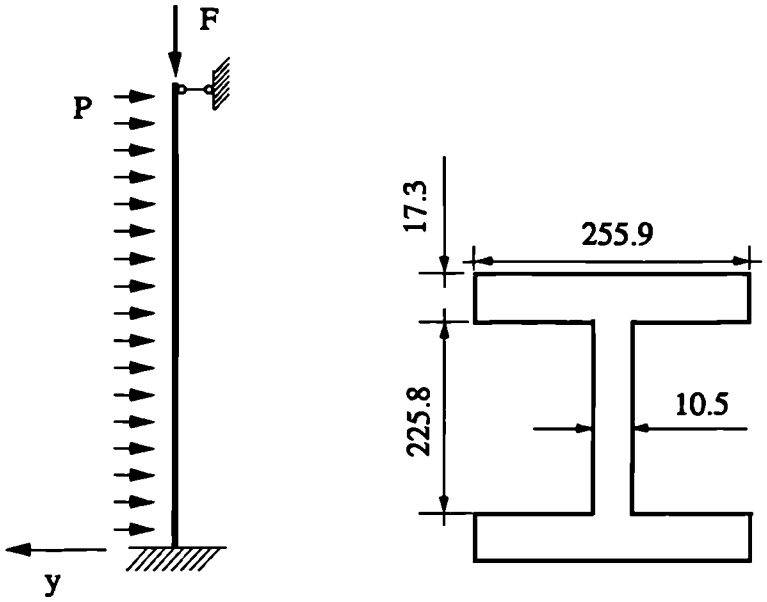


Figure 9.1 Column under blast and fire loading

9.1.1 Material Properties

The combined rate-sensitive and thermal material model, described in Chapter 5, is used. At ambient temperature, Young's modulus is taken as 205 GPa, and the yield stress is taken as 275 MPa. The column is considered as strain-rate sensitive under blast loading. The parameters for the rate sensitive model are taken as S=31.19 MPa, $\dot{\varepsilon}_* = 4.65\times10^{-3}$ sec^{-1}, and it is assumed that the strain-rate effect ceases 5 seconds after the explosion. The reduction factors for the material properties at elevated temperatures, as well as the thermal strain, are givenin Table 9.1.

Table 9.1 Reduction factors and thermal strains at elevated temperatures

	Young's modulus			Yield strength			Strain hardening factor			Thermal strain		
T(°C)	100	700	1200	400	800	1200	400	600	1200	750	860	1200
R	1.0	0.13	0.0	1.0	0.11	0.0	0.0	0.02	0.0	0.011	0.011	0.0178

9.1.2 Loading

An axial force F is applied at the top of the column as an initial load. The blast loading, represented by a uniformly distributed load, is applied on the left side of the column about its major axis, as shown in Figure 9.1. The variation of the blast overpressure with time is shown in a normalised form in Figure 9.2, which is a typical pressure time history for a gas-air mixture in a vented confined explosion (Harris, 1983; Smith & Hetherington, 1994). The load factor λ_P is used to scale the applied overpressure P, with λ_P=1 corresponding to the 154.5 kN/m.

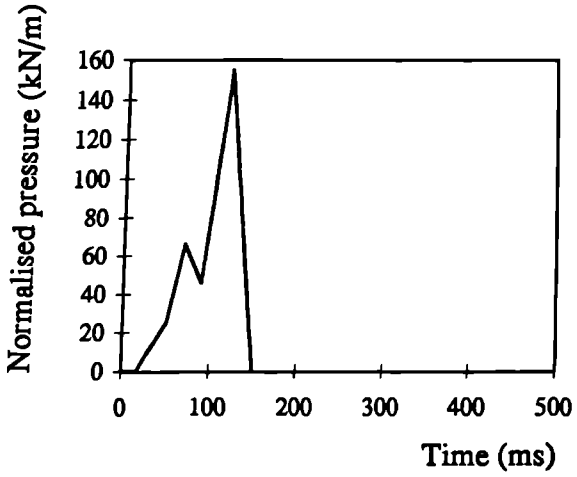


Figure 9.2 Pressure variation for a typical internal gas explosion (Smith & Hetherington, 1994)

9.1.3 Parameteric Study

The parameters varied in this study are a) the axial load factor $\lambda_F = F/F_c$, where F_c=3.1×10^3 kN is the plastic axial capacity of the column at ambient temperature, b) the blast load factor λ_P, and c) the temperature gradient over the column depth.

Two axial load factors λ_F are considered: 0.3 and 0.68. The temperature distribution is considered to be i) uniformly distributed through the cross section and along the length, ii) uniformly distributed along the length but with a temperature gradient of 1.1T °C/m through the cross section, in which T is the centroidal temperature, or iii) uniformly distributed along the length with a temperature gradient of -1.1T °C/m through the cross section. In the second case, the temperature in the left flange is higher. Since the temperature gradient through the cross section would cause bowing in the member, it is of interest to examine if this effect would be beneficial or detrimental to the column's

fire resistance. For each of the above cases, different blast loading factors are considered.

9.1.4 Results

In Figures 9.3 and 9.4, the change in the fire resistance of the 5.2m long column is shown against the blast load factor λ_p for axial load factors λ_F of 0.68 and 0.3, respectively. As mentioned before, the cause of the failure of the column is its instability. The change in the fire resistance is determined by the change in the limit temperature.

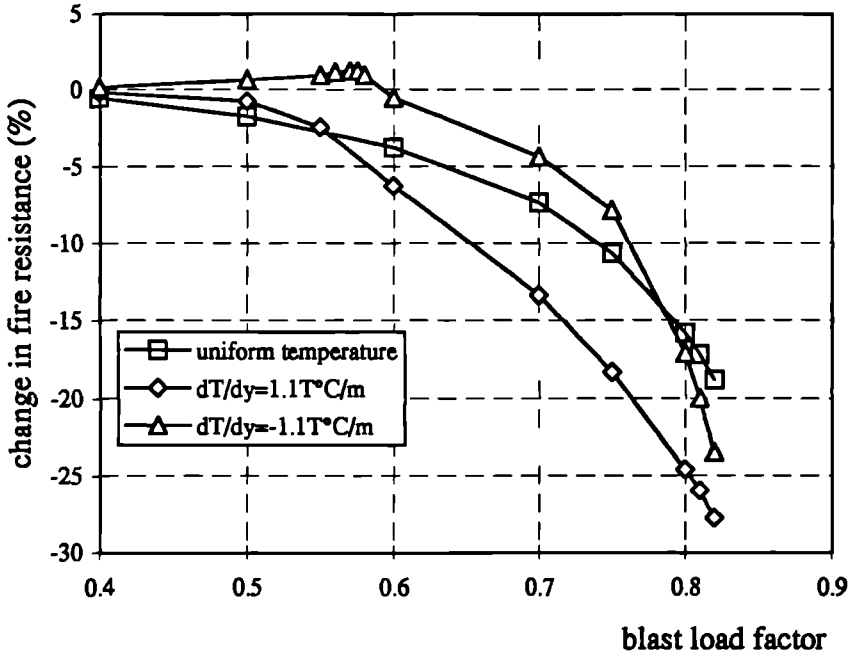


Figure 9.3 Column (5.2 m) with $\lambda_F = 0.68$

For $\lambda_F = 0.68$, the blast load factor shown in Figure 9.3 ranges from 0.4 to 0.85. When it is less than 0.4 it was found that blast has no noticeable effect on the fire resistance of the column, whereas if the blast load factor is greater than 0.85, the deformation of the column directly after the blast would be considerable. In general, sufficiently large blast loading can reduce the fire resistance of the column, with the reduction registering up to 27% for the column considered here. It is worth noting that a blast loading in the range of $0.5<\lambda_F<0.72$ has a beneficial effect on the fire resistance for the negative temperature gradient case, although the advantage is not very significant here.

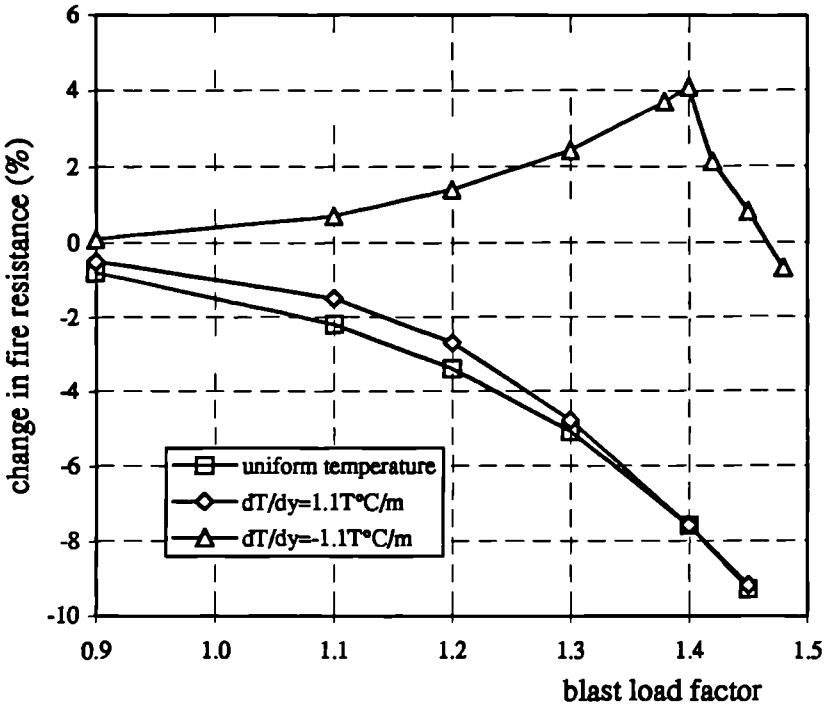


Figure 9.4 Column (5.2 m) with $\lambda_F = 0.3$

For $\lambda_F = 0.3$, the blast load factor λ_p is varied between 0.9 and 1.45. When λ_p is less than 0.9, the effect of the blast on the fire resistance is not significant. Figure 9.4 shows that for the cases of uniform temperature distribution, or higher temperature on the flange directly facing the blast pressure, the fire resistance of the column is reduced by up to 9.5%. Interestingly, if the flange facing the blast has a lower temperature than the other flange, the blast can enhance the fire resistance of the column by a maximum of 4% for this particular case.

This enhancing of the fire resistance is attributed to the shifting of the neutral axis. The buckling direction with blast is to the right. With an increasing temperature gradient, Young's Modulus has an uneven value over the cross section. As the left side of the column is cooler, the Young's modulus is greater to the left. Hence, the bending neutral axis moves gradually to the left. This reduces the eccentricity of the axial loading relative to the bending neutral axis, and results in a higher buckling load. However, if the blast is sufficiently great, plasticity occurs within a large part of the column facing the blast. The shifting of the neutral axis does not dominate the buckling mode. This is further confirmed by the similar observation made for the 3 m column.

The change in fire resistance of the 3 m long column is given in Figures 9.5 and 9.6. The

blast load factor λ_p is varied between 1.4 and 3.4 for $\lambda_F = 0.68$, and between 3.9 and 5.5 for $\lambda_F = 0.3$. When λ_p is less than 0.9 in the case of $\lambda_F = 0.68$, and 3.9 for the case of $\lambda_F = 0.3$, the effect of the blast on the fire resistance is not significant. Again, figures 9.5 and 9.6 show that for the cases of uniform temperature distribution, or higher temperature on the flange directly facing the blast pressure, the fire resistance of the column is reduced. For the case of negative temperature gradients, the blast enhances the fire resistance of the column by 5% for this particular case.

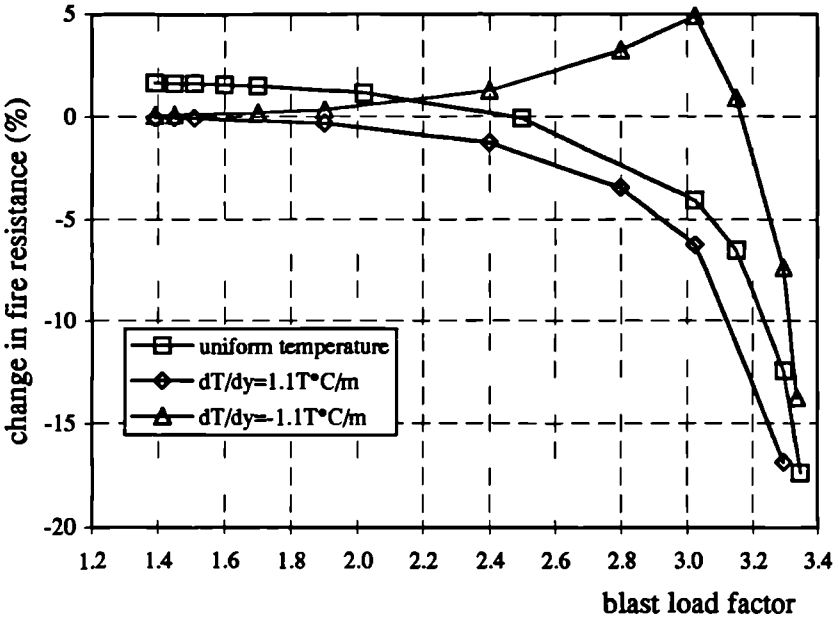


Figure 9.5 Column (3m) with $\lambda_F = 0.68$

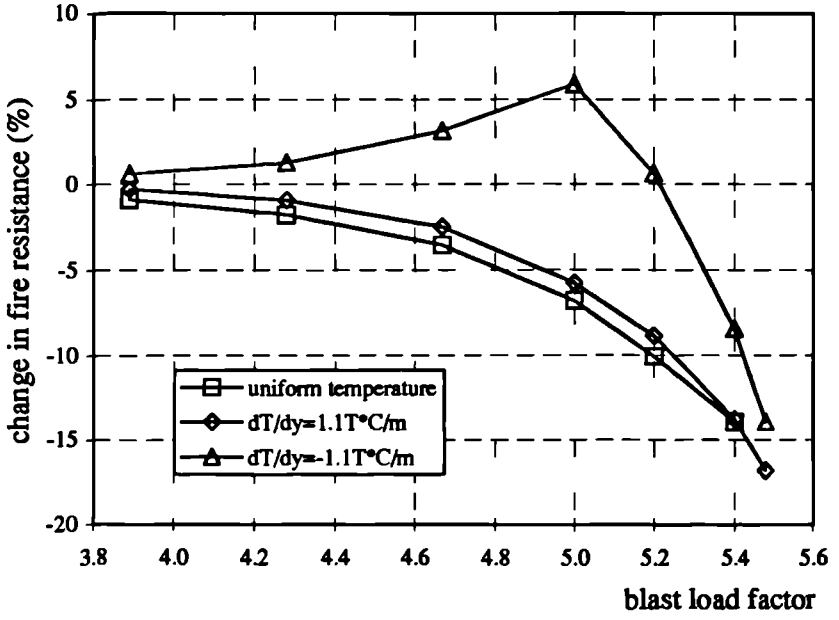


Figure 9.6 Column (3m) with $\lambda_F = 0.3$

9.2 STEEL FRAME UNDER EXPLOSION AND FIRE

The structure considered is a plane frame, eight storeys by three bays, representing a typical office block, as illustrated in Figure 9.7. In this frame, columns are bent about their major axes and rigid connections are assumed throughout the investigation. Design loads uniformly applied on the floor are transferred as uniformly distributed loads to the beams and concentrated loads on the top of each column, with w = 29.025 kN/m, and P = 120 kN. The dimensions of the structural members are given in Table 9.2. An initial imperfection of 1/1000 of the height is assumed. The centres of all internal beams are assumed to be fixed horizontally, representing the action of braces in preventing the frame from moving sideways.

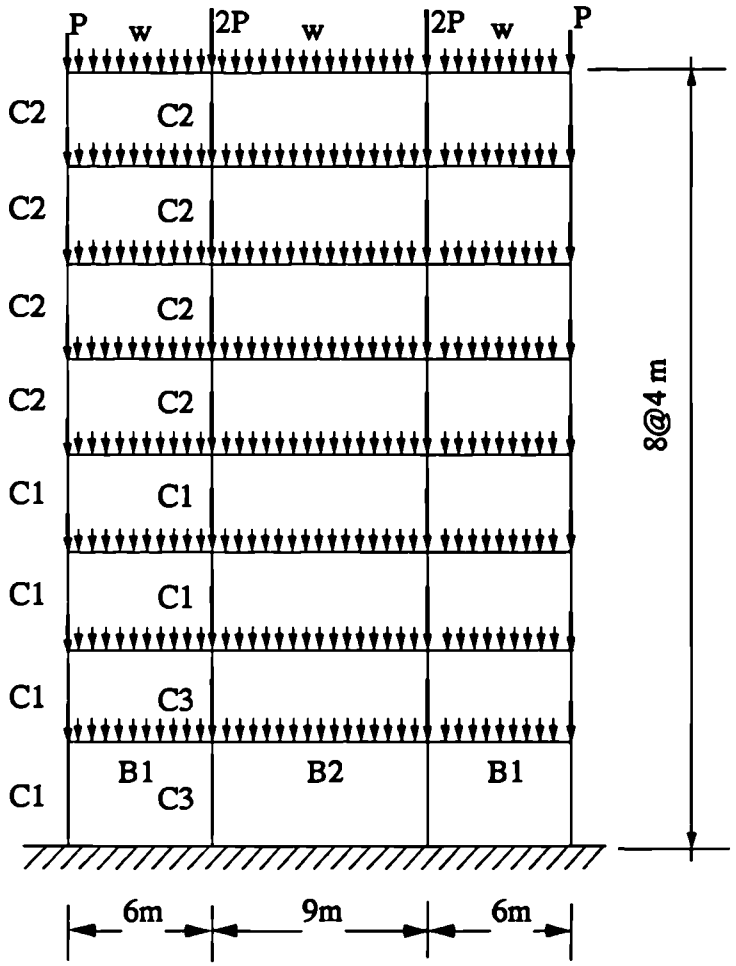


Figure 9.7 Plane steel frame under fire and blast

Table 9.2 Steel member dimensions

Name	Member size	Grade	D (mm)	B (mm)	t_f (mm)	t_w (mm)
B1	356x171UB45	50B	352.0	171.0	9.7	6.9
B2	610x229UB101	43A	606.2	227.6	14.8	10.6
C1	305x305UC118	50B	314.5	306.8	19.7	11.9
C2	254x254UC89	50B	260.4	255.9	17.3	10.5
C3	305x305UC137	50B	320.5	308.7	21.7	13.8

9.2.1 Material Properties

At ambient temperature, Young's modulus is taken as 205 GPa and the yield stress is 275 MPa and 355 MPa for Grade 43A and 50B, respectively. The combined rate-sensitive and thermal model described in Chapter 5 is used. The parameters for the rate sensitive model and the reduction factors for the material properties at elevated temperatures, as well as the thermal strain, are the same as those given for the column in Section 9.1.

9.2.2 Loading

The design load on the structure is applied as an initial load while explosion and fire are applied as loading over the time domain.

Consideration is given to the loading scenario of a gas explosion occurring in one compartment followed by fire. The profile of the overpressure generated in the explosion is the same as that shown in Figure 9.2, with a maximum overpressure assumed to be 618 N/mm. It is assumed that the compartments are vented and the explosion occurs close to one of the compartment columns. Hence, the blast is considered not to affect the other beams and columns. The blast load is represented by uniformly distributed loading, whereas the temperature due to fire loading is assumed to vary linearly with time, rising to 800°C in 30 minutes. The fire is assumed to start five seconds after the explosion, with the temperature rising uniformly in the compartment.

9.2.3 Parametric Study

The study carried out in this section aims to establish answers to the following

questions. Firstly, how does blast affect the overall behaviour of a steel frame in fire? If a steel structure can survive an explosion, will it still possess the same fire resistance as one never experiencing an explosion? Secondly, if blast affects the fire resistance of the steel frame, is the location of the blast be of importance?

Due to the unpredictable nature of explosion and fire, it is necessary to include general loading cases in the study. The loading cases considered are:

1) Ground floor central compartment; explosion affecting left internal column, followed by a fire;
2) Ground floor left compartment; explosion affecting left column, followed by fire;
3) Third floor central compartment; explosion affecting left internal column followed by fire.

9.2.4 Results

Analyses were performed for the previously stated load cases. The most significant findings are reported below.

Figure 9.8 shows the variation of vertical displacement at the top of the left internal column with temperature for all three load cases. For load case (1), the frame sustains

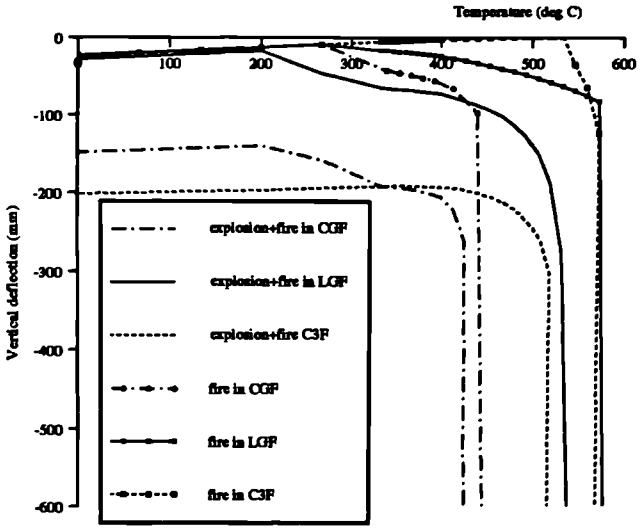
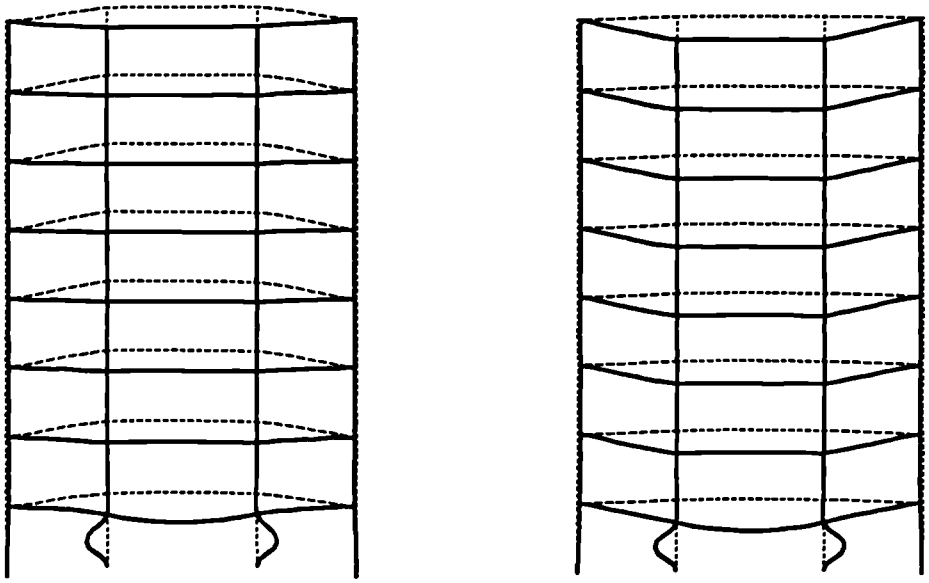


Figure 9.8 Vertical displacement at top of the left internal column

the applied loads up to 430°C, at which point the frame loses its overall stability. Without experiencing the explosion, the frame will not lose its stability until the temperature reaches 462°C. Thus the effect of the explosion is a 7% reduction in the fire resistance. Deflected shapes of the frame approaching failure are shown in Figure 9.9.



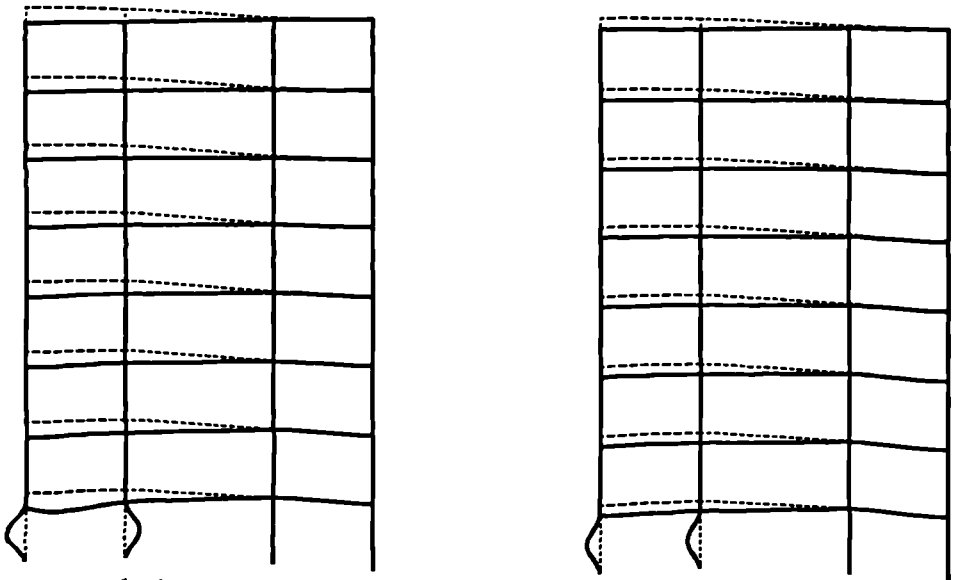
(a) explosion and fire (b) explosion

Figure 9.9 Deflected shapes approaching failure for load case (1)

For load case (2), the frame fails at 547°C under combined explosion and fire. Under the action of fire loading only, the frame fails at 582°C. Therefore, the fire resistance of the frame is reduced by 6% due to the effect of explosion in the left ground floor compartment. It is noted that the reduction in the fire resistance is considerable in the first case as the inner columns are much more heavily loaded than the other columns, although the magnitude of the explosion is the same. This suggests that for members which are loaded to a considerable extent, the fire resistance would be reduced significantly by blast loading. This is further demonstrated in load case (3), where the same blast loading is applied to the middle compartment on the third floor. In this case, the frame maintains its stability until a compartment temperature of 545°C. When subjected to blast loading first, the limit temperature reduces to 575°C, leading to only a 5% reduction in fire resistance.

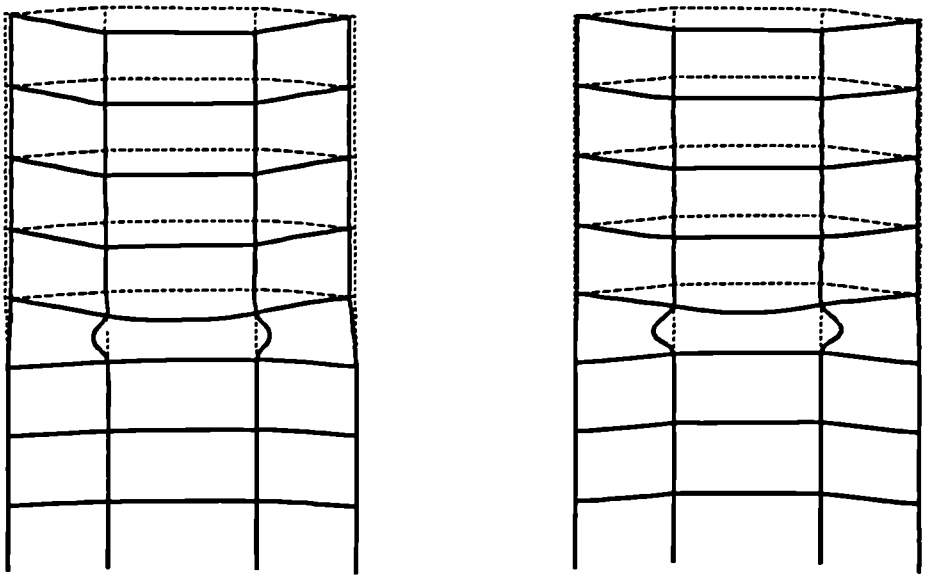
From the results of the previous analysis, the conclusion that blast loading could considerably reduce the fire resistance of a steel frame can be drawn. The significance

of this effect varies with the location of the blast, and is related to the extent of the loading of the members affected by the blast. Generally, the greater the loading taken by a column, the more severely its fire resistance is reduced by the blast, which has also been observed in the column parameteric studies of Section 9.1.



(a) explosion and fire (b) fire only

Figure 9.9 Deflected shapes for load case (2)



(a) explosion and fire (b) fire only

Figure 9.10 Deflected shapes for load case (3)

CHAPTER 10
SUMMARY AND CONCLUSIONS

This work was prompted by the realisation that designing steel structures with adequate fire and blast resistance is considerably facilitated by the availability of a well-verified and calibrated analysis tool, with sufficient accuracy and efficiency, for predicting the structural behaviour under fire and blast conditions.

This research has focused on developing a computationally efficient environment for integrated nonlinear analysis of steel frames under fire and explosion loading. This analysis tool was then calibrated against available experimental results, particularly those obtained from the experiment carried out by the Building Research Establishment (BRE) on a full-scale steel building at Cardington.

The main conclusions of this work are summarised as follows:

- the behaviour of a steel framed structure is predictable with a realistic modelling of the nonlinear material response at elevated temperatures;

- the influence of the slab action on the overall structural response under fire is significant;

- blast has a considerable influence on the fire resistance of steel structures;

- the developed analysis tool provides considerable computational and modelling savings through its adaptive analysis procedure, which has significant implications with regard to its suitability for parametric studies aimed at generating design guidance.

The main developments of this work are highlighted in the following sections, and proposals for further research work are also made.

10.1 NONLINEAR MATERIAL MODELS FOR ELEVATED TEMPERATURE

In order to analyse steel structures under fire conditions, a model of the stress-strain response of steel subject to a temperature variation is required. For steel structures

under blast, the material model must account for the effect of high strain rates. Bilinear and elliptical models were developed to represent the nonlinear material response at elevated temperatures occurring under fire conditions, and a creep model was developed which complements the bilinear model in considering the effect of creep. Finally, the combined model was developed to deal with the transient material response under high strain-rates and elevated temperatures during combined explosion and fire scenarios.

10.1.1 Bilinear Model

The bilinear model uses one straight line to represent the elastic range and another to represent the plastic range. It assumes kinematic strain-hardening, and hence the elastic range remains constant after plastic deformation. The variation of the elastic modulus with temperature is represented by a trilinear function. Trilinear functions are also used to represent the variation of the effective yield strength, the strain-hardening parameter and the thermal strain with temperature. Verification examples in Chapter 4 showed that the bilinear material model provides a reasonable prediction of the elevated temperature response of steel structures, with the advantage of being computationally efficient.

10.1.2 Elliptical model

The elliptical model is defined by Young's modulus, the proportional limit, the yield strength and their variation with temperature. It is characterised by an initially linear progression up to the elastic stress limit, followed by an elliptical progression up to the yield strength, and another tangential straight line to the limiting strain for the yield strength. An isotropic strain-hardening rule is adopted for this model so that the effects of stress reversals can be modelled realistically. The variations of elastic modulus, the proportional limit and the yield strength with temperature, are defined by means of piece-wise linear curve with 5 segments. This model represents the nonlinear behaviour of stress-strain response more realistically than the bilinear material model. It is thus more accurate in analysis, as illustrated by the verification examples in Chapter 4, although it can be more computationally demanding than the bilinear model.

10.1.3 Creep Model

The creep model adopted in this work is based on Plem's work (Plem, 1975). The creep strain is assumed to be dependent on the magnitude of the stress and the temperature-compensated time. Under constant stress, the primary phase is defined by a parabolic curve and the secondary phase by a linear slope, while the tertiary creep leading to fracture is ignored. The strain-hardening rule is used to predict the creep strain under varying stress from the creep strain under constant stress. The creep effect can be significant in the structural response under fire conditions, particularly when the period is prolonged, as illustrated by the calibration against the BRE experiment in Chapter 8.

10.1.4 Combined Material Model for Rate-sensitivity and Elevated Temperatures

The material properties of steel are significantly affected by temperature and strain-rate in a transient manner during fire and blast scenarios. Thus, a combined material model is developed, with the bilinear model used in conjunction with an existing rate-sensitive model in ADAPTIC, developed by Manzocchi (1990), to provide a material model for structural analysis when explosion and fire actions coexist. The implementation of this combined material model into ADAPTIC provided an essential component of the integrated analysis environment for blast and fire conditions.

10.2 FORMULATION FOR STEEL DECKED COMPOSITE SLAB

In the absence of adequate numerical models for the two-way response of composite steel-decked slab, pioneering work has been undertaken in this thesis aimed at developing a new elastic slab formulation which takes into account the different slab cross-sections in the two orthogonal directions. A novel approach has been developed which employs the concepts of two-level interpolation, on the level of one element and one block, and of additional rib freedoms. The first concept derives from the fact that the element response would be considerably over-stiff if conventional finite element interpolation were employed, and therefore proposes interpolation on the block level which is coupled at the block boundaries to conventional interpolation on the element level. The second concept introduces additional transverse extension freedoms at the bottom of the ribs, thus providing an improved interpolation of displacements over the rib depth in comparison with the conventional slab formulation which assumes that a straight line normal to the reference plane remains

straight after deformation. In combination, these two concepts lead to a realistic elastic composite slab element. Several examples were presented to illustrate the significance of the new concepts introduced in the composite slab formulation. Most importantly, these examples demonstrated the ability of the proposed formulation to model the different slab response in the longitudinal and transverse direction. Further more, very good agreement was established against available experimental results in the linear elastic range.

10.3 INTEGRATED ADAPTIVE ANALYSIS OF STEEL FRAMES SUBJECT TO FIRE AND EXPLOSION

ADAPTIC was extended to provide a unique integrated analysis environment for steel frames under coexistent fire and explosion loading. The developed procedure considers transient material response according to the active loading, and allows different time-steps at respective stages of analysis for explosion and fire, in view of the much shorter duration of explosion overpressure in comparison with that of fire. This integrated analysis environment enables the evaluation of the effects of blast on the structural fire resistance.

As significant, this integrated analysis environment is evaluated by the advanced nonlinear adaptive analysis methods. With the adaptive method, analysis starts with one elastic element per structural member, and automatic mesh refinement into elasto-plastic elements is performed only when and where necessary during the analysis within the structure, respectively. In addition to the modelling advantages, significant computational saving were demonstrated by several examples, where adaptive analysis out-performed the conventional nonlinear analysis by 3 to 5 times, without loss of accuracy.

10.4 VERIFICATION AND CALIBRATION

The developed computational tool for steel frames under fire has been satisfactorily verified and calibrated against available experimental results on the member level, the scaled frame level and the full-scale frame level. In all cases, from single beam to framed structures, the computational predictions showed good agreement the respective experimental results.

10.4.1 Verification on Beams

Two beam tests carried out by Rubert and Schaumann (1986) and Cooke (1987) were simulated using ADAPTIC. The variation of the midspan vertical displacement with temperature, for various values of applied loading, was investigated. Favourable comparison was achieved between the experimental results and the predictions of ADAPTIC. Minor discrepancies, which were observed at larger displacements, may be attributed to uncertainties in the material properties at elevated temperatures.

10.4.2 Verification on Scaled Frame Tests

A series of frame tests, performed by Rubert and Schumann (1986) on three 1/6-1/4 scale plane steel frames at elevated temperatures, were also used in verifying the developed analysis tool. The calculated failure temperatures showed good agreement with the test results for all three configurations. The available test displacements were compared with those obtained from analysis, where the computational prediction was shown to follow the test results closely, up to the failure.

10.4.3 Calibration against the Cardington Full-scale Fire Test

The full-scale fire test carried out by BRE with a natural fire in a corner compartment was used to calibrate the developed nonlinear fire analysis tools implemented within ADAPTIC.

The fire compartment is modelled along with the immediately adjacent structural components, subjected to appropriate boundary conditions. Within the fire compartment, the nonlinear behaviour of the composite slab has been approximated by one-dimensional composite T-beams in the span direction and concrete beams acting compositely along the steel beams. The variation of the temperature distribution with time over each structural component in the compartment has been incorporated to reflect as closely as possible the thermocouple data provided by BRE. The proposed new slab formulation was used in modelling the cold composite slab outside the fire compartment.

Good agreement was shown between the analytical predictions and the experimental results. The two considerations which proved most important for achieving a favourable comparison were the deterioration of the steel deck stiffness and strength at elevated temperatures and the creep effects in steel at elevated temperatures.

10.5 PARAMETRIC STUDY

Application of the integrated nonlinear analysis environment in parametric studies concentrated on the effect of blast on the fire resistance of steel structures. A column under axial load was subjected to a blast loading, followed by a fire. Parameters including load factor, magnitude of blast loading and temperature profile were considered. The parametric study showed that blast could significantly reduce the fire resistance of a steel column, particularly for heavily loaded columns, with a reduction of up to 28% in terms of survival time, while a beneficial effect of 4% increase in fire resistance was found for a favourable temperature distribution over the column.

A plane steel frame representing a typical 8 storey office block is also considered. In this building, the effect of different blast locations is examined. It is found that blast loading indeed reduces the fire resistance of steel structures and the severity of this effect varies with the location of the blast even for the same blast loading.

10.6 FUTURE WORK

With the development and implementation of the material models for elevated temperature, the new slab formulation and the integrated analysis environment, ADAPTIC provides an accurate and efficient analysis tool for predicting the behaviour of steel framed structures under fire and explosion loading. However, there are several areas where further research work is required.

- The developed slab formulation is capable of modelling the elastic behaviour of composite steel decked concrete slabs. The deterioration of material properties under fire conditions, as well as the effects of large displacements, were not included in this formulation. Therefore, a more advanced formulation, taking into account the above aspects, would provide a more realistic model for analysing steel framed structures under fire and blast conditions.

- Connections are important components in building steel structures, and it is evident that their performance is affected by elevated temperatures. It would be important to investigate the behaviour of connections under fire conditions experimentally, and to provide appropriate analytical models of their response at elevated temperatures.

- Experimental evidence from the BRE full scale fire test has shown that fire protection is not essential for all the steel beams, provided that the floor slab can be relied upon to support the vertical loads at elevated temperatures. These observations were supported by the analytical predictions in this work. Further parametric studies are required to establish the extent to which these observation can be generalised to compartments of various size and aspect ratios.

- Further experiments would be useful for additional calibration of the developed nonlinear analysis tools, particularly for members and structures under blast loading where reported experimental results are lacking.

In this work, the development of the integrated analysis tool enables the analysis of a steel framed structure subjected to explosion followed by fire. However, a loading scenario in which fire is followed by explosion was not considered due to the lack of information on material properties under high strain rates at elevated temperatures. Therefore, this is an area where further experimental work is needed.

REFERENCES

1. Aasen B., 1985, "An Experimental Study on Steel Column Behaviour at Elevated Temperatures", The Norwegian Institute of Technology, Trondheim.

2. American Institute of Steel Construction, 1978, "Manual of Structural Steel for Building".

3. American Institute of Steel Construction, 1987, "Manual of Structural Steel for Building".

4. Anderberg Y., 1988, "Modelling Steel Behaviour", Fire Safety Journal, 13, pp.17-26.

5. Armer, G.S.T., and Moore, D.B., 1994, "Full-scale Testing on Complete Multistorey Structures", The Structural Engineer, 72, pp.30-31.

6. Ayrton W.E. and Perry J., 1886, "On struts", The Engineer, 62, pp.464.

7. Bailey C.G., Burgess I.W. and Plank R.J., 1996, "Computer Simulation of a Full Scale Structural Fire Test", The Structural Engineer, 74, pp.93-100.

8. Bailey C.G., Burgess I.W. and Plank R.J., 1996, "The Lateral-torsional Buckling of Unrestrained Steel Beams in Fire", Journal of Construction Steel Research, 2, pp.101-109.

9. Bangash M.Y.H., 1993, "Impact and Explosion: Analysis and Design", Blackwell Scientific Publications.

10. Berg G.V., 1989, "Elements of Structural Dynamics", Prentice-Hall, New Jersey.

11. Bodner and Symonds, 1960, "Plastic Deformation in Impact and Impulsive Loading in Beams", Proceedings of the 2nd Symposium on Naval Structural Mechanics, Rhode Island.

12. Boyle J.T. and Spence J., 1983, "Stress Analysis for Creep", Butterworths & Co. Ltd, London.

13. British Standard Institution, 1965, "Composite Construction in Structural Steel and Concrete: Simply-supported Beams in Building, CP117: Part 1".

14. British Standards Institute, 1990, "BS 5950, Part 8, Code of Practice for the Fire Protection of Structural Steelwork".

15. British Standards Institution, 1987, "BS 476, Fire Tests on Building Materials and Structures, Part 20: Methods for Determination of the Fire Resistance of Elements of Construction (Gerneral Principles)", BSI, London.

16. British Standards Institution, 1987, "BS 476: Fire Tests on Building Materials and Structures, Part 21: Methods for Determination of the Fire Resistance of Load Bearing Elements of Constructions", BSI, London.

17. British Standards Institution, 1990, "BS 5950: Part 8: Structural Use of Steelwork in Building, Code of Practice for Fire Resistance Design".

18. Bryl, S., 1967, "The Composite Effect of Profiled Steel Plate and Concrete in Deck Slabs", Acier Stahl Steel, October.

19. Burgess I.W. and Najjar S.R., 1994, "A Simple Approach to the Behaviour of Steel Columns in Fire", Journal of Construction Steel Research, 31, pp.115-134.

20. Burgess I.W., El-Rimawi J.A. and Plank R.J., 1988, "A Secant stiffness Approach to the Fire Analysis of Steel Beams", Journal of Constructional Steel Research, 11, pp.105-120.

21. Burgess I.W., El-Rimawi J.A. and Plank R.J., 1990, "Analysis of Beams with Non-Uniform Temperature Profile Due to Fire Exposure", Journal of Constructional Steel Research, 16, pp.169-192.

22. Burgess I.W., El-Rimawi J.A. and Plank R.J., 1991, "Studies of the Behaviour of Steel Beams in Fire", Journal of Constructional Steel Research, 19, pp.285-312.

23. Burgess I.W., Olawale A.O., and Plank R.J., 1993, "Failure of Steel Columns in Fire", Fire Safety Journal, 18, pp.183-201.

24. Caughey R.G. and Hoyt W.B., 1955, "Effects Cyclic Overloads on the Creep Rates and Rupture Life of Inconel at 1700°F and 1800°F", NAUORD Rept. 3404, D79, US Naval Ordnance Test Station, California.

25. Chang K.C. and Lee G.C., 1987, "Strain Rate Effect of Structural Steel under Cyclic Loading", Journal of Engineering Mechanic, ASCE, 133, pp.1292-1301.

26. Chen W.F. & Kish N., 1986, "Data Base of Steel Beam-to-Column Connection", Volumes I and II, School of Civil Engineering, Purdue University.

27. Cheng W.C. and Mak C.K., 1975, "Computer Analysis of Steel Frame in Fire", ASCE Journal of the Structural Division, 101, pp.855-867.

28. Cheng W.C., 1983, "Theory and Application on the Behaviour of Steel Structures at Elevated Temperatures", Computers and Structures, 16, pp.27-35.

29. Chou Y.J. and Lin Y.R., 1992, "A Study on the Fire Response of Flexibly Jointed Steel Frames", Computers and Structures, Vol 45, pp.439-451.

30. Clark, CL, 1953, High Temperature Alloys, Pitman.

31. Commission of the European Communities, 1992, "Eurocode 3: Design of Steel Structures. Part 1.1: General Rules and Rules for Building", ENV 1993-1-1.

32. Commission of the European Communities, 1993, "Eurocode 3, Design of Steel Structures, Part 1.2: Fire Resistance".

33. Conway J.B., 1962, "Numerical Methods for Creep and Rupture Analysis", Gordon and Breach, Science Publishers, New York.

34. Cook, R.D., Malkus, D.S. and Plesha, M.E., 1989, "Concepts and Applications of Finite Element Analysis", Third Edition, John Wily & Sons.

35. Cooke G.M.E. and Latham D.J., 1987, "The Inherent Fire Resistance of a Loaded Steel Frame Work", Steel Construction Today, 1, pp.49-58.

36. Cooke G.M.E., 1987, "The structural Response of Steel I-section Members subjected to elevated Temperature Gradients across the section", PhD Thesis, Department of Civil Engineering, City University, London.

37. Cooke G.M.E., 1988, "An Introduction to Mechanical Properties of Structural Steel at Elevated Temperatures", Fire Safety Journal, 13, pp.45-54.

38. Corradi L, Poggi, C ,and Setti, P, 1990, "Interaction Domains for steel beam-columns in fire conditions", Journal of Construction and Steel Research, 17, pp.217-235.

39. Critescu, N., 1963, "Dynamic Plasticity", North Holland Publishing Company, Amsterdam.

40. Culver C.G., 1972, "Steel Column Buckling under Thermal Gradient", Journal of the Structural Division, ASCE, 98, pp.1853-1865.

41. Culver C.G., Aggarwal V and Ossenbruggen PJ, 1973, "Buckling of Steel Columns at Elevated Temperature", ASCE Journal of the Structural Division, 99, pp.715-726.

42. Daniels, B.J., and Crisinel, M., 1993-a, "Composite Slab Behavior and Strength analysis. Part I: Calculation Procedure", Journal of Structural Engineering, ASCE, 119, pp. 16-35.

43. Daniels, B.J., and Crisinel, M., 1993-b, "Composite Slab Behavior and Strength analysis. Part II: Comparison with Test Results and Parametric Analysis", Journal of Structural Engineering, ASCE, 119, pp. 36-49.

44. Dorn J.E., 1954, "Some Fundamental Experiments on High Temperature Creep", Journal of the Mechanics and Physics of Solids, 3, pp.88-138.

45. Douns S, and Golrang B, 1982, "Mechanical Properties at High Temperatures-Further Development of Steel Bahaviour Model", Division of Building Fire Safety and Technology, Lund Institute of Technology, Lund.

46. Dowling PJ, Knowles P, and Owens GW, 1988, "Structural Steel Design", The Steel Construction Institute, Butterword.

47. ECCS, Technical Committee 3, 1983, "European Recommendation for he fire Safety of Steel Structures", Elsevier Scientific Publishing Company, Oxford.

48. Ekberg, C.E., Jr., and Schuster, R.M., 1968, "Floor Systems with Composite Form-Reinforced Concrete Slabs", Finial Report, International Association for Bridge and Structural Engineering, 8th Congress, New York, pp. 385-394.

49. El-Rimawi J.A., Burgess I.W. & Plank R.J., 1997, "The Influence of Connection Stiffness on the Behaviour of Steel Beams in Fire", Journal of Constructional Steel Research, 43, pp.1-5.

50. Elnashai A.S. & Izzuddin B.A., 1993, "Modelling of Material Nonlinearities in Steel Structures Subjected to Transient Dynamic Loading", Earth Engineering and Structural Dynamics, 22, pp.509-532.

51. European Committee for Standardisation, 1990, "Eurocode 3 – Design of Steel Structures: Part 1.2 Structural Fire Design".

52. European Convention for Constructional Steel Work, 1981, "European recommendations for the design of Profiled Sheeting and Sections — Part 1", Constrado.

53. Evans H.E., 1984, "Mechanisms of Creep Fracture, Elsevier Applied Science Publishers", London.

54. Evans R.W. and Wilshire B., 1993, "Introduction to Creep", The Institute of Materials, London.

55. Evans, H.R. and Wright, H.D., 1988, "Steel-Concrete Composite Flooring Deck Structures", Steel-Concrete Composite Structures, Stability and Strength, Edited by R. Narayanan, Elsevier Applied Science.

56. Fessler H. and Hyde T.H., 1978, "Creep Deformation of Metals, Creep of Engineering Materials", A Journal of Strain Analysis Monograph, Edited by Pomeroy C.D., Mechanical Engineering Publication Limited.

57. Fischer, J.W., 1970, "Design of Composite Beams with Formed Metal Deck", Engineering Journal, American Institute of Steel Construction, 7, pp. 88-96.

71. HMSO, 1985, "The Building Regulation", London.

72. Irvine H.M., 1986, "Structural Dynamics for the Practicing Engineer", Allen and Unwin, London.

73. Izzuddin B.A. & Elnashai A.S., 1993, "Adaptive Space Frame Analysis Part II: A Distributed Plasticity Approach", Proceedings of the Institute of Civil Engineers Structures & Buildings, 99, pp.317-326.

74. Izzuddin B.A., 1991, "Nonlinear Dynamic Analysis of Framed Structures", PhD Thesis, Imperial College of Science and Technology, University of London.

Izzuddin B.A., 1997, "Quartic Formulation for Elastic Beam-Columns subject to Thermal Effect", Journal of Engineering Mechanics, ASCE, pp.861-871.

75. Izzuddin B.A., Song L., and Elnashai A.S., 1995, "Adaptive Analysis of Steel Frames subject to Fire Loading", Computing in Civil and Building Engineering, Edited by Phalli P.J. and Werner H., Proceedings of the 6th International Conference on Computing in Civil and Building Engineering, Berlin, Germany, pp.643-649.

76. Izzuddin, B.A., and Elnashai, A.S., 1992, "ADAPTIC: A Program for the Adaptive Dynamic Analysis of Space Frames", User Manual, Imperial College of Science and Technology, London.

77. Jackson P., Thirlwall I., and Veale C.J.R. 1995, "Basic Guildlines for Enhancing Building Resilience", Blast Effects on Building, Edited by Mays G.C. and Smith P.D., Thomas Telford.

78. Jain P.C. and Rao M.N.G., 1983, "Analysis of Steel Frames under Fire Environment, International Journal for Numerical Methods in Engineering", 19, pp.1467-1478.

79. Jauss J. and Minne R., 1981/1982, "Buckling of Steel Columns in Fire Conditions", Fire Safety Journal, 4, pp.227-235.

80. Jeanes D.C., 1985, "Application of the Computer in Modelling Fire Endurance of Structural Steel Floor Systems", Fire Safety Journal, 9, pp.119-135.

81. Jian P.C. and Rao M.N.G., 1983, "Analysis of steel Frames Under Fire Environment", International Journal for Numerical Methods in Engineering, 19, pp.1467-1478.

82. Jolly C.K. and Zumair A.K.M., 1987, "The Efficiency of Shear-bond Interlock Between Profiled Steel Sheeting and Concrete", Composite Steel Structures, Advances, Design and Construction, Edited by R. Narayanan, Elsevier Applied Science, pp. 127-136.

83. Kirby B.R., 1986, "Recent Development and Application in Structural Fire Engineering Design - A Review", Fire Safety Journal, 11, pp.17-26.

84. Klaiber F.W. and Porter, M.L., 1981, "Uniform Loading for Steel-Deck-Reinforced Slabs", Journal of the Structural Division, ASCE, 107, pp. 2097-2109.

85. Kolsky, 1949, Proceedings of the Physics Society, 62, pp 676-700.

86. Kouhia R, Paavola J, and Tuomala, M, 1988, "Modelling the fire Behaviour of Multistorey Buildings", 13th Congress of the International Association for Bridge and Structural Engineering, Helsinki, pp.623-628.

87. Kruppa J., 1979, "Collapse Temperature of Steel Structures", Journal of the Structural Division, ASCE, 105, pp.1769-1788.

88. Kruppa J., 1981/1982, "Some Results on the Fire Behaviour of External Steel Columns", Fire Safety Journal, 4, pp.247-257.

89. Latham D.J., Thomson G. and Kirby B.R., and Wainman D.E., 1986, "Second Natural Fire Test on a Loaded Steel Frame at Cardington", RS/RSC/7281/12/86/E., British Steel Corporation, Swinden Laboratories.

90. Lathem D.J., Kirby B.R. and Thomson G., 1987, "The Temperature Attained by Unprotected Structural Steelwork in Experimental Nature Fire", Fire Safety Journal, 12, pp.139-152.

91. Lawson, R.M., 1983, "Composite Beams and Slabs with Profiled Steel Sheeting", Construction Industry Research and Information Association.

92. Lennon T, 1995, "Cardington Fire Tests: Instrumentation Locations for Corner Fire Test", N152/95, Building Research Establishment.

93. Lie T.T., 1972, "Fire and Building", Applied Science Publishers Ltd., London.

94. Liu T.C.H., 1996, "Finite Element Modelling of Behaviour of Steel Beams and Conditions in Fire", Journal Constructional Steel Research, 36, pp.181-199.

95. Long A.E., 1994, EPSRC research and the Cardington Facility, First Results from the Large Building Test Facility, First Cardington Conference, Cardington, November.

96. Ludwick, 1909, Physik Z, 10, pp.411-417.

97. Luttrell, L.D. and Davison, J.H., 1973, "Composite Slabs with Steel Deck Panels", Proceedings of the 2nd Speciality Conference on Cold-Formed Steel Structures, University of Missouri-Rolla, Rolla, pp. 573-603.

98. Luttrell, L.D., 1987, "Flexural Strength of Composite Slabs", Composite Steel Structures, Advances, Design and Construction, Edited by R. Narayanan, Elsevier Applied Science, pp. 106-116.

99. Madas P.J., 1993, "Advanced Modelling of Composite Frames subjected to Earthquake Loading", PhD Thesis, Imperial College of Science, Technology and Medicine, London.

100. Magnusson S.E., 1974, "Structural Behaviour and Load-bearing Capacity of Fire-Exposed Steel".

101. Malhotra, H.L, 1982, "Design of fire-resisting structures", Surrey University Press.

102. Malvern, 1951, "The Propagation of Longitudinal Waves of Plastic Deformation in a Bar of Material Exhibiting Strain Rate Effect", Journal of Applied Mechanics, ASME, 18, pp.203-208.

103. Manson S.S., 1961, "Creep under Nonsteady Temperature and Stress", Mechanical Behavior of Materials at Elevated Temperature, Edited by Dorn J.E., McGarw-Hill Book Company, INC, New York, pp.419-476.

104. Manzocchi G.M.E., 1991, "The Effect of Strain Rate on Steel Structures", MSc Dissertation, Civil Engineering Department, Imperial College.

105. Marriott D.L. and Leckie F.A., 1963-1964, "Some Observations on the Deflections of Structures and Components", The Institute of Mechanical Engineering, Proceedings 178, Part 3L, pp.115-125.

106. Martin D.M., 1994, "The Behaviour of a Multi-storey Steel Framed Building subjected to Natural Fires", First Results from the Large Building Test Facility, First Cardington Conference, Cardington, November.

107. Mays G.C. and Smith P.D., 1995, "Blast Effects on Building", Thomas Telford, London.

108. Mays G.C., 1995, "Design of Elements in Reinforced Concrete and Structural Steel", Blast Effects on Building, Edited by Mays GC and Smith PD, Thomas Telford

109. Miller J., 1954, "Effect of Temperature Cycling on the Rupture Strength of Some High Temperature Alloys", Symposium on Effect of Cyclic Heating and Stressing on Metals at Elevated Temperatures, ASTM Special Technical Publication, 165, pp.53.

110. Mosley W.H. and Bungey J.H., 1990, "Reinforced Concrete Design", Basingstoke, Macmillan.

111. Nishihara T., Tazra S., Tanaka K. and Ohji K., 1957, "On the Creep of Low Carbon Steel Under Fluctuating Stress", Proceedings of the Seventh Japan National Congress for Applied Mechanics, pp.31-34.

112.Norton F.H., 1929, "Creep of Steel at High Temperatures", McGraw-Hill Book Co., Inc.

113.O'leary D. El-Dharat A. and Duffy C., 1987, "Composite Reinforced End-Anchored Concrete Floors", Composite Steel Structures, Advances, Design and Construction, Edited by R. Narayanan , Elsevier Applied Science, pp.117-126.

114.Ohji K. and Marin J., 1963-64, "Creep of Metals under Non-steady Conditions of Stress", The Institute of Mechanical Engineering, Proceedings 178, Part 3L, pp.126-134.

115.Olawale A.O. and Plank R.J., 1988, "The Collapse Analysis of Steel Columns in Fire using a Finite Strip Method", International Journal of Numerical Method in Engineering, 26, pp.2755-2764.

116.Ossenbruggen P.J., Aggarwal V and Culver CG, 1973, "Steel column Failure under thermal gradient", Journal of the Structural Division, ASCE, 99, pp.727-739.

117.Paz M., 1980, "Structural Dynamics: Theory and Computation", Von Nostrand-Reinhold, New York.

118.Pettersson O., 1988, "Practical Need of Scientific Material Models for Structural Fire Design - General Review", Fire Safety Journal, 13, pp.1-8.

119.Plem E., 1975, "Theoretical and Experimental Investigations of Point Set Structures", Swedish Council for Building Research, Document, D9:1975.

120.Poh K.W. and Bennets I.D., 1995, "Analysis of structural members under elevated temperature conditions", Journal of Structural Engineering, 121, pp.664-675.

121.Poh K.W. and Bennets I.D., 1995, "Behaviour of steel columns at Elevated Temperature", Journal of Structural Engineering, 121, pp.676-684.

122.Poh K.W. and Wttard M.M., 1993, "Calculating the Load-deflection Behaviour of Simply-supported Composite Slabs with Interface Slip", Engineering Structures, 15, pp.359-367.

123.Porter, M.L., 1968, "Investigation of Light Gage Steel Forms as Reinforcement for Concrete Slabs", PhD Thesis, Iowa State University, Ames, Iowa.

124.Porter, M.L., 1974, "The Behavior and Analysis of Two-way Simply Supported Concrete Composite Floor Slabs Constructed with Cold-Formed Steel Decking", PhD Thesis, Iowa State University, Ames, Iowa.

125.Porter, M.L., and Ekberg, C.E., 1971, "Investigation of Cold-Formed Steel-Deck Reinforced Concrete Floor Slabs", Proceedings of the 1st Speciality Conference on Cold-Formed Steel Structures, University of Missouri-Rolla, Rolla, pp. 179-185.

126.Porter, M.L., and Ekberg, C.E., 1972, "Summary of Full-scale Laboratory Tests of Concrete Slabs Reinforced with Cold-Formed Steel Decking", Preliminary Report, International Association for Bridge and Structure Engineering, 9th Congress, Amsterdam, pp. 173-183.

127.Porter, M.L., and Ekberg, C.E., 1976, "Design Recommendations for Steel Deck Floor Slabs", Journal of the Structural Division, ASCE, 102, pp. 2121-2136.

128.Prasannan, P.C. and Lutterll, L.D., 1984, "Flexural Strength Formulations for Steel-Deck Composite Slabs", Technical Report, Department of Civil Engineering, West Virginia University.

129.Purkiss J.A., 1996, "Fire Safety Engineering Design of Structures", Butterworth-Heinemmann, Oxford.

130.Ramberg W., and Osgood W., 1943, "Description of Stress-Strain Curves by Three Parameters", NACA Technical Note No. 902, National Advisory Committee Aeronautics.

131.Roberston A., 1925, "The Strength of Struts", Institute of Civil Engineer, Selected Engineering Papers, 28.

132.Robinson E.L., 1938, "Effects of Temperature Variation on the Creep Strength of Steel", Transaction of ASME, 60, pp.253.

133.Robinson J., 1994, "Industrial Viewpoint on Whole Building Studies", First Results from the Large Building Test Facility, First Cardington Conference, Cardington, Novermber.

134.Robinson, H., 1967, "Composite Beam Incorporating Cellular Steel Decking", Journal of the Structural Division, ASCE, 93, pp.355-380.

135.Robinson, H., 1967, "Tests on Composite Beams with Cellular Deck", Journal of The Structural Division, ASCE, 93, pp.139-164.

136.Roeder, C.W., 1981, "Point Loads on Composite Deck-Reinforced Slabs", Journal of the Structural Division, ASCE, 107, pp.2421-2429.

137. Rubert A. and Schaumann P., 1985, "Tragverhalten Stählerner Rahmensteme bei Brandbeanspruchung", Stahlbau, 54, pp.280-287.

138.Rubert A. and Schaumann P., 1986, "Structural Steel and Plane Frame Assemblies under Fire Action", Fire Safety Journal, 10, pp.173-184.

139.Saab H.A. and Nathercot D.A., 1991, "Modelling steel frame behaviour under fire conditions", Engineering and Structures, 13, pp.371-382.

140.Schuster, R.M., 1970, "Strength and Behaviour of Cold-Rolled Steel-Deck Reinforced Concrete Floor Slabs", PhD Thesis, Iowa State University, Ames, Iowa.

141.Schuster, R.M., 1972, "Composite Steel-Deck Reinforced Concrete Systems Failing in Shear Bond", Preliminary Report, International Association for Bridge and Structure Engineering, 9th Congress, Amsterdam, pp. 185-191.

142.Schuster, R.M., 1976, "Composite Steel-Deck Concrete Floor Systems", Journal of the Structural Division, ASCE, 102, pp. 899-917.

143.Setti P., 1983, "Buckling of Axially Loaded Steel Columns with Imperfections at Elevated Temperature", Proceedings of the Third International Colloquium on Stability of Metal Structures, Paris, pp.167-174.

144.Shen Z.Y. and Zhao J.C., 1995, "Modelling Fire Resistance Behaviour of Multi-storey Steel Frames", Computing in Civil and Building, pp.1089-1094, Pahl & Wemer, Rotterdam

145.Sherby O.D., Trozera T.A., Dorn J.E., 1956, "Effects of Creep Stress History at High Temperature on the Creep of Aluminium Alloys", Proceedings American Society of Testing Materials, 56, pp.789-804.

146.Showronski W., 1988, "A Study of the Steel Beam Deformation during Fire", Building and Environment, 23, pp.159-168.

147.Showronski W., 1993, "Buckling Fire Endurance of Steel Columns", Journal of Structural Engineering, 119, pp.1712-1732.

148.Smith P.D. and Hetherington J.G., 1994, "Blast and Ballistic Loading of Structures", Buttertworth-heinemann, Oxford.

149.Smith, P.D., 1995, "Blast Loading, Blast Effects on Buildings", Edited by GC Mays and PD Smith, Thomas Telford

150.Song L., Izzuddin B.A. and Elnashai A.S., 1995, "Nonlinear Analysis of Steel Frames subjected to Explosion and Fire Loading", Proceedings of the 2nd International Conference on Structural Dynamics, Vibrations, Noise and Control, Hong Kong, December, pp.622-626.

151.Song L., Izzuddin B.A., Elnashai A.S. and Dowling, P.J., 1994, "Effects of Elevated Temperatures on Steel Frames", Technical Report CE/94/2, Civil Engineering Department, Imperial College of Science Technology and Medicine, London.

152.Stirland C., 1980, "Supporting Technical Data to the BSC Proposed Revision of Chapter 2 of the European Recommendations for the Design of Steel Structures Exposed to the Standard Fire", September, Private Communication.

153.Symonds, 1984, "Simple Elastic-plastic Method for Pulse Loading, Comparison with Experiment and Finite Element Solutions", Proceedings of the 3rd Conference on Mechanical Properties at High Rates of Strain, pp.479-486.

154.Talamona D., 1994, Interaction M-N Comparison Between LENAS and Tests, CTICM report INC-94/246-DT.

155.The British Iron and Steel Research Association, 1953, "Physical Constants of Some Commercial Steels at Elevated Temperatures", Butterworths Scientific Publications, London.

156.The Steel Construction Institute, 1990, "Investigation of Broadgate Phase 8 Fire", The Steel Construction Institute, Ascot, UK.

157.The Steel Construction Institute, 1995, "BRE Frame Fire Tests, Modelling of Corner Test", RT458, Report to British Steel/BRE.

158.Thomson W.T., 1988, "Theory of Vibrations with Applications", Unwin Hyman, London.

159.Thor J., 1972, "Deformation and Load Bearing Capacity of Statically Determinate Steel Beams Affected by Fire, An Experimental and Theoretical Study", Jernkontorets Forskning, Series D, No 54, Stockholm.

160.Thor J., 1973-a, "Deformations and Critical Loads of Steel Beams under Fire Exposure Conditions", National Swedish Building Research Document D16.

161.Thor J., 1973-b, "Investigation of the Creep Properties of Various Types of Structural Steel When Exposed to Fire", Stockholm.

162.TM5-1300, 1990, "US Department of the Army Technical Manual, Design of Structures to Resist the Effects of Accidental Explosions", Washington DC.

163.Wainman D.E. and Kirby B.R., 1987, "Compendium of UK Standard Fire Test Data, Unprotected Structural Steel", Vol. 1 Ref. No. RS/RSC/S10328/1/87/B and Vol. 2, Ref. No. RS/R/S1199/88/B, British Steel Corporation, Swinden Laboratories.

164.Wakabayashi, 1980, "Dynamic Effects on the Structural Performance of concrete and Steel Materials and Beams", Proceedings of the 7th World Conference on Earthquake Engineering, 6, pp.271-278.

165.Wang Y.C. and Lennon T., 1992, "A Computer Program for Structural Analysis at Elevated Temperatures", Building Research Establishment Client Report.

166.Wang Y.C. and Moore D.B., 1995, "Steel Frames in Fire: Analysis, Engineering Structure", 17, pp.462-472.

167.Wang, Y.C., 1997, "The Effects of Frame Continuity on the Behaviour of Steels Columns under Fire Conditions and Fire Resistance Design Proposals", Journal of Constructional Steel Research, 41, pp.93-111.

168.Wang, Y.C., Lennon T. and Moore D.B., 1995, "The Behaviour of Steel Frames Subject to Fire", Journal of Construction in Steel Research, 35, pp.291-322.

169.Wickström, U., 1979, "TASEF-2 A Computer Program for the Temperature Analysis of Structures Exposed to Fire", Lund Institute of Technology, Sweden.

170.Wickström, U., 1981/1982, "Temperature Calculation of Insulated Steel Columns Exposed to Natural Fire", Fire Safety Journal, 4, pp.219-225.

171.Wickström, U., 1985, "Temperature of Heavily Insulated Steel Structures Exposed to Fire, Fire Safety Journal", 9, pp.281-285.

172.Wickström, U., 1986, "A Very Simple Method for Estimating Temperatures in Fire Exposed Structures", New Technology to Reduce fire Losses and Costs, Edited by S.J. Grayson and D.A. Smith, Elsevier applied Science, London, pp.186-194.

173.Winter, G., 1971, "Discussion of Design of Composite Beams with Formed Metal", Engineering Journal, American Institute of Steel Construction, 8. No.1.

174.Witteveen J., Twilt L., and Bijlaard F.S.K., 1977, "The Stability of Braced and Unbraced Frames at Elevated Temperatures", International Symposium on Stability o steel Structures, Liege, April, Preliminary Report.

175.Woolman J. and Mottram R.A., "The Mechanical and Physical Properties of the British Standard Ensteels", Vol. 1, En 1 to En 10, Published on behalf of the British Iron and Steel Research Association by the Macmillan company, New York, 1964.

176.Wright, H.D., Evans, H.R., and Harding, P.W., 1986, "The Use of Profiled Steel Sheeting in Floor Construction", Journal of Construction Steel Research, 7, pp. 279-295.

177.Zienkiewicz, O.C. and Taylor, R.L., 1989, "The Finite Element Method", Volume 1, Mcgraw-Hill Book Company, Fourth Edition.

APPENDIX A
PARAMETERS IN MATERIAL MODELS

A.1 BILINEAR MODEL

The bilinear material model requires the specification of Young's modulus, the yield strength, the strain-hardening factor, the thermal expansion and their variations with temperature. Table A.1 lists the 20 parameters required for this model. The parameters are defined as given in Figures 2.6, 2.7 and A.1

Table A.1 Parameters for the bilinear material model

No. of parameters	20
Parameters	Young's modulus and temperatures used for trilinear description $(E_1, E_2, T_1, T_2, T_3)$ Yield strength and temperatures for trilinear description $(\sigma_{y1}, \sigma_{y2}, T_{\sigma 1}, T_{\sigma 2}, T_{\sigma 3})$ Strain-hardening factor and temperatures for trilinear description $(\mu_1, \mu_2, T_{\mu 1}, T_{\mu 2}, T_{\mu 3})$ Thermal expansion and temperatures $(\alpha_1, \alpha_2, T_{\alpha 1}, T_{\alpha 2}, T_{\alpha 3})$

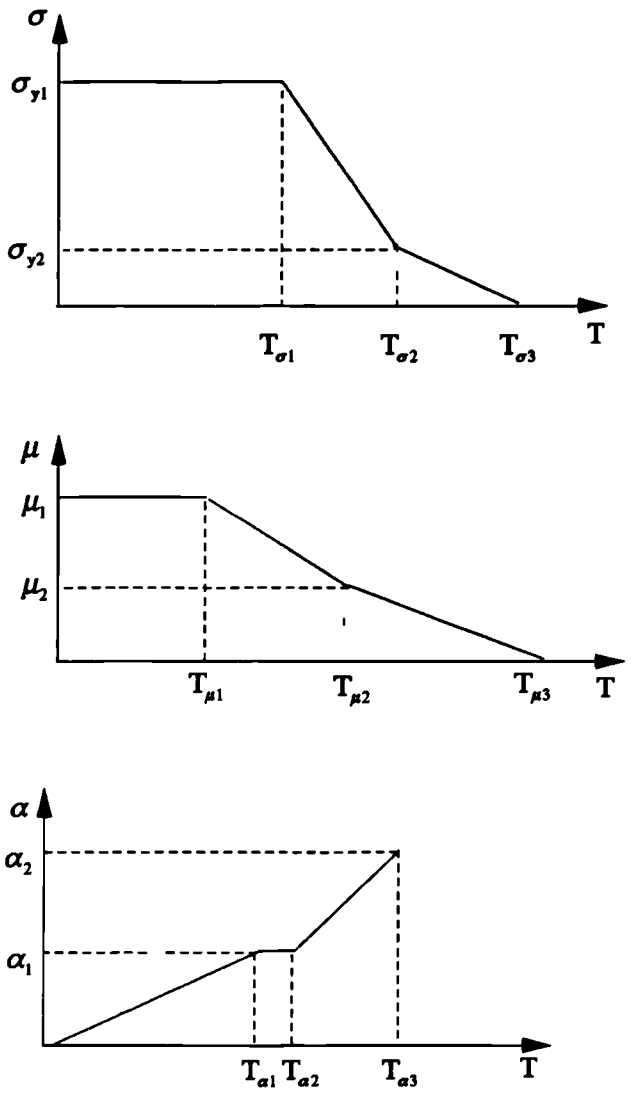


Figure A.1 Parameters for the bilinear model

A.2 ELLIPTICAL MODEL

The elliptical model in ADAPTIC requires 36 parameters in total to describe Young's modulus, the proportional limit, the yield strength, the thermal expansion and their variations with temperature, as given in Table A.2. The nine parameters used to define the proportional limit and its variation with temperature are illustrated in Figure A.2. The other parameters are defined in the same sequence.

Table A.2 Parameters for the elliptical material model

No. of parameters	36
Parameters	Young's modulus and corresponding temperatures $(E_1, E_2, E_3, E_4, T_1, T_2, T_3, T_4, T_5)$ Yield strength and corresponding temperatures $(f_{y1}, f_{y2}, f_{y3}, f_{y4}, T_{y1}, T_{y2}, T_{y3}, T_{y4}, T_{y5})$ Proportional limit and corresponding temperatures $(f_{p1}, f_{p2}, f_{p3}, f_{p4}, T_{p1}, T_{p2}, T_{p3}, T_{p4}, T_{p5})$ Thermal expansion and corresponding temperatures $(\alpha_1, \alpha_2, \alpha_3, \alpha_4, T_{\alpha 1}, T_{\alpha 2}, T_{\alpha 3}, T_{\alpha 4}, T_{\alpha 5})$

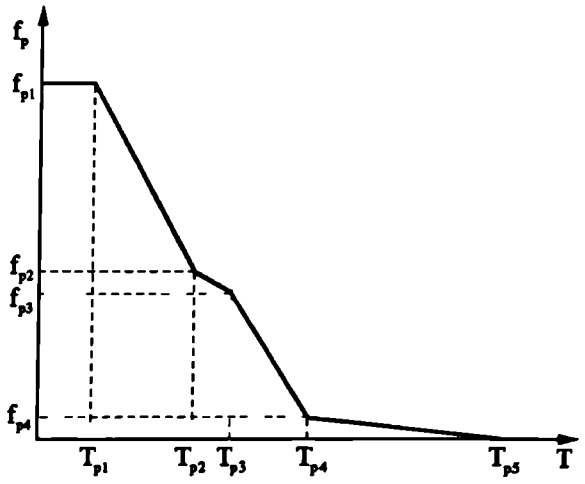


Figure A.2 Description of the variation of the proportional limit with temperature

A.3 CREEP MODEL

The creep model utilises 28 parameters. In addition to the 20 parameters for the bilinear material model, 8 more parameters are required to specify the creep response of the material, as discussed in Chapter 3.

Table A.3 Parameters for the creep model

No. of parameters	28
Parameters	The first 20 properties are the same as those of the bilinear model. Material constants for modelling creep (A, B, C, D, F, G, ΔH, R, σ^*) (as defined in Chapter 3)

APPENDIX B
PARAMETERS FOR THE SLAB ELEMENT

B.1 GEOMETRY

To define the geometry of a composite steel decked slab element requires the specification the dimensions of the cross section and the reinforcement, as listed in Table B.1.

Table B.1 Parameters for the cross section dimensions of a composite steel decked slab

No. of parameters	10
Parameters	Concrete depth (t) Rib depth (H) Rib width (x_1) Rib Space (x_2) Ratio of rib width at bottom to x_1 (R) Thickness of steel decking (t_s) Thickness of longitudinal reinforcement (Area of reinforcement/per unit length) Thickness of transversal reinforcement (Area of reinforcement/per unit length) Position of longitudinal reinforcement (d_l) Position of transversal reinforcement (d_t)

B.2 SLAB ELEMENT

A slab element is defined by 12 nodes, as illustrated in Figure B.2. The first two nodes define the local x-axis.

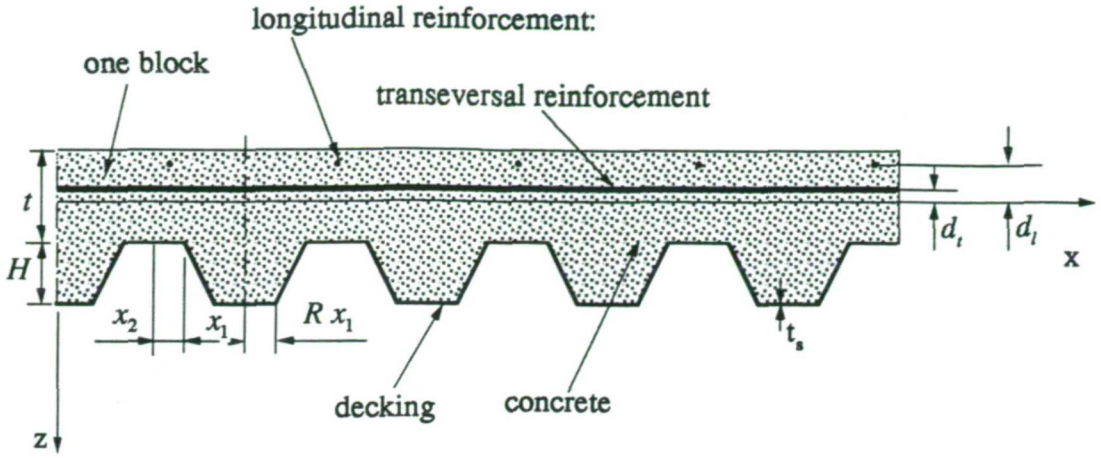


Figure B.1 Cross section of a composite steel decked slab

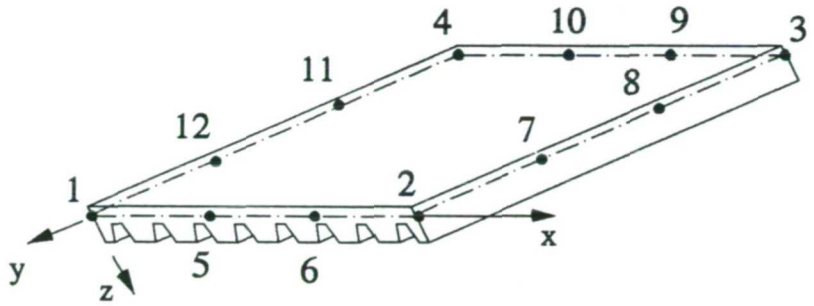


Figure B.2 Nodal sequence for a slab element

APPENDIX C
BLOCK INTERNAL DISPLACEMENTS

In Chapter 6, a procedure is presented for interpolating the displacement fields within a block domain in terms of 15 parameters. As mentioned, the 6 external parameters can be obtained from the first level displacement interpolation, the element cubic shape functions. A simplified method for evaluating the other 9 internal parameters is described below.

From the formulation given in Chapter 6, a block, shown in Figure C.1, can be considered as a structure consisting of three short beams which have a bending stiffness associated with w and θ_X, and axial stiffness associated with u. If the block stiffness is known, a procedure of static condensation and recovery can be carried out to obtain the internal displacement parameters. For this purpose, the stiffness of one unit is first obtained.

Each unit is considered as one beam element, as shown in Figure C.1(b), allowing for transverse shear deformation. Thus, a plane initially normal to the mid-surface remains straight but not necessarily normal. θ_X represents the rotation of a line that is initially normal to the undeformed longitudinal axis of the beam. This beam element has 7 degrees of freedom, giving linear interpolation of u and θ_X, and parabolic interpolation of w. The second level displacement interpolation defined in Section 2.3 is applicable to this element:

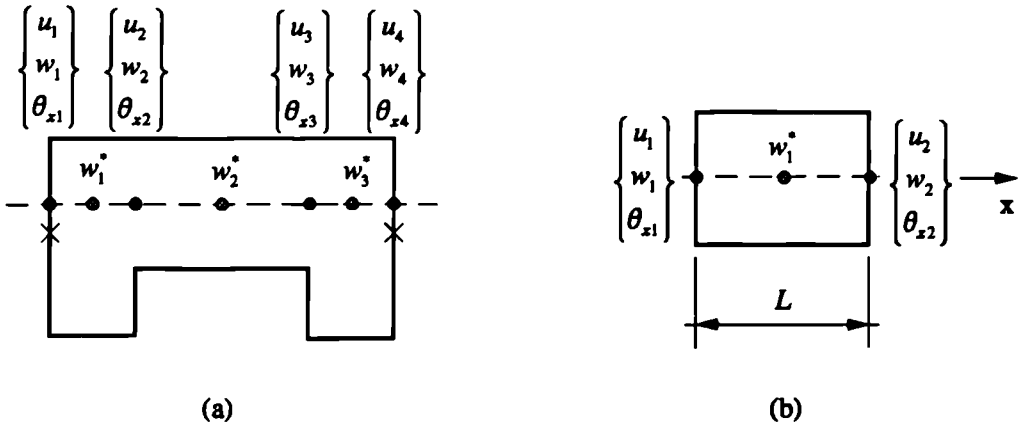


Figure C.1 One block consisting of three short beams

$$\{u\} = \left[\frac{1}{2}(1-\bar{\xi}) \quad \frac{1}{2}(1+\bar{\xi})\right]\begin{Bmatrix} u_1 \\ u_2 \end{Bmatrix} = [H_u]\begin{Bmatrix} u_1 \\ u_2 \end{Bmatrix} \tag{C.1}$$

$$\{\theta_x\} = \left[\frac{1}{2}(1-\bar{\xi}) \quad \frac{1}{2}(1+\bar{\xi})\right]\begin{Bmatrix} \theta_{x1} \\ \theta_{x2} \end{Bmatrix} = [H_\theta]\begin{Bmatrix} \theta_{x1} \\ \theta_{x2} \end{Bmatrix} \tag{C.2}$$

$$\{w\} = \left[\frac{1}{2}(\bar{\xi}-\bar{\xi}^2) \quad \frac{1}{2}(\bar{\xi}+\bar{\xi}^2) \quad 1-\bar{\xi}^2\right]\begin{Bmatrix} w_1 \\ w_2 \\ w_1^* \end{Bmatrix} = [H_w]\begin{Bmatrix} w_1 \\ w_2 \\ w_1^* \end{Bmatrix} \tag{C.3}$$

The coordinate x follows the same interpolation as displacement u and one order lower than w, hence the element is an iso-subparametric element. Construction of the element stiffness matrix requires the following derivatives,

$$[J] = \left[\frac{\partial x}{\partial \bar{\xi}}\right] = \frac{L}{2} \tag{C.4}$$

$$\frac{\partial u}{\partial x} = [J]^{-1}\frac{\partial u}{\partial \bar{\xi}} = \frac{1}{L}[-1 \quad 1]\begin{Bmatrix} u_1 \\ u_2 \end{Bmatrix} = [B_u]\begin{Bmatrix} u_1 \\ u_2 \end{Bmatrix} \tag{C.5}$$

$$\frac{\partial \theta_x}{\partial x} = [J]^{-1}\frac{\partial \theta_x}{\partial \bar{\xi}} = \frac{1}{L}[-1 \quad 1]\begin{Bmatrix} \theta_{x1} \\ \theta_{x2} \end{Bmatrix} = [B_\theta]\begin{Bmatrix} \theta_{x1} \\ \theta_{x2} \end{Bmatrix} \tag{C.6}$$

$$\frac{\partial w}{\partial x} = [J]^{-1}\frac{\partial w}{\partial \bar{\xi}} = \frac{1}{L}[(2\xi-1) \quad (2\xi+1) \quad -4\xi]\begin{Bmatrix} w_1 \\ w_2 \\ w^* \end{Bmatrix} = [B_w]\begin{Bmatrix} w_1 \\ w_2 \\ w^* \end{Bmatrix} \tag{C.7}$$

The element stiffness matrix may be considered as having three parts, corresponding to axial, bending and shear actions, respectively:

$$\begin{aligned}[\mathbf{K}] = &\int_{-1}^{1}[B_u]^T EA[B_u]Jd\xi + \int_{-1}^{1}[B_\theta]^T EI[B_\theta]Jd\xi \\ &+\int_{-1}^{1}[B_w - H_\theta]^T GAk[B_w - H_\theta]Jd\xi\end{aligned} \tag{C.8}$$

With respect to element displacement vector $\{u_1 \quad w_1 \quad \theta_1 \quad u_2 \quad w_2 \quad \theta_2 \quad w_1^*\}^T$, the above integration gives the following element stiffness matrix:

$$[\mathbf{K}] = \begin{bmatrix} \frac{EA}{L} & 0 & 0 & -\frac{EA}{L} & 0 & 0 & 0 \\ & \frac{7GAk}{3L} & \frac{5GAk}{6} & 0 & \frac{GAk}{32} & \frac{GAk}{6} & \frac{-8GAk}{3L} \\ & & \frac{GAkL}{3}+\frac{EI}{L} & 0 & -\frac{GAk}{6} & \frac{GAkL}{6}-\frac{EI}{L} & \frac{-2GAk}{3} \\ & & & \frac{EA}{L} & 0 & 0 & 0 \\ & & & & \frac{7GAk}{3L} & -\frac{5GAk}{6} & \frac{-8GAk}{3L} \\ & \text{sym.} & & & & \frac{GAkL}{3}+\frac{EI}{L} & \frac{2GAk}{3} \\ & & & & & & \frac{16GAk}{3L} \end{bmatrix} \quad \text{(C.9)}$$

in which, E is Young's modulus, G is the shear modulus, A is the area of beam cross section, and k is a shape factor accounting for a parabolic distribution of the shear stress over a rectangular cross section (k=6/5).

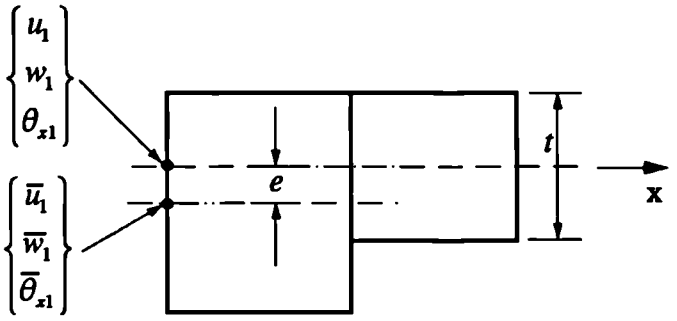


Figure C.2 Eccentricity of the end beam

Since the neutral axes of the end units do not coincide with that of the middle unit when they are considered as individual beams, transformation will be performed to take the eccentricity into account. From Figure C.2, the two sets of displacement at the left end, on the beam neutral axis and the required reference axis respectively, can be related to each other through the following expression:

$$\begin{Bmatrix} \bar{u}_1 \\ \bar{w}_1 \\ \bar{\theta}_{x1} \end{Bmatrix} = \begin{bmatrix} 1 & 0 & -e \\ 0 & 1 & 0 \\ 0 & 0 & 1 \end{bmatrix} \begin{Bmatrix} u_1 \\ w_1 \\ \theta_{x1} \end{Bmatrix} \quad \text{(C.10)}$$

$$\{\bar{\delta}\} = [H]\{\delta\} \quad \text{(C.11)}$$

where $\{u_1 \quad w_1 \quad \theta_{x1}\}^T$ is block end displacement vector, $\{\bar{u}_1 \quad \bar{w}_1 \quad \bar{\theta}_{x1}\}^T$ is the displacement at the beam neutral axis, and e is the eccentricity. So for the unit displacements, the following relationship exists,

$$\begin{Bmatrix} \bar{\delta}_1 \\ \bar{\delta}_2 \\ w^* \end{Bmatrix} = \begin{bmatrix} H & & \\ & H & \\ & & 1 \end{bmatrix} \begin{Bmatrix} \delta_1 \\ \delta_2 \\ w^* \end{Bmatrix} = [T_e] \begin{Bmatrix} \delta_1 \\ \delta_2 \\ w^* \end{Bmatrix} \tag{C.12}$$

in which the subscripts 1 and 2 correspond to two ends of the unit, respectively.

After the generation of element stiffness, the block stiffness can be assembled from each beam unit.

To evaluate the internal displacement in terms of the block end displacements, static condensation is undertaken. If $\{\mathbf{d}\}$ is the block displacement vector consisting of all the 15 freedoms, and is partitioned so that $\{\mathbf{d}\} = [d_e \quad d_i]^T$, where $\{d_e\}$ are the block external displacements and $\{d_i\}$ are the internal degrees of freedom, then the equilibrium equation of the block becomes:

$$\begin{bmatrix} \mathbf{k}_{ee} & \mathbf{k}_{ei} \\ \mathbf{k}_{ie} & \mathbf{k}_{ii} \end{bmatrix} \begin{Bmatrix} d_e \\ d_i \end{Bmatrix} = \begin{Bmatrix} r_e \\ r_i \end{Bmatrix} \tag{C.13}$$

If the load is assumed to apply at the block ends only, with $\{r_i\} = 0$, the internal displacement can be obtained from

$$\{d_i\} = -[\mathbf{k}_{ii}]^{-1}[\mathbf{k}_{ie}]\{d_e\} = [T]\{d_e\} \tag{C.14}$$